MICROCOPY RESOLUTION TEST CHART

NATIONAL BUREAU OF STANDARDS-1963-A

AFGL-TR-85-0021

ELECTRON AND ION DISTRIBUTIONS AT HIGH LATITUDES
AS MEASURED BY THE AIR FORCE POLAR ORBITING SATELLITES

M. Susan Gussenhoven

Boston College
Physics Department
Chestnut Hill, Massachusetts 02167

Final Report
1 April 1985 - 30 September 1983

2 February 1985

DTIC
SELECTE
MAY 06 1985
E

85 04 08 037

"This technical report has been reviewed and is approved for publication"

DAVID A. HARDY
Contract Manager

E.G.MULLEN, Chief
Space Particles Environment Branch

FOR THE COMMANDER

RITA C. SAGALYN, Director
Space Physics Division

This report has been reviewed by the ESD Public Affairs Office (PA) and is releasable to the National Technical Information Service (NTIS).

Qualified requestors may obtain additional copies from the Defense Technical Information Center. All others should apply to the National Technical Information Service.

If your address has changed, or if you wish to be removed from the mailing list, or if the addressee is no longer employed by your organization, please notify AFGL/DAA, Hanscom AFB, MA 01731. This will assist us in maintaining a current mailing list.

AD-A153 242

REPORT DOCUMENTATION PAGE

1a. REPORT SECURITY CLASSIFICATION	1b. RESTRICTIVE MARKINGS
Unclassified	

2a. SECURITY CLASSIFICATION AUTHORITY	3. DISTRIBUTION/AVAILABILITY OF REPORT
	Approved for public release; distribution unlimited
2b. DECLASSIFICATION/DOWNGRADING SCHEDULE	

4. PERFORMING ORGANIZATION REPORT NUMBER(S)	5. MONITORING ORGANIZATION REPORT NUMBER(S)
	AFGL-TR-85-0021

6a. NAME OF PERFORMING ORGANIZATION	6b. OFFICE SYMBOL (If applicable)	7a. NAME OF MONITORING ORGANIZATION
Boston College Physics Department		

6c. ADDRESS (City, State and ZIP Code)	7b. ADDRESS (City, State and ZIP Code)
Chestnut Hill, MA 02167	

8a. NAME OF FUNDING/SPONSORING ORGANIZATION	8b. OFFICE SYMBOL (If applicable)	9. PROCUREMENT INSTRUMENT IDENTIFICATION NUMBER
Air Force Geophysics Laboratory	PHG	F19628-81-K-0032

8c. ADDRESS (City, State and ZIP Code)	10. SOURCE OF FUNDING NOS.			
Hanscom AFB, MA 01731	PROGRAM ELEMENT NO.	PROJECT NO.	TASK NO.	WORK UNIT NO.
	61102F	2311	G1	BA

11. TITLE (Include Security Classification) Electron and Ion Distributions at High Latitudes (over)

12. PERSONAL AUTHOR(S)
M. Susan Gussenhoven

13a. TYPE OF REPORT	13b. TIME COVERED	14. DATE OF REPORT (Yr., Mo., Day)	15. PAGE COUNT
Final Report	FROM 04/01/81 TO 09/30/83	85/2/26	241

16. SUPPLEMENTARY NOTATION

17.	COSATI CODES		18. SUBJECT TERMS (Continue on reverse if necessary and identify by block number)
FIELD	GROUP	SUB. GR.	auroral boundaries, auroral activity, precipitating electrons, precipitating ions, DMSP Satellite, SCATHA Satellite, pitch angle diffusion, beam-induced electromagnetic waves, (over)

19. ABSTRACT (Continue on reverse if necessary and identify by block number)

The Final Report for Contract F19628-81-K-0032 presents the results of major studies using Air Force Satellite particle data. These are divided into three main categories: auroral boundary studies; statistical studies of precipitating electrons; and particle dynamics along field lines. In the first, the variation of the equatorial electron boundary is determined as a function of solar wind velocity, IMF-Bz component, Kp, AE and Dst. The systematic variation of the boundary with Kp is used to create an auroral boundary index. In addition, comparison of the variation in the equatorward ion boundary with the electron boundary is given. In the second section the large-scale properties of precipitating electrons measured at low altitudes, empirical contributions to the baseline magnetosphere, and statistical maps of electron precipitation are presented. The occurrence and properties of extremely high latitude (polar cap) auroras are studied using both particle data and DMSP images; a morphology of the polar rain is also developed. Finally, in the third section, the problem of particle dynamics along magnetospheric (over)

20. DISTRIBUTION/AVAILABILITY OF ABSTRACT	21. ABSTRACT SECURITY CLASSIFICATION
UNCLASSIFIED/UNLIMITED ☒ SAME AS RPT. ☐ DTIC USERS ☐	Unclassified

22a. NAME OF RESPONSIBLE INDIVIDUAL	22b. TELEPHONE NUMBER (Include Area Code)	22c. OFFICE SYMBOL
David A. Hardy	617-861-3981	PHG

DD FORM 1473, 83 APR EDITION OF 1 JAN 73 IS OBSOLETE.

Block 11 Contd

as Measured by the Air Force Polar Orbiting Satellites

Block 18 Contd

polar cap arcs, polar rain

Block 19 Contd

field lines is addressed by studies comparing electrons at geosynchronous and low altitudes both statistically and near-simultaneously in case studies; and by a study of induced electromagnetic waves from electron beams.

Additional keywords: DMSP Satellite; SCATHA Satellite.

85 04 08 027

TABLE OF CONTENTS

I. INTRODUCTION

The overall purpose of the scientific research reported here is to use particle data (principally, precipitating electron data) taken aboard polar orbiting U.S. Air Force satellites to conduct broadly based statistical surveys of the high latitude magnetosphere in order a) to determine global magnetospheric activity in near real time, and b) to further efforts to model magnetospheric dynamics.

Figure 1 is a schematic diagram of the noon-midnight meridional cross-section of the magnetosphere showing major features. Solar wind entry at the front of the magnetosphere and along the magnetopause populates the cusp and the mantle (Region 2). Direct entry downtail may also precipitate in the polar caps (Region 1). Various processes, including convection from the mantle in a dawn-dusk electric field (shown in dashed lines) populate the plasmasheet. The magnetospheric tail lobes (regions between the mantles and the plasmasheet) are very sparsely populated. The magnetic field lines at low latitudes in the distant tail occupy these regions and pass through the polar caps and the auroral zones. Thus, for particles that originate in the solar wind the low altitude, high latitude regions of the Earth can be a sink: the time histories of these particles end here. The processes by which particles enter and leave, traverse, and are deposited in the magnetosphere is the major subject of magnetospheric physics. Examination of a class of these particles near the end of their histories can provide more or less information on the large-scale processes within the magnetosphere, the lesser or greater is the ability of small-scale or transient features to obscure them.

Low altitude polar orbiting satellites sample the footprints of the particle populations shown in Figure 1. Four types of precipitation are of particular interest. Two typically manifest themselves as auroras: diffuse

3

auroras and discrete auroras. The other two are principally defined by regions: the cusp and the polar cap. Auroras may also occur in these regions. Each type or region of precipitation is discussed briefly below to indicate current problems to which detailed analysis of Air Force satellite data has been directed.

Diffuse Aurora. The diffuse aurora is identified on DMSP images that show the midnight sector auroral oval as the structureless, relatively faint, region of auroral luminosity on the equatorward edge of the auroral oval. It can be several degrees wide in latitude or only a fraction of a degree. It is always present in the midnight sector. (This statement requires verification from particle data since at very quiet times the diffuse auroral luminosity can fall below imaging instrument detectibility.)

Particle studies of the diffuse aurora show it to be a result of precipitating electrons and protons which have highly thermalized (near Maxwellian) particle distributions (Frank, and the references therein, 1975; and Eather, 1975). The temperatures of the electrons and protons are on the order of 1 keV, with number densities near 1 cm^{-3}. The plasmasheet is now generally accepted as the source of the precipitating particles that cause the diffuse aurora (Vasyliunas, 1968). Plasmasheet particles in the loss cone penetrate directly to low latitudes, and additional acceleration or transport mechanisms are not needed to explain their distributions. Pitch angle diffusion, however, is required to maintain a loss cone population. The inner (most Earthward) edge of the plasmasheet maps into the equatorward edge of the diffuse aurora. Therefore, the dynamics of the inner edge is directly reflected in the motion of the diffuse aurora. Conversely, the dynamics of the inner edge is directly reflected in the motion of the diffuse aurora.

The motion of low energy electrons in the plasmasheet is mainly

4

controlled by the large-scale magnetospheric electric field (Kivelson, 1976). Gradient and curvature drifts from magnetic field spatial variations are energy dependent and are evidenced in trajectories of keV or greater particles. The trajectories of low energy particles (zero energy, to be exact) are electric field equipotentials; the trajectories are displaced radially outward for higher energy particles. Figure 2 is a schematic diagram of equatorial particle trajectories. Near the Earth, the equipotentials will be circular, due to corotation, and closed: zero-energy particles in the plasmasheet do not have access to these equipotentials. The transition between open and closed equipotentials, the first path on which plasmasheet particles have access, is called the zero-energy Alfven layer. The zero-energy Alfven layer, when mapped to the ionosphere, is the equatorward boundary of the diffuse aurora. It is determined entirely by the magneto-spheric electric field.

Analytic models of the magnetospheric electric field combining corotation and cross-tail fields have been developed (Stern, 1975; and Volland, 1973) and predictions compared to a wide variety of measurements, most of which indicate that the cross-tail component increases with radial distance, r, from the Earth as r^γ, where γ is between 2 and 3 (Eijiri et al., 1978; Hughes et al., 1979; and Southwood and Kaye, 1979).

The DMSP precipitating electron data provide the opportunity to monitor the auroral zones along the subsatellite track with high precision and temporal coverage. Two passes, one of the north pole and one of the south pole, are obtained every 100 minutes. Gussenhoven et al. (1981) used these data to determine over 6000 equatorward auroral boundaries in the dawn and dusk sectors. They were found to be ordered by K_p in a highly linear way (absolute values of the correlation coefficients ~ 0.9). The results for the

5

northern and southern hemispheres, for the local time sector 19-20, are shown in Figure 3. The high degree of linearity with which K_p orders the equatorward boundaries indicates that the magnetospheric electric field is also well-ordered by K_p. The boundaries were mapped by a Mead-Fairfield magnetic field model to the magnetic equatorial plane and compared to the zero-energy Alfven layers predicted by electric field models. The results are shown in Figure 4. In addition to showing that the value of γ is indeed between 2 and 3, it is apparent that the direction of the cross-tail electric field, which is along the axis of symmetry of the zero-energy Alfven layer, is a function of magnetic activity. Figure 4 also shows a slight tendency for γ to decrease with increasing K_p (indicated by more elongated boundaries for smaller γ).

Other studies show that the boundary continues through the midnight sector (Sheehan and Carovillalno, 1978; and Kamide and Winningham, 1977). The work performed here extends the DMSP electron boundary studies to the noon and midnight sectors, examines their variations with solar wind parameters and other magnetic indices, and uses the electron boundaries to define an auroral activity index. In addition, preliminary work on the variation of precipitating ion boundaries is also presented. These studies are given in Section II.

Large-scale statistical maps of precipitating electrons were assembled using the DMSP data, and these give more detailed information on the diffuse aurora and its variation with magnetic activity. These are presented in Section III. Comparisons of the precipitating electron populations in the diffuse aurora and their source population in the plasmasheet are given in the first two papers of Section IV.

Discrete Auroras. Discrete auroral arcs occur in and poleward of the diffuse aurora. They are thicker and brighter in the midnight and evening

6

sectors than in the morning and dayside. While arcs can continue through the morning sector during active times, they are more typically characterized as a family of short, weak arcs, particularly during substorm recovery phases (Eather, 1975). The entire collection of morning arcs can move to ~xtremely high latitudes, decreasing in intensity with increasing latitude. Discrete arcs are the most dramatic manifestation of the substorm, a violent surge of magnetic and auroral activity lasting 1-2 hours.

Discrete arcs lie near the boundary between open and closed field lines, a boundary which is expected to be highly variable, particularly in the open magnetosphere. The energy dispersion of precipitating electrons that cause discrete arcs is described by the 'inverted-V' and indicates that they have undergone an acceleration process along magnetic field lines (Frank and Ackerson, 1972; and Lin and Hoffman, 1979). The most frequently suggested acceleration process is that resulting from parallel electric fields that lie below an altitude of several Earth radii and are short-lived compared to overall magnetospheric electric field changes. While the most poleward discrete auroral arc is often, particularly during times of high activity, coincident with the poleward boundary of the auroral oval, as determined by precipitating electrons, this is not always the case. On the morningside, in particular, high fluxes of low energy particles, in which discrete arcs may be imbedded, can reach very high latitudes. Therefore, the poleward boundary of the oval is dynamic and likely a result of several competing processes. Statistical studies of the poleward boundary are unlikely, at this stage of theoretical understanding, to do anything but average out the small scale processes of greatest interest.

One of the major outstanding problems associated with discrete arcs is a clear picture of the magnetic topology of the field lines on which they lie.

Work done on the ISIS satellite data (<u>Venkatarangan et al.</u>, 1975) indicates that in the midnight sector they lie on closed field lines. However, a study of the spatial occurrence of over 200 inverted-V events by <u>Lin and Hoffman</u> (1979) shows them to reach to latitudes >80° CGM, outside the accepted range of closed field lines. Particle pitch angle signatures are often used in fairly simple ways to choose between open and closed field lines. The most sophisticated work in this field has been done in the area of energetic solar particle access to the polar cap, i.e., along open magnetic field lines (see the review by <u>Paulikas</u>, 1974) and an extension of this work to investigate the relationship between trapping boundaries and energetic particle boundaries may help to clarify the problem. Two very different approaches to discrete auroral dynamics were taken here. The first was to make statistical maps of auroral precipitation, and to study their variation with magnetic activity. The results are given in the first two papers of Section III. The average properties of precipitating electrons were also used as input to ionospheric electron production codes to determine average values for Hall and Pedersen conductivities which, in turn, couple with convection and acceleration processes in discrete arc formation. The second is a theoretical study of wave production by electron beams. This study is presented in Section III.

The Polar Cusp. The polar cusp is conceptually perceived as the region on the dayside of the magnetosphere where $B_s \rightarrow 0$: B_s being the component of the Earth's magnetic field along the magnetospheric boundary (i.e., along the magnetopause). That is, the cusp is the dayside region between closed magnetic field lines and field lines that are swept back into the magnetotail (or alternately, that lie on open field lines). A cusp configuration is anticipated for both open and closed models of the magnetosphere (Figure 5).

The cusp has occupied a prominent position in magnetospheric physics for

8

some time because it is a region of direct entry of solar wind particles (via the magnetosheath) into the magnetosphere (Paschmann et al., 1976). How the particles penetrate to low altitudes and how their original distribution functions are altered in the process depends greatly on the transport mechanism which, in turn, may depend on magnetospheric model. For instance, Reiff et al. (1977) have suggested two mechanisms: cross-magnetic field line diffusion, appropriate to both closed and open models; and a merging process, appropriate only to the open model. Evidence for both is given by them. A large body of data shows the cusp to be a region of considerable turbulence over a wide range of altitudes (see review by D'Angelo, 1977; and Potemra et al., 1978). The type of instability involved may also be strongly dependent on magnetic field model. Therefore, determination of the cusp particle populations at both high and low altitudes; the shape of the cusp, as determined by particles, waves, currents, and electric fields; and the dynamics of the shape of the cusp have, taken as a whole, been expected to lead to definitive evidence for one magnetospheric model or the other. Even a cursory examination of the abundant research conducted in the dayside cusp shows that the often designated 'zone of confusion' is still far from being understood.

Particle signatures show the cusp to be located at latitudes 75°-80° CGM and to extend several hours around local noon. Controversy exists a) about the type of field line the cusp spans: open, closed, or both (McDiarmid et al., 1976; Reiff et al., 1977; and Potemra et al., 1977); b) about its relation to discrete and diffuse auroras; c) whether it changes location primarily as a function of interplanetary magnetic field (IMF) (Kamide et al., 1976) or substorm current systems (Eather et al., 1979); d) about the variation of particle energy with latitude; and e) even whether the region is

9

best described by a cusp (pointlike) or a cleft (extended in longitude).

A major cause of these differences may well be that the cusp signature itself is ambiguous, not only between types of measurements: particle, photometric, waves, currents; but also for a class of measurements, say, particles. As particles with direct penetration from the magnetosheath, the cusp particles should have low energies: tens of eV for electrons and ~ 1 keV for protons; and should be flowing down the Earth's magnetic field lines. Therefore, sharp increases in both low energy electrons and protons with increased pitch angle in the distributions along field lines are the ideal signature of the cusp in particle measurements. Satellites without the full complement of instruments required to make this determination (equipped, say, with electron detectors only) have been used to study the cusp. Further, it is found that the turbulence in the cusp can so affect the electron distribution as a function of energy and pitch angle that it bears little resemblance to the ideal signature (Potemra et al., 1978).

Another source of disagreement may be the result of using only a relatively small number of cases (order of magnitude, 10) to discuss cusp dynamics. When variations with magnetic activity and IMF direction are studied, a much larger statistical sample is required for meaningful results. The statistical nature of the cusp region at low altitudes is addressed in Section III.

The Polar Cap. Compared to the auroral zones, the very high latitude regions of the ionosphere are generally quiet and uniform. Without further specificity as yet, we may, as is commonly done, use quietness and uniformity in whatever phenomenon is being measured as the definition of the polar caps. For some phenomena and at specific times, the cap boundaries appear to be quite sharp. And at other times and for a variety of measured quantities, a

10

much less well-defined transition occurs. Even though the boundaries may be sharp, not surprisingly, they differ from event to event and from kind of measurement to kind of measurement. In short, the high latitude edge of oval-auroral arcs and related phenomena is complex and dynamic.

That there should be a polar cap boundary at all is not clear from magnetospheric models, open or closed. In each group of theories, the auroral oval, or active precipitation region, is centered on the region of transition from closed to open field lines. However, there is this important difference: Open models of the magnetosphere are _open_ to being affected by, perhaps even driven by, changes in the solar wind magnetic field since the Earth's field lines at high latitudes merge with those of the solar wind. In closed models, the solar wind field is swept by the magnetosphere without direct connection, and in these models it is difficult to see how changes in the solar wind field could drive internal magnetospheric dynamics since the inner magnetosphere is _closed_ to the solar wind field (or the interplanetary magnetic field, IMF).

Interest in the polar caps is, then, twofold. First, as the upper limit to oval activity, a polar cap not only provides a boundary condition to be met in oval studies, but must itself be explained. Second, the dynamics of the upper limit, or the plasticity of the cap, may, by relation to other variations in the solar wind or in the magnetosphere, provide substantial evidence for or against open and closed magnetospheric models.

There is much increased interest in particle precipitation morphology across the caps. Earlier investigations tended to ignore particle activity above the auroral oval since it is minimal there. The lack of interest persisted until very recently, but that is now being corrected by the programs of the ISIS and DMSP satellites which are polar orbiting at low altitudes. Studies are clearly initial. No comprehensive picture of particle activity in

11

the caps has emerged.

Winningham and Heikkila (1974) find a persistent, weak, low energy (100 eV), structureless electron precipitation in the caps which they call the polar rain. Polar showers and polar squalls -- indicating more intense and more structured precipitation and, for the latter, a harder energy spectrum -- are also identified by them. The existence of low energy electron precipitation in these regions at higher altitudes is supported by the work of Burch (1968), Frank and Gurnett (1971), and Yeager and Frank (1976). The polar rain intensity across the cap from dawn to dusk has been shown by Meng et al. (1977) to depend on the y-component of the IMF. The dependency is in the same sense found by Heppner (1972) for increases in the convection electric field across the cap, and by Hardy et al. (1979) for preferentially observing the plasma mantle in the distant tail lobes which map into the caps. No differentiation has yet been attempted for a B_z dependence of the precipitation. The picture that emerges is one in which the motion of the low energy magnetosheath particles is determined principally by the convection electric field in the cap. Analytic models of the cap convection electric field could then be verified by statistical studies of low energy cap precipitation.

Evidence for strong correlations between the electric and magnetic field variations in the polar caps and the various components of the interplanetary magnetic field have been compiled from both ground and satellite measurements (Mansurov, 1969; Heppner, 1972, 1977; Svalgaard, 1973; Paulikas, 1974; Friis-Christensen and Wilhjelm, 1975; Langel, 1975; McDiarmid and Burrows, 1977; Stern, 1977; and Maezawa, 1976, 1978). Some evidence for correlations of the field variations with season also exists.

Theoreticians who favor an open magnetosphere model have great encourage-

ment from these polar cap studies. In particular, vacuum models of the magnetosphere -- models for which there are no magnetospheric particles and therefore only field interactions (direct addition of fields) -- have been constructed by Stern (1973) and Hill and Rassback (1975). These suffer from excessive simplicity, but have produced some clean, quantitative predictions.

Auroral arcs are found to occur infrequently in the polar caps; they have been sighted from the ground at magnetic latitudes greater than 80° over many decades. More recently, optical imaging devices on satellites show these extremely high latitude arcs to vary greatly in length, intensity, internal structure and orientation. They also can emanate from (or terminate in) almost all sectors of the auroral oval. The arcs can occur in groups across significant portions of the cap, or singly. The most dramatic of the polar cap arcs is the single, sun-aligned arc stretching from midnight to noon. (Akasofu, 1972; Eather and Akasofu, 1969; Lassen and Danielson, 1978; and Meng and Akasofu, 1976.)

All problems associated with an explanation of discrete auroral oval arcs also must be dealt with in an explanation of polar cap arcs, the principal one being an acceleration mechanism of appropriate magnitude and duration. In addition, a polar cap arc theory must come to terms with the question of particle source. Discrete oval arcs lie on magnetic field lines that extend through or near the plasmasheet, a constant source of thermalized, hot particles. If one traces the locus of a sun-aligned arc occurring in the central polar cap along magnetic field lines to the outer magnetosphere using one of the stationary magnetic field models in the literature, the mapped locus stretches across the central tail lobe from the magnetosheath to the plasmasheet, that is, through a region charcterized as tenuous and cool. The more common precipitation found in the polar caps, the polar rain, is a

13

steady, low intensity, low energy flux that varies slowly spatially. A tail lobe particle population is an appropriate source for polar rain, but appears unable to account directly for discrete arcs.

On the other hand, since polar cap arcs can occur distinctly isolated from the diffuse aurora, they may more readily yield information about auroral arc acceleration processes, or specific models of arcs, than auroral oval arcs have been able to.

In this report, two studies on polar cap arcs are presented in Section III. Also presented is a statistical study on the morphology of polar rain.

In summary, we report work done on this contract in three sections: Section I presents the results of auroral boundary studies using both precipitating electrons and ions; Section II presents the results of large-scale statistical studies of the auroral oval and the polar cap. In addition, studies on polar cap arcs are presented to understand more fully the nature of polar cap precipitation. Section IV gives studies that compare particle populations at high and low altitudes and work relating to wave-particle processes that link the two. Finally, in Section V, a list of publications and presentations supported by this contract is given.

REFERENCES

Akasofu, S.-I., Midday auroras and polar cap auroras, Geofys. Publ., 29, 73, 1972.

Burch, J.L., Low energy electron fluxes at latitudes above the auroral zone, J. Geophys. Res., 73, 3585, 1968.

D'Angelo, N., Plasma waves and instabilities in the polasr cusp: A review, Rev. Geophys. Sp. Phys., 15, 299, 1977.

Eather, Robert H., Advances in magnetospheric physics: Aurora, Rev. Geophys. Sp. Phys., 13, 925, 1975.

Eather, R.H., and S.-I. Akasofu, Characteristics of polar cap auroras, J. Geophys. Res., 74, 4794, 1969.

Eather, R.H., S.B. Mende, and E.J. Weber, Dayside aurora and relevance to substorm current systems and dayside merging, J. Geophys. Res., 84, 3339, 1979.

Ejiri, M., R.A. Hoffman, and P.H. Smith, The convection electric field model for magnetosphere based on Explorer 45 observations, J. Geophys. Res., 83, 4811, 1978.

Frank, L.A., Magnetospheric and auroral plasmas: A short survey of progress, Rev. Geophys. Sp. Phys., 13, 974, 1975.

Frank, L.A., and K.L. Ackerson, Local time survey of plasma at low altitudes over the auroral zone, J. Geophys. Res., 77, 4116, 1972.

Frank, L.A., and D.A. Gurnett, Distributions of plasmas and electric fields over the auroral zones and polar caps, J. Geophys. Res., 76, 6829, 1971.

Friis-Christensen, E., and J. Wilhjelm, Polar cap currents for different directions of the interplanetary magnetic field in the Y-Z plane, J. Geophys. Res., 80, 1248, 1975.

Gussenhoven, M.S., D.A. Hardy, and W.J. Burke, DMSP/F2 electron observations
of equatorward auroral boundaries and their relationship to
magnetospheric electric fields, J. Geophys. Res., 86, 768, 1981.

Hardy, D.A., H.K. Hills, and J.W. Freeman, Occurrence of the lobe plasma at
lunar distances, J. Geophys. Res., 84, 72, 1979.

Heppner, J.P., Polar cap electric field distributions related to the
interplanetary magnetic field direction, J. Geophys. Res., 77, 4877, 1972.

Heppner, J.P., Empirical models of high-latitude electric fields, J. Geophys.
Res., 82, 1115, 1977.

Hill, T.W., and M.E. Rassbach, Interplanetary magnetic field direction and the
configuration of the day side magnetosphere, J. Geophys. Res., 80, 1,
1975.

Hughes, W.J., R.L. McPherron, J.N. Barfield, and B.H. Mauk, A compressional
Pc4 pulsation observed by three satellites in geostationary orbit near
local midnight, Planet. Sp. Sci., 27, 821, 1979.

Kamide, Y., and J.D. Winningham, A statistical study of the "instantaneous"
nightside auroral oval: the equatorial boundary of electron
precipitation as observed by the Isis 1 and 2 satellites, J. Geophys.
Res., 82, 5573, 1977.

Kamide, Y., J.L. Burch, J.D. Winningham, and S.-I. Akasofu, Dependence of the
latitude of the cleft on the interplanetary magnetic field and substorm
activity, J. Geophys. Res., 81, 698, 1976.

Kivelson, M.G., Magnetospheric electric fields and their variations with
geomagnetic activity, Rev. Geophys. Sp. Phys., 14, 189, 1976.

Langel, R.A., A comparison of electric and magnetic field data from the OGO 6
spacecraft, J. Geophys. Res., 80, 4661, 1975.

Lassen, K., and C. Danielsen, Quiet time pattern of auroral arcs for different

directions of the interplanetary magnetic field in the y-z plane,

J. Geophys. Res., 83, 5277, 1978.

Lin, C.S., and R.A. Hoffman, Characteristics of the inverted-V event,

J. Geophys. Res., 84, 1514, 1979.

Maezawa, K., Magnetospheric convection induced by the positive and negative z

components of the interplanetary magnetic field: quantitative analysis

using polar cap magnetic records, J. Geophys. Res., 81, 2289, 1976.

Maezawa, K., Dependence of geomagnetic activity on solar wind parameters: a

statistical approach, Solar Terrestrial Environmental Research in Japan,

2, 103, 1978.

Mansurov, S.M., New evidence of a relationship between magnetic fields in

space and earth, Geomagn. Aeron., 9, 622, 1969.

McDiarmid, J.B., and J.R. Burrows, Comparison of magnetic field perturbations

at high latitudes with charged particles and IMF measurements, EOS,

Transactions, American Geophysical Union, 58, 478, 1977.

McDiarmid, J.B., J.R. Burrows, and E.E. Budzinski, Particle properties in the

dayside cleft, J. Geophys. Res., 81, 221, 1976.

Meng, C.I., S.-I. Akasofu, The relation between the polar cap auroral arc and

the auroral oval arc, J. Geophys. Res., 81, 4004, 1976.

Meng, C.I., S.-I. Akasofu, and K.A. Anderson, Dawn-dusk gradient of the

precipitation of low-energy electrons over the polar cap and its relation

to the interplanetary magnetic field, J. Geophys. Res., 82, 5271, 1977.

Paschmann, G., G. Haerendahl, N. Schopke, and H. Rosenbauer, Plasma and

magnetic field characteristics of the distant polar cusp near local noon:

The entry layer, J. Geophys. Res., 81, 2883, 1976.

Paulikas, G.A., Tracing of high-latitude magnetic field lines by solar

particles, Revs. of Geophys. and Space Phys., 12, 117, 1974.

17

Potemra, T.A., W.K. Peterson, J.P. Doering, C.O. Bostrom, R.W. McEntire, and R.A. Hoffman, Low-energy particle observations of the quiet dayside cusp from AE-C and AE-D, J. Geophys. Res., 82, 4765, 1977.

Potemra, T.A., J.P. Doering, W.K. Peterson, C.O. Bostrom, R.A. Hoffman, and L.H. Brace, AE-C observations of low-energy particles and ionspheric temperatures in the turbulent polar cusp: evidence for the Kevin-Helmholz instability, J. Geophys. Res., 83, 3877, 1978.

Reiff, P.H., T.W. Hill, and J.L. Burch, Solar wind plasma injection at the dayside magnetospheric cusp, J. Geophys. Res., 82, 479, 1977.

Sheehan, R.E., and R.L. Carovillano, Characteristics of the equatorward auroral boundary near midnight determined from DMSP images, J. Geophys. Res., 83, 4749, 1978.

Southwood, D.J., and S.M. Kaye, Drift boundary approximations in simple magnetospheric convection models, J. Geophys. Res., 84, 5773, 1979.

Stern, D.P., A study of the electric field in an open magnetospheric model, J. Geophys. Res., 78, 7297, 1973.

Stern, D.P., The motion of a proton in the equatorial magnetosphere, J. Geophys. Res., 80, 595, 1975.

Stern, D.P., Large-scale electric fields in the earth's magnetosphere, Revs. Geophys. and Space Phys., 15, 156, 1977.

Svalgaard, L., Polar cap magnetic variations and their relationship with the interplanetary magnetic sector structure, J. Geophys. Res., 78, 2066, 1973.

Vasyliunas, V.M., A survey of low energy electrons in the evening sector of the magnetosphere with OGO 1 and OGO 3, J. Geophys. Res., 73, 2839, 1968.

Venkatarangan,P., R.R. Burrows, and I.B. McDiarmid, On the angular

distributions of electrons in "inverted-V" substructures, J. Geophys. Res., 80, 66, 1975.
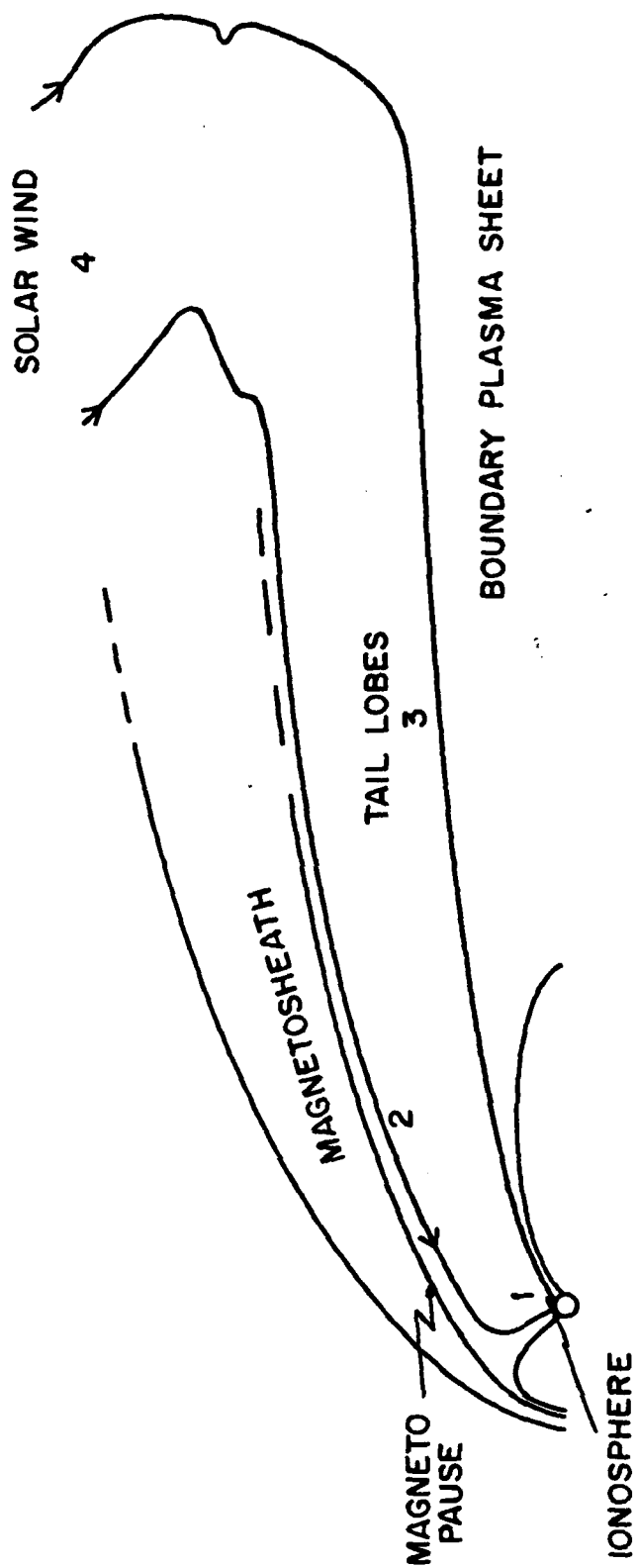
Volland, H., A semiempirical model of large scale magnetospheric electric fields, J. Geophys. Res., 78, 171, 1973.
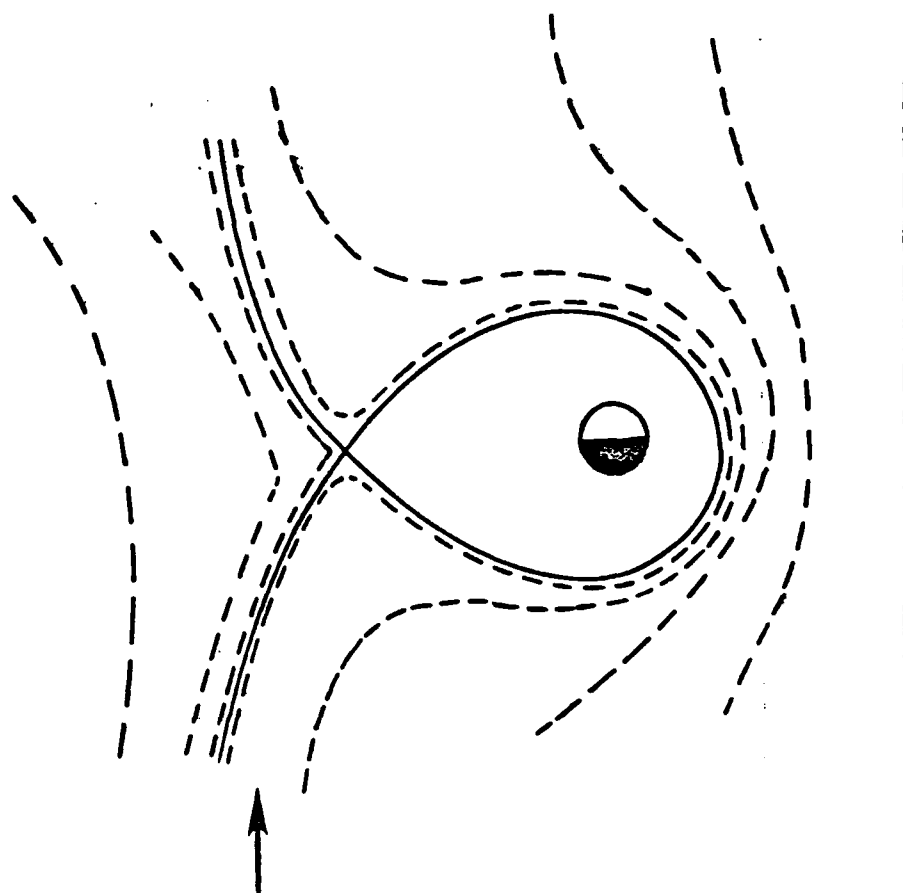
Winningham, J.D., and W.J. Heikkila, Polar cap auroral electron fluxes observed with Isis I, J. Geophys. Res., 79, 949, 1974.
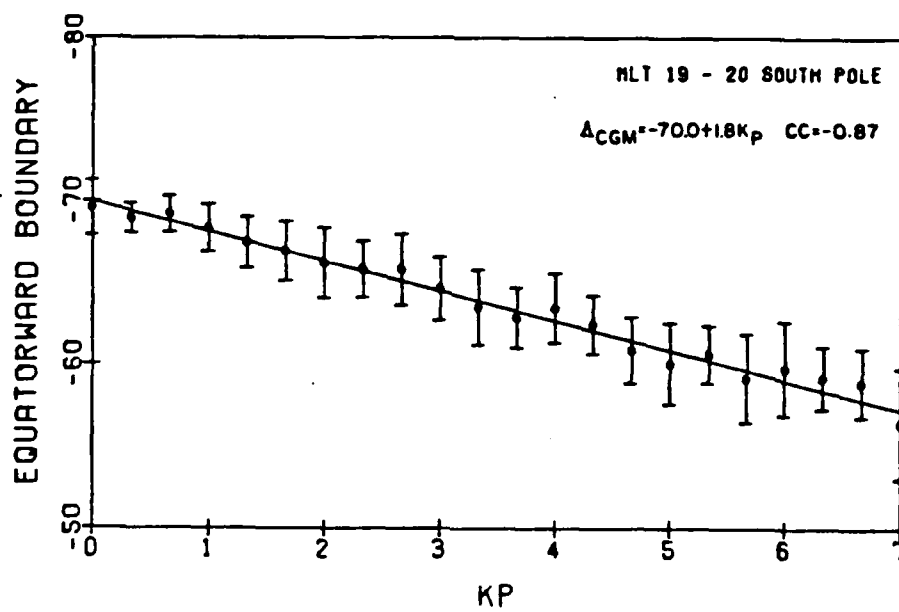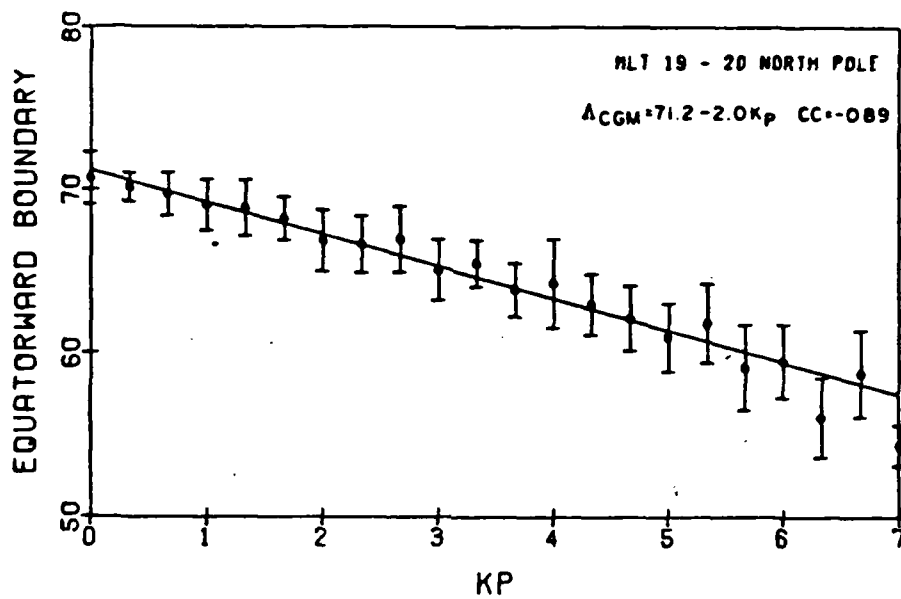
Yeager, D.M., and L.A. Frank, Low-energy electron intensities at large distances over the earth's polar cap, J. Geophys. Res., 81, 3966, 1976.
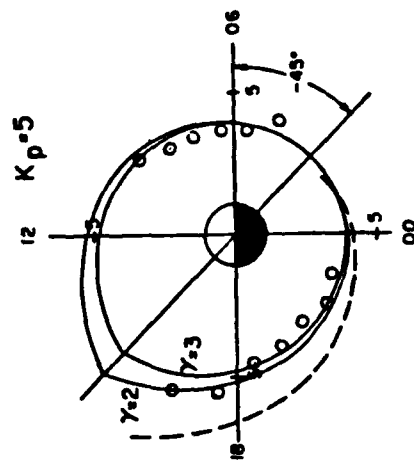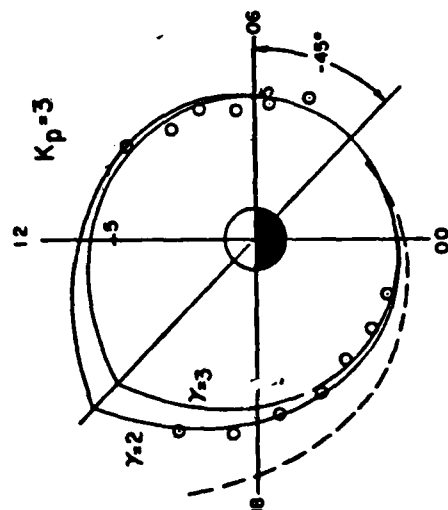
FIGURE CAPTIONS

Figure 1   Schematic diagram of the magnetosphere showing the cusp and cap
            regions (1), the plasma mantle (2), the tail lobes (3), and
            possible direct connection to the solar wind downtail (4). Also
            shown is the region of the boundary plasmasheet.

Figure 2   Schematic diagram of particle trajectories in the equatorial
            plane. Particles move from the pre-midnight region (near the
            arrow), under the influence of magnetospheric electric and
            magnetic fields, to the dayside (dashed lines). The solid line
            represents the zero-energy Alfven layer. No particles from the
            plasmasheet penetrate the closed portion of this boundary.

Figure 3   Mean values and standard deviations of equatorward boundaries in
            each K_p bin plotted as a function of K_p for north and south poles
            in the 19-20 MLT sector. The solid line results from a linear
            regression performed using individual boundary determinations.

Figure 4   Volland-Stern injection boundaries for $\gamma = 2$ and $\gamma = 3$ rotated to
            fit the inner edge of the plasmasheet as determined by the
            DMSP-F2 auroral boundaries, for various K_p. The Mauk-McIlwain
            injection boundary is also shown (dashed line).

Figure 5   Schematic diagram of the magnetic field lines in the cusp region
            for a) the closed magnetosphere; and b) the open magnetosphere.

SOLAR WIND
4

MAGNETOSHEATH

TAIL LOBES
3

BOUNDARY PLASMA SHEET

MAGNETO
PAUSE

IONOSPHERE

2

1

21

MLT 19 - 20 NORTH POLE

$\Lambda_{CGM} = 71.2 - 2.0 K_P \quad CC = -0.89$

MLT 19 - 20 SOUTH POLE

$\Lambda_{CGM} = -70.0 + 1.8 K_P \quad CC = -0.87$

23

(a)

MAGNETOPAUSE

(b)

MAGNETOPAUSE
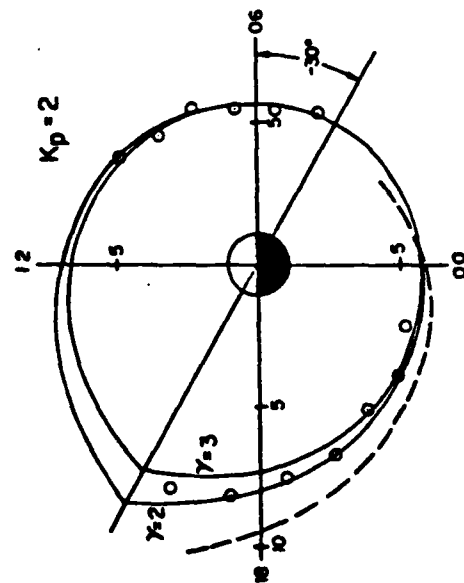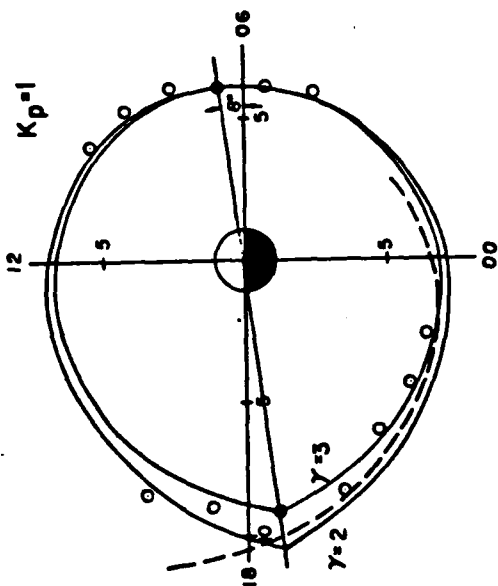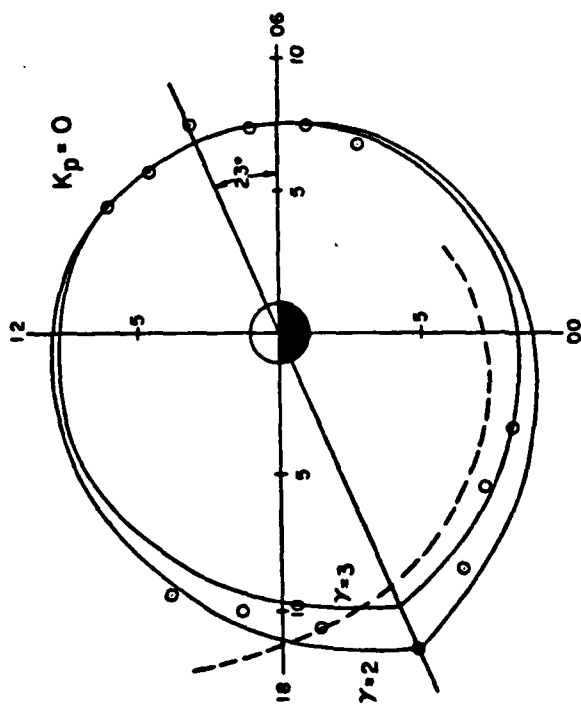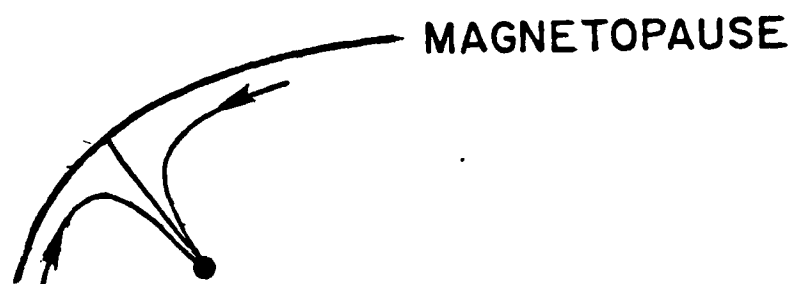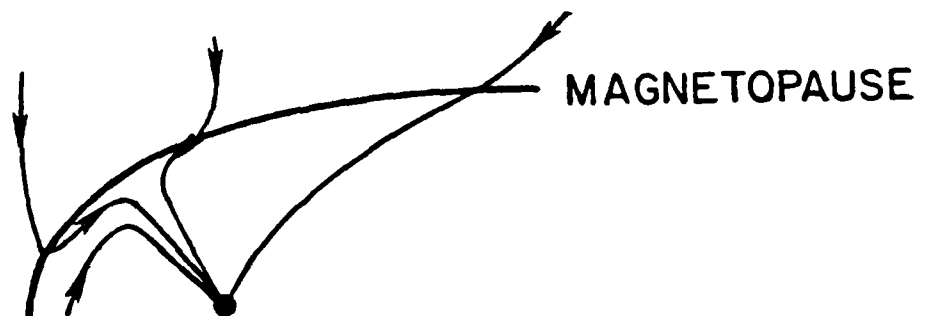
II. AURORAL BOUNDARY STUDIES

See also: 1978 Diffuse Auroral Boundaries and a Derived Auroral Boundary Index. M.S. Gussenhoven, D.A. Hardy, N. Heinemann, and E. Holeman, Rep. AFGL-TR-82-0398, Air Force Geophysical Laboratory, Hanscom AFB, MA, 1982, ADA130175.

Precipitating Electron and Ion Detectors (SSJ/4) for the Block 5D/Flights 6-10 DMSP Satellites: Calibration and Data Presentation, D.A. Hardy, L.K. Schmitt, M.S. Gussenhoven, F.J. Marshall, H.C. Yeh, T.L. Schumaker, A. Huber, and J. Pantazis, AFGL-TR-84-0317, Air Force Geophysics Laboratory, Hanscom AFB, MA, 1985 (in press).

DMSP/F2 Electron Observations of Equatorward Auroral Boundaries and Their Relationship to the Solar Wind Velocity and the North-South Component of the Interplanetary Magnetic Field

D. A. HARDY AND W. J. BURKE

Air Force Geophysics Laboratory, Hanscom Air Force Base, Massachusetts 01731

M. S. GUSSENHOVEN AND N. HEINEMANN

Physics Department, Boston College, Chesnut Hill, Massachusetts 02167

E. HOLEMAN

Physics Research Division, Emmanuel College, Boston, Massachusetts 02115

Approximately 2500 equatorward boundaries of auroral electron precipitation were determined for times when hourly averages of the interplanetary magnetic field and solar wind velocity V were available. The equatorward boundaries were determined from data returned by the SSJ/3 electron detector on board the DMSP/F2 satellite in magnetic local sectors between 0400 and 1100 hours on the morningside of the oval and between 1500 and 2300 hours on the eveningside of the oval. The boundary data were separated into 1-hour zones in magnetic local time. Within each zone the boundary locations were studied as functions of B_z and B_z^2, VB_z and VB_z^2. Significant results were obtained when the boundaries were correlated with hourly average of B_z and VB_z for the hour preceding the one in which the boundary was measured and when the linear regression was performed separately for data points where $B_z \leq 1$ nT and $B_z > 1$ nT. For points where $B_z \leq 1$ nT, the correlation with B_z and VB_z gave slopes generally between $0.8°$ and $1.2°/$nT and between $1.5°$ and $2.5°/$mV/m, respectively, with correlation coefficients of ~ 0.7. The latitudes of the intercepts tend to decrease with increasing local time in the evening sector and with decreasing local time in the morning sector. In the range above 1 nT, the slope of the best fit line for correlation with B_z and VB_z changes sign. Slopes fall in the range $-0.1°$ to $-0.4°/$nT and $0.21°$ to $1°/$mV/m. Correlation coefficients are typically worse than -0.4. Correlations of the boundary with B_z^2 and VB_z^2 for both ranges of B_z are uniformly worse than those for B_z and VB_z. The trend in slopes and intercepts with magnetic local time for $B_z \leq 1$ nT is found to be similar to that previously found for the correlation of the boundaries with Kp (Gussenhoven et al., 1981). In this range of B_z, Kp and VB_z are found to be related by the equation $Kp = 2.01 - 0.91 \, VB_z$ (mV/m). From the work of Ejiri et al. (1978) an equation relating the magnetospheric electric potential to VB_z is derived. The results are in agreement with the general features of the half-wave rectifier model of the magnetosphere and measurements of polar cap potential.

INTRODUCTION

The equatorward boundary of electron precipitation in the auroral zone maps along magnetic field lines to the inner edge of the plasma sheet [*Vasyliunas*, 1970; *Lassen*, 1974; *Winningham et al.*, 1975; *Lui et al.*, 1977]. The inner edge of the plasma sheet corresponds to the zero-energy Alfvén layer in the equatorial magnetosphere, i.e., the boundary between corotating and noncorotating plasma [*Mauk and McIlwain*, 1974; *Freeman*, 1974]. The position of the zero-energy Alfvén layer depends directly on the strength and distribution of the magnetospheric electric field [*Kivelson and Southwood*, 1975]. Thus measurements of variations in the equatorward boundary of auroral electron precipitation, as functions of magnetic local time, and changes in solar wind parameters can provide significant information concerning large-scale convection pattern in the magnetosphere and coupling between solar wind and magnetospheric electric fields.

Numerous investigators have established that the auroral oval as a whole moves equatorward with increasing geomagnetic activity. *Akasofu and Chapman* [1963] showed that the position of quiet auroral arcs during geomagnetic storms

moved equatorward as a function of increasing $Dst(H)$. *Feldstein and Starkov* [1967] showed that the entire oval moved to lower latitudes with both increasing Q and increasing Kp. In terms of the equatorward boundary, however, these results must be viewed as primarily qualitative owing to the limitation of the photographic techniques used [*Eather*, 1973]. The equatorward motion has been confirmed by *Lui et al.* [1975] using satellite particle data and has been well quantified more recently by *Slater et al.* [1980] and by *Gussenhoven et al.* [1981]. These latter works show that the position of the equatorward boundary and Kp are linearly related in most magnetic local time zones.

The relationship between oval motion and solar wind variation has been studied much less exhaustively. Earlier works [*Akasofu et al.*, 1973; *Kamide and Akasofu*, 1974; *Pike et al.*, 1974] have shown a qualitative relationship between the equatorward motion of auroral phenomena and increasing values of the southward component of the interplanetary magnetic field (IMF). A more quantitative study of the interdependence of the two phenomena performed by *Kamide and Winningham* [1977] using particle data from the ISIS satellites has shown that there is a reasonable linear relationship between the boundary and B_z in magnetic local times from 2000 to 0400 hours. Their study was restricted to only studying the relation-
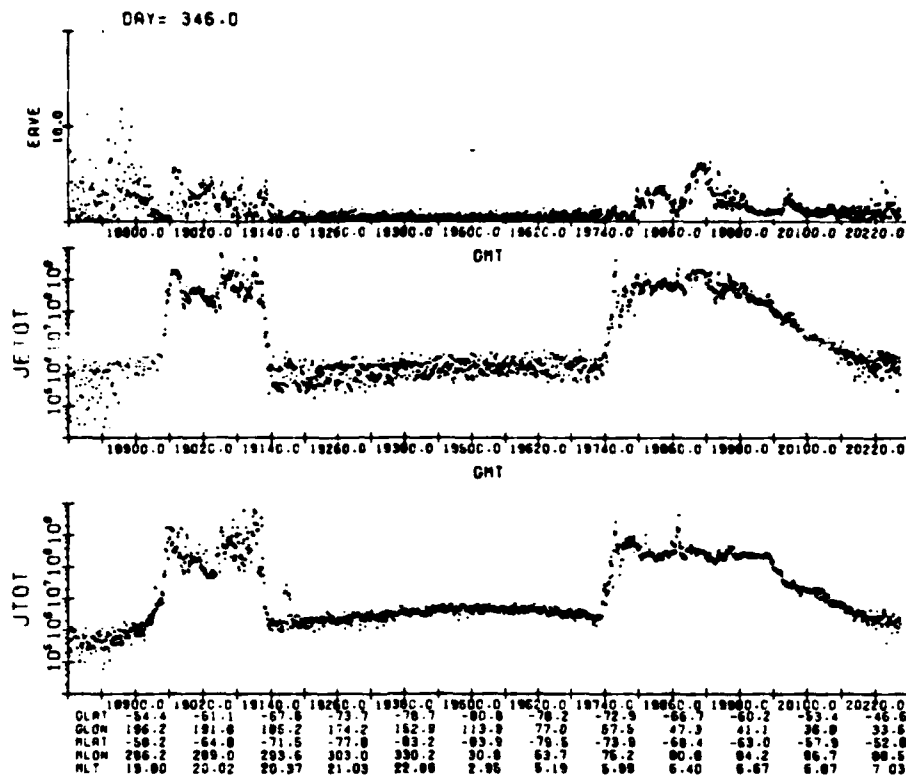
Fig. 1. Electron data from a typical pass of the DMSP/F2 satellite in the southern hemisphere. From the top, the three panels show the integral flux in $(cm^2\ sr\ s)^{-1}$, energy flux in keV $(cm^2\ sr\ s)^{-1}$, and average energy in keV. These are plotted as functions of universal time (in seconds), geographic latitude and longitude of the subsatellite position, corrected geomagnetic latitude and longitude of the satellite position projected along a Jensen-Cain magnetic field to 110 km, and magnetic local time.

ship of the boundary to B_z and to a relatively small number (351) of boundary determinations.

This paper is primarily an extension and reexamination of the work of Kamide and Winningham [1977]. A much larger data set is used to enable analysis of the relationship between solar wind plasma parameters and the boundary location in more detail. The solar wind velocity is included so that quantities other than B_z could be tested for their effects on the boundary location. Also, the present study has been extended over a wider range in magnetic local times.

The instrument used in this study and the methods of data analysis are summarized in the following section. Correlation results are then presented. The best correlations are found between the oval boundaries and 1-hour delayed values of the Y component of the interplanetary electric field (VB_z). Similarities between these correlations and those previously obtained with Kp lead to a linear relationship between VB_z and Kp subject to the constraints $B_z < 1$ nT. The result is confirmed by direct correlation of these quantities. The discussion section contains three subsections. The first is a detailed comparison of our results with those of Kamide and Winningham [1977]. In the second subsection we use the relationship between Kp and VB_z to write a quasi-empirical expression for the magnetospheric electric potential distribution. Cross-magnetospheric potential drops calculated from this expression are in good agreement with measured polar cap potential drops as a function of Kp. The final subsection gives a comparison between our results and the general features of the half-wave rectifier model of the magnetosphere.

INSTRUMENTATION AND DATA ANALYSIS

Data used in this study came from the SSJ/3 sensor on board the F2 satellite of the Defense Meteorological Satellite Program (DMSP). The F2 satellite is three-axis stabilized in a near sun synchronous orbit and at an altitude of ~840 km. The orbital period is ~101 min, and the nominal inclination is 98.75°. The orbit initially was centered near the 0700-1900 meridian but was subject to a very slow precession toward later local time. The orbit restricted boundary determinations to magnetic local times between 0400 and 1100 hours on the morningside and between 1500 and 2300 hours on the eveningside of the oval.

The particle detector on DMSP/F2 consists of two curved plate electrostatic analyzers that measure the fluxes of electrons in 16 energy channels between 50 eV and 20 keV once per second. The apertures of the analyzers always face toward local vertical. At auroral and polar cap latitudes they detect precipitating rather than backscattered and/or trapped electrons. One analyzer covers the energy range from 50 eV to 1 keV with a geometric factor of 4×10^{-4} cm^2 sr and a $\Delta E/E$ of 10%. The other analyzer covers the energy range from 1 keV to 20 keV with a geometric factor of 10^{-3} cm^2 sr and a $\Delta E/E$ of 12%. The large geometric factors insure that the flux level for the electrons in the diffuse aurora are well above the detector's sensitivity. A detailed description of the detector is given by Hardy et al. [1979].

The boundaries of the oval were chosen from plots similar to those shown in Figure 1. In the figure we have plotted from
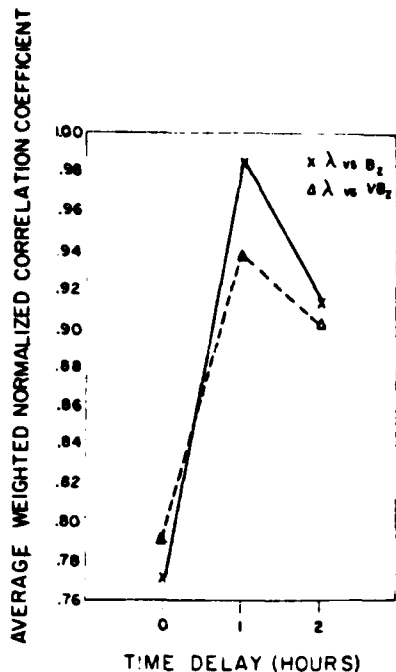
Fig. 2. The average weighted normalized correlation coefficient for the boundaries with B_z and VB_z as a function of the hourly average of the IMF and velocity used.

top to bottom E_{AVE}, the average energy of the precipitating electrons in keV, JE_{TOT}, the directional energy flux (keV/cm² s sr), and J_{TOT}, the directional number flux (el/cm² s sr). These quantities are plotted as functions of universal time in seconds of the day, the geographic latitude and longitude of the subsatellite position, the corrected geomagnetic latitude and longitude of the satellite projected to an altitude of 110 km, and the magnetic local time. Values of the equatorial boundaries (Λ_B) of the auroral oval are assigned to the corrected geomagnetic latitudes >45° at which J_{TOT} rises noticeably above background. This is essentially the same method used by *Kamide and Winningham* [1977] The problems associated with selection of the boundary have been discussed in detail by *Gussenhoven et al.* [1981].

CORRELATION RESULTS

An initial set of 6000 boundary locations was available for this study. These boundary locations were taken from data obtained between September 1977 and December 1978 with the majority obtained from September 1977 to March 1978. This set was merged with the hourly averages of the IMF B_z component and solar wind speed available from the National Space Science Data Center [*King*, 1979]. Each boundary crossing was tagged with V and B_z values for the hour of the crossing as well as 1 and 2 hours prior to the crossing. Such V and B_z data were available for approximately 2500 boundary crossings. The hourly averages of the B_z component were provided in the solar magnetospheric coordinate system.

The boundary data were separated into 1-hour zones in magnetic local time and were further separated by hemisphere. Since the data came exclusively from the DMSP/F2 satellite, the magnetic local time coverage was restricted to between 0400–0800 and 1800–2300 in the northern hemisphere and between 0600–1100 and 1500–2000 in the southern hemi-

sphere. Within each zone the correlation was tested between the boundary location and (1) B_z, (2) B_z^2, (3) VB_z and (4) VB_z^2. The correlations were performed separately by using the three different sets of IMF and solar wind speed data with which each boundary was tagged.

To determine the optimum time delay between V/B_z, the solar wind parameters, and boundary variations we first identified the delay that produced the highest correlation coefficient in each MLT zone. We then normalized the three values of the correlation coefficient in each zone by setting the peak value to 1.0. Only MLT zones that had 20 or more boundary crossings were considered. Finally, we averaged the normalized coefficients for each delay time, weighting each MLT zone by the number of boundaries in that zone. The results for B_z and VB_z are shown in Figure 2. It is clear that the quality of the correlation varies with the time delay. The highest correlation is obtained for a time delay between 1 and 2 hours. This result is consistent with time delays reported between southward turning of the IMF and substorm onset [*Foster et al.*, 1971; *Meng et al.*, 1973]. Since we have only 1-hour averages of the IMF and solar wind speed, any more detailed analysis is not possible, and for the remainder of this paper we consider only correlations with a 1-hour time delay.

Correlation coefficients using all data points are listed in Table 1 for B_z, B_z^2, VB_z, and VB_z^2. There are two points of note. First, none of the relationships show a very high correlation coefficient. In most zones of magnetic local time the correlation coefficient is less than 0.5, even though the correlation contains several hundred points. Second, although all correlations are marginal in terms of significance, B_z and VB_z give better results than B_z^2 or VB_z^2. The average weighted correlation coefficients for B_z and VB_z are 0.44 and 0.47 as compared to 0.29 and 0.33 for B_z^2 and VB_z^2. For later comparison, the slopes and intercepts from the linear regressions for VB_z are listed in Table 2.
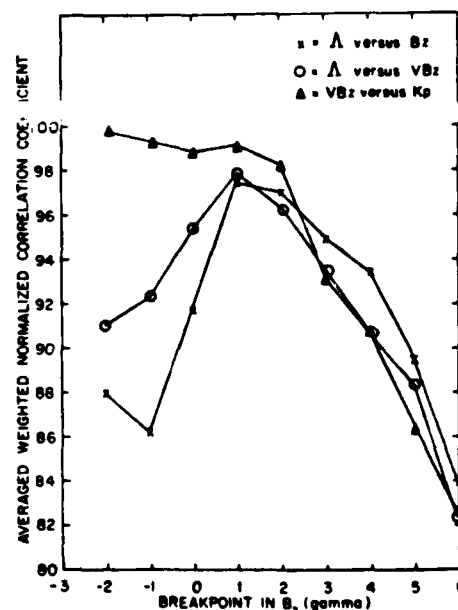

Fig. 3. The average weighted normalized correlation coefficient for the equatorward boundaries with B_z and VB_z and for VB_z versus Kp for boundaries with B_z less than the breakpoint as a function of the breakpoint.

TABLE 1. Number of Boundary Locations (N) in Each Zone of Magnetic Local Time and Correlation Coefficients (cc) Obtained for Linear Regressions With B_z, B_z^2, VB_z, and VB_z^2

	NORTH POLE						SOUTH POLE					
	N	B_z cc	B_z^2 cc	N	VB_z cc	VB_z^2 cc	N	B_z cc	B_z^2 cc	N	VB_z cc	VB_z^2 cc
0400-0500	102	.30	.12	85	.23	.10						
0500-0600	187	.31	.12	173	.36	.17						
0600-0700	174	.50	.27	157	.47	.25	226	.37	.29	198	.37	.28
0700-0800	156	.49	.36	139	.52	.37	161	.40	.11	150	.53	.43
0800-0900							117	.40	.26	106	.37	.25
0900-1000							71	.58	.46	65	.62	.52
1000-1100							41	.47	.44	37	.53	.47
1500-1600												
1600-1700												
1700-1800							22	.09	-.10	21	.49	-.14
1800-1900	72	.55	.46	66	.55	.44	55	.46	.36	48	.56	.52
1900-2000	218	.57	.42	191	.58	.41	104	.45	.38	96	.49	.42
2000-2100	219	.53	.38	206	.56	.40	149	.42	.28	139	.42	.29
2100-2200	281	.41	.26	252	.44	.29	230	.46	.26	204	.51	.41
2200-2300	30	-.18	-.41	23	-.44	-.55	83	.55	.51	73	.61	.55

B_z <cc> = .44

B_z^2 <cc> = .29

VB_z <cc> = .47

VB_z^2 <cc> = .33

The table is separated into morning and evening sections and by pole. The correlations are for a 1-hour delay in the value of the interplanetary magnetic field (IMF) used and with no separation in the data by B_y.

TABLE 2. Intercepts (A₀), Slopes, Correlation Coefficients (cc), and Sample Sizes (N) for the Linear Regression of the Boundary Location With VB_z, in Each Magnetic Local Time Zone

A Vs. VBz (HOUR MINUS ONE)

MLT	NORTH POLE				SOUTH POLE			
	A₀	Slope	cc	N	A₀	Slope	cc	N
0400-0500	64.8	.736	.23	85				
0500-0600	62.8	.770	.36	173				
0600-0700	63.1	.939	.48	157	63.8	.925	.37	198
0700-0800	64.9	1.30	.52	139	63.1	1.25	.53	150
0800-0900					64.1	.824	.37	106
0900-1000					65.2	1.30	.62	65
1000-1100					66.2	.467	.53	37
1500-1600					68.0	1.50	.49	21
1600-1700					68.4	.992	.56	48
1700-1800					67.8	.761	.49	96
1800-1900	67.7	1.22	.55	66	66.5	.666	.42	139
1900-2000	66.7	1.17	.58	191	65.6	1.01	.51	204
2000-2100	64.3	.973	.56	206	65.1	1.46	.61	73
2100-2200	65.0	.898	.44	252				
2200-2300	65.3	-.753	-.44	23				

The correlations are for a 1-hour delay in the value of the IMP used and with no separation in the data by B_y.

31

TABLE 3. Intercepts (A₀), Slopes, Correlation Coefficients (cc), and Sample Sizes (N) for the Linear Regression of the Boundary Location With B_z in Each Magnetic Local Time Zone

A Vs Bz (HOUR MINUS ONE)

	NORTH POLE				SOUTH POLE			
MLT	A₀	Slope	cc	N	A₀	Slope	cc	N
B_z < 1 nT								
0400-0500	65.2	1.20	.53	54	64.5	.750	.55	136
0500-0600	63.7	.965	.57	119	63.8	.923	.57	100
0600-0700	64.3	.868	.69	120	65.3	1.07	.65	175
0700-0800	66.2	1.25	.62	96	65.4	.836	.67	44
0800-0900					66.2	.734	.61	27
0900-1000								
1000-1100								
1600-1700	68.7	.933	.79	47	69.4	.953	.72	30
1700-1800	67.4	.810	.66	142	68.6	.687	.68	65
1800-1900	65.4	.956	.66	141	67.3	.781	.66	90
1900-2000	65.8	.874	.68	152	66.8	.881	.67	151
2000-2100					66.0	.957	.60	49
2100-2200								
B_z > 1 nT								
0400-0500	66.0	-.070	-.05	48	65.6	-.313	-.16	90
0500-0600	65.5	-.325	-.39	68	66.5	-.306	-.38	61
0600-0700	66.2	-.305	-.30	54	67.4	-.328	-.34	42
0700-0800	67.0	-.067	-.05	60	67.6	-.134	-.11	27
0800-0900								
0900-1000								
1600-1700	69.7	-.298	-.34	25	69.1	.077	.11	25
1700-1800	68.9	-.184	-.17	76	70.0	-.426	-.41	39
1800-1900	65.8	-.037	-.04	78	69.3	-.310	-.42	59
1900-2000	66.6	-.149	-.17	129	66.4	.020	.02	79
2000-2100					67.2	-.055	-.04	34
2100-2200								

The correlations are for a 1-hour delay in the value of the IMF used. The linear regressions are run separately for boundaries with $B_z \le 1$ nT and $B_z > 1$ nT.

TABLE 4. Same as Table 3 With the Linear Regression of the Boundary Location With $V8$,
A vs VRz (HOUR MINUS ONE)

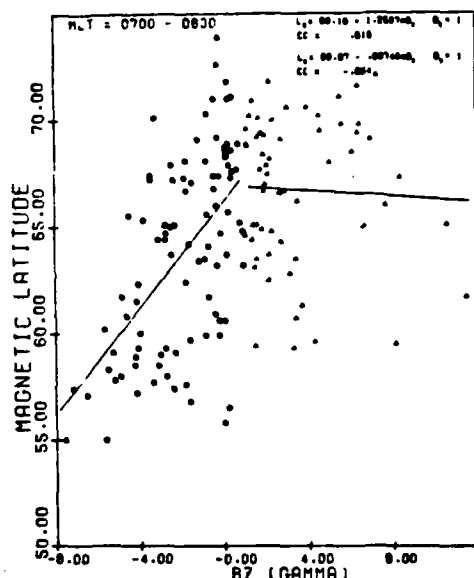|	NORTH POLE				SOUTH POLE			
MLT	A_0	Slope	cc	N	A_0	Slope	cc	N
$B_z < 1$ nT								
0400-0500	65.1	3.28	.52	43	64.4	1.70	.56	124
0500-0600	63.6	1.94	.61	110	63.7	1.95	.61	94
0600-0700	64.2	1.80	.70	105	65.1	2.27	.69	68
0700-0800	66.1	2.56	.68	85	65.5	1.74	.74	38
0800-0900					65.8	.44	.59	19
0900-1000								
1000-1100								
1600-1700	68.6	2.49	.81	44	69.5	1.89	.82	26
1700-1800	67.3	1.76	.68	123	68.6	1.36	.74	57
1800-1900	65.2	1.71	.70	130	67.2	1.60	.70	83
1900-2000	65.5	1.91	.71	132	66.6	1.81	.70	141
2000-2100					65.8	2.01	.64	44
2100-2200								
$B_z > 1$ nT								
0400-0500	66.5	-.685	-.19	42	66.0	-.994	-.27	74
0500-0600	65.5	-.811	-.42	63	67.0	-1.00	-.37	56
0600-0700	66.1	-.693	-.35	52	67.8	-1.14	-.54	38
0700-0800	67.9	-.487	-.22	54	67.6	-.333	-.12	27
0800-0900								
0900-1000								
1600-1700	69.6	-.380	-.35	22	69.2	-.524	-.02	22
1700-1800	68.8	-.020	-.19	68	69.9	+.033	-.46	39
1800-1900	66.0	-.415	-.01	76	69.2	-.954	-.48	56
1900-2000	66.7	-1.29	-.20	120	67.4	-.670	-.24	63
2000-2100					67.3	-.562	-.07	29
2100-2200								

33

Fig. 4. Scatter plot of the magnetic latitude of the equatorward boundary of electron precipitation in the magnetic local time zone 0700–0800 versus the hourly average of the IMF B_z component in solar magnetospheric coordinates with a 1-hour time delay. The two solid lines give the least squares fits to the data for points with $B_z < 1$ nT and $B_z > 1$ nT. In the upper right-hand corner the linear equations and correlation coefficients for both ranges are listed.

Scatter plots of boundary locations versus B_z and VB_z (e.g., Figures 4–7, discussed below) indicate that the low correlations are partially caused by including boundaries from periods with $B_z > +1$–2 nT. Relatively strong trends for boundary locations to move equatorward with increasingly negative B_z appear below these values. For $B_z > 2$ nT little or no correla-
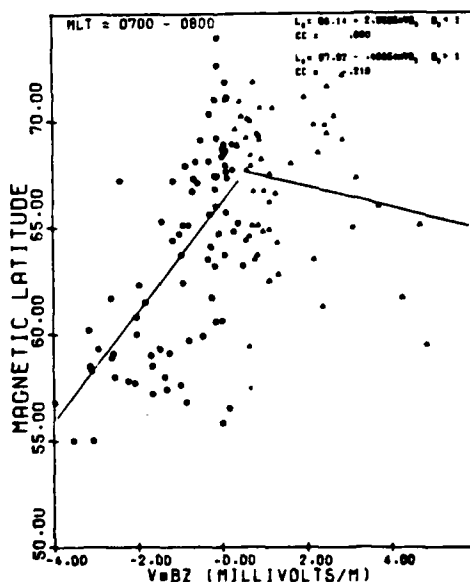

Fig. 5. Scatter plot of the magnetic latitude of the equatorward boundary of electron precipitation in the magnetic local time zone 0700–0800 versus the hourly average of VB_z with a 1-hour time delay. B_z is determined in a solar magnetospheric coordinate system. The two solid lines are least square fits to the data for points with $B_z < 1$ nT and $B_z > 1$ nT In the upper right-hand corner the equations from the linear fit and correlation coefficients for both ranges are listed
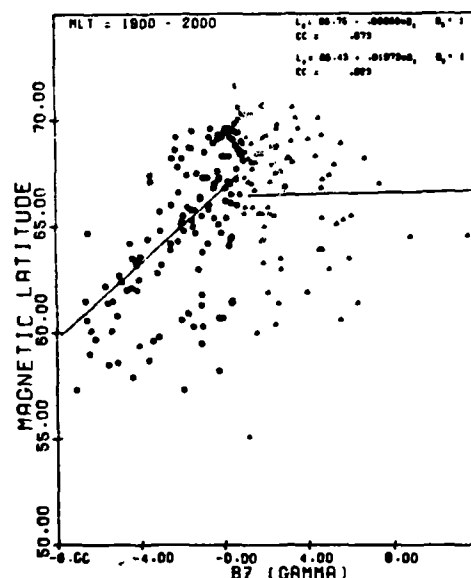
Fig. 6. Same as Figure 5 for the magnetic local time zone 1900–2000.

tions are visually evident. To quantify this perception we first divided data in each MLT zone into two sets separated at a breakpoint in B_z. The data were then tested separately for the correlation for all points greater than and less than the breakpoint. The breakpoint was set successively at $-2, -1, 0, 1, 2, 3, 4, 5$, and 6 nT, and linear regressions were determined for the boundary location versus both B_z and VB_z. Only B_z and VB_z were treated because of the much lower initial correlations with B_z^2 and VB_z^2.

To determine the breakpoint that maximized the correlation for the entire data set, we followed a procedure similar to that performed in determining the best time delay. In each local time zone the breakpoint that maximized the correlation coefficient was determined. The correlation coefficients in that time zone for all the other breakpoints were normalized to that value. An average weighted by the number of points in each zone was then calculated for each breakpoint over all magnetic local time zones. The results of such a procedure are shown for both B_z and VB_z in Figure 3. For VB_z the best correlation is obtained for a division at $B_z = 1$ nT, and for B_z the best division is obtained for B_z equal to between 1 and 2 nT positive. In both cases there is a well defined peak with the quality of the correlation decreasing significantly for the breakpoint moved toward more positive or negative values of B_z.

The straight line fits from the linear regression for a breakpoint and 1 nT positive for both B_z and VB_z are given in Tables 3 and 4. From consideration of these tables in comparison with Table 1 and 2, several points are clear.

1. The correlation coefficients obtained over the range below the breakpoint are significantly higher than those obtained over the entire range in B_z or for the points above the breakpoint.

2. The slopes obtained for the values below the breakpoint are much larger than for the other two cases, between 0.7° and 1.2°/nT for B_z and between 1.4° and 3.2°/mV/m for VB_z.

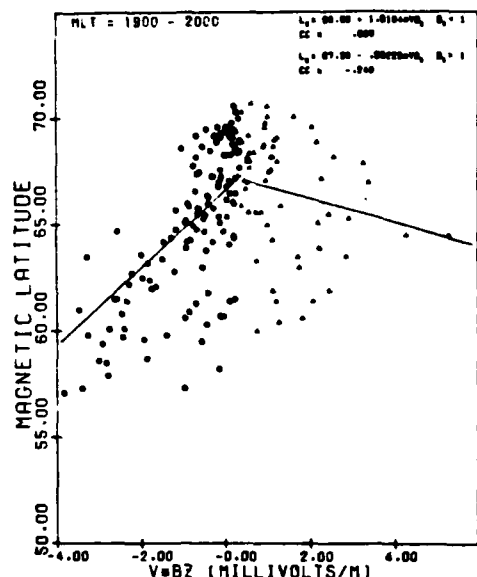3. The correlation for points above the breakpoint is poor.

Fig. 7. Same as Figure 6 for the magnetic local time zone 1900-2000.

The correlation coefficients are between 0 and −0.4, with the weighted correlation coefficient being only −0.18 and −0.20, respectively, for B_z and VB_z.

4. Even though the correlation for points above the breakpoint is poor, the slope of the best fit line has the opposite sign to that for points below the breakpoint.

5. In 16 of 18 magnetic local time zones the correlation of the boundary is higher with VB_z than with B_z for points below the breakpoint. The weighted averaged correlation coefficients for B_z and VB_z, with the breakpoint at $B_z = 1$ nT, are 0.64 and 0.66, respectively.

6. On both morningside and eveningside of the oval there is a trend in the intercepts of the straight line fits for the points below the breakpoint to decrease as a function of time toward midnight. On the eveningside in particular, there is a clear tendency for the intercept to decrease for increasing magnetic local time toward midnight. Except in the 2100-2200 MLT zone the equatorward shift of the intercept is between 0.5° and 1.0° per hour local time.

In Figures 4 through 7 we show typical examples of the correlations. The first two of these plots shows the distribution of points and straight line fits for the boundary locations versus B_z and VB_z, respectively, for the local time zone 0700-0800. The last two plots are for the evening zone 1900-2000 hours. In both sets the trend in the points below the breakpoint and the lack of a trend above the breakpoint are evident. The scatter in the data, however, is quite large over the both ranges. We attribute this either to uncertainties introduced by the use of hourly averages in the IMF, to the action of other quantities in the solar wind, or to intervening processes in the magnetosphere. We consider this point in more detail in the discussion section.

We have pointed out that the intercepts for the fits to points below the breakpoint show a systematic trend to lower values as the magnetic local time zone approaches midnight from both dawn and dusk sides of the oval. In Table 5 we show results for morning and evening sectors from our previous work, where we ordered the data by Kp [Gussenhoven et al., 1981]. The important point to note is that the trend in intercepts and

to a lesser extent the trend in slopes is the same for ordering the boundaries by VB_z for points below the breakpoint and for Kp. This implies that Kp and VB_z are related in the range blow the breakpoint. To quantify the relationship, slopes and intercepts from available MLT zones were used to form weighted, average relationships between the magnetic latitude of the boundary (Λ) and Kp (Table 5) and VB_z (Table 4). Eliminating Λ_ρ from these relationships gives

$$Kp = 1.97(\pm0.15) - 1.06(\pm0.16)VB_z, \quad mV/m \quad B_z < 1 \, nT (1)$$

Values in parentheses represent standard deviations in the 17 MLT zones of overlapping data. The small standard deviations support our contention that Kp and VB_z are related.

To investigate the relationship of VB_z and Kp directly, we ran the correlation for Kp with VB_z for the value associated with each magnetic local time zone separately. This is equivalent to dividing the total number of pairs of values of Kp and VB_z into a series of randomly selected subsets and testing the correlation in each subset. As before, the correlation was run for values of the breakpoint in B_z between −2 and +6 nT in integral steps. At each value of the breakpoint the weighted average correlation coefficient was determined. The results are shown in Figure 3. Again the correlation decreases sharply for the breakpoint above 2 nT positive. Unlike the earlier case, however, the correlation coefficient is approximately constant below the breakpoints. For a breakpoint at $B_z = 1$ nT, the weighted average correlation coefficient for points below the breakpoint is 0.71, and weighted average values of slope and intercept are

$$Kp = 2.09(\pm0.20) - 0.91(\pm0.19)VB_z, \quad B_z < 1 \, nT \quad (2)$$

The values in parentheses are the weighted standard deviation over the 17 magnetic local time zones. A typical example of the correlation is shown in Figure 8. As expected, the relationship obtained by eliminating the boundaries from the two sets (equation (1)) has nearly the same slope and intercept as that obtained for a direct correlation of VB_z and Kp. For the data above the breakpoint of $B_z = 1$ nT, the weighted average correlation coefficient is 0.38 and the average equation is

$$Kp = 1.30(\pm0.24) + 0.416(\pm0.14)VB_z, \quad mV/m \quad B_z > 1 \, nT \quad (3)$$

DISCUSSION

In the previous section we presented results of a statistical analysis of DMSP measurements of the magnetic latitudes of the equatorward boundary of the auroral oval (Λ_ρ) as functions of MLT and various solar wind/IMF parameters. Not surprisingly, the results showed that the boundaries moved equatorward with increasingly negative B_z. The best correlations were obtained with 1-hour delayed values of solar wind/ IMF parameters. When the entire data set was used, irrespective of the sign of B_z, correlations were quite weak. The correlations improved considerably when a breakpoint was introduced at $B_z = 1$ NT. For $B_z < 1$ nT, strong negative slopes were found in both Λ_ρ versus B_z and Λ_ρ versus VB_z relationships. In 16 of the 18 MLT zones studied here, better correlation was found with VB_z than with B_z alone. For $B_z > 1$ nT, correlations were always weak. In some instances slopes of Λ_ρ versus B_z and VB_z reversed directions. That is, Λ_ρ moved equatorward with increasingly positive B_z.

In this section we first compare DMSP results with those

TABLE 5. Intercepts (Λ_0), Slopes, Correlation Coefficients (cc), and Sample Sizes (N) for the Linear Regression of the Boundary Location with Kp [Gussenhoven et al., 1981]

| MLT	NORTH				MLT	SOUTH			
	Λ_0	α	N	cc		Λ_0	α	N	cc
04-05	67.4	-1.35	171	-.58	04-05				
05-06	67.8	-1.87	365	-.75	05-06				
06-07	68.5	-1.96	403	-.82	06-07	67.4	-1.67	376	-.74
07-08	70.2	-2.15	367	-.83	07-08	68.3	-1.97	411	-.81
08-09					08-09	68.7	-1.88	302	-.72
09-10					09-10	69.1	-1.64	217	-.67
16-17	-	-	-	-	16-17	71.3	-1.19	107	-.65
17-18	-	-	-	-	17-18	70.7	-1.20	256	-.69
18-19	71.6	-2.00	103	-.90	18-19	70.6	-1.60	327	-.80
19-20	71.2	-1.96	426	-.89	19-20	70.0	-1.82	447	-.87
20-21	69.4	-1.85	452	-.82	20-21	69.5	-1.89	345	-.84
21-22	68.7	-1.66	556	-.83	21-22	-	-	-	-
22-23	68.3	-1.79	184	-.63					
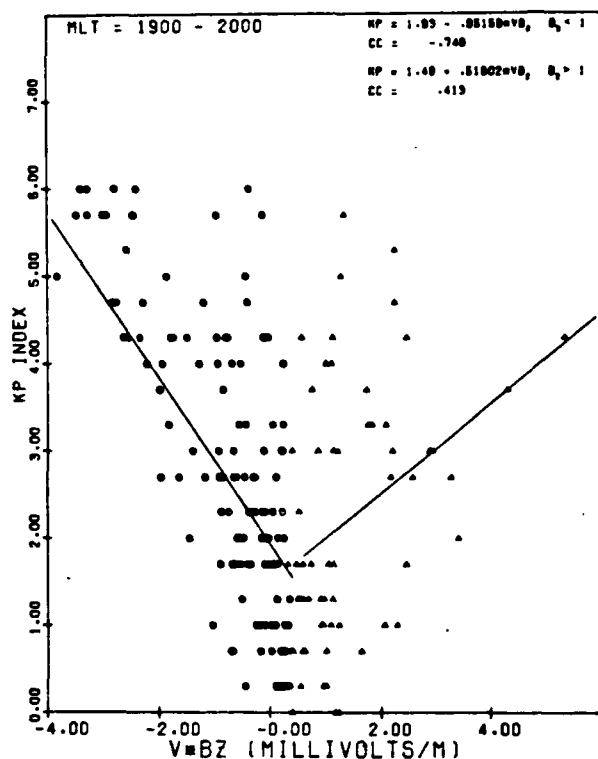
Fig. 8. Scatter plot of the Kp index versus VB_z. The two solid lines are the linear least square fits to the data with $B_z < 1$ nT and $B_z > 1$ nT. The equations from the linear fit and the correlation coefficients are listed in the top right-hand corner.

from a similar study of ISIS data [*Kamide and Winningham,* 1977]. We next use the present results to extend the magnetospheric potential expression given by *Gussenhoven et al.* [1981]. The model is then used by us to calcualte cross-magnetospheric potential drops. Finally, we show how results can be interpreted in terms of the half-wave rectifier model of the magnetosphere.

Kamide and Winningham [1977] studied the relationship between Λ_B and B_z using 351 boundary crossings of ISIS 1 and 2 in the late evening through early morning MLT sector. There are only two MLT zones of overlap with DMSP measurements, 20–21 MLT and 21–22 MLT. Within these zones Kamide and Winningham found

$$\Lambda_B(20\text{–}21) = 65.8° - 0.48\, B_z \quad \text{nT} \quad cc = 0.68 \quad (4)$$

and

$$\Lambda_B(21\text{–}22) = 65.7° - 0.50\, B_z \quad \text{nT} \quad cc = 0.61 \quad (5)$$

From the DMSP data sets with no separation by B_z (Table 1) the equivalent correlation equations are

$$\Lambda_B(20\text{–}21) = 64.2° - 0.48\, B_z \quad \text{nT} \quad cc = 0.53 \quad (6)$$

and

$$\Lambda_B(21\text{–}22) = 65.0° - 0.35\, B_z \quad \text{nT} \quad cc = 0.41 \quad (7)$$

Although the regression equations are comparable, the DMSP correlation coefficients are considerably lower than those found with ISIS measurements. The reason for this is unclear. It could reflect the difference in the hourly averages of the IMF used in the two analyses. In the work of Kamide and

Winningham the average was over the hour, terminating at the time the boundary was measured. In our analysis, since we restricted ourselves to preexisting hourly averages and used a 1-hour delay, the termination points of our averages are randomly distributed between 0 and 1 hour before the time of the boundary measurement.

When the DMSP analysis only includes boundary crossings with $B_z < 1$ nT, the relationship is (Table 3)

$$\Lambda_B(20\text{–}21) = 65.4° - 0.96\, B_z \quad \text{nT} \quad cc = 0.66 \quad (8)$$

and

$$\Lambda_B(21\text{–}22) = 65.8° - 0.87\, B_z \quad \text{nT} \quad cc = 0.68 \quad (9)$$

Here the correlation coefficients and intercepts are comparable with the ISIS results, but the slopes from the DMSP data are steeper. By using the ISIS data plotted in Figure 3a of *Kamide and Winningham* [1977], we made a more direct comparison by performing a linear regression on just the points where $B_z \leq 1$ nT. This yields the relationship

$$\Lambda_B(20\text{–}21) = 66.8° - 0.96\, B_z \quad \text{nT} \quad cc = 0.78 \quad (10)$$

A similar plot of ISIS data from the 21–22 MLT zone is not available. It is evident, however, that in the 20–21 sector, restricting measurements to $B_z < 1$ nT brings the DMSP and ISIS slopes into reasonable agreement.

One final point of comparison: to avoid possible contamination effects due to ring current inflation of the magnetosphere, all cases with $Dst < -40$ nT were eliminated from the ISIS data set. This restriction was not placed on the DMSP measurements. As a test we eliminated cases with $Dst < -40$ nT from the data, but found negligible changes in correlational results. We thus conclude that in the region of overlap the DMSP and ISIS results are consistent.

In the previous DMSP study *Gussenhoven et al.* [1981] projected auroral boundary locations as a function of MLT and Kp into the magnetospheric equatorial plane using the Mead-Fairfield model [*Fairfield and Mead,* 1975]. The projected boundaries were fit to shapes of zero-energy Alfvén boundaries derived by *Ejiri et al.* [1978]. Best fits were obtained with shaping factors between 2 and 3 and with the axis of symmetry rotated away from the dawn-dusk meridian. The results were then used to express the magnetospheric electrostatic potential distribution as a function of Kp.

$$\Phi(L, \phi) = \Omega B_0 R_E^2 [(1.6 + 2.4\, Kp) \cdot 10^{-4} L^2 \sin(\phi - \phi_0) - 1/L] \quad (11)$$

where Ω is the angular spin velocity of the earth, B_0 is the magnetic field strength at the magnetic equator on the earth's surface, R_E is the radius of the earth, ϕ is the local time measured counter-clockwise from midnight, ϕ_0 is the counter-clockwise rotation of the stagnation point from the dawn-dusk meridian, and L is the McIlwain parameter. This equation was derived for a shaping factor of 2.

The present study has shown that there is a linear relationship between VB_z and Kp for $B_z < 1$ nT. Combining (11) and (2) gives an expression for the magnetospheric potential distribution as a function of the interplanetary electric field.

$$\Phi(L, \phi) = \Omega B_0 R_E^2 [(6.6 - 2.2\, VB_z) \cdot 10^{-4} L^2$$
$$\cdot \sin(\phi - \phi_0) - 1/L] \quad B_z < 1\, nT \quad (12)$$

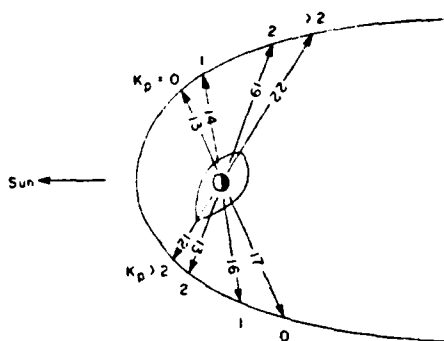where VB_z is in millivolts per meter. To test the validity of this

Fig. 9. The shape of the magnetopause in the equatorial plane as given by McIlwain [1972]. The lines with arrows show the values of L used to calculate the cross-magnetospheric potential for different values of Kp.

equation, we calculate the cross-magnetospheric potential drop ($\Delta\Phi_m$) and compare its values with measured cross polar cap potential drops ($\Delta\Phi_{pc}$).

To estimate $\Delta\Phi_m$ we use an expression for the position and shape of the magnetopause in the equatorial plane given by McIlwain [1972]. In this representation the magnetopause lies at a distance of 11 R_L near the subsolar point and flares to a distance of 15 R_L at the dawn-dusk meridian. We ignore storm-time compressions of the magnetosphere in our calculations. Two methods of calculating $\Delta\Phi_m$ are used. The first method sets $\phi_0 = 0$ in (11) and (12), making the axis of symmetry the dawn-dusk meridian. The second method uses empirical values of ϕ_0 given in Figure 12 of Gussenhoven et al. [1981]. For $Kp = 0$, the axis is tilted with the dusk stagnation point 23° to the nightward side of the dawn-dusk meridian. For higher values of Kp the stagnation point rotates sunward, reaching a constant value of $-45°$ for $Kp > 2$. In Figure 9 we have sketched the axes of symmetry, indicating approximate distances to the dawnside and duskside of the magnetopause for $Kp = 0, 1, 2$ and $Kp > 2$.

In Figure 10, $\Delta\Phi_m$ is plotted as a function of Kp, VB_z, and B_z. VB_z is positive when the interplanetary electric field (IEF) is directed from dawn to dusk (positive Y in standard geocentric, solar magnetospheric coordinates). Values of B_z are derived from VB_z by using a solar wind speed of 400 km/s. The solid line calculations assume $\phi_0 = 0$, i.e., the dawn-dusk meridian is the axis of symmetry. For this case, $\Delta\Phi_m$ increases linearly from 6.5 kV for $Kp = 0$ to 65 kV for $Kp = 6$. The dotted-dashed line indicates values of $\Delta\Phi_m$ by using empirical values of ϕ_0 and axes of symmetry indicated in Figure 9. In these calculations $\Delta\Phi_m$ ranges from 5.5 kV for $Kp = 0$ to 95 kV for $Kp = 6$. We note that in these calculations there is an abrupt transition in the trend of $\Delta\Phi_m$ near $Kp = 2$. This is close to our independently derived 'breakpoint' in B_z. A possible interpretation is discussed below.

For reference, in Figure 10 we have also plotted average values of $\Delta\Phi_{pc}$ (dashed line) as a function of Kp based on the 2 weeks of OGO 6 electric field measurements. Heppner [1973] found that $\Delta\Phi_{pc}$ increased linearly from 20 kV for $Kp = 0$ to 100 kV at $Kp = 6$. At low values of Kp, the DMSP values of $\Delta\Phi_m$ are not sensitive to the value of ϕ_0 and are considerably less than Heppner's $\Delta\Phi_{pc}$. With values of $\phi_0 = -45°$ for $Kp > 2$, $\Delta\Phi_m$ and $\Delta\Phi_{pc}$ are of comparable magnitudes. In a time average sense $\Delta\Phi_{pc}$ and $\Delta\Phi_m$ are coupled through the process of magnetic reconnection in the magnetotail. The two quantities

must be roughly the same, since on average, the amount of magnetic flux transferred to the nightside magnetosphere must equal the amount being returned to the dayside magnetosphere.

We emphasize that these are 'average' results in the sense that they represent least square fits to the data. Heppner [1973] pointed out that the $\Delta\Phi_{pc}$ frequently exceeds 100 kV during periods of high Kp. Similarly, both in the present work and in the previous work of Gussenhoven et al. [1981] for cases of large negative B_z and high Kp, respectively, the latitude of the boundary is often much lower than the average. Since such cases correspond to the Alfvén boundary closer to the earth than average, they also correspond to potentials exceeding 100 kV.

Although the 'average' results from DMSP and OGO are in excellent agreement, the DMSP data do show a very large scatter. Much of this results most likely from the limitations of using hourly averages of the IMF and the fixed time delays. In addition, however, the relationship between the interplanetary and magnetospheric electric fields will be obscured by any process producing changes in the electric field restricted in magnetic local time. Inductive electric fields thought to be associated with substorms [Heikkila and Pellinen, 1977; Hekkila et al., 1979] could produce such local effect. Indeed, Kamide and Winningham [1977] showed that for a given value of B_z, the boundary is shifted equatorward by 2 or 3 degrees between nonsubstorm and substorm periods consistent with an inductive field.

We also note that Kivelson [1976] reviewed values of uniform magnetospheric electric fields required by various models in the literature. The results summarized in Figure 1 of Kivelson [1976] show electric fields that range from 0.5 to 0.7 kV/R_E at $Kp = 0$ and from 1.4 to 1.6 kV/R_E at $Kp = 5$. For a distance of 30 R_E between the dawn and dusk magnetopause, $\Delta\Phi_m$ ranges from 15 to 21 kV at $Kp = 0$ and from 42 to 48 kV at $Kp = 5$. While these values agree with Heppner's $\Delta\Phi_{pc}$ for low Kp, they are significantly below both OGO 6 and DMSP values for $Kp = 5$.

That the best boundary correlations are obtained with 1-hour delayed values of solar wind/IMF parameters and that the correlations break down with $B_z > 1$ nT are consistent
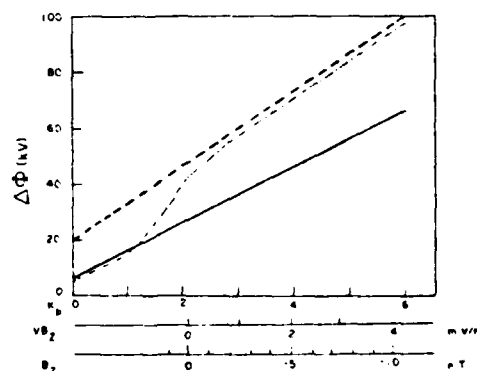

Fig. 10. A comparison of the cross polar cap potential drop as a function of Kp from Heppner [1973] (dashed line), the cross-magnetospheric potential calculated from equation (5) with $\phi_0 = 0$ (solid line), and the cross-magnetospheric potential calculated from equation (5) by using the empirical values of ϕ_0 in the work of Gussenhoven et al. [1981] (dotted-dashed line).

38

with the picture of the magnetosphere as a 'half-wave recti-fier' [*Burton et al.*, 1975]. According to this model, at the time of a southward turning of the IMF, magnetic flux is transferred from the dayside to the nightside magnetotail. The rate of transfer across the dawn-dusk meridian (in webers per second) is equal to the cross polar cap potential (in volts). Typically, magnetic energy is built up in the magnetotail for about 30 min before stresses are relieved by substorm-associated ring current injection events. Thus the establishment of stable, zero-energy Alfvén layers should take place more than a half-hour after the southward turning of IMF B_z. An earlier study of the data set presented here [*Gussenhoven et al.*, 1981] showed a high correlation between Λ_e and Kp. This result places an upper bound of 3 hours for the establishment of stable Alfvén boundaries.

The half-wave rectifier model implies that an IEF with a positive Y component is able to penetrate to the inner magnetosphere. Exactly how such an IEF is transmitted into the magnetosphere across the magnetopause is unclear. We have shown that for an IEF of 4 mV/m, $\Delta\Phi_m$ and $\Delta\Phi_{pc}$ are approximately 100 kV. For such a case, assuming a magnetospheric cross-sectional diameter of 30 R_L, the cross-magnetospheric potential drop in the solar wind is 750 kV. If magnetic field lines connecting the polar cap and magnetopause are equipotentials, then the window across which the IEF of 4 mV/m is transmitted must have a solar magnetospheric Y extent of ~4 R_E in order to produce the observed values of $\Delta\Phi_m$ and $\Delta\Phi_{pc}$.

In the half-wave rectifier model for periods of northward B_z, the IEF is decoupled from the inner magnetosphere. This is consistent with the present DMSP results and with results from other recent investigations. For $B_z > 1$ nT we have shown that Λ_e is not strongly correlated with either B_z or the strength of the IEF VB_z. In some sectors Λ_e moved equatorward with increasingly positive B_z. *Maezawa* [1976] found that with $B_z > 1$ nT, polar cap currents are consistent with sunward convection (dusk to dawn electric field) in the polar cap. This hypothesis has been confirmed in polar cap [*Burke et al.*, 1979] and terella [*Podgorney et al.*, 1978] electric field measurements. Following *Russell* [1972], *Maezawa* [1976] interpreted sunward convection in the polar cap as resulting from magnetic merging at the poleward edge of the dayside cusp. In this model convection is contained entirely in two [*Maezawa*, 1976] or one [*Crooker*, 1979] convection cells in the polar cap. In agreement with the half-wave rectifier model, the IEF drives a polar cap convection that is decoupled from the inner magnetosphere. *Burke et al.* [1979] found that with $B_z > 0.7$ nT and sunward-antisunward convection cells in the polar cap there was still significant sunward convection in the auroral oval. *Crooker* [1979] suggested that sunward convection in the auroral zones (which cannot be explained by merging theory) is the return flow from antisunward flow in the magnetospheric boundary layer. The DMSP results presented here support this contention. In a recent study of the ionospheric projection of the boundary layer near the dawn-dusk meridian, *Smiddy et al.* [1980] found potential drops of ≤3 kV on the duskside. Assuming similar potential drops across the dawnside boundary layer, we get a total potential drop of ≤6 kV. This agrees with calculated values of $\Delta\Phi_m$ required to maintain zero-energy Alfvén boundaries during periods of low magnetic activity. The equatorward movement of Λ_e during periods of increasingly positive B_z would then reflect as yet unexplained stronger coupling between the solar wind and the boundary layer during these periods.

CONCLUSION

We have investigated the relationship between the interplanetary magnetic field B_z component, the solar wind speed V, and the position of the equatorward boundary of electron precipitation in the auroral zone. We find that the boundary correlates reasonably well with both B_z and VB_z for values of B_z less than approximately 1 nT. Above 1 nT, the correlation is extremely weak and the slope of the linear fit is negative. No meaningful correlations are found with either B_z^2 or VB_z^2. The trend in the slopes and intercept for the correlations of the boundary with VB_z for $B_z < 1$ nT are found to be similar to those previously reported by *Gussenhoven et al.* [1981] for correlation with Kp. On this basis we are able to show that Kp and VB_z are linearly related for $B_z < 1$ nT by the equation

$$Kp = 2.09(\pm0.20) - 0.91(\pm0.19)VB_z$$

where VB_z is measured in millivolts per meter. From the work of *Gussenhoven et al.* [1981] we derived an equation for the average configuration of the magnetosphere potential as a function of VB_z:

$$\Phi(L, \phi) = \Omega B_0 R_E^2[(6.6 - 2.2\, VB_z) \cdot 10^{-4}L^2$$
$$\cdot \sin(\phi - \phi_0) - 1/L] \qquad B_z < 1\ \text{nT}$$

The potential drop across the magnetosphere from this equation is found to be consistent with *Heppner*'s [1973] measurement of the variation of the cross polar cap potential as a function of Kp. We interpret the breakdown of the correlation at $B_z = 1$ nT in terms of the half-wave rectifier model of the magnetosphere [*Burton et al.*, 1975]. Below 1 nT the solar wind electric field is able to penetrate into the magnetosphere. Above 1 nT the systems are decoupled.

REFERENCES

Akasofu, S.-I., and S. Chapman, The lower limit of latitude (US sector) of northern quiet auroral arcs and its relationship to *Dst(H)*, *J. Atmos. Terr. Phys.*, *25*, 9, 1963.

Akasofu, S.-I., P. D. Perreaults, F. Yasuhara, and C.-I. Meng, Auroral substorms and the interplanetary magnetic field, *J. Geophys. Res.*, *78*, 7490, 1973.

Burke, W. J., M. C. Kelley, R. C. Sagalyn, M. Smiddy, and S. T. Lai, Polar cap electric field structures with a northward interplanetary magnetic field, *Geophys. Res. Lett.*, *6*, 21, 1979.

Burton, R. K., R. L. McPherron, and C. T. Russell, An empirical relationship between interplanetary conditions and D_{ST}, *J. Geophys. Res.*, *80*, 4204, 1975.

Crooker, N. U., Antiparallel merging, the half-wave rectifier response of the magnetosphere, and convection, Proceedings of the Chapman Conference on Magnetospheric Boundary Layers, *ESA SP-148*, pp. 343-349, Eur. Space Agency, Paris, 1979.

Eather, R. H., The auroral oval—A reevaluation, *Rev. Geophys. Space Phys.*, *11*, 155, 1973.

Ejiri, M., R. A. Hoffman, and P. H. Smith, The convection electric field model for the magnetosphere based on Explorer 45 observations, *J. Geophys. Res.*, *83*, 4811, 1978.

Fairfield, D. H., and G. D. Mead, Magnetospheric mapping with a quantitative geomagnetic field model, *J. Geophys. Res.*, *80*, 535, 1975.

Feldstein, Y. I., and G. V. Starkov, Dynamics of auroral belts and polar geomagnetic disturbances. *Planet Space Sci., 15*, 209, 1967.

Foster, J. C., D. H. Fairfield, K. W. Ogilvie, and T. J. Rosenberg, Relationship of interplanetary parameters and occurrence of magnetospheric substorm, *J. Geophys. Res., 6*, 6971, 1971.

Freeman, J. W., *Kp* dependence of the plasma sheet boundary, *J. Geophys. Res., 79*, 4315, 1974.

Gussenhoven, M. S., D. A. Hardy, and W. J. Burke, DMSP/F2 electron observations of equatorward auroral boundaries and their relationship to magnetospheric electric fields, *J. Geophys. Res., 86*, 768, 1981.

Hardy, D. A., M. S. Gussenhoven, and A. Huber, The precipitating electrons detectors (SSJ/3) for the block 5D/Flights 2-5 DMSP satellites: Calibration and data presentation, *Rep. AFGL-TR-79-0210*, Air Force Geophys. Lab., Hanscom Air Force Base, Mass., 1979.

Heikkila, W. J., and P. J. Pellinen, Localized induced electric fields within the magnetotail, *J. Geophys. Res., 82*, 1610, 1977.

Heikkila, W. J., R. J. Pellinen, C.-G. Falthammer, and L. P. Block, Potential and inductive electric fields in the magnetosphere during auroras, *Planet. Space Sci., 27*, 1383, 1979.

Heppner, J. P., High latitude electric fields and the modulations related to interplanetary magnetic field parameters, *Radio Sci., 8*, 933, 1973.

Kamide, Y., and S.-I. Akasofu, Latitudinal cross section of the auroral electrojet and its relationship to the interplanetary magnetic field polarity, *J. Geophys. Res., 79*, 3755, 1974.

Kamide, Y., and J. D. Winningham, A statistical study of the instantaneous nightside auroral oval: The equatorward boundary of electron precipitation as observed by the ISIS 1 and 2 satellites, *J. Geophys. Res., 82*, 5573, 1977.

King, J. H., *Interplanetary Medium Data Book Supplement 1, 1975-1978, Rep. NSSDC/WDC-A-R&S 79-08*, NASA Goddard Space Flight Center, Greenbelt, Md., 1979.

Kivelson, M. G., Magnetospheric electric fields and their variation with geomagnetic activity, *Rev. Geophys. Space Phys., 14*, 189, 1976.

Kivelson, M. G., and D. J. Southwood, Approximations for the study of drift boundaries in the magnetosphere, *J. Geophys. Res., 80*, 3528, 1975.

Lassen, K., Relation of the plasma sheet to the nighttime auroral oval, *J. Geophys. Res., 79*, 3857, 1974.

Lui, A. T. Y., C. D. Anger, and S.-I. Akasofu, The equatorward boundary of the diffuse aurorae and auroral substorms as seen by the ISIS 2 auroral scanning photometer, *J. Geophys. Res., 80*, 3603, 1975.

Lui, A. T. Y., D. Venkatesan, C. D. Anger, S.-I. Akasofu, W. J. Heik-

kila, J. D. Winningham, and J. R. Burrows, Simultaneous observations of particle precipitations and auroral emissions by the ISIS 2 satellite in the 19-24 MLT sector, *J. Geophys. Res., 82*, 2210, 1977.

Maezawa, K., Magnetospheric convection induced by the positive and negative *z* components of the interplanetary magnetic field: Quantitative analysis using polar cap magnetic records, *J. Geophys. Res., 81*, 2289, 1976.

Mauk, B. H., and C. E. McIlwain, Correlation of *Kp* with the substorm-injected plasma boundary, *J. Geophys. Res., 79*, 3193, 1974.

McIlwain, C. E., Plasma convection in the vicinity of geosynchronous orbit, in *Earth's Magnetospheric Processes*, edited by B. M. McCormac, p. 268, D. Reidel, Hingham, Mass., 1972.

Meng, C.-I., B. Tsurutani, K. Kawasaki, and S.-I. Akasofu, Cross correlation analysis of the AE index and the interplanetary magnetic field *B*, component, *J. Geophys. Res., 78*, 617, 1973.

Pike, C. P., C.-I. Meng, S.-I. Akasofu, and J. A. Whalen, Observed correlation between interplanetary magnetic field variations and the dynamics of the auroral oval and the high-latitude ionosphere, *J. Geophys. Res., 79*, 5129, 1974.

Podgorny, I. M., E. M. Dubinin, and Yu. N. Potanin, The magnetic field on the magnetospheric boundary from laboratory simulation data, *Geophys. Res. Lett., 4*, 207, 1978.

Russell, C. T., The configuration of the magnetosphere, in *Critical Problems of Magnetospheric Physics*, edited by E. R. Dyer, p. 1, Inter-Union Commission on Solar-Terrestrial Physics, National Academy of Sciences, Washington, D. C., 1972.

Slater, D. W., L. L. Smith, and E. W. Klecknes, Correlated observations of the equatorward diffuse auroral boundary, *J. Geophys. Res., 85*, 531, 1980.

Smiddy, M., W. J. Burke, M. C. Kelley, N. A. Saflekos, M. S. Gussenhoven, D. A. Hardy, and F. J. Rich, Effects of high-latitude conductivity on observed convection electric fields and Birkeland currents, *J. Geophys. Res., 85*, 6811, 1980.

Vasyliunas, V. M., Low energy particle fluxes in the geomagnetic tail, in *Polar Ionosphere and Magnetospheric Processes*, edited by G. Skavli, Gordon and Breach, New York, 1970.

Winningham, J. D., F. Yasuhara, S.-I. Akasofu, and W. J. Heikkila, The latitudinal morphology of 10-eV to 10-eV electron fluxes during magnetically quiet and disturbed times in the 2100-0300 MLT sector, *J. Geophys. Res., 80*, 3148, 1975.

DMSP F-2 (1977, 1979) AND
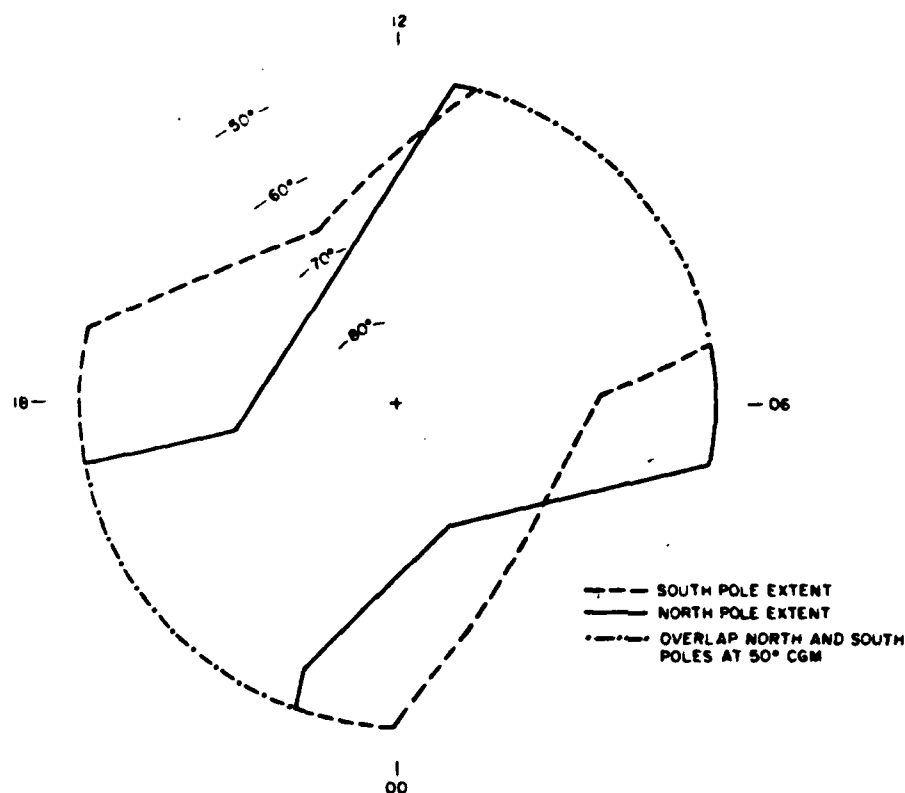F4 COVERAGE, 50°-90°(CGM)

Fig. 2. Combined north pole and south pole coverage of the orbital ranges shown in Figure 1.

sector boundaries. We summarize them here and extend their application to the midnight and noon sectors.

The evening boundary was generally found to be unambiguous (90% of the time) and was determined by an abrupt change in JTOT. The point at which JTOT exceeded 10^7 (cm² s sr)$^{-1}$ was a good 'zero order' boundary choice. In addition, the evening diffuse aurora characteristically showed a dispersion in energy as would be expected if the boundary region maps to quasi-stationary Alfvén layers resulting from the large-scale cross-tail electric field, i.e., the equatorward boundary of electrons with increasingly higher energies is found at higher latitudes (greater distance from the earth in the plasma sheet).

The morning boundary, on the other hand, presented many more problems and could only be unambiguously determined 70% of the time. The principal reason for this is a gradient in JTOT with increasing latitude, with JTOT often only slowly rising from background values. In addition, the energy dispersion of electrons with latitude was found to be quite variable. Often, increases in higher-energy (1-5 keV) electrons occurred at lower latitudes than increases in the lower-energy populations (100-400 eV). Thus the morning diffuse auroral boundary is often marked by the onset of a weak flux of low-energy electrons and/or a weak flux of higher-energy electrons, both of which make the position of the boundary difficult to determine precisely. In GHB we assumed both morning and evening boundaries mapped to the inner edge of the plasma sheet.

In adding midnight sector boundaries the only problem additional to those for the evening sector was found in the post-

midnight region (0000-0200 MLT). Here the satellite orbit is more nearly east-west such that the boundary is approached obliquely, making the transition from background into the aurora a long one in both time and distance covered. This presents no major difficulty, however, since the change in magnetic latitude over this time interval is small such that the corresponding error in the identification of the latitude of the boundary is small.

The noon sector boundaries have all the ambiguities associated with the morning boundaries, and more. The diffuse auroral electron flux continues to decrease as magnetic local time increases toward noon. Often in the noon sector no diffuse auroral precipitation is seen within the sensitivity of the sensor and the first clear increase in number flux is associated with

TABLE 1. Latitudinal Coverage for Given MLT Bins

MLT	Coverage in CGM*
0000-0100	51°-90'
0100-0200	60'-90
0200-0300	64'-90'
0300-0400	66'-90'
0400-0500	55'-90
1200-1300	60'-90
1300-1400	64'-90
1400-1500	64'-90'
1500-1600	60'-90'

*Corrected geomagnetic latitude.

43
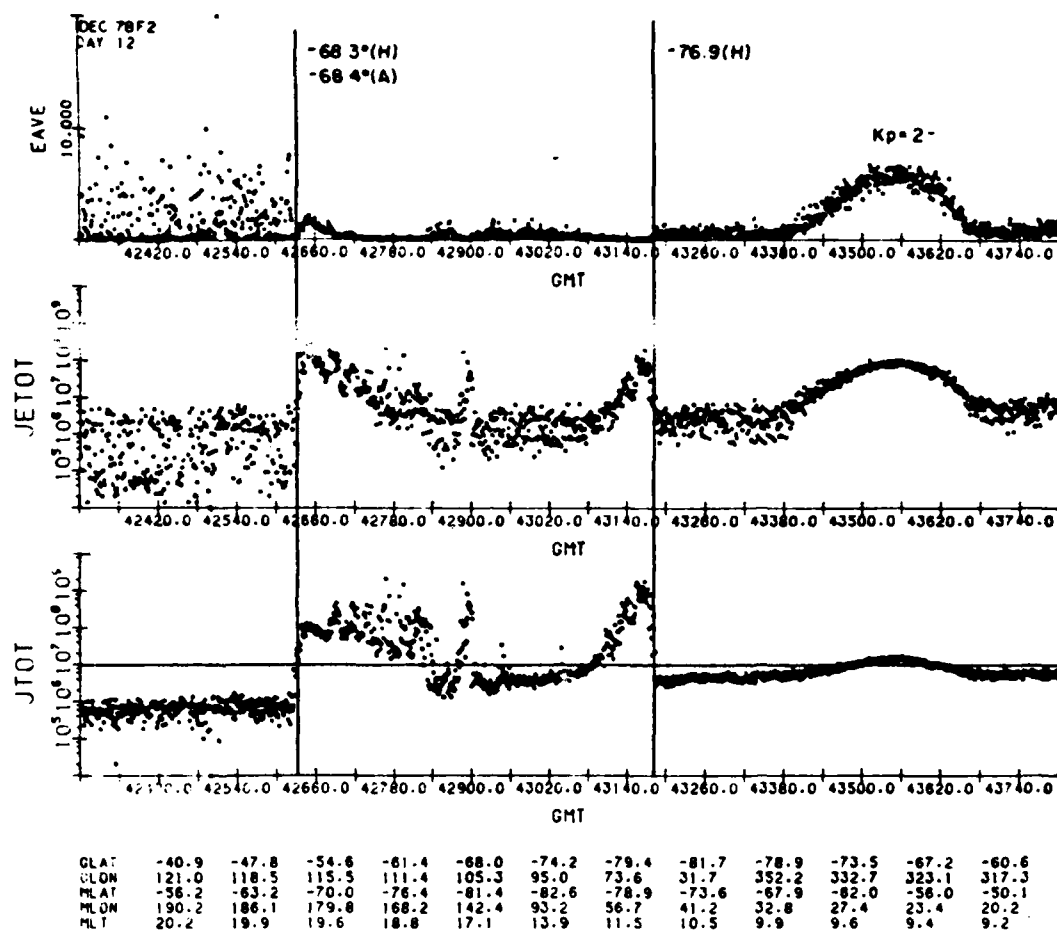
Fig. 3. Integral flux in $(cm^2 \text{ s sr})^{-1}$ (bottom panel), energy flux in keV/cm^2 sr s (middle panel), and average energy in keV (top panel) of precipitating electrons measured by the DMSP/F2 satellite passing over the south pole on December 12, 1978. These values are plotted as functions of universal time (in seconds), geographic and corrected geomagnetic latitudes and longitudes, and the magnetic local time of the satellite all projected to an altitude of 110 km. The horizontal line is drawn at the 10^- integral flux level. The vertical line at $-68.3°$ ($-76.9°$) marks the evening equatorward diffuse auroral boundary (the equatorward cusp boundary).

cusp precipitation. The percentage of cases for which no diffuse aurora are seen ranges from 1 to 2% between 0900-1100 to 7 to 8% between 1100 and 1300, rising finally to 30 to 90% between 1300 and 1500. An example of a case of no discernible dayside diffuse aurora is given in Figure 3. The satellite first passes over the evening sector near 2000 MLT. A typical clear evening auroral boundary, marked by a vertical solid line, is encountered at ~426 24 UT, $\Lambda_{CGM} = -68.3°$. The ramp in EAVE indicates a dispersion in energy from low to higher values as the satellite passes to higher latitude. The satellite passes over the polar cap and moves out of the auroral region at ~1100 MLT. The most equatorward dayside precipitation with JTOT > 10^- $(cm^2 \text{ s sr})^{-1}$ is clearly cusp precipitation: the average energy (EAVE is plotted on a linear scale) is less than a few hundred eV, and for the size of the number flux (JTOT) the energy flux (JETOT) is low. (Compare to the evening diffuse aurora.) The low-latitude (-50 to -60), smooth increases in JTOT, JETOT, and EAVE that lie below the cusp on the dayside in Figure 3 are due to channeltron contamination from radiation belt particles and are not of interest except when they obscure an auroral boundary. The problem of radiation belt

contamination in boundary selection is discussed in detail both in GHB and by *Gussenhoven et al.* [1982].

Figure 3 is a particularly clear example of no perceptible dayside diffuse aurora. Such cases are easily flagged. What complicates the dayside boundary determination are cases for which diffuse auroral precipitation is very weak or very irregular. For such cases the equatorward boundary is difficult to determine in a consistent manner. Furthermore, we were unable to find any relationship between the occurrence of weak or irregular dayside diffuse aurora and *Kp* and/or magnetic local time. That is, the full range from regular diffuse aurora to no diffuse aurora has been seen in all r.. sector local time bins and for all levels of magnetic activity. A detailed study of the dayside diffuse aurora has been undertaken in order to investigate the nature of particle dynamics in this region and will be presented elsewhere.

More than 20,000 auroral boundaries were manually selected using the data sets from the two satellites. The data used were obtained from 1977 to 1980. In order to have a good statistical sample for correlations with *Kp* a concerted effort was made to obtain at least 20 boundaries for each *Kp* level between 0 and

TABLE 2. $\Lambda = \Lambda_0 + \alpha Kp$

MLT	Number*	Λ_0	α	CC†
0000–0100	312	66.1	−1.99	−0.80
0100–0200	220	65.1	−1.55	−0.68
0400–0500	267	67.7	−1.48	−0.57
0500–0600	1123	67.8	−1.87	−0.71
0600–0700	2462	68.2	−1.90	−0.74
0700–0800	3159	68.9	−1.91	−0.76
0800–0900	2159	69.3	−1.87	−0.73
0900–1000	1178	69.5	−1.69	−0.66
1000–1100	864	69.5	−1.41	−0.57
1100–1200	513	70.1	−1.25	−0.52
1200–1300	353	69.4	−0.84	−0.35
1500–1600	63	70.9	−0.81	−0.34
1600–1700	204	71.6	−1.28	−0.66
1700–1800	526	71.1	−1.31	−0.69
1800–1900	997	71.2	−1.74	−0.82
1900–2000	2469	70.4	−1.83	−0.82
2000–2100	3309	69.4	−1.89	−0.82
2100–2200	3092	68.6	−1.86	−0.79
2200–2300	1482	67.9	−1.78	−0.77
2300–2400	461	67.8	−2.07	−0.81

*Number of boundaries used in each regression.
†Correlation coefficient.

5+ in each MLT bin, or about 300 boundaries per bin. In addition, for creating an auroral boundary index, we determined the boundaries for every polar pass of the F2 satellite in the year 1978. The 1978 boundaries disproportionately increase the size of the dawn and dusk local time samples.
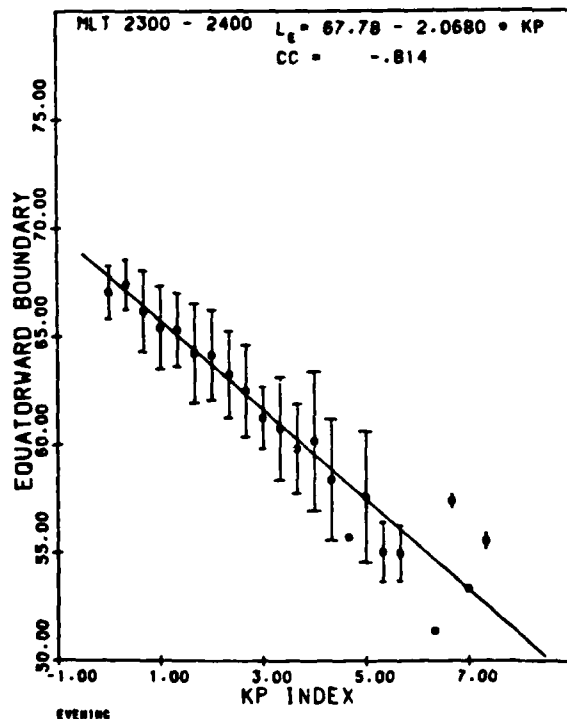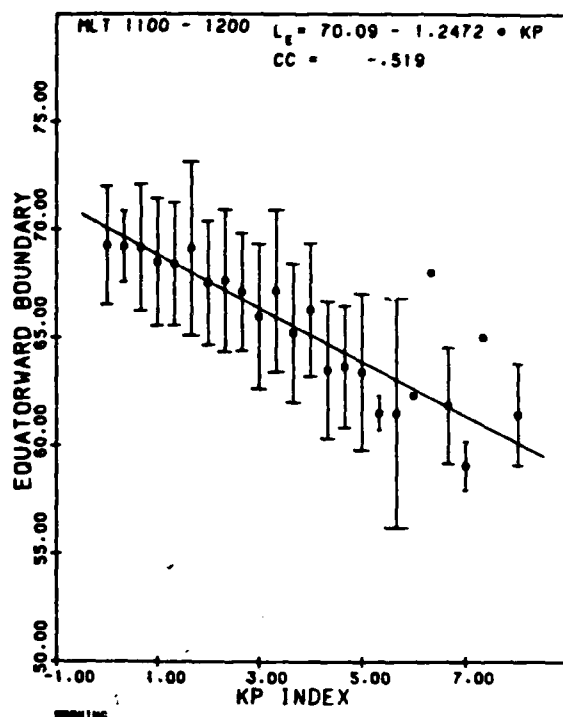

Fig. 4b. Same as Figure 4a but for the 1100–1200 MLT sector.

4. VARIATIONS OF BOUNDARIES WITH Kp

The equatorward diffuse auroral boundaries were sorted into one-hour magnetic local time bins. No separation was made by hemisphere. Within each bin a linear regression was performed on the boundaries as a function of Kp, resulting in a linear fit to the data of the form

$$\Lambda = \Lambda_{0i} + \alpha_i Kp \qquad (1)$$

In (1), Λ refers to the boundary predicted from the regression; Λ_{0i} and α_i are the intercept and slope, respectively, for the ith magnetic local time bin. Table 2 lists the values of Λ_0 and α for all local time bins except the four in which there were insufficient data. Also given are the number of boundaries used in each regression and the correlation coefficient. As expected, those magnetic local time bins that are limited in latitudinal range (and therefore in Kp range) have correlation coefficients that are significantly smaller (i.e., less negative) than those from neighboring local times.

For a given regression the average and standard deviation is calculated for the boundaries at each Kp value. Figures 4a and 4b are plots of the averages and the standard deviations as a function of Kp for the local time intervals 2300–2400 and 1100–1200, respectively. The straight-line fit that resulted from using all values of Λ_{CGM} (as given in Table 2) is also shown in each figure.

The boundary behavior in the midnight sector shows many features similar to those of the evening boundaries and presented in GHB. The averages for each Kp bin fall close to the regression line. The standard deviations from the averages vary from $\sim \pm 1°$ to $\sim \pm 3°$, increasing with increasing activity.

The boundaries in the noon sector have much higher standard deviations, and the averages have considerable scatter

Fig. 4a. Mean values and standard deviations in each Kp bin as a function of Kp for the 2300–2400 MLT sector. The solid line results from a linear regression performed with individual boundary determinations.

around the regression line. The much greater scatter in noon sector boundaries when ordered by Kp reflects the lack of consistency inherent in choosing the boundaries, as discussed above. The scatter results in much weaker correlations in the linear regression of the boundaries with Kp. Table 2 shows a continuous decrease in the absolute value of the correlation coefficient from dawn to noon. Figure 4b also illustrates that the slope α of the linear fit is much less in the noon sector than the midnight sector. This greater insensitivity of the boundary to magnetic activity persists from prenoon to 1800 MLT. In this MLT interval, α is 40–70% of the nighttime values.

A direct measure of the degree of scatter in the data set unaccounted for by the ordering in Kp is obtained by subtracting the appropriate regression equation from each boundary measurement ($\Delta \equiv \Lambda_{CGM} - \Lambda$) and determining the frequency distribution of these residuals (Δ). The residuals were binned in intervals of $1/10°$. The number in each bin was normalized to a total of 1000 points. The percentages of the total number of cases for which the residual scatter is within $\pm 1°$, $\pm 2°$, $\pm 3°$ of zero are 36, 65, 82%, respectively, for the entire data set. A plot of the distribution of the residual scatter is given in Figure 5 for the normalized total number. The distribution is approximately Gaussian with a sigma of about $2°$.

The statistically determined auroral oval boundary is shown globally for $Kp = 0$ and $Kp = 5$ in Figure 6. Here the values of Λ_0 ($\Lambda_0 + 5\alpha$) are plotted as crosses (circles) in MLT-CGM coordinates. Also shown are best circular fits to the data. In each case the circle is offset from the magnetic pole along the 0240 MLT longitude. For $Kp = 0$, the circle is centered at 87.6° and has a radius of 21.2°. This is essentially the same result
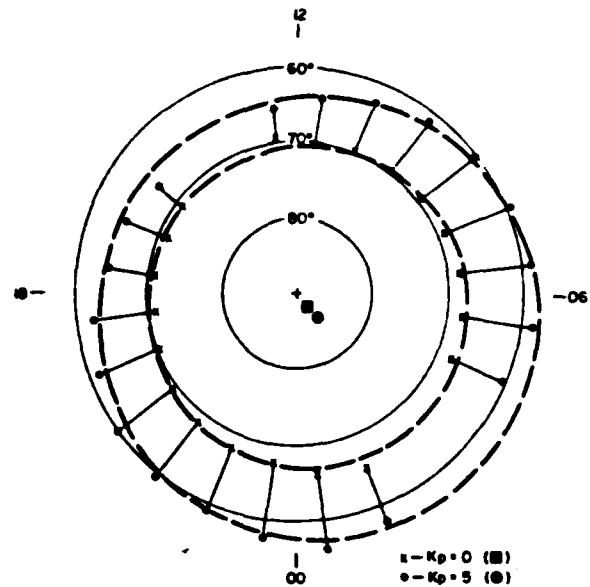
Fig. 6. Equatorward boundary of the auroral oval in MLT-CGM coordinates for high and low levels of magnetic activity. The points plotted are values resulting from linear regressions performed on all boundary values. The dashed circles are best fits to the data.

reported in GHB fitting only the dawn and dusk points. For $Kp = 5$ the circle is centered at 85.8° and has a radius of 29.1°.

As in GHB, we identify the equatorward diffuse auroral boundary with the inner edge of the plasma sheet and project the ionospheric boundaries to the equatorial plane of the magnetosphere by means of the Mead-Fairfield magnetic field mapping [Fairfield and Mead, 1975]. Figure 7 shows the projected boundaries for Kp 0,5 in local time/L shell coordinates (solid lines). We have chosen to project the circular fits in Figure 6 instead of either the actual averaged values, $\bar{\Lambda}_{CGM}$, or the linear regressed values, Λ, at Kp 0,5 since this results in smoothly varying projected plasma sheet boundaries. For low Kp and therefore high-latitude ionospheric boundaries the distorted magnetic field geometry is such that only a few degrees variation in the ionosphere can map to a large fraction of an L shell variation in the ecliptic plane. For this case using the circular fit can result in some inaccuracy. For the $Kp = 5$ case, however, the field lines along which the boundary is projected are more nearly dipolar and therefore quite insensitive to small variations in the boundary position. Also shown in Figure 7 (dashed lines) are the plasma sheet boundaries for Kp 0,5 that are predicted in GHB using a Volland-Stern convection electric field with $\gamma = 2$ and for the empirically fit stagnation distances. The offset in the low-Kp auroral oval appears to require a noon-midnight offset in the symmetry of the convection electric field to best fit the data. Otherwise, the agreement between the full data set and the earlier determined dependencies of E on Kp are quite good and will not be repeated or modified here. It is important to note that the need to rotate the axis of symmetry of the convection electric field in local time as a function of Kp which was reported in GHB is also found here.

5. AURORAL BOUNDARY INDEX

The systematics of the ionospheric auroral boundary were used in section 4 and in GHB to model large-scale statistical variations in the convection electric field. We can also use the
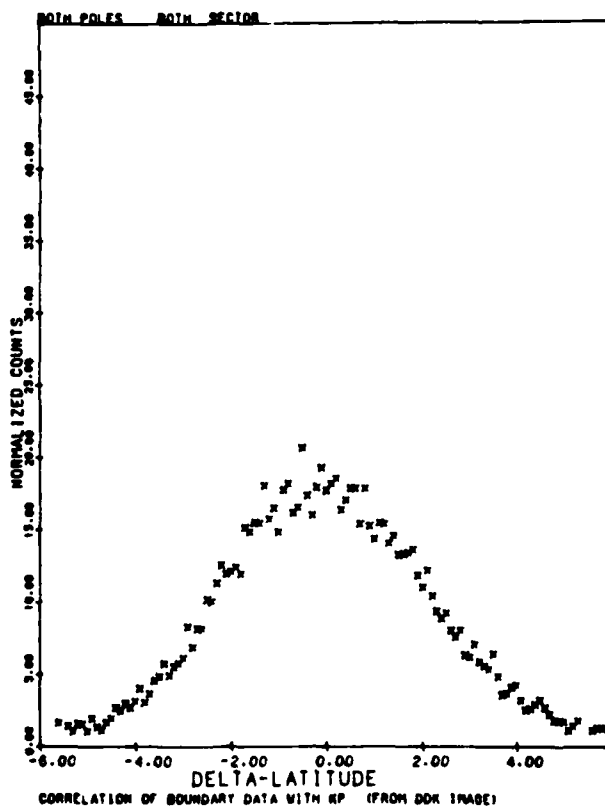

Fig. 5. Distribution of the residual scatter in the boundary set when compared to linear regression values. The distribution is accumulated in 0.1 bins and normalized to 1000 cases.

individual boundary measurement as an indicator of iono-
spheric auroral activity and to estimate the position of the
entire oval. The question we address in this section is in what
form should the boundary information be presented in order to
serve as an index of auroral activity?

A measured boundary, Λ_{CGM}, in the ith MLT bin, can, by
inverting equation (1), predict a value of Kp:

$$Kp' = (\Lambda_{CGM} - \Lambda_{0i})/\alpha_i \qquad (2)$$

In (2) the predicted Kp value is labeled Kp', and the values of
Λ_{0i} and α_i are given in Table 2. The Kp' in (2) is an instanta-
neous value, not a 3-hour averaged value, as is Kp. A 3-hour
averaged value of Kp', $\overline{Kp'}$, can be constructed by directly
averaging values of Kp' found from all the boundaries obtained
within the same 3-hour interval used for Kp. A scatter plot of
Kp versus $\overline{Kp'}$ (labeled KPRIME) for the month of March 1978
is shown in Figure 8. The straight lines show the results of
performing the linear regressions on both Kp versus $\overline{Kp'}$ (line
ending in dot) and $\overline{Kp'}$ versus Kp. The correlation coefficients
are greater than 0.8. Correlation coefficients for similar regres-
sions on data from the other months in 1978 range from 0.77 to
0.89.

Although there is great familiarity with the Kp index among
magnetosphere researchers, and an estimate of its value from
satellite data is of interest, particularly if produced in real time,
there are several reasons why a Kp index derived from bound-
ary measurements could be confusing or even misleading. First,
the boundary measurement is not a magnetic activity measure-
ment, as is Kp. From the high correlation between boundary
position and Kp we conclude that the two are strongly coupled;
however, the relationship is not a clear causal one. A derived
$\overline{Kp'}$, as such, confuses the nature of the source of the index and
suggests that the magnetic activity drives the boundary posi-
tion. Second, it is clear from Figure 8 that a rather broad range
of $\overline{Kp'}$ values occurs for a given Kp: in excess of ± 1 units. This
directly reflects the range of boundaries that can occur in a
given MLT bin for a given Kp and is not necessarily a measure
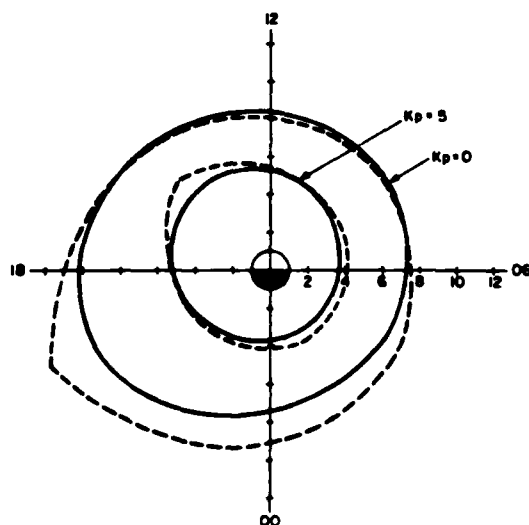of the quality of the $\overline{Kp'}$ index. Such comparisons will be hard
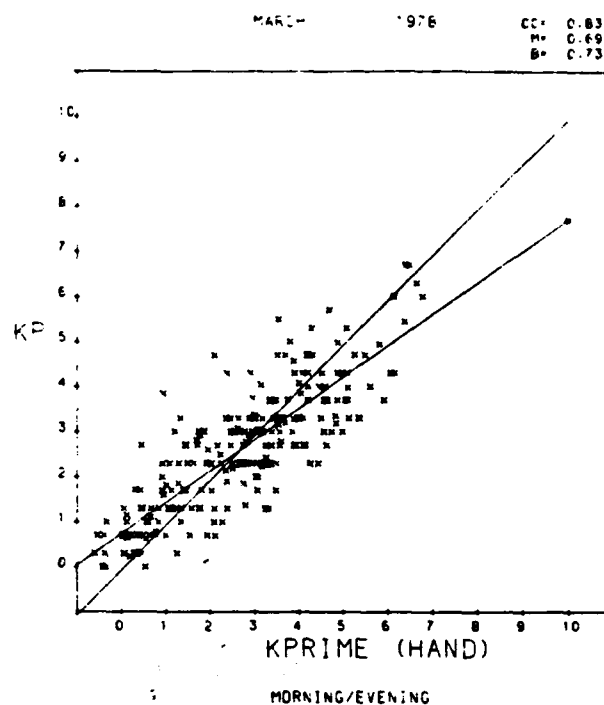
Fig. 8. Scatter plot of the values of Kp versus corresponding
3-hour average value of Kp' (labeled KPRIME) when $\overline{Kp'}$ is calculated
using morning and evening equatorward auroral boundaries obtained
in March 1978. The result of performing a linear regression on Kp
$(\overline{Kp'})$ versus $\overline{Kp'}$ (Kp) is shown by the straight line ending in a dot (not
ending in a dot). The correlation coefficient, slope, and intercept of the
Kp versus $\overline{Kp'}$ line are shown in the upper right-hand corner.

to avoid if $\overline{Kp'}$ is used. Third, because of the nature of the
boundary data the $\overline{Kp'}$ will contain a nonuniform number of
points, from 0 to 11, depending on data gaps and where in the
3-hour interval the first boundary falls. In addition, the averag-
ing process itself decreases the possible temporal resolution.
The boundary measurements (2 per 50 min) have a time resolu-
tion more appropriate to substorm activity than the 3-hour Kp
interval. Using an instantaneous Kp' is again promoting con-
fusion in interpretation.

The most direct index is simply the boundary itself, tagged by
both universal and local time. The large offset of the auroral
oval in magnetic coordinates toward higher latitudes at noon
and lower latitudes at midnight makes use of multi-local time
values of the boundary difficult at best. We can, however, scale
each boundary to a boundary in a single MLT bin by way of
Kp'. This procedure necessarily involves use of the statistical
results in section 2 (as would be the case if $\overline{Kp'}$ were used), but
there is no avoiding this in any attempt at removing local time
effects from the boundary set. If the boundaries are scaled to
midnight, the equivalent midnight boundary is

$$\Lambda_M = \Lambda_{0M} + \alpha_M Kp' \qquad (3)$$

where the subscript M stands for the local time sector 2300–
2400. Substituting from (2) to eliminate Kp' gives

$$\Lambda_M = \left(\Lambda_{0M} - \frac{\alpha_M}{\alpha_i}\Lambda_{0i}\right) + \frac{\alpha_M}{\alpha_i}\Lambda_{CGM} \qquad (4)$$

Thus Λ_M is the midnight oval boundary which is predicted

Fig. 7. Projections of circular fits of Kp 0,5 ionospheric auroral
boundaries to the ecliptic plane using the magnetic field models for
$Kp < 2$, > 2, respectively (solid lines); and plasma sheet boundaries
calculated from a Volland-Stern convection electric field model with
$\gamma = 2$ and stagnation and rotation values fitted by GHB (dashed lines).
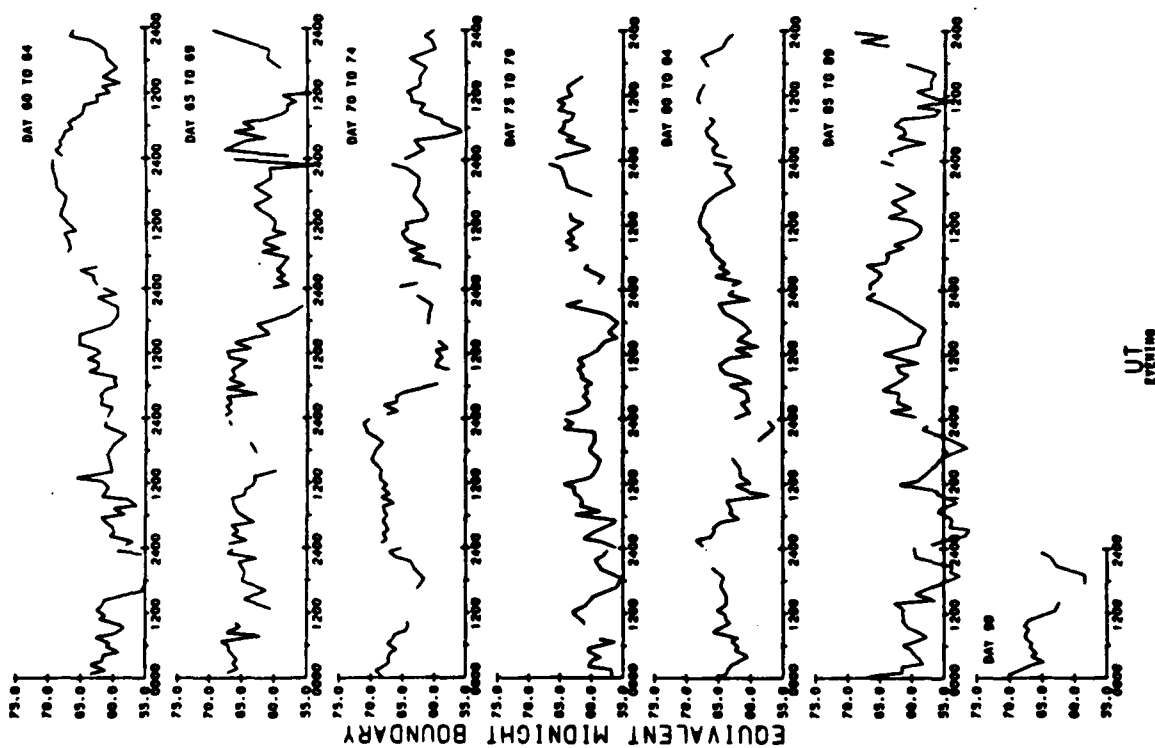
Fig. 9a. Equivalent midnight boundary calculated from the evening equatorward auroral boundary set, plotted as a function of universal time for March 1978.
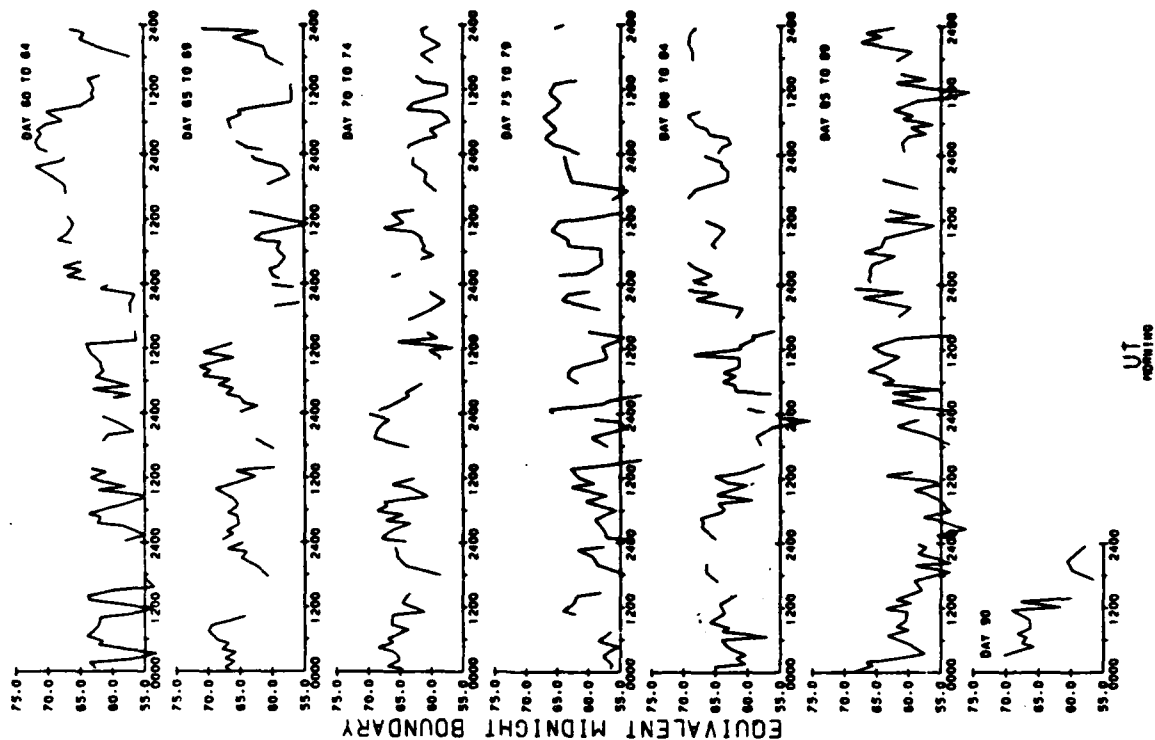
Fig. 9b. Same as Figure 9a only using the morning equatorward auroral boundary set.

from the measured boundary, A_{CGM}, in the ith local time bin, using the statistically determined oval position summarized in Table 2.

Equivalent midnight boundaries plotted as a function of universal time for March 1978 are given in Figures 9a and 9b, separately calculated from the evening and the morning boundaries, respectively. In principle the two sets of equivalent boundaries should be combined to give the the highest possible time resolution. However, in comparing the two sets it is clear that there are times when the equivalent midnight boundary derived from morning sector boundaries is systematically higher (day 64) than that derived from the evening sector boundaries, lower (day 71), is lagging the evening increases or decreases (days 76, 81), or is nearly the same (day 88). In addition, the equivalent midnight boundaries derived from the morning sector boundaries have more abrupt and larger variations from point to point than those derived from the evening sector due, at least in part, to the weaker correlation with Kp and greater ambiguity in boundary selection. For these reasons we choose to reduce the temporal resolution in the auroral boundary index by using only equivalent midnight boundaries from the evening sector for index values. To reiterate, evening is chosen over the morning for three reasons: (1) the evening boundaries are easier to choose with greater confidence than the morning boundaries, (2) the correlations of the evening boundaries with Kp in a given local time bin have smaller scatter and higher correlation coefficients than morning boundaries, and 3) the midnight equivalent boundary derived from the evening boundary varies more smoothly than that derived from the morning boundary.

We define the auroral boundary index to be the projected midnight equatorward boundary found using an evening sector boundary determined from precipitating electron increases and the statistically determined systematic local time variation of the oval. During periods of good data accumulation there will be one index value approximately every 55 min. The auroral boundary index is presented month by month for 1978 in the appendix Figures A1–A12.

6.   SUMMARY AND DISCUSSION

The systematics of the diffuse auroral oval boundary statistically determined from precipitating electron data and presented here extend previous results to include almost all local time sectors of the oval. Overall, the boundary is found to be well ordered by Kp, moving to lower latitudes with increasing magnetic activity. The boundary is most sharply defined in the evening and midnight sectors, where it has a well-ordered dispersion in energy with latitude and can be determined with a high degree of confidence. The boundary in these sectors also correlates most highly with Kp and is most sensitive to variations in Kp. For local times from the midnight to the dawn sector the precipitation onset becomes more gradual, the dispersion in energy irregular, and the confidence level in the boundary choice decreases. The boundary still responds to changes in Kp but more weakly, and the scatter from average values increases. From dawn to the noon sector the diffuse auroral boundary becomes progressively less clear and can disappear altogether. Although an expansion of the dayside boundary with Kp is still found to exist statistically, the correlation with Kp is much reduced and the overall variation from low to high magnetic activity less than in any part of the midnight sector.

In magnetic local time (and corrected geomagnetic latitude)

the equatorward auroral boundary can be well fit by a circle whose center is offset from the magnetic pole in the postmidnight direction. A circular fit is good at each Kp level, the circular radius increasing with increasing activity.

It is just this systematic behavior that makes the equatorward auroral boundary a potential index of auroral activity and of large-scale magnetospheric particle dynamics. It also allows a statistical projection of the entire oval from a single boundary measurement. To be useful to a wide range of researchers, an index for a physical system should fulfill certain criteria. Some that are suggested by the success (and failure) of other indices are as follows: The index should have a clear relationship to those factors that determine the dynamics of the system. The possibility of ambiguity in interpretation should be minimized. The index should have appropriate temporal resolution and consistent temporal coverage. The index should not consume excessive resources in preparation, and, if at all possible, should be prepared automatically, in near real time.

Since the first criterion is fundamental, we address it first. The magnetic activity index Kp was used to order the equatorward boundaries. It was used primarily because of its availability and widespread use. However, Kp was found to order the boundaries better than either the solar wind parameters [Hardy et al., 1981] or other magnetic indices, such as AE, Dst, etc. (unpublished). Both the increase in magnetic activity measured at ground stations (Kp), and the motion of the diffuse auroral boundary (A_{CGM}) are principally responsive phenomena: that is, they occur as a result of dynamical processes throughout the magnetosphere. As such, their relation to one another is of lesser importance and has less research value than their individual relationships to magnetospheric configurations.

There is widespread agreement that the immediate source of precipitating diffuse auroral electrons is the central plasma sheet [Vasyliunas, 1970; Lassen, 1974; Winningham et al., 1975; Lui et al., 1977; Meng et al., 1979]. The inner, or earthward, boundary of the central plasma sheet is principally determined by a quasi-static magnetospheric convection electric field which is the sum of cross-tail and corotation electric fields. Electrons are convected toward the earth from the distant tail by the cross-tail field. As they near the earth they also drift counterclockwise under the influence of the increasing corotation field. The combined motion ultimately moves electrons not lost through precipitation into the ionosphere out through the dayside magnetopause. Calculations of trajectories of particles in the crossed magnetic and electric fields of the magnetosphere have been made by many researchers [see, e.g., Kivelson and Southwood, 1975; Cowley and Ashour-Abdalla, 1976; Ejiri, 1978; Southwood and Kaye, 1979]. Under the following conditions: (1) time stationary, (2) no polarization electric fields, and (3) no electron losses; the electron motion in a dipolar magnetic field and a Volland-Stern electric field has the following properties: (1) The trajectories are symmetric about the dawn-dusk axis, as is the most earthward trajectory, (2) the trajectories of electrons with increasing kinetic energy (or more precisely, magnetic moment, which is a conserved quantity) are confined to positions increasingly distant from the earth, and (3) electrons of given magnetic moment that reach positions nearest the earth are convected in from the dusk flank of the tail.

Figure 7 clearly shows that the projected plasma sheet boundary is not symmetric about the dawn-dusk axis. We suggest three possible causes for this asymmetry: (1) shielding
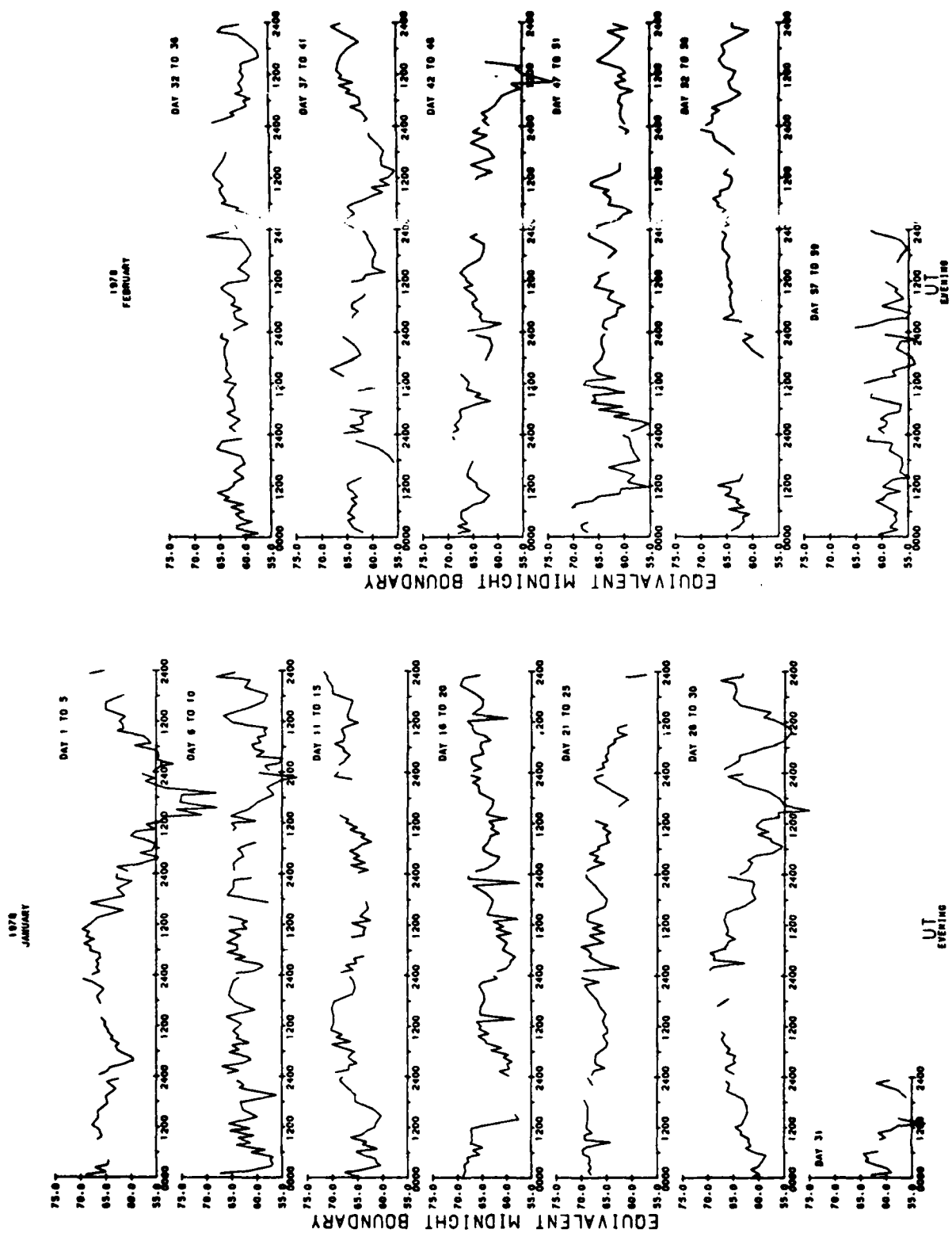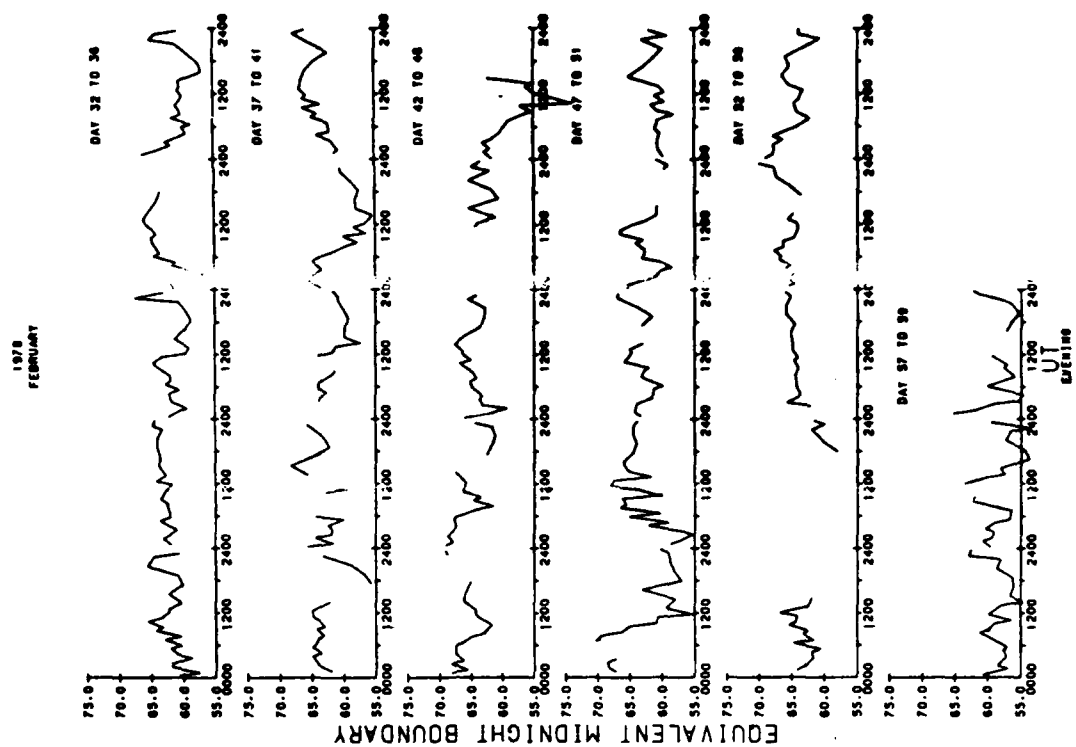
49

Fig. A2. Auroral boundary index for February 1978

Fig. A1. Auroral boundary index for January 1978.
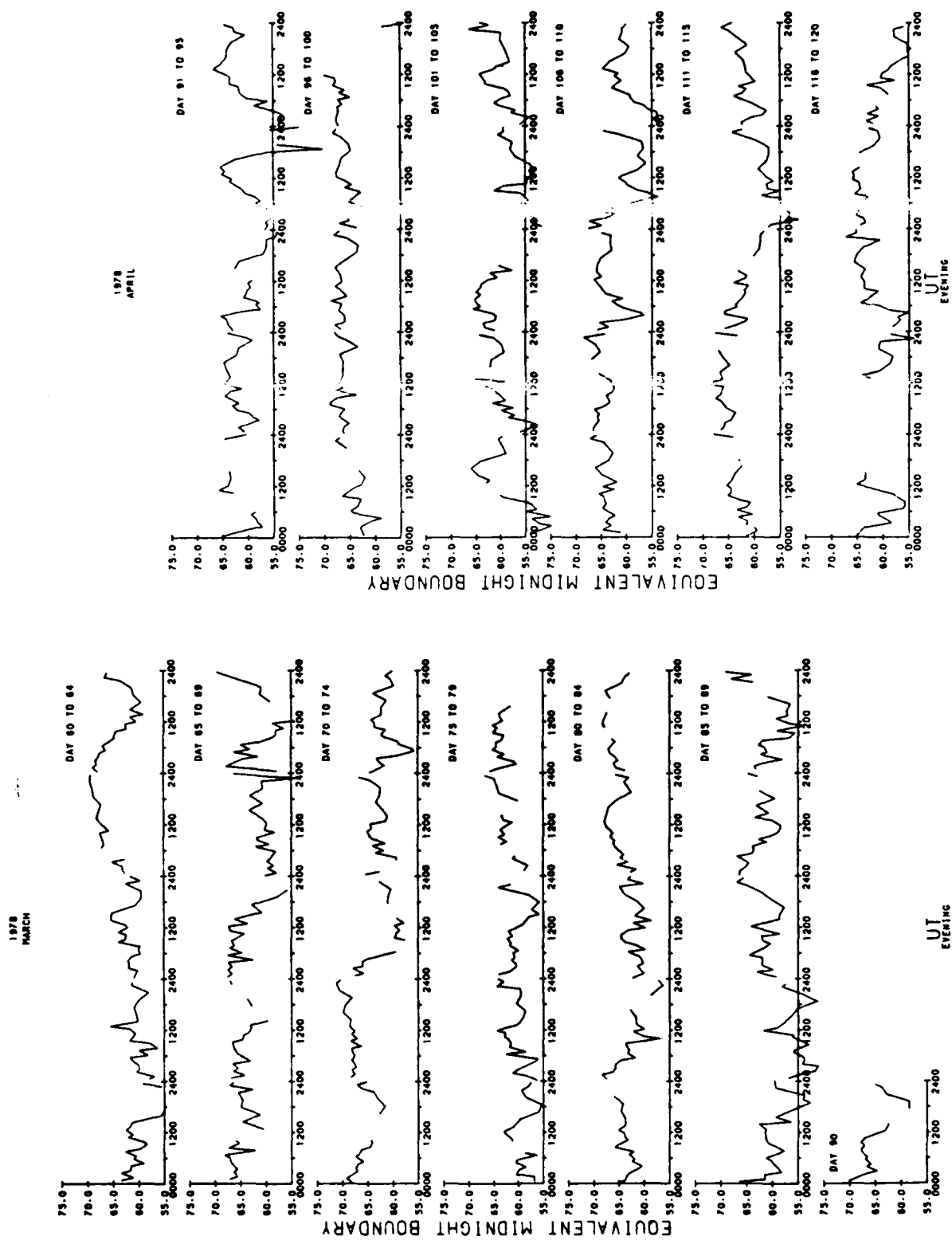
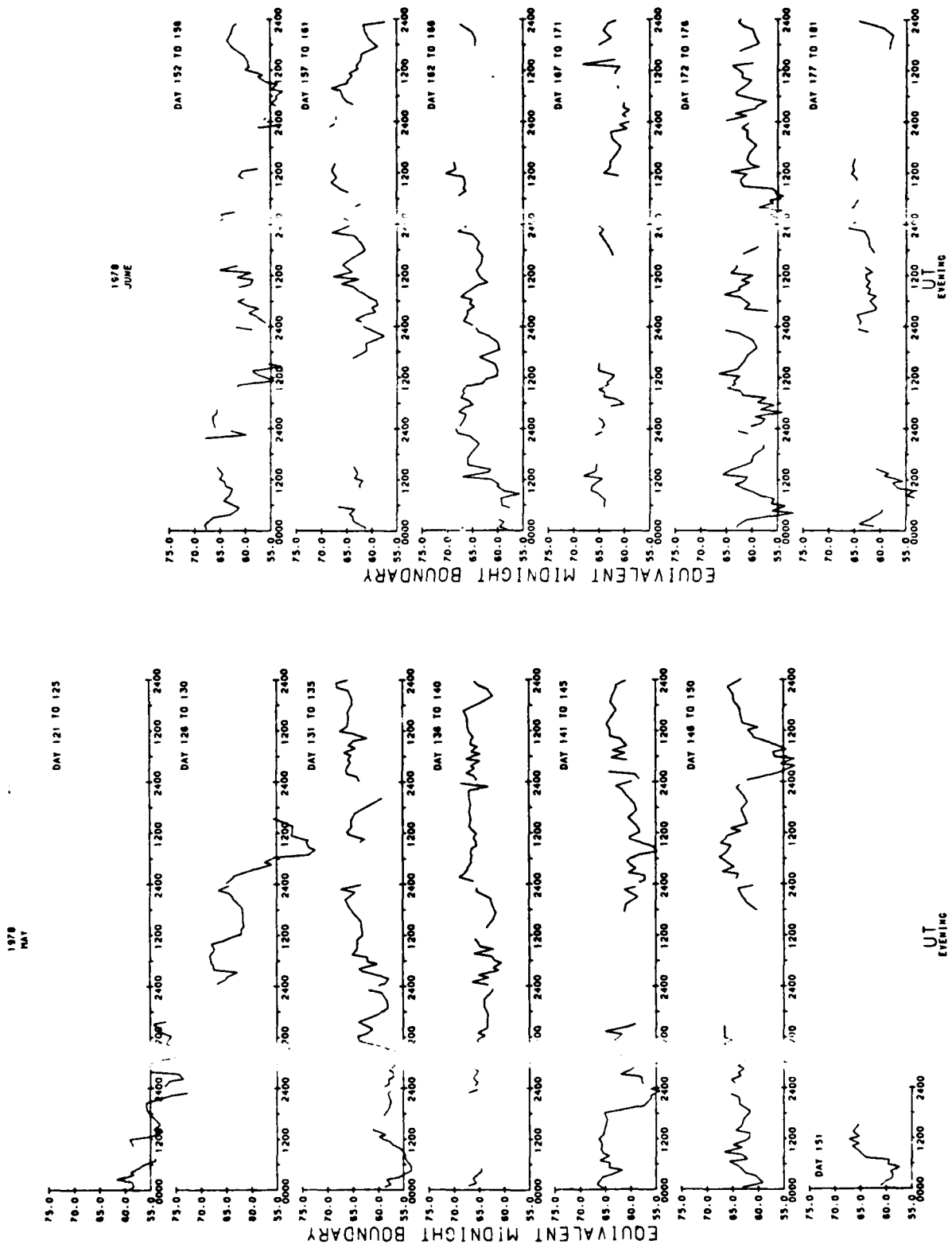Fig. A4. Auroral boundary index for April 1978.
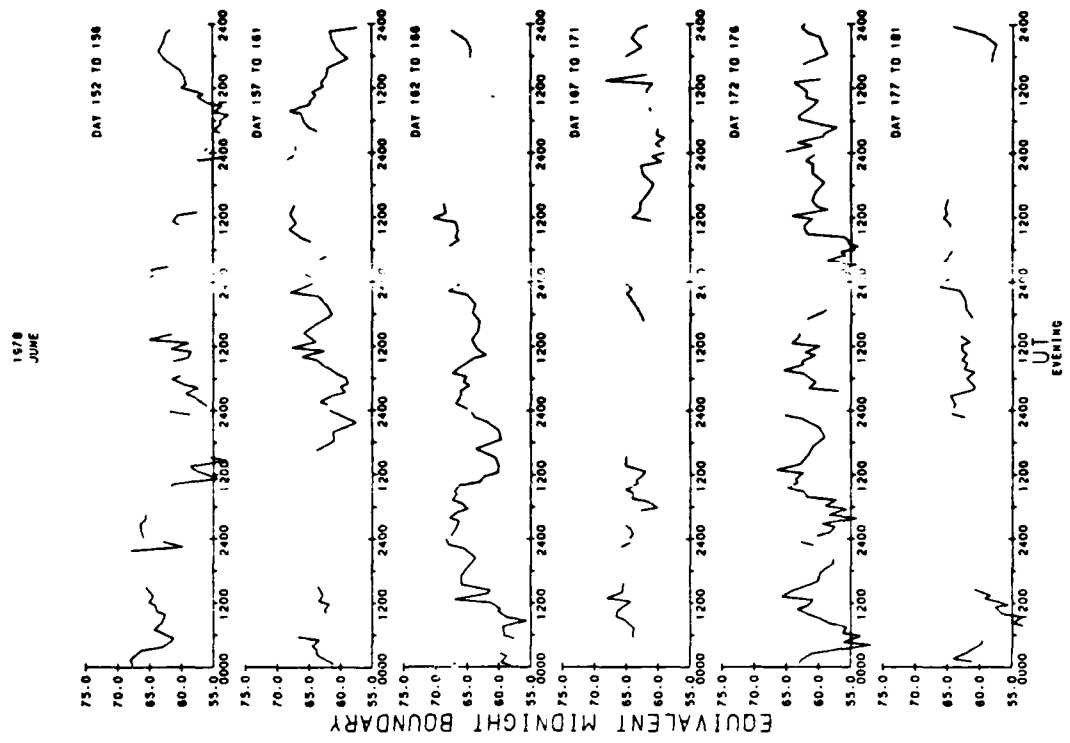

Fig. A3. Auroral boundary index for March 1978.

Fig. A6. Auroral boundary index for June 1978.

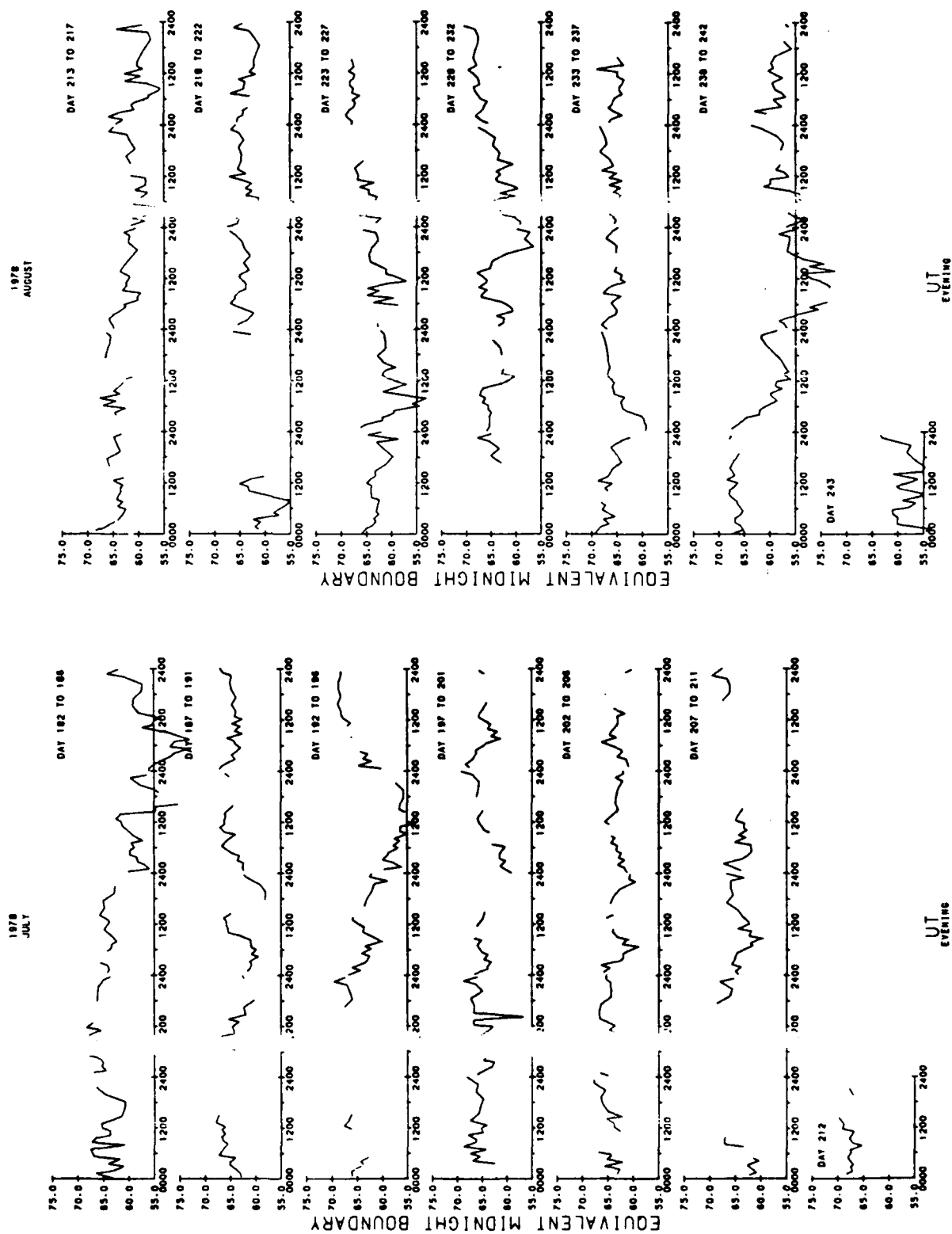Fig. A5. Auroral boundary index for May 1978.

Fig. A8. Auroral boundary index for August 1978.

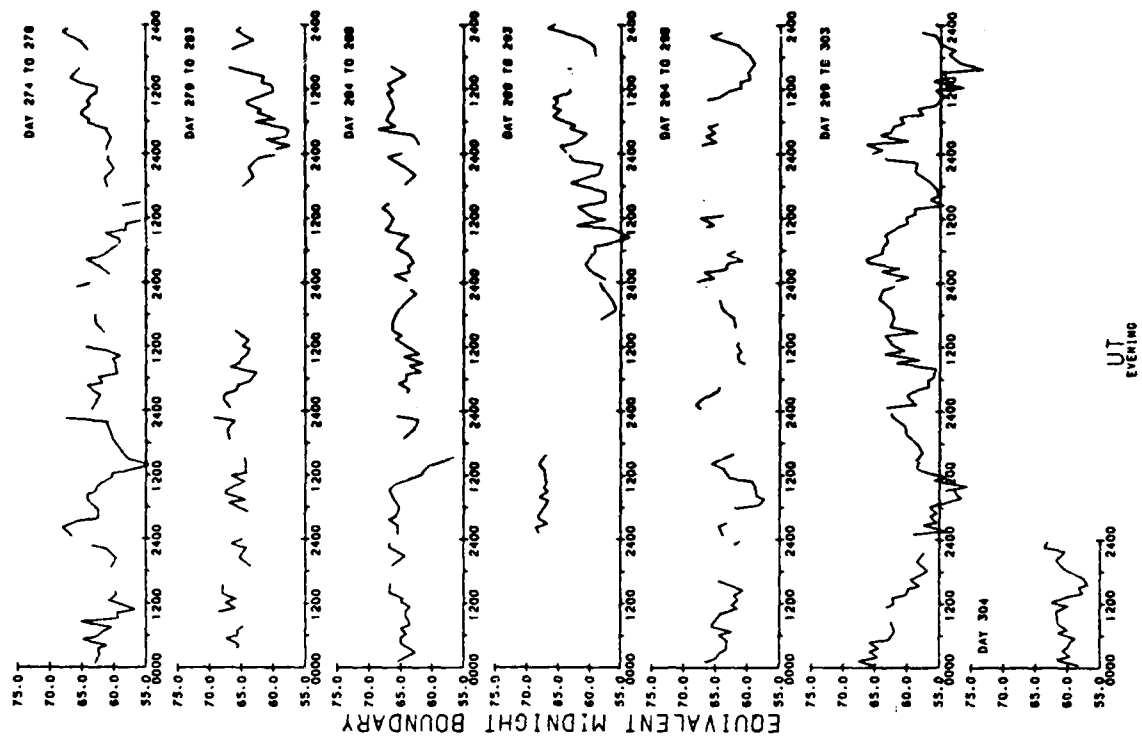Fig. A7. Auroral boundary index for July 1978.
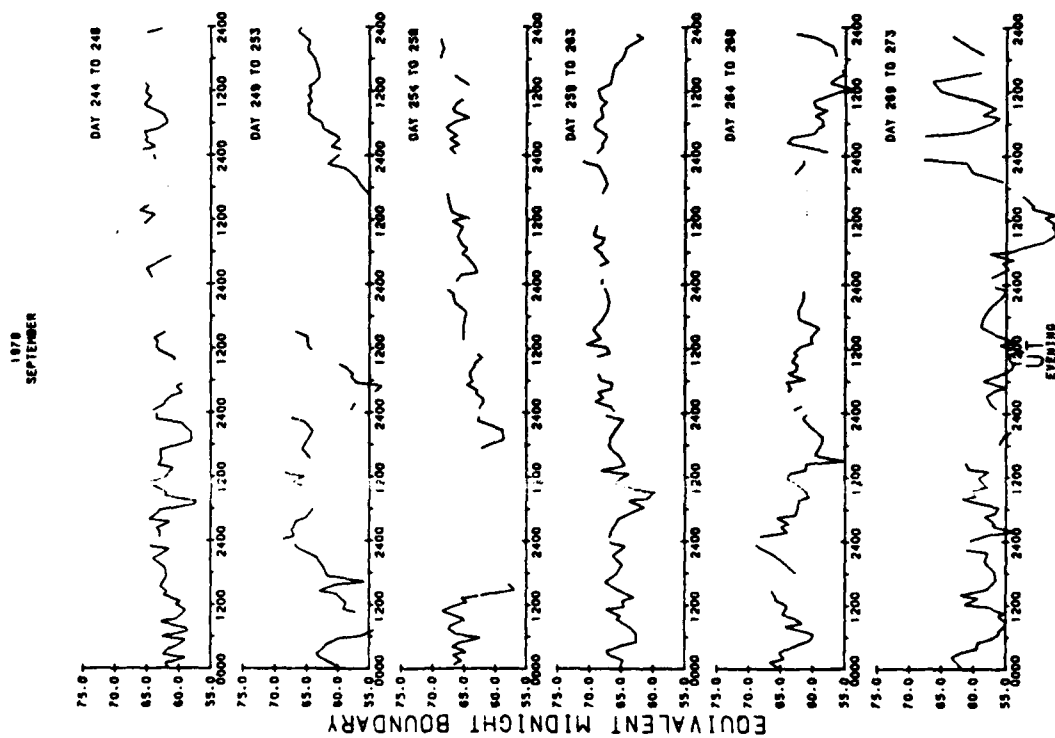
Fig. A10. Auroral boundary index for October 1978.

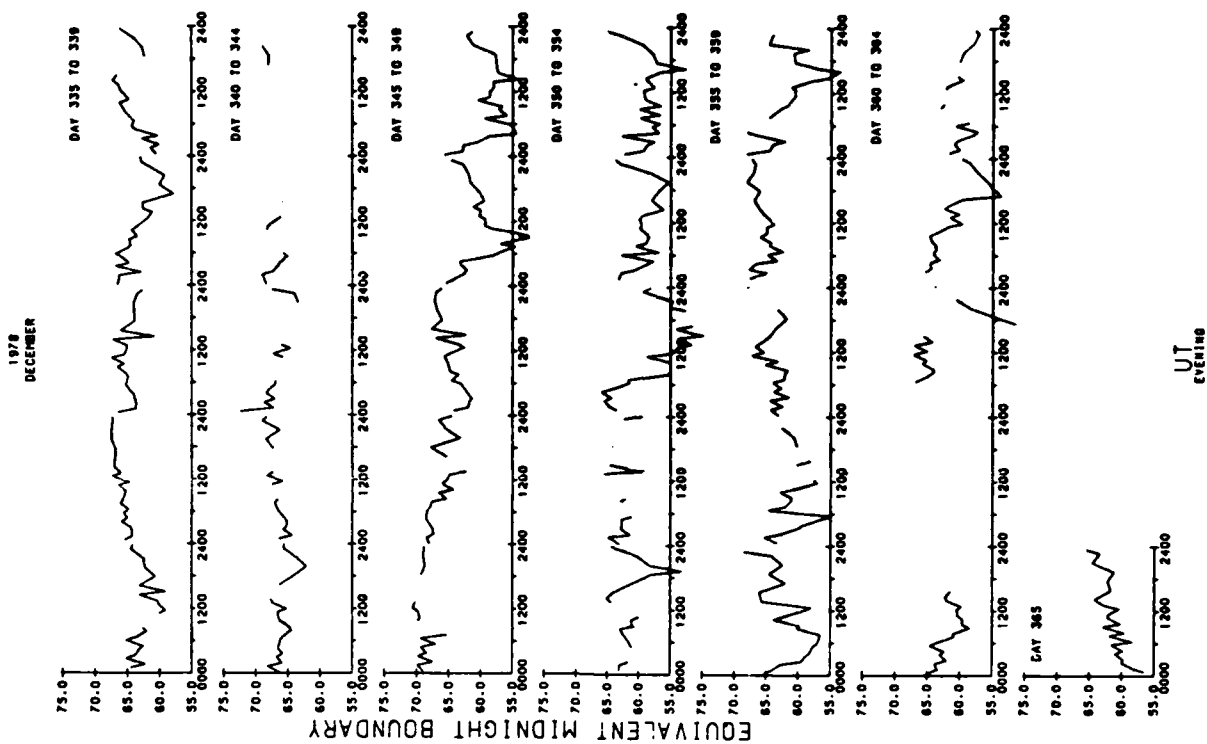

Fig. A9. Auroral boundary index for September 1978.

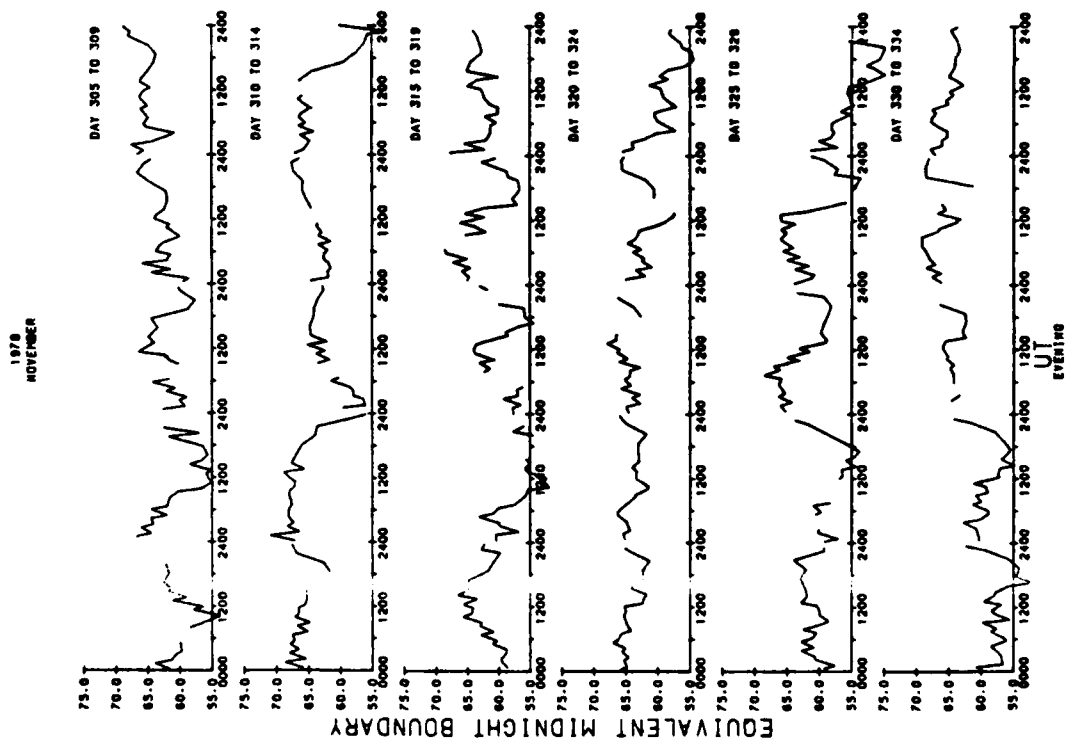Fig. A12.　Auroral boundary index for December 1978.

Fig. A11　Auroral boundary index for November 1978.

polarization electric fields, (2) an energy-dependent loss mechanism, and (3) a local-time-dependent loss mechanism. In the first of these a charge separation electric field is established in the plasmasphere that cancels out the imposed magnetospheric electric field. Electrons are thus excluded from this region because their trajectories take them to greater radial distances or to the magnetopause. The second possibility is that the rate at which electrons of a given energy precipitate is high enough that all electrons of that energy are lost before they have time to convect around to the noon sector. If this effect were more pronounced for low-energy electrons, we would expect to see a less well-defined boundary and a harder diffuse aurora from midnight to noon, as is the case. The boundary is then at a higher latitude and no longer reflects the projection of the zero energy Alfvén layer. Finally, the mechanisms that continually scatter electrons into the loss cone, causing diffuse auroral precipitation, could be weaker in the noon sector for low-energy particles. Again, the effect would be to move the boundary poleward. By limiting the auroral boundary index to evening boundary measurements we more directly reflect the state of the magnetospheric convection electric field and, in particular, the field found in the dusk flank of the magnetosphere.

Although the morning boundaries are not used in the index, they constitute a valid data set that can be applied to studies of diffuse auroral processes. The high correlations of morning boundaries with Kp for local times well past dawn indicate that the loss processes are not great enough to erode the parent plasma sheet population to the point that large-scale convective patterns are destroyed. The convection electric field still dominates the boundary systematics. Nevertheless, if the next most important quasi-stationary effect on the position and energy characteristics of the diffuse aurora is the loss process, the morning boundary data set could be used to evaluate models of loss when they include the convection electric field. There are reports of such calculations [*Fontaine and Blanc*, 1983] which have interesting conclusions concerning the applicability and nonapplicability of strong pitch angle diffusion. At this stage in the development of such models, case studies rather than statistical studies are probably a more appropriate form of analysis. Until a quantitative assessment of particle loss on the morning boundary position is made, identifying other differences between morning and evening projected equivalent boundaries with previous levels of magnetic activity, interplanetary conditions, magnetospheric asymmetries, and other effects is speculative at best.

The second criterion, that the index should be unambiguous, is the reason the evening boundaries are scaled to one local time (2300–2400 MLT). The scaling requires use of the statistical variations of the boundaries with Kp in order to eliminate the local time dependence. There are a variety of other ways to do this: by coordinate redefinition, statistically ordering boundaries in two different local time sectors, and so on. However, scaling by means of the Kp dependence appeared to be the clearest and simplest alternative.

The ... resolution and ... stages ... the index plots in the Appendix. For the large-scale variation, and that which probably reflects the magnetospheric convection electric field, the resolution is good. For more impulsive events, such as substorms, it is marginal.

Finally, it should be again noted that the index given in the appendix was created from equatorward boundaries which were chosen by hand. The process was tedious and required an extensive and time-consuming system of checking to avoid recording and interpolation errors. It has been pointed out

above that the DMSP satellites are operational. Thus barring satellite failure, the data base for continuous production of the index will exist. In order to make index production feasible an algorithm for choosing the equatorward boundary from the raw telemetry data stream has been developed [*Hardy and Holeman*, 1983]. The algorithm was tested and revised by comparison of 1978 computer-chosen boundaries with the 1978 hand-chosen boundaries. Although a small percentage of cases did show large boundary differences, overall the two methods were comparable. Perhaps more important, each set had approximately the same internal consistency. The algorithm is currently in place for the DMSP F6 satellite. A report on the comparison of the two sets of boundaries as well as a listing of all 1978 boundaries is available in the work by *Gussenhoven et al.* [1982].

APPENDIX: AURORAL BOUNDARY INDEX

Each value of the auroral boundary index is a projected midnight equatorward auroral boundary found using an actual evening sector boundary and the statistically determined systematic local time variation of the auroral oval. The index is presented in Figures A1–A12 as a function of universal time, by month, for 1978.

REFERENCES

Cowley, S. W. H., and M. Ashour-Abdalla, Adiabatic plasma convection in a dipole field: Electron forbidden-zone effects for a simple electric field model, *Planet Space Sci.*, 24, 805, 1976.

Ejiri, M., Trajectory traces of charged particles in the magnetosphere. *J. Geophys. Res.*, 83, 4798, 1978.

Fairfield, D. H., and G. D. Mead, Magnetospheric mapping with a quantitative geomagnetic field model, *J. Geophys. Res.*, 80, 535, 1975.

Fontaine, D., and M. Blanc, Theoretical approach to the morphology and dynamics of diffuse auroral zones. *J. Geophys. Res.*, in press, 1983.

Gussenhoven, M. S., D. A. Hardy, and W. J. Burke, DMSP F2 electron observations of equatorward auroral boundaries and their relationship to magnetospheric electric fields, *J. Geophys. Res.*, 86, 768, 1981.

Gussenhoven, M. S., D. A. Hardy, N. Heinemann, and E. Holeman, 1978 diffuse auroral boundaries and a derived auroral boundary index, *Rep. AFGL-TR-82-0398*, Air Force Geophys. Lab., Hanscom AFB, Mass., 1982.

Hardy, D. A., and E. Holeman, The global auroral boundary code for the Global Weather Central of the Air Weather Service, technical report, Air Force Geophys. Lab., Hanscom AFB, Mass., in press, 1983.

Hardy, D. A., W. J. Burke, M. S. Gussenhoven, N. Heinemann, and E. Holeman, DMSP F2 electron observations of equatorward auroral boundaries and their relationship to ... solar wind velocity and the north-south component of the interplanetary magnetic field, *J. Geophys. Res.*, 86, 9961, 1981.

Hardy, D. A., M. S. Gussenhoven, and A. Huber, The precipitating electron detectors (SSJ/3) for the block 5D flights 2–5 DMSP satellites: Calibration and data presentation. *Rep. AFGL-TR-79-0210*, Air Force Geophys. Lab., Hanscom AFB, Mass., 1979

Kamide, Y., and J. D. Winningham, A statistical study of the 'instantaneous' nightside auroral oval: The equatorial boundary of electron precipitation as observed by the ISIS 1 and 2 satellites. *J. Geophys. Res.*, 82, 5573, 1977.

Kivelson, M. G., and D. J. Southwood, Approximations for the study of drift boundaries in the magnetosphere, *J. Geophys. Res.*, *80*, 3528, 1975.

Lassen, K., Relation of the plasma sheet to the nighttime auroral oval, *J. Geophys. Res.*, *79*, 3857, 1974.

Lui, A. T. Y., C. D. Anger, and S.-I. Akasofu, The equatorward boundary of the diffuse aurora and auroral substorms as seen by the ISIS 2 auroral scanning photometer, *J. Geophys. Res.*, *80*, 3603, 1975.

Lui, A. T. Y., D. Venkatesan, C. D. Anger, S.-I. Akasofu, W. J. Heikkila, J. D. Winningham, and J. R. Burrows, Simultaneous observations of particle precipitations and auroral emissions by the ISIS 2 satellite in the 19–24 MLT sector, *J. Geophys. Res.*, *82*, 2210, 1977.

Meng, C.-I., R. H. Holzworth, and S.-I. Akasofu, Auroral circle delineating the poleward boundary of the quiet auroral oval, *J. Geophys. Res.*, *82*, 164, 1977.

Meng, C.-I., B. Mauk, and C. E. McIlwain, Electron precipitation of evening diffuse aurora and its conjugate electron fluxes near the magnetospheric equator, *J. Geophys. Res.*, *84*, 2545, 1979.

Sheehan, R. E., and R. L. Carovillano, Characteristics of the equatorward auroral boundary near midnight determined from DMSP images, *J. Geophys. Res.*, *83*, 4749, 1978.

Slater, D. W., L. L. Smith, and E. W. Kleckner, Correlated observations of the equatorward diffuse auroral boundary, *J. Geophys. Res.*, *85*, 531, 1980.

Southwood, D. J., and S. M. Kaye, Drift boundary approximations in simple magnetospheric convection models, *J. Geophys. Res.*, *84*, 5773, 1979.

Stern, D. P., The motion of a proton in the equatorial magnetosphere, *J. Geophys. Res.*, *80*, 595, 1975.

Vasyliunas, V. M., Low energy particle fluxes in the geomagnetic tail, in *Polar Ionosphere and Magnetospheric Processes*, edited by G. Skavli, Gordon and Breach, New York, 1970.

Volland, H., A semiempirical model of large-scale magnetospheric electric fields, *J. Geophys. Res.*, *78*, 171, 1973.

Winningham, J. D., F. Yasuhara, S.-I. Akasofu, and W. J. Heikkila, The latitudinal morphology of 10-eV to 10-keV electron fluxes during magnetically quiet and disturbed times in the 2100–0300 MLT sector, *J. Geophys. Res.*, *80*, 3148, 1975.

EQUATORWARD AURORAL BOUNDARY VARIATIONS WITH AE AND DST

R.E. Sheehan and M.S. Gussenhoven
Department of Physics, Boston College
Chestnut Hill, MA 02167

D.A. Hardy
Air Force Geophysics Laboratory
Hanscom AFB, MA 01731

ABSTRACT

Equatorward boundaries of electron precipitation in the auroral zone measured by the DMSP/F2 satellite in 1978 are correlated with D_{st} and AE indices. In the evening local time sector (19-22 corrected geomagnetic local time), linear correlation coefficients of the boundary latitude versus AE are highest (.80-.87) when AE is averaged over intervals of 4-5 hours preceding a boundary determination. In the morning sector (04-08 CGLT), maximum correlations are lower (cc=.70-.80) and occur for AE averages of 2-3 hours. Multiple linear correlations involving one hour D_{st} values, AE, and AE^2 yield correlation coefficients of .88 at 19-22 CGLT (4 hour AE averages) and .83-.85 at 04-06 CGLT (2 hour averages).

I. INTRODUCTION

A data base of equatorward auroral boundaries has been established using precipitating electron data from the SSJ/4 sensors on the DMSP/F2 and F4 satellites from 1978 to 1980 (Gussenhoven et al., 1981, 1983). The variations of the boundaries with magnetic activity, as measured by KP, and with solar wind parameters have been studied as a means of investigating magnetospheric electric fields under the assumptions a) that the inner edge of the electron

population in the central plasma sheet is the electric-field-produced zero-energy Alfven boundary, and b) that the inner edge maps to the equatorward boundary of the diffuse aurora (Gussenhoven et al., 1981; Hardy et al., 1981; and for justification of the assumptions, see Lui et al., 1975; and Fontaine and Blanc, 1983). The systematic nature of the boundary variations with KP has been established using either particle or optical data by several other research groups as well (Lui et al., 1975; Meng et al., 1977; Kamide and Winningham, 1977; Sheehan and Caronllano, 1978; and Slater et al., 1980). The extremely high correlations of the boundary with KP in one-hour evening local time zones (better than 0.8), and the regularity of boundary crossings by the DMSP satellites led Gussenhoven et al. (1983) to introduce an index of auroral activity derived from the projection of boundaries measured at various local times to midnight.

Despite the proven regularity of variations in the equatorward auroral boundary with KP, the use of KP as an organizing parameter of these and other auroral data is frequently criticized, the principal reason being difficulty in relating KP directly to magnetospheric processes. This paper uses the existing set of DMSP auroral electron boundaries to study the variations in the boundary position for given magnetic local times as a function of the auroral electrojet (AE) and D_{st} magnetic indices. AE is a high latitude index that monitors electrojet current strength from a set of magnetometer stations around the auroral zone. D_{st} is a low latitude index sensitive to ring current fluctuations in response to magnetospheric conditions, especially magnetic storms. These indices are more physical than the Kp index and can be easily averaged over any desired time interval.

59

II. THE AURORAL BOUNDARY DATA BASE

The auroral boundaries used in this study are taken from the listings given in Gussenhoven et al. (1982). A full description of the DMSP orbits, the SSJ/4 sensor, and the method of selecting electron boundaries is given in Gussenhoven et al. (1981, 1983). The boundaries we use here are confined to the year 1978, for which AE data were readily available at the time of the study. The data from which the 1978 boundaries were derived are taken onboard the DMSP/F2 satellite. Briefly, the DMSP/F2 satellite has a dawn-dusk, sun-synchronous, polar orbit at 840 km altitude and a period of 101 min. Good magnetic local time coverage of the high latitude region extends from 05 to 10 on the morningside, and 17 to 22 on the eveningside, when data from both hemispheres are combined. The SSJ/4 particle detectors onboard measured precipitating electrons in the energy range 50 eV to 20 keV in 16 energy channels and returned a complete spectrum once per second. The equatorward precipitating electron boundaries are determined by examining the variation in the directional integral number flux over the high latitude region. The boundary is chosen when the flux rises and stays above background as one proceeds poleward from low latitudes on either side of the oval. In general, this boundary is very well defined on the eveningside (and can often be quantitatively specified as the point at which the flux exceeds 10^7 e/cm^2 s st). The morning boundaries are also clear for the most part, but because of extended gradients in the flux at the boundaries, have more ambiguity than on the eveningside. Details of other problems in selecting boundaries can be found in the above references.

III. BOUNDARY VARIATIONS WITH AE AND DST

Correlations with AE. One minute average values of the auroral

60

electrojet index, AE, were assigned to the auroral boundaries. The boundaries were sorted in 50 nT bins of AE for each one-hour corrected magnetic local time (CGLT) bin, and averaged. Figure 1 shows the variation in the average as a function of AE for the hourly local time interval 21-22 CGLT and for north pole data. Error bars indicate the standard deviation of the averages, given by σ_s/N, where σ_s is the sample standard deviation, and N is the number of points in the sample. Except for fluctuations at the highest AE values, the boundaries show a systematic decrease with increasing AE.

Linear regressions were performed for each local time bin using the corresponding one minute AE value for each boundary. Data from the north and south poles were maintained separately. The results are given in Table 1. Local times for which the sample number is less than 300 are not listed in the table. Here, N is the number of samples; λ_0 is the intercept, and α the slope in the regression formula: $\lambda = \lambda_0 + \alpha \cdot AE$, where λ is the measured boundary; and CC is the correlation coefficient for the regression. For these same local time zones, the previous correlation coefficients for the boundary variations with KP ranged from 0.66 to 0.82, with approximately the same internal variations with local time. Thus, the "instantaneous" AE value orders the equatorward boundary of electron precipitation less well, in a linear sense, than KP.

Two straightforward reasons for lower correlations of the boundaries with AE than with KP suggest themselves. One is that KP, a three-hour index, integrates over many magnetospheric parameter changes taking place on multiple time scales to which the boundary cannot be individually sensitive. The second is that a linear functional form is not the best for fitting to AE. Since KP is a quasi-logarithmic measure of magnetic activity and AE gives a linear response, a functional form which is logarithmic, or has higher powers

of AE, may be more appropriate. That this is the case is also suggested by Figure 1. We examine, in detail, the first possibility below, and discuss the refinements in correlation made by changing the functional form of AE in the section on multiply correlating AE and D_{st}.

Table 2 is a summary of the results of performing a regression analysis on the equatorward boundary when the corresponding AE value used is the average over the one-hour interval preceding the boundary determination. With the exception of one local time bin (05-06, north pole), an improvement in correlation results. The increase in the correlation coefficient, in the negative sense, is typically between 0.05 and 0.1 points.

Another byproduct of averaging AE is a systematic effect involving the regression line parameters. Comparison of Table 1 (1 min AE averages) and Table 2 (1 hour AE averages) reveals that averaging produces somewhat steeper regression line slopes and intercepts at higher latitudes. This occurs because boundaries associated with extremely large and extremely small one minute index values usually become associated with more typical values upon averaging over some interval containing the exceptional value. In a scatter plot of boundary latitude versus index value, high latitude boundaries found typically with small one minute AE values would usually shift to the right, to a higher averaged AE value, while low latitude boundaries associated with large one minute values would shift to the left upon averaging. More typical data points would be less affected by averaging. The net result is to squeeze data points at the left and right hand extremes of the scatter plot toward the center, effectively steepening the slope and raising the intercept of a least-squares linear fit.

The effect of increasingly longer averaging intervals for AE is shown in Figures 2 and 3 for the evening and morning local time sectors, respectively.

Each plot represents north hemisphere observations in the indicated CGLT interval. The number of boundaries for each case is given in parentheses. We have included here the earliest morning local time bin although the number of cases is small. The absolute values of the correlation cofficients of boundary latitude versus AE averaged over intervals from 1 to 8 hours duration immediately preceding the time of a boundary measurement are shown. Correlations are also run with 1 minute values and 15 and 30 minute averaged values. It is evident that there is a clear distinction between the correlation behaviors in the pre- and post-midnight local time sectors. The correlations maximize for averaging intervals of 2-3 hours duration on the morningside and for intervals of 4-5 hours duration on the eveningside. In addition, peak values of the coefficient are somewhat higher ($\geq$ .8) in the evening and drop off somewhat more slowly than in the morning. The peak values of the correlation coefficients exceed those for linear regressions with KP by $\sim$ .05 points.

The AU and AL indices which make up the total AE index were also tested for correlations with the boundary, both for one minute values and averages up to one hour. In addition, one hour averages of AE, AU, AL, were computed for intervals centered on the boundary time. Although AL approaches AE in performance, the consistently best correlations are obtained when AE is averaged over intervals preceding the boundary time.

<u>Correlations with D_{st}</u>. One hour D_{st} index values were assigned to each of the auroral boundaries and linear regressions performed between the two in one hour CGLT zones. The results are given in Table 3. Although AE is an index of auroral zone magnetic activity, and D_{st} of low-latitude magnetic variations, the D_{st} index performs nearly as well as the one minute averaged AE values (comparing Tables 1 and 3). Again, the correlation with KP is

63

somewhat better.

Multiple Correlations with AE, AE^2, lnAE, and D$_{st}$. Table 4 summarizes correlations obtained with KP, D$_{st}$, and AE taken individually and in various combinations at one local time sector in the north hemisphere. Figure 4 plots the correlation coefficients for some of the functions listed in Table 3 at those local time sectors having a reasonably large number of cases. Functional forms using D$_{st}$, AE, and AE^2 yield the best results at all local times. Most correlations are nearly the same whether AE is averaged over 2 or 4 hours preceding a boundary determination. The largest differences occur in the morning sector. Functions with ln(AE) do not increase the correlations appreciably, suggesting than an AE^2 term alone accounts for the dependence sufficiently well.

By using both AE and D$_{st}$ and by averaging AE for times comparable to that of the KP index, very high correlations are found, well exceeding those of KP alone. The correlations are uniformly better on the eveningside as compared to the morningside, no doubt reflecting the higher confidence level in the nine well-defined evening boundaries.

IV. DISCUSSION

We summarize the results of the above statistical study as follows:

1. Neither one minute averaged values of AE or hourly averaged values of D$_{st}$ order the variations in the equatorward auroral boundary as well as KP.

2. The ability of AE to order the boundary variations is maximized by averaging AE in 2-5 hour intervals preceding the boundary determination. For the maximizing averaging interval, AE orders the boundary variations better than KP.

3. The ability of AE to order the boundary variation is increased by

64

adding non-linear terms. Adding a term in AE^2 is equally as good as using lnAE.

4. Maximum ordering of boundary variations is achieved by a combination of D_{st}, AE, and AE^2, when AE is averaged from 2-5 hours prior to the boundary determination. The result of performing the multiple regression yields correlation coefficients approaching 0.9.

The relationship between the boundary latitude and an index of magnetic activity depends on two interrelated factors, the sources of current contributing to the index and the time scales controlling the boundary position. The fact that the boundary responds more clearly for indices averaged on the order of hours and does not react to rapid changes in magnetospheric conditions is likely a consequence of the time required to achieve balance between earthward convection allowed by shielding mechanisms and processes governing the lifetimes of drifting particle populations. Shielding and lifetime effects also contribute to the asymmetry of the boundary relative to a dawn-dusk axis (Gussenhoven et al., 1983). The increased ordering of the boundaries by increasing the time-average of AE was also found by Sauvaud et al. (1983) for multiple correlations involving AE and soft electron boundaries at 2200-2400 CGTLT measured by the AUREOL-1 -2 satellites. They found a maximum correlation peak with averaging intervals of 4-5 hours duration. They attribute "inertia" of the boundary to two separate factors. (1) an inhibition of inward convection by polarization electric fields which prevent inward penetration of convection electric fields during periods of increasing activity, and (2) weak precipitation of injected plasma during periods of decreasing activity. Our study indicates that the time scale of the boundary dynamics differs from morning to evening.

It should not be surprising that the KP index succeeds so well in

65

correlations with the boundary because it combines a long time scale (3 hours) and nonlinearity, two properties involved in maximizing correlations with AE. Since correlations with a combination of D_{st} and AE exceed either index used alone, the boundary position appears to be physically related, in a complex way, to the ring current and ionospheric currents. Using a lumped circuit approach, Siscoe (1982) modeled the link between the solar wind and the magnetosphere via field-aligned (Birkeland) currents. The solar wind is transmitted to the polar cap by region 1 Birkeland currents that, in turn, feed region 2 Birkeland currents through resistive Pedersen currents in the ionosphere. Region 2 currents then connect with the ring current, modeled as an equivalent resistance and inductance in series. The model is restricted to a single source of potential, the constant solar wind electric field, and excludes electric induction in the magnetospheric tail. Temporal changes in the constant potential are treated as relaxations from one steady state to another. One result of this model is that D_{st} varies with IMF B_z^2 and AE varies with IMF B_z, if the potential itself is linearly proportional to southward IMF B_z. In fact, a plot of boundary latitude versus D_{st} (not shown) is generally linear, while the overall dependence with AE, seen earlier in Figure 1, is decidedly nonlinear. Thus, high correlation with a linear D_{st} term and a squared AE term suggests that the boundary position reflects coupling between the current sources.

Equatorward motion of the boundary over several hours indicates extended periods of magnetic and auroral activity. In addition to the classical substorm pattern operating on a time scale of 1-2 hours, shorter and longer time scales are also seen. Bursts of auroral activity lasting 15-30 minutes are a common feature in montages of all-sky camera pictures (Krukonis and Whalen, 1980). From a statistical study of over 700 DMSP images, Sheehan et

66

al. (1982) also found that images showing active auroral conditions tended to recur over several successive orbits. The short period bursts appear to correspond to rapid AE fluctuations and motions of discrete auroral arcs, while the long period activity governs the motion of diffuse aurora and the electron boundary.

REFERENCES

Fontaine, D., and M. Blanc, Theoretical approach to the morphology and dynamics of diffuse auroral zones, J. Geophys. Res., 88, 7171, 1983.

Gussenhoven, M.S., D.A. Hardy, and W.J. Burke, Comment on 'diurnal variation of the auroral oval size', by C.-I. Meng, J. Geophys. Res., 85, 2373, 1980.

Gussenhoven, M.S., D.A. Hardy, and W.J. Burke, DMSP/F_2 electron observations of equatorward auroral boundaries and their relationship to magnetospheric electric fields, J. Geophys. Res., 86, 768, 1981.

Gussenhoven, M.S., D.A. Hardy, N. Heinemann, and E. Holeman, 1978 diffuse auroral boundaries and a derived auroral boundary index, Rep. AFGL-TR-82-0398, Air Force Geophys. Lab., Hanscom AFB, Mass., 1982 ADA130175.

Gussenhoven, M.S., D.A. Hardy, and N. Heinemann, Systematics of the equatorward diffuse auroral boundary, J. Geophys. Res., 88, 5692, 1983.

Hardy, D.A., W.J. Burke, M.S. Gussenhoven, N. Heinemann, and E. Holeman, DMSP/F_2 electron observations of equatorward auroral boundaries and their relationship to the solar wind velocity and the north-south component of the interplanetary magnetic field, J. Geophys. Res., 86, 9961, 1981.

Kamide, Y., and J.D. Winningham, A statistical study of the 'instantaneous' nightside auroral oval: the equatorward boundary of electron precipitation as observed by the ISIS 1 and 2 satellites, J. Geophys.

Res., 82, 5573, 1977.

Krukonis, A.P., and J.A. Whalen, Occurrence and lifetimes of discrete auroras near midnight, J. Geophys. Res., 85, 119, 1980.

Lui, A.T.Y., C.D. Anger, and S.I. Akasofu, The equatorward boundary of the diffuse aurorae and auroral substorms as seen by the ISIS 2 auroral scanning photometer, J. Geophys. Res., 80, 3603, 1975.

Lui, A.T.Y., D. Venkatesan, C.D. Anger, S.-I. Akasofu, W.J. Heikkila, J.D. Winningham, and J.R. Burrows, Simultaneous observations of particle precipitations and auroral emissions by the ISIS 2 satellite in the 19-24 MLT sector, J. Geophys. Res., 82, 2210, 1977.

Meng, C.-I, R.H. Holzworth, and S.-I. Akasofu, Auroral circle delineating the poleward boundary of the quiet auroral oval, J. Geophys. Res., 82, 164, 1977.

Savaud, J.A., J. Crasnier, Yu.I. Galperin, and Y.I. Feldstein, A statistical study of the equatorward boundary of the diffuse aurora in the pre-midnight sector, submitted to Geophys. Res. Lett., 1983.

Sheehan, R.E., and R.L. Carovillano, Characteristics of the equatorward auroral boundary near midnight determined from DMSP images, J. Geophys. Res., 83, 4749, 1978.

Sheehan, R.E., R.L. Carovillano, and M.S. Gussenhoven, Occurrence and recurrence of auroral activity in DMSP images, J. Geophys. Res., 87, 3581, 1982.

Siscoe, George L., Energy coupling between regions 1 and 2 Birkeland current systems, J. Geophys. Res., 87, 5124, 1982.

Slater, D.W., L.L. Smith, and E.W. Kleckner, Correlated observations of the equatorward diffuse auroral boundary, J. Geophys. Res., 85, 531, 1980.

Table 1. Regression parameters (intercepts and slopes) and correlation
coefficients for electron equatorward boundary latitude and one
minute AE values in 1978; λ = λ + α AE

North Pole					South Pole			
CMLT	N	λ_o	α	CC	N	λ_o	α	CC
05-06	844	65.7	-0.012	-0.69				
06-07	1347	65.6	-0.010	-0.64	320	66.4	-0.014	-0.60
07-08	1057	67.1	-0.011	-0.69	1097	66.1	-0.010	-0.66
08-09	383	67.7	-0.010	-0.62	671	67.0	-0.012	-0.66
09-10					452	67.9	-0.009	-0.60
17-18					361	69.8	-0.007	-0.69
18-19					521	69.1	-0.009	-0.75
19-20	759	68.1	-0.011	-0.78	810	68.2	-0.011	-0.75
20-21	1209	67.1	-0.009	-0.75	953	67.1	-0.011	-0.73
21-22	1390	66.3	-0.010	-0.71				
22-23	792	66.3	-0.010	-0.63				

69

Table 2. Regression parameters (intercepts and slopes) and correlation coefficients for electron equatorward boundary latitude and AE values averaged over one hour preceding a boundary determination: $\lambda = \lambda_o + \alpha\ AE$

North Pole					South Pole			
CMLT	N	λ_o	α	CC	N	λ_o	α	CC
05–06	841	65.3	−0.010	−0.64				
06–07	1346	66.4	−0.013	−0.75	320	66.8	−0.015	−0.64
07–08	1055	67.4	−0.012	−0.77	1097	66.5	−0.012	−0.74
08–09	383	68.2	−0.013	−0.69	671	67.4	−0.013	−0.74
09–10					452	68.3	−0.011	−0.72
17–18					360	70.1	−0.009	−0.74
18–19					521	69.5	−0.010	−0.80
19–20	759	68.5	−0.013	−0.84	807	68.5	−0.012	−0.81
20–21	1209	67.3	−0.010	−0.77	953	67.4	−0.013	−0.78
21–22	1389	66.8	−0.012	−0.79				
22–23	792	66.6	−0.012	−0.69				

Table 3. Regression parameters and correlation coefficients for boundary latitude (λ) with one hour D_{st} index values in 1978:
$$\lambda = \lambda_o + \alpha \cdot D_{st}$$

North Pole					South Pole			
CGLT	N	λ_o	α	CC	N	λ_o	α	CC
05-06	844	65.0	0.091	0.52				
06-07	1347	65.2	0.097	0.61	320	66.5	0.104	0.54
07-08	1057	66.5	0.096	0.65	1097	65.8	0.094	0.64
08-09	383	67.4	0.082	0.67	671	66.2	0.089	0.63
09-10					452	67.6	0.093	0.65
17-18					361	69.6	0.078	0.65
18-19					521	68.8	0.085	0.70
19-20	759	67.9	0.102	0.69	810	67.7	0.094	0.73
20-21	1209	66.6	0.087	0.70	953	66.9	0.103	0.72
21-22	1390	65.9	0.090	0.66				
22-23	792	65.9	0.084	0.58				

Table 4. Correlation coefficients resulting from the indicated terms in the fitting function. North hemisphere boundaries at 2100 CGLT.

| Term(s)	CC
D_{st} (1 hour)	.66
AE (1 minute)	.71
AE (1 hour)	.79
K_p	.79
D_{st}, AE (1 minute)	.80
D_{st}, AE, AE^2 (2 hour)	.88
D_{st}, AE, AE^2 (4 hour)	.88
D_{st}, ln (AE), ln $(AE)^2$ (4 hour)	.88

FIGURE CAPTIONS

Figure 1   Average boundary latitude vs. AE at 2100-2200 CGLT in the north
hemisphere. Boundaries averaged in 50nT bins; error bars indicate
standard deviations of the averages.

Figure 2   Correlation coefficients of boundary latitude vs. AE averaged over
intervals of 1-8 hours duration immediately preceding a boundary
determination. North hemisphere boundaries in the evening sector.
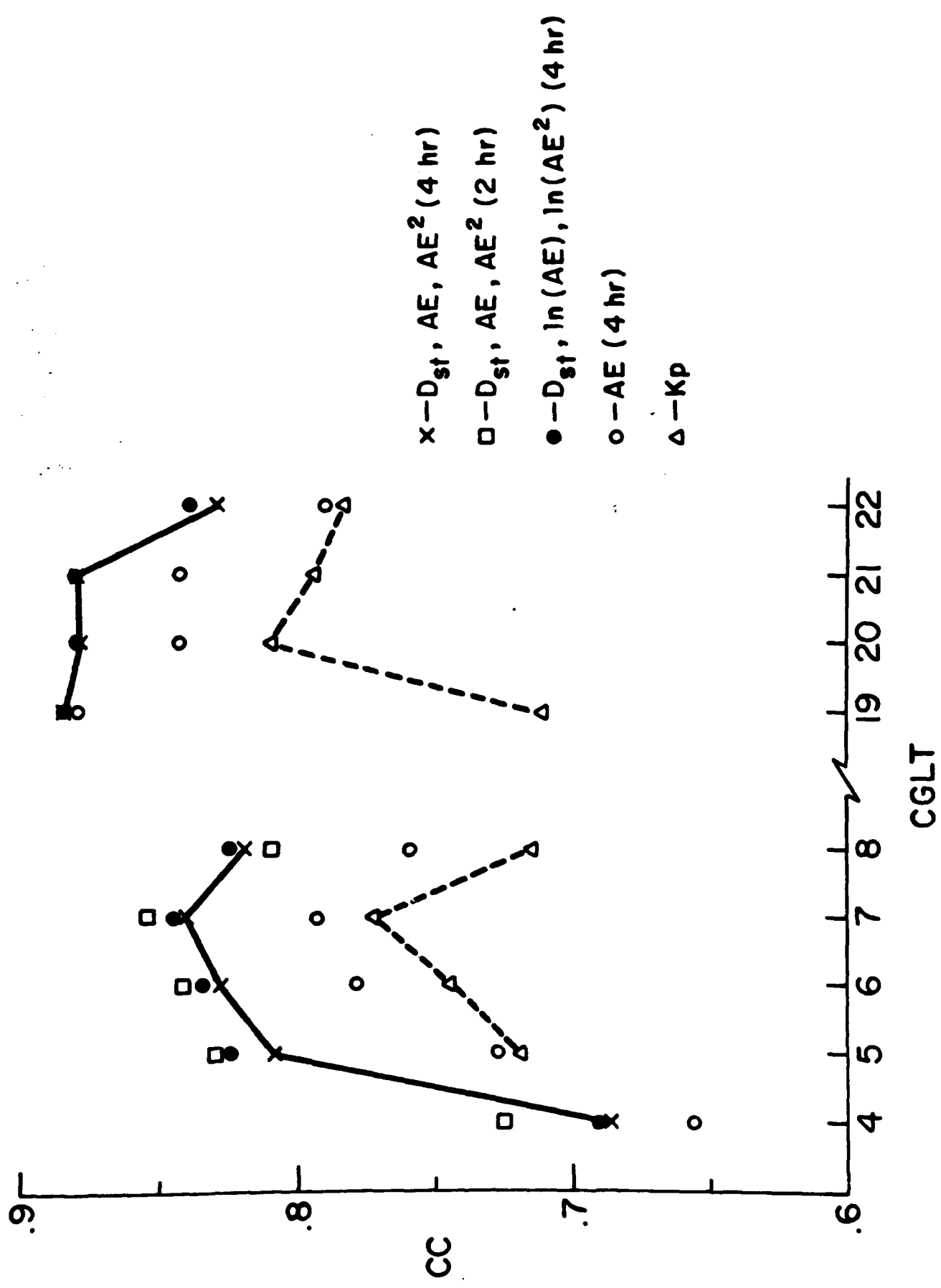Number of cases is indicated in parentheses.

Figure 3   Same as Figure 3 except for morning boundaries.

Figure 4   Correlation coefficients of boundary latitude with various
combinations of magnetic indices in the morning and evening
sectors. North hemisphere boundaries.

21 CGLT

CGLAT (deg)

AE (nT)

74

75

77
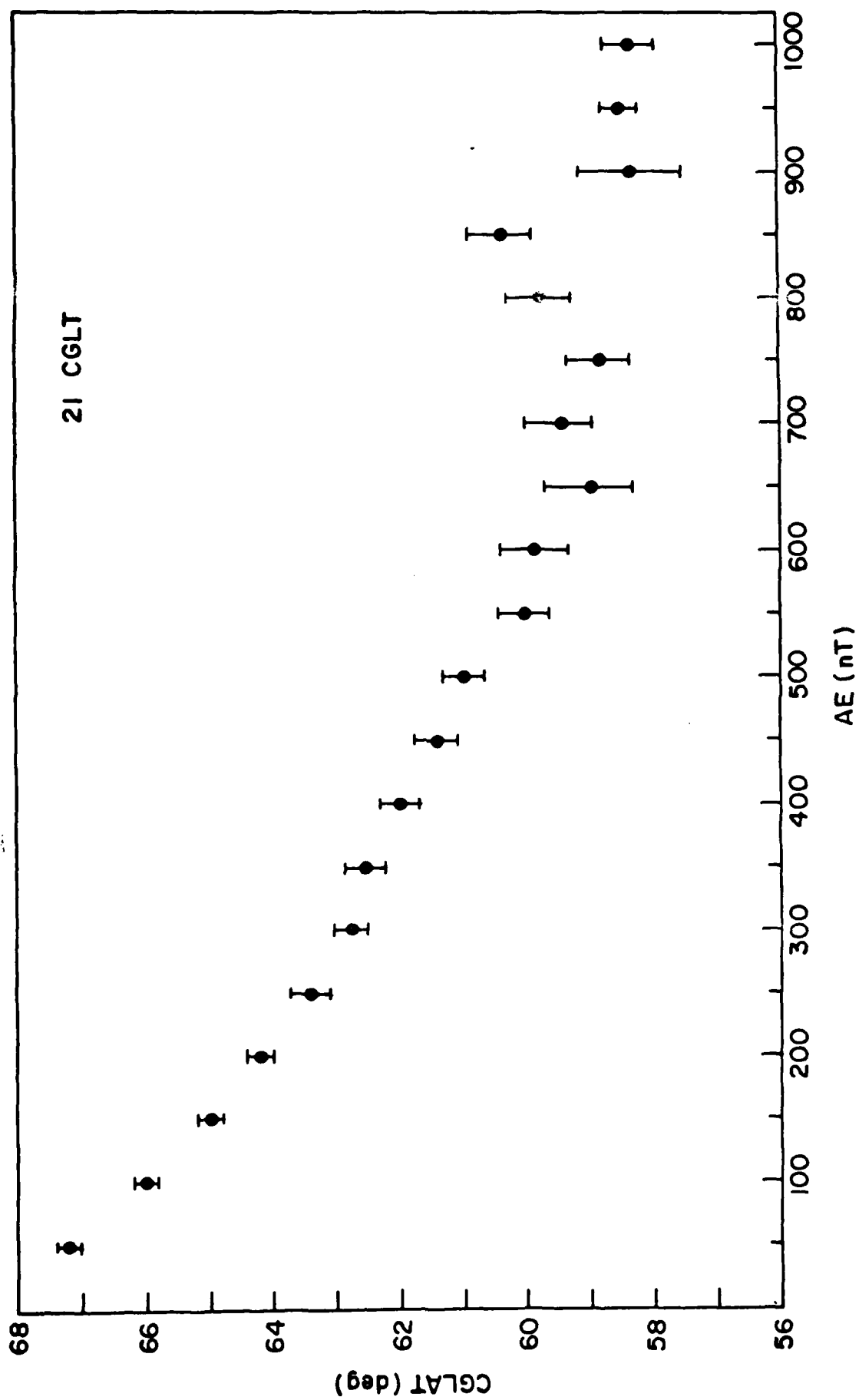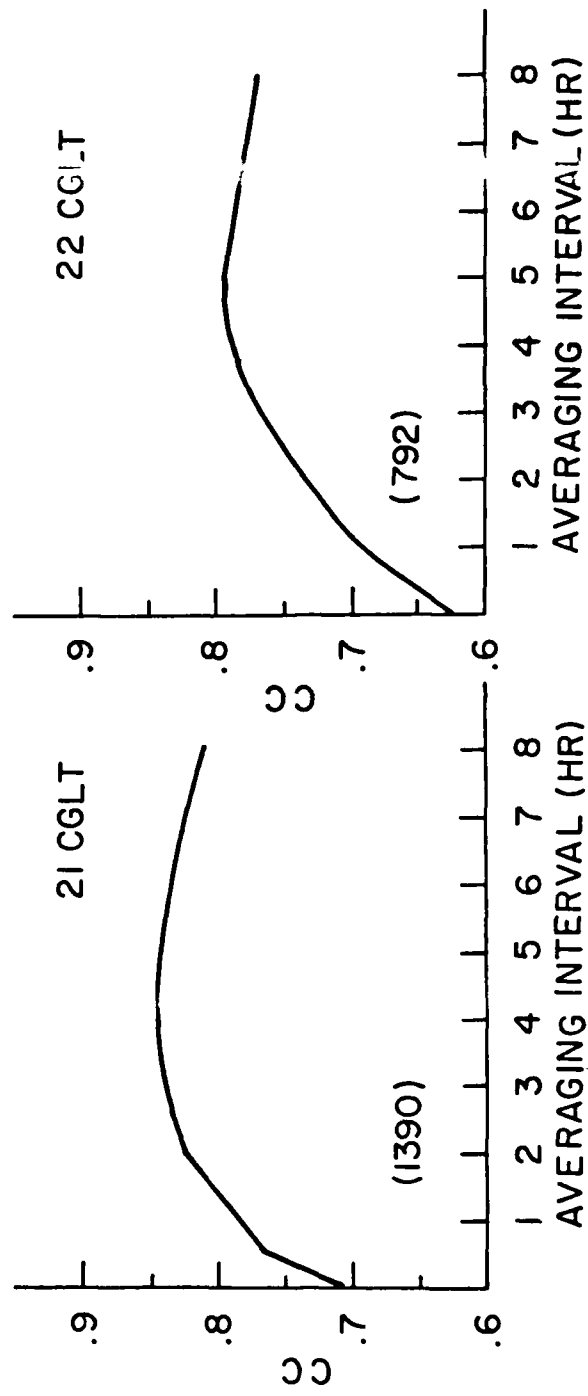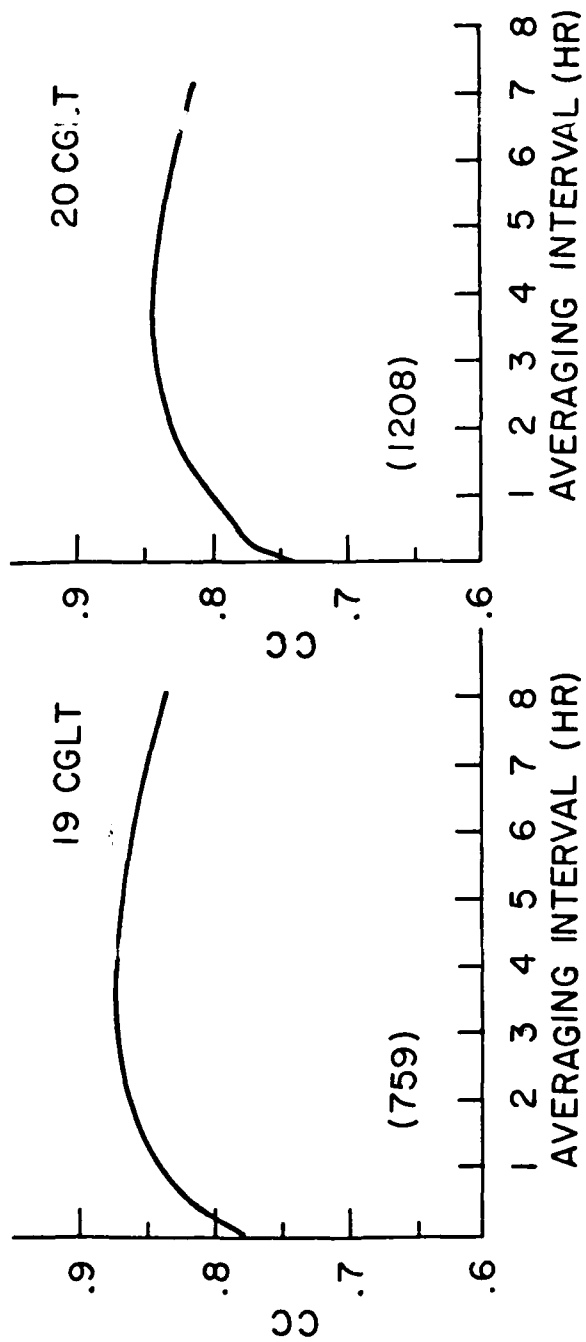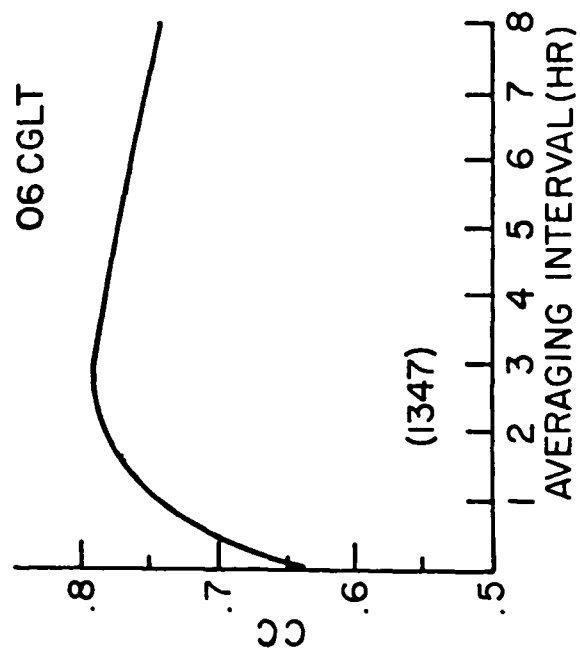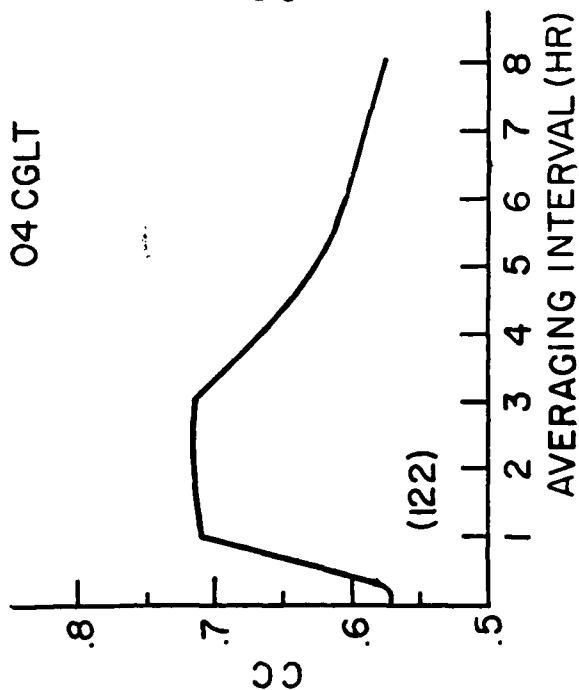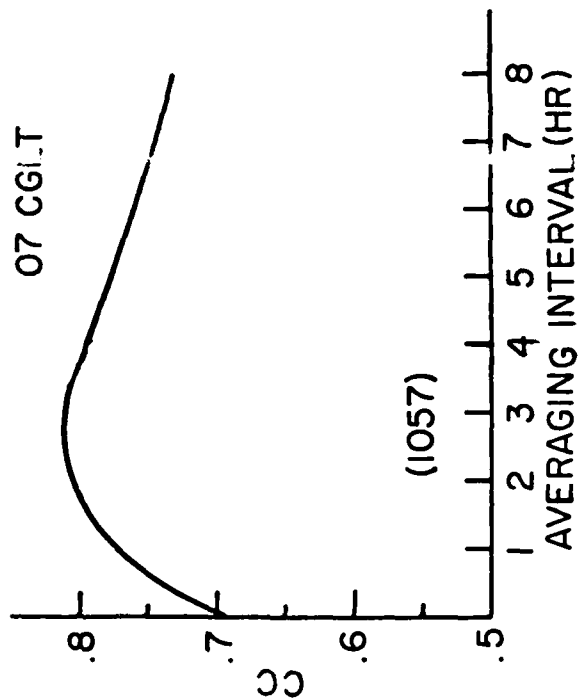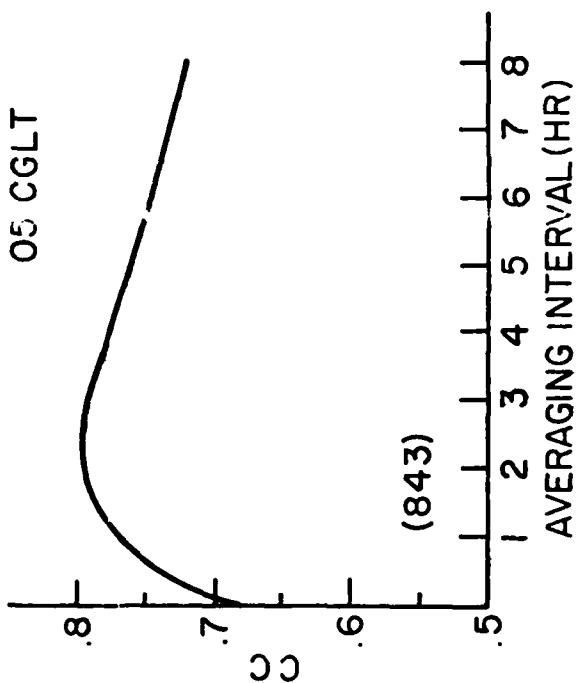
I. INTRODUCTION

It is generally accepted that the diffuse aurora is produced by the electrons and ions originating in the central plasma sheet (Winningham et al., 1975; Lui and Anger, 1973; and Meng et al., 1979). There is growing evidence that only a slow rate of pitch angle diffusion is necessary in order to maintain the level of electron precipitation producing the electron diffuse aurora (Fontaine and Blanc, 1983). This means that the minimum radial distance in the equatorward plane to which electrons can penetrate is determined primarily by the combined action of the convection electric field and the gradient and curvature drifts, rather than by the loss of all electrons on a flux tube (Cowley and Ashour-Abdalla, 1975, and Kivelson and Southwood, 1975). Since the inner boundary of the plasma sheet electrons maps to the equatorward boundary of auroral electron precipitation, the systematics of the low altitude electron equatorward boundary reflect similar systematics in the plasma sheet boundary. The variations in the plasma sheet boundary can be related, in turn, to the strength and spatial distribution of the cross-tail convection electric field (Gussenhoven et al., 1981; Hardy et al., 1981, and Kamide and Winningham, 1977). This is important since in situ determination of the morphology of both the plasma sheet boundary and the convection electric field are difficult (Freeman, 1974; Mauk and McIlwain, 1974; and Baumjohann, et al. 1985).

To date, a number of studies have been published on the location of the low altitude electron boundaries and their variation with geomagnetic activity, substorms, and solar wind parameters (Gussenhoven et al., 1981; Hardy et al., 1981; Gussenhoven et al., 1983; Slater et al., 1980; Makita et al., 1983; and Savaud et al., 1983). No similar analysis has been performed for the ion boundaries. This is due to the lack of detectors on polar

orbiting satellites with sufficiently large geometric factors to unambiguously determine the latitudinal extent of auroral ion precipitation. Large geometric factors are required since diffuse aurora ion precipitation has typically one to two orders of magnitude less intensity than electron precipitation. The most systematic measurements of the extent of ion precipitation and the relationship of electron and ion fluxes have been made photometrically and principally from the ground (See reviews by Eather, 1967, and Hultqvist, 1979; also Vallance-Jones, 1974, 1982; and Lambert and Sutcliffe, 1981). Low altitude energy dispersion on the boundary (Sauvaud et al., 1981) and high altitude studies of proton boundaries (Ejiri, 1978) have contributed to the notion that the ion motion in the plasma sheet is, like that of the electrons, strongly affected by the convection electric field, and can be used to model the convection electric field. The relative importance, however, of transport by convection and loss by pitch angle diffusion in forming low altitude boundaries has not been established for ions (Ashour-Abdalla and Thorne, 1978).

To determine the ion boundary systematics, we have used the new ion detectors onboard the DMSP/F6 satellite to make an initial determination of the variations with KP of the auroral ion equatorward boundaries for several hours in magnetic local time (MLT) about the dawn-dusk meridian. The boundary variations are determined both absolutely and in relationship to the electron boundaries. The paper is organized as follows: Section II describes the orbit of the DMSP/F6 satellite and the electron-ion detector. Section III describes the boundary selection. In Section IV, the results are presented. Section V is a discussion of the results.

II. ORBIT AND INSTRUMENTATION

DMSP/F6 is a three-axis stabilized satellite that was launched into a

near sun-synchronous, dawn-dusk circular orbit in December 1982. The altitude

of the satellite is 840 km, the orbital period is 101 min., the nominal

inclination is 98.75°. The satellite is nonspinning. Owing to the offset

between the Earth spin axis and the magnetic axis, the orbit is subject to

significant diurnal variation in Magnetic Local Time (MLT)-Corrected

Geomagnetic Latitude (MLAT) coordinates. This variation is shown in Figure 1.

The south pole orbital path (dashed line) is offset toward magnetic local

noon; the north pole orbital path (solid line) is offset toward magnetic local

midnight.

The SSJ/4 sensor on DMSP/F6 (also flown on F7, and planned for F8 through

F14) consists of four cylindrical curved plate electrostatic analyzers

arranged in two pairs. One pair measures electron fluxes in 20 energy

channels between 30 eV and 30000eV; the other measures ion fluxes in a similar

fashion, over the same range. The apertures of the analyzers always face

local vertical such that at auroral and polar cap latitudes, they detect

precipitating, rather than backscattered or trapped particles. The analyzers

for ions and electrons are identical except that the polarity on the plates

are opposite, and the low energy ion apertures are larger than the low energy

electron apertures. One electron analyzer covers the energy range from 30 eV

to 1 keV with a geometric factor of $\sim 2.2 \; 10^{-4} \; cm^2$ sr and a $\Delta E/E$ of 9.8%.

The other electron analyzer covers the energy range from 1 to 30 keV with a

geometric factor of $8.7 \; 10^{-4} \; cm^2$ sr and a $\Delta E/E$ of 9.3%. The corresponding

analyzers for ions have geometric factors of $3.2 \; 10^{-2} \; cm^2$ sr and 8.6

$10^{-4} \; cm^2$ sr, respectively, and $\Delta E/E$ of 9.8% and 9.3%, respectively. For

ions, the geometric factors of this instrument are unusually large compared to

others flown at comparable altitudes, resulting in count levels well above

background in the auroral oval. Both electron and ion detectors employ post

acceleration (100 volts for electrons; 1000 volts for ions) to insure unit

channeltron efficiency at low energies. A complete 20-point spectrum both for

electrons and ions is returned once per second. Details of the detector and

its calibration are given in Hardy et al. (1984).

III. DATA SELECTION AND DATA BASE

Figures 2a and 2b are survey plots of the SSJ/4 electron and ion data,

respectively, for a DMSP/F6 north polar pass on 13 January 1983, during which

KP was 3-. In each figure, the following three quantities are plotted from

top to bottom as a function of universal time in seconds: the particle

average energy (EAVE) in keV; the particle total energy flux (JETOT) in

keV/cm^2 sec sr; the total particle number flux (JTOT) in particles/cm^2 sec sr.

At each two-minute interval, the values are given for the satellite's geo-

graphic latitude and longitude, corrected geomagnetic latitude and longitude,

and magnetic local time, all projected along the magnetic field to 110 km.

Figure 2 shows that the satellite traversed the morningside auroral oval

(04-05 MLT), the polar cap (up to 88.9° MLAT), and the eveningside oval (17-18

MLT). Below the evening oval, slight contamination of the channeltrons from

radiation belt particles occurs from ~ 10800-10980 UT.

In Figure 2, the equatorward precipitating electron and ion boundaries

are indicated by vertical lines. The criteria which are used for selection of

electron boundaries from these data have been extensively documented

(Gussenhoven et al., 1981, 1982) and will not be repeated here. The electron

boundaries, in this case, are unambiguous, and are at 60.6° MLAT in the 04-05

MLT zone, and 69.1° MLAT in the 17-18 MLT zone. For the example in Figure 2b,

the ion boundaries are also clear and are chosen from increases in JTOT above

equatorward background values. The boundaries chosen are at 65.4° MLAT in the

04-05 MLT zone, and 68.2° MLAT in the 17-18 MLT zone. For this pass, as is the general case, the electron (ion) boundary lies more equatorward of the ion (electron) boundary on the morningside (eveningside) of the oval.

Figure 2 illustrates several common features of the average particle energy which appear in nearly every dawn-dusk pass. 1) The average ion energy reaches higher values in the evening auroral oval than in the morning. The electron average energy varies in the opposite sense, and on both morning and evening sides is smaller than for the ions. These features are also characteristic of the source populations measured at near-geosynchronous orbits (Garrett, 1981; and Mullen and Gussenhoven, 1983). 2) The average ion energy is high at the equatorward edge of the evening oval and decreases poleward. (In this case there is a small spur of low energy flux ions which have also been included within the boundary.) On the other hand, a relatively broad region of low (less than 1 keV) average energy ions is found on the edge of the morning oval. This is in agreement with observations of Sauvaud et al. (1981) following injections into the near-Earth plasma sheet.

In selecting the ion boundaries, many of the criteria used for electron boundary selection were applied. The ion boundaries were picked at a clear rise in total number flux above background and typically were easier to determine than the electron boundaries. However, there were cases where the ion number flux showed irregular fluctuations at the equatorward edge of the precipitation, often extending over several degrees of latitude. The extent of these fluctuations is larger than in corresponding cases for electrons, and even though the fluxes are low level, the boundary was chosen at the lowest latitude to which the fluctuations extended. On occasion, the diffuse auroral ion precipitation on a given side of the oval, principally the morningside, appeared as a double or divided population. In these cases, both regions were

83

included in the boundary.

For this study, the electron and ion boundaries were determined for each DMSP/F6 pass in January, 1983, giving a set of approximately 900 boundaries for ion precipitation and the same for electrons. For each pair of ion and electron boundaries, the appropriate KP values were assigned; the difference between the two boundaries, $\Delta \lambda = \lambda_e - \lambda_i$, was determined; and the boundaries and their differences were binned in one-hour local time zones. Boundaries were excluded from the data set if the electron and ion boundaries in a given pair occurred in different local time bins; 15% of the morning boundaries and 6% of the evening boundaries had such differences. Many of these cases occurred on the dayside where the satellite cuts the auroral oval obliquely. Magnetic Local Time zones for which there were at least 100 boundries were 04-07 MLT, and 17-21 MLT. For these zones, data were available for a KP range from 0+ to 5, and linear regressions were performed on the boundary values against KP.

IV. ION AND ELECTRON BOUNDARY DIFFERENCES

Before looking at the statistical results, we first show the electron and ion boundary configuration for a period of extended quiet on 26 February 1983, from 04 UT to 22 UT. During this time, KP varied from 1- to 1+. In addition, the polar cap was well-defined by clear intervals of polar rain. We interpret this to mean that although the magnetic activity was small, the z-component of the interplanetary magnetic field was either near-zero or slightly negative. In such cases, the energy transfer from the solar wind to the magnetosphere is small, as is the cross-tail convection electric field. We expect a contrac-ted, but relatively stable auroral oval. Under these conditions, a relatively large fraction of the whole oval is sampled by successive passes of the DMSP

84

satellite.

Both equatorward and poleward electron and ion boundaries were chosen for this period and plotted in MLAT-MLT coordinates. North and south pole data were combined. The results are shown in Figure 3. Here, dots (crosses) represent ion (electron) boundaries, and the equatorward boundaries are circled. Connecting lines show electron and ion boundary pairs. We point out that although not shown, almost all the morning equatorward boundary ion populations have low average energy ($<$ 1 keV), and the evening boundaries high average energy ($\gtrsim$ 10 keV), similar to those shown in Figure 2. In many cases, the equatorward boundary electron populations also had relatively high average energies (a few keV), particularly on the morningside. Smooth lines (solid for electrons, dashed for ions) are drawn as a fit to the equatorward boundaries. A similar line is drawn for the polar cap boundary using both electron and ion values.

The equatorward boundaries show the following properties: a) When the electron and ion boundary pairs are considered, their difference, $\Delta \lambda$, is always negative in the morning and positive in the evening. b) Unpaired boundaries occur only on the dayside where the ion boundaries continue to persist to low latitudes, and either the electron diffuse aurora died out, or ... ... c) There is considerable variation in the actual boundaries from an attempt to make a smooth fit to them. d) Except on the dayside, the ion and electron boundaries generally move to higher or lower latitudes together, although not necessarily by the same amount. e) The variation in $\Delta \lambda$ is generally smaller on the eveningside as midnight is approached, as found in the average sense. On the morningside, however, the minimum $\Delta \lambda$ is near dawn, rather than near midnight.

The poleward boundaries are shown in contradistinction to the equatorward boundaries. Many of the electron-ion poleward boundary differences are near zero. The variation in the boundaries from pass to pass is considerable, particularly on the morningside. Trends in the variations are difficult to identify. The time scales for these higher latitude processes appear to be much shorter than those that map to the inner magnetosphere.

We return to the set of equatorward boundaries for all of January, 1983, to see which of the trends observed for the quiet oval persist in a statistical sense and over a wider variety of conditions. Figures 4a and b are occurrence plots for $\Delta \lambda$ for morning and evening boundary pairs, respectively. Boundaries for the entire MLT and KP ranges are used, and the boundary differences ($\Delta \lambda$) are binned in units of 0.2° MLAT. Figure 4a shows that, with few exceptions, the morning electron boundary occurs at lower latitudes than the ion boundary. Of the 432 boundaries, 15 electron boundaries are higher than ion boundaries (3%) and 11 coincide (2.5%). The average difference is -2.62° $\pm$ 1.71° MLAT, which is indicated by the vertical line in Figure 4a. For the evening boundaries, Figure 4b, the reverse trend occurs: the ion boundaries occur at lower latitude than the electron boundaries, with 34 of the 470 boundaries (7%) higher and 36 (8%) coincident. The average difference is +1.37 $\pm$ 1.21° MLAT.

The large spread in the average differences on both the morning- and eveningsides, as shown by the relatively large standard deviations, indicates that the effect of KP, pole, and MLT should be considered. The data were separated into two KP ranges, 0 to 2+ and $\geq$ 3-, and the averages of the differences in electron and ion boundaries again calculated. The results are given in Table 1. The differences between the averages of the two KP ranges are small: 0.18° on the morningside, and 0.13° on the eveningside, indicating

86

that magnetic activity does not account for the variation in differences. Table 2 shows the averages of the differences when separation is made by pole. Here, the difference between the averages for the two poles is greater and seemingly of significance: 0.82° on the morningside, and 0.54° on the eveningside. Because different MLT zones are crossed in the two poles, separation was next made by MLT for zones with sufficient boundary crossings (> 100 boundaries). In this case, separation by pole was not made for regions of overlapping local time zones.

Figures 5a and b are occurrence plots for $\Delta \lambda$ as a function of local time in one-hour zones for morning and evening boundary pairs, respectively. In both figures, the local time zone closest to midnight is plotted in the bottom panel, moving toward dayside in the upper panels. As in Figure 4, the average $\Delta \lambda$ is indicated by a vertical line in each panel. Figure 5 shows that the closer the MLT zone is to midnight, the smaller the average divergence between the electron and ion equatorward boundaries. Not only does the average difference between the boundary pairs increase for MLT zones on the dayside, but the scatter in the differences also tends to increase.

Finally, we show the results of performing a linear regression on all boundary points in a given MLT zone with KP. In Figures 6a and b, the linear fit to the data is shown for the 04-05 and the 18-19 MLT zones, respectively. Data from both poles are combined in overlapping time zones. We also show the average boundary value for each KP value: solid (open) circles for electron (ion) boundary averages. (Note: the linear regressions were performed on the full data set in each zone, not the averages.) As shown before for electron boundaries, and as shown here to be the case for ion boundaries as well, the equatorward edge of the precipitation for both populations expands to low latitude with increasing KP. In addition, the offset between electron and ion

87

boundaries found in the occurrence plots and for 26 February clearly exists over the entire KP range sampled. The 04-05 MLT equatorward electron boundaries are consistently about 2-3° lower than the ion boundaries, on average; and the 18-19 MLT equatorward electron boundries are consistently 1-2° higher than the ion boundaries, on average. The linear regression result for the MLT zones in which there are ~ 100 boundaries are given in Table 3. Here, n is the number of boundaries in the given MLT zone, λ_o is the intercept at KP = 0, α is the slope in degrees of MLAT per unit KP, and cc is the correlation coefficient.

The electron results can be compared to those previously published for the DMSP F2 and F4 data in which a much larger data set was used. Because the KP range is not as complete here, particularly at low and high values, the correlation coefficients are anticipated to be, and in fact are, somewhat smaller than for the larger data set. In addition, there is some discrepancy in the trend of the slopes. Previously, the evening electron boundaries had slopes that increased in the negative sense as midnight is approached. Here no consistent trend is shown. On the morningside, the slope here is smaller (~ -1.6) compared to ~ -1.9, and the trend to smaller slopes as midnight is approached, although slight, is opposite the trend in the large data set. We attribute these differences to small data samples that are not required to be near-uniformly distributed in KP.

Here, we are mostly interested here in the relation between electron and ion boundaries, and the table shows that the same type of non-uniformity in slope variations on the eveningside also occurs in the ion regressions. On the morningside, the trends for the electron boundaries are as found before and are again duplicated in the ion boundaries.

V. DISCUSSSION

From the measurement of approximately 1800 electron and ion boundaries in January, 1983, we draw the following conclusions:

1. The systematics of the equatorward ion boundary are similar to those of the equatorward electron boundary: both move to lower latitudes in a regular fashion with increasing magnetic activity, here measured by KP.

2. On the morningside of the oval, the electron equatorward boundary is, on average 2.6° MLAT <u>lower</u> than the equatorward ion boundary.

3. On the eveningside of the oval, the equatorward electron boundary is, on average 1.4° MLAT <u>higher</u> than the equatorward ion boundary.

4. The difference between the electron and ion equatorward boundaries is not a strong function of KP.

5. The difference between the equatorward electron and ion boundaries increases as local time of occurrence approaches noon, and decreases as local time of occurrence approaches midnight.

REFERENCES

Ashour-Abdalla, M., and R.M. Thorne, Toward a unified view of diffuse auroral precipitation, J. Geophys. Res., 83, 4755, 1978.

Baumjohann, W., G. Haerendel, and F. Melzner, Magtnetospheric convection observed between 0600 and 2100 LT: Variations with Kp, J. Geophys. Res., 90, 393, 1985.

Cowlely, S.W.H., and M. Ashour-Abdalla, Adiabatic plasma convection in a dipole field: Variation of plasma bulk parameters with L, Planet. Sp. Sci., 23, 1527, 1975.

Eather, R.H., Auroral precipitation and hydrogen emissions, Rev. of Geophys., 5, 207, 1967.

Ejiri, Masaki, Trajectory traces of charged particles in the magnetosphere, J. Geophys. Res., 83, 4798, 1978.

Fontaine, D., and M. Blanc, Theoretical approach to the morphology and dynamics of diffuse auroral zones, J. Geophys. Res., 88, 7171, 1983.

Freeman, J.W., Kp dependence of the plasma sheet boundary, J. Geophys. Res., 79, 4315, 1974.

Garrett, H.B., D.C. Schwank, and S.E. DeForest, A statistical analysis of the low-energy geosynchronous plasma environment- II. Ions, Planet. Sp. Sci., 29, 1045, 1981.

Gussenhoven, M.S., D.A. Hardy, and W.J. Burke, DMSP/F2 observations of equatorward auroral boundaries and their relationship to magnetospheric electric fields, J. Geophys. Res., 86, 768, 1981.

Gussenhoven, M.S., D.A. Hardy, N. Heinemann, and E. Holeman, 1978 Diffuse Auroral Boundaries and a Derived Auroral Boundary Index, AFGL-TR-82-0398, Hanscom AFB, MA 01731, 1982, ADA130175.

Gussenhoven, M.S., D.A. Hardy, and N. Heinemann, Systematics of the
equatorward diffuse auroral boundary, J. Geophys. Res., 88, 5692, 1983.

Hardy, D.A., W.J. Burke, M.S. Gussenhoven, N. Heinemann, and E. Holeman,
DMSP/F2 electron observations of equatorward auroral boundaries and their
relationship to the solar wind velocity and the north-south component of
the interplanetary magnetic field, J. Geophys. Res., 86, 9961, 1981.

Hardy, D.A., L.K. Schmitt, M.S. Gussenhoven, F.J. Marshall, H.C. Yeh, T.L.
Schumaker, A. Huber, and J. Pantazis, Precipitating Electron and Ion
Detectors (SSJ/4) for the Block 5D/Flights 6-10 DMSP Satellites:
Calibration and Data Presentation, Hanscom AFB, MA 01731,
AFGL-TR-84-0317, 1985 (in press).

Hultqvist, Bengt, The hot ion component of the magnetospheric plasma and some
relations to the electron component- Observations and physical
implications, Sp. Sci. Rev., 23, 581, 1979.

Kamide, Y., and J.D. Winningham, A statistical study of the 'instantaneous'
nightside auroral oval: The equatorial boundary of electron
precipitation as observed by the ISIS 1 and 2 satellites, J. Geophys.
Res., 82, 5573, 1977.

Kivelson, M.G., and D.J. Southwood, Approximations for the study of drift
boundaries in the magnetosphere, J. Geophys. Res., 80, 3528, 1975.

Lambert, Sheridan, and Peter R. Sutcliffe, Photometric observations of the
proton aurora at Sanae, J. Atmos. & Terr. Phys., 43, 355, 1981.

Lui, A.T.Y., and C.D. Anger, A uniform belt of diffuse auroral emission seen
by the ISIS-2 scanning photometer, Planet. Sp. Sci., 21, 799, 1973.

Makita, K., C.-I Meng, and S.-I. Akasofu, The shift of the auroral electron
precipitation boundaries in the dawn-dusk sector in association with
geomagnetic activity and interplanetary magnetic field, J. Geophys. Res.,

<u>88</u>, 7967, 1983.

Mauk, B.H., and C.E. McIlwain, Correlation of Kp with the substorm-injected plasma boundary, <u>J. Geophys. Res.</u>, <u>79</u>, 3193, 1974.

Meng, C.-I, B. Mauk, and C.E. McIlwain, Electron precipitation of evening diffuse aurora and its conjugate electron fluxes near the magnetospheric equator, <u>J. Geophys. Res.</u>, <u>84</u>, 2545, 1979.

Mullen, E.G., and M.S. Gussenhoven, SCATHA Environmental Atlas, AFGL-TR-83-0002, Hanscom AFB, MA 01731, 1983, ADA131456.

Sauvaud, J.A., J. Crasnier, K. Mouala, R.A. Kourazhkin, and N.J. Jorjio, Morning sector ion precipitation following substorm injections, <u>J. Geophys. Res.</u>, <u>86</u>, 3430, 1981.

Sauvaud, J.A., J. Crasnier, Yu.I. Galperin, and Y.I. Feldstein, A statistical study of the equatorward boundary of the diffuse aurora in the pre-midnight sector, <u>Geophys. Res. Lett.</u>, <u>10</u>, 749, 1983.

Slater, D.W., L.L. Smith, and E.W. Kleckner, Correlated observations of the equatorward diffuse auroral boundary, <u>J. Geophys. Res.</u>, <u>85</u>, 531, 1980.

Vallance-Jones, A., <u>Aurora</u>, D. Reidel, Hingham, Mass., 1974.

Vallance-Jones, A., F. Creutzberg, R.L. Gattinger, and F.R. Harris, Auroral studies with a chain of meridian-scanning photometers 1. Observations of proton and electron aurora in magnetospheric substorms, <u>J. Geophys. Res.</u>, <u>87</u>, 4489, 1982.

Winningham, J.D., F. Yasuhara, S.-I. Akasofu, and W.J. Heikkila, The latitudinal morphology of 10-eV to 10-keV electron fluxes during magnetically quiet and distrubed times in the 2100-0300 MLT sector, <u>J. Geophys. Res.</u>, <u>80</u>, 3148, 1975.

ILLUSTRATIONS

Figure 1.   Orbital coverage in magnetic local time and corrected
            geomagnetic latitude for DMSP/F6. The solid line encloses the
            regions covered in the north pole; the dashed line, the south
            pole.

Figure 2a.   Integral flux in $(cm^2 \text{ s sr})^{-1}$ (bottom panel), energy flux in
            keV/cm^2 sr s (middle panel), and average energy in keV (top
            panel) of precipitating electrons measured by the DMSP/F6
            satellite passing over the north pole on January 13, 1983.
            These values are plotted as functions of universal time (in
            seconds), geographic and corrected geomagnetic latitudes and
            longitudes, and the magnetic local time of the satellite all
            projected to an altitude of 110 km. The vertical lines at 60.4°
            and 69.1° indicate the morning and evening electron equatorward
            auroral boundaries.

Figure 2b.   Same as Figure 2a for ions, with the vertical lines at 65.4° and
            68.2° indicating the morning and evening ion equatorward auroral
            boundaries.

Figure 3.   Polar plot in corrected geomagnetic latitude and magnetic local
            time electron (x's) and ion ('s) equatorward and poleward
            boundaries measured on February 23, 1983. Connecting lines
            indicate electron and ion boundary pairs. Smooth lines (solid
            for electrons, dashed for ions) are drawn as a fit to the

equatorward boundary. A similar line is drawn for the polar cap

boundary using both electron and ion values.

Figure 4a. Occurrence plot for differences ($\Delta\lambda$) between all electron and

ion boundary pairs measured on the morningside. $\Delta\lambda$'s are binned

in units of 0.2° MLAT. The vertical line shows the mean

difference.

Figure 4b. Same as Figure 4a for electron and ion boundary pairs measured

on the eveningside.

Figure 5a. Same as Figure 4a, but separated into 1 hour MLT bins.

Figure 5b. Same as Figure 4b, but separated into 1 hour MLT bins.

Figure 6a. Mean values and standard deviations in each Kp bin for electrons

(●'s) and ions (o's) as a function of Kp for the 0400-0500 MLT

sector. The solid line (dashed line) results from a linear

regression performed with individual boundary determinations of

electrons (ions).

Figure 6b. Same as 6a for the 1800 to 1900 MLT sector.

Table 1

Boundary Separation by KP

KP	Mean (Morning)	Mean (Evening)
0 – 2+	$-2.72° \pm 1.73°$ (n = 184)	$+1.45° \pm 1.10°$ (n = 199)
$>$ 3-	$-2.55° \pm 1.70°$ (n = 248)	$+1.30° \pm 1.28°$ (n = 271)

Table 2

Boundary Separation by Pole

Pole	Mean (Morning)	Mean (Evening)
North	$-2.36° \pm 1.61°$ (n = 279)	$+1.19° \pm 1.13°$ (n = 288)
South	$-3.11° \pm 1.79°$ (n = 153)	$+1.64° \pm 1.28°$ (n = 182)

Table 3

Linear Regression Results

	Electrons					Ions			
MLT	N	λ_o	α	cc	MLT	N	λ_o	α	cc
04-05	179	65.9	-1.68	-0.60	04-05	176	69.1	-1.96	-0.65
05-06	130	66.7	-1.62	-0.61	05-06	113	69.7	-1.59	-0.62
06-07	132	67.5	-1.57	-0.53	06-07	118	70.0	-1.30	-0.54
17-18	96	72.5	-1.45	-0.64	17-18	104	70.7	-1.40	-0.64
18-19	160	70.6	-1.16	-0.55	18-19	162	69.1	-1.20	-0.59
19-20	99	71.4	-2.01	-0.72	19-20	108	69.5	-1.75	-0.71
20-21	109	68.8	-1.17	-0.55	20-21	97	67.9	-1.10	0.55
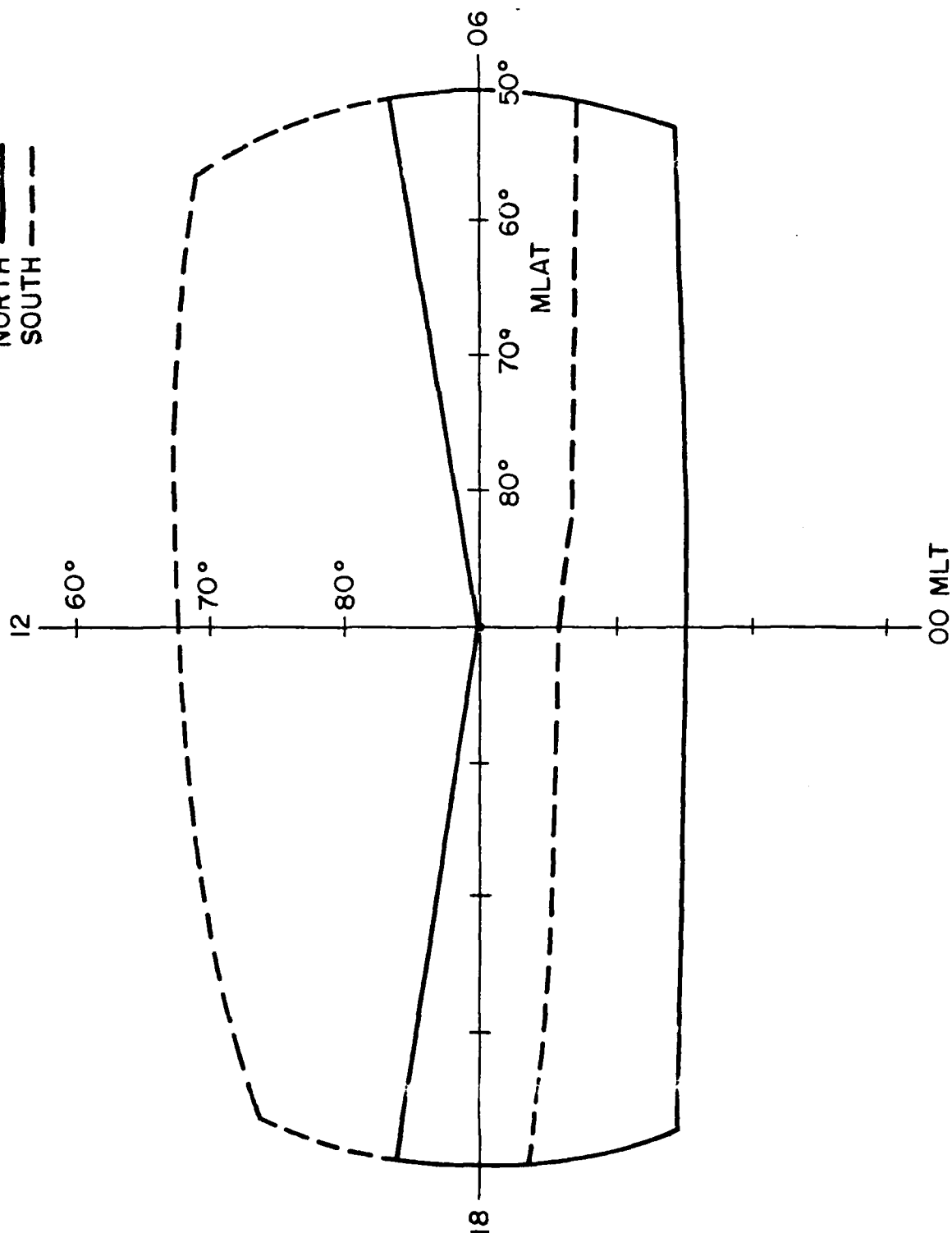
MICROCOPY RESOLUTION TEST CHART

NATIONAL BUREAU OF STANDARDS-1963-A

$K_p = 3^-$

97

$K_p = 3^-$

68.2 (17-18)

65.4 (04-05)

EAVE

10.000

JETOT

10^5 10^6 10^7 10^8 10^9

JTOT

10^5 10^6 10^7 10^8 10^9

GMT

9660.0 9780.0 9900.0 10020.0 10140.0 10260.0 10380.0 10500.0 10620.0 10740.0 10860.0 10980.0

UANB3S6
DAY .13
ION
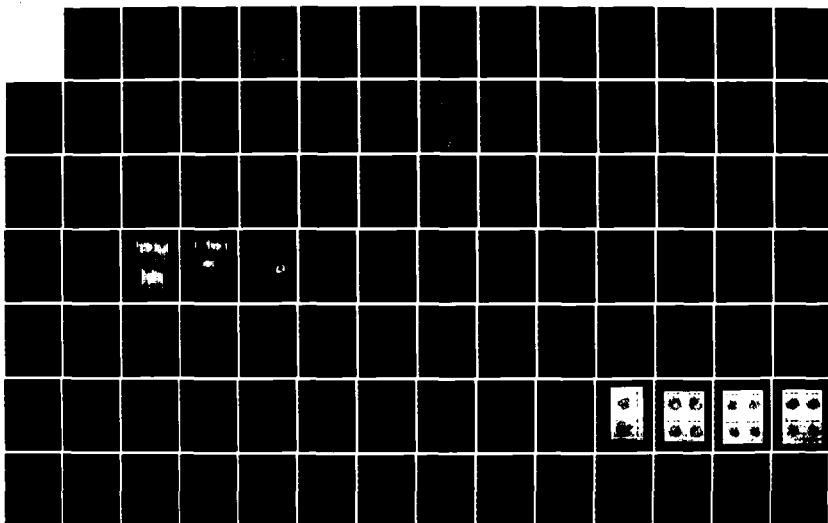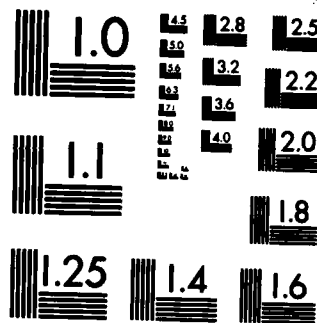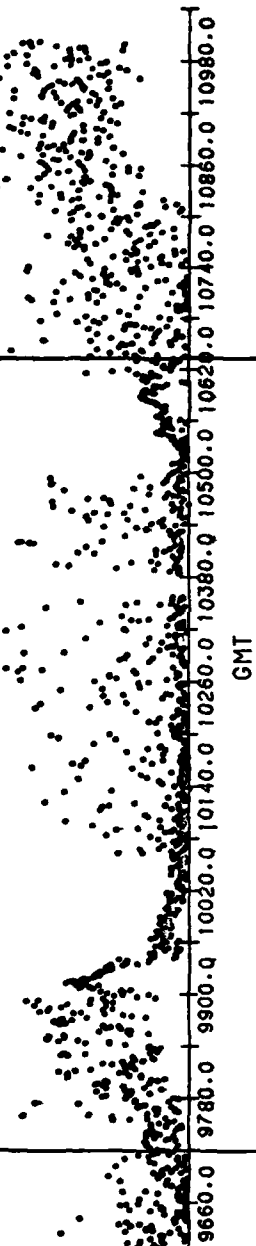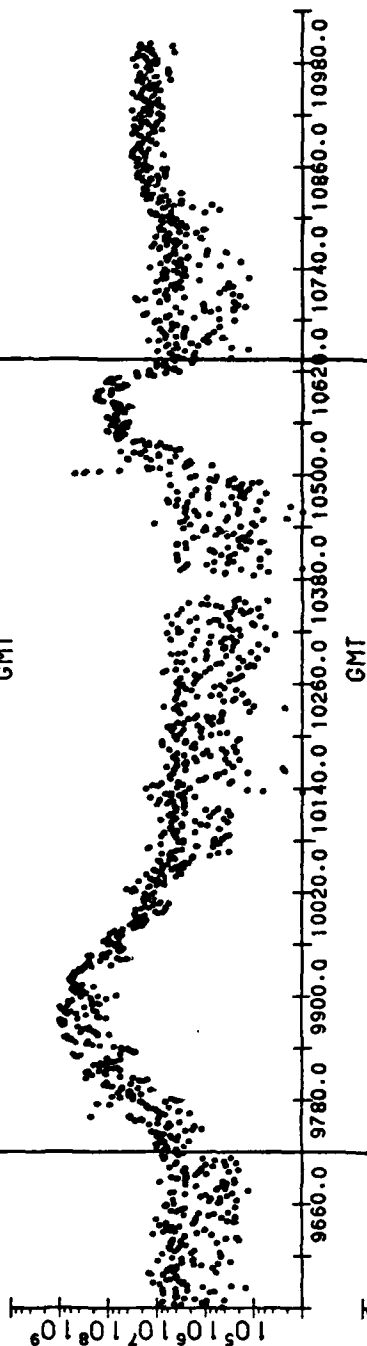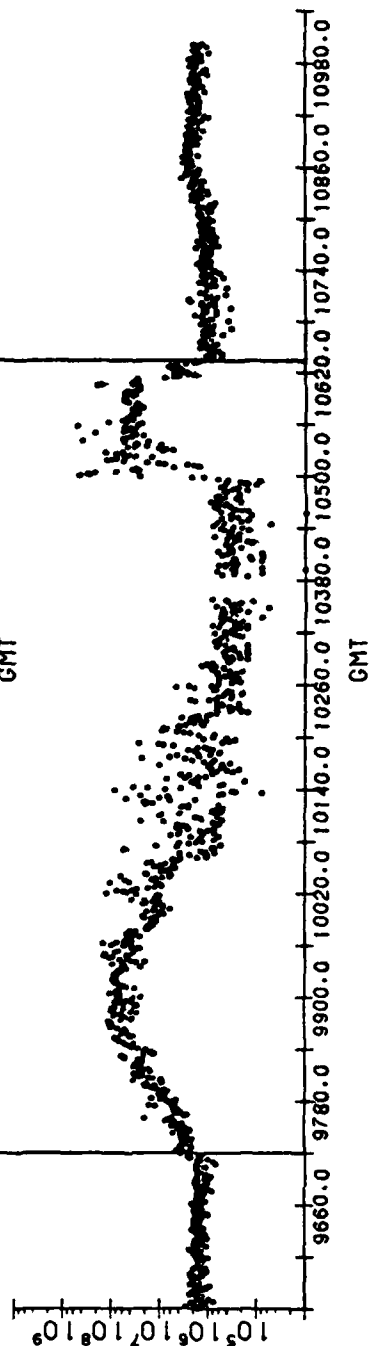
GLAT	59.5	66.2	72.5	78.1	81.1	79.4	74.3	68.1	61.5	54.7	47.8	40.9
GLON	37.9	32.1	22.7	4.3	327.8	286.3	263.2	251.9	245.4	240.9	237.7	235.1
MLAT	57.4	63.8	70.3	76.7	83.0	88.9	83.7	76.9	70.0	62.9	55.9	48.9
MLON	114.2	113.0	111.9	110.2	105.9	56.1	301.1	296.9	295.3	294.5	294.1	294.0
MLT	5.0	4.9	4.9	4.8	4.5	1.3	17.6	17.4	17.3	17.3	17.3	17.3

26 FEBRUARY 1983

- - - ⊚ ; • ION
——— ⊕ ; x ELECTRON

$\Delta\lambda = \lambda_c - \lambda_i$

MEAN = −2.6°   ±1.71°

n = 2

NORNING

$\Delta\lambda$

NUMBER

30

20

10

0

−9   −8   −7   −6   −5   −4   −3   −2   −1

100

EVENIN

$\Delta\lambda = \lambda_e - \lambda_i$

MEAN = +1.37° ± 1.21°

n = 470

$\Delta\lambda$

NUMBER

101

$$\Delta\lambda = \lambda_e - \lambda_i$$

$$\Delta\lambda = \lambda_e - \lambda_i$$

17-18 MLT

18-19 MLT

19-20 MLT

20-21 MLT

NUMBER

$\Delta\lambda$

04-05 MLT

• ELECTRONS ——
∘ IONS — — —

$\lambda_e = 65.9 - 1.68\, K_p$
C.C. = -0.60

$\lambda_i = 69.1 - 1.96\, K_p$
C.C. = -0.65

18 — 19 MLT

● ELECTRONS ——
○ IONS   - - - -

$\lambda_e = 70.6 - 1.16\, K_p$
C.C. = -0.55

$\lambda_i = 69.1 - 1.2\, K_p$
C.C. = -0.59
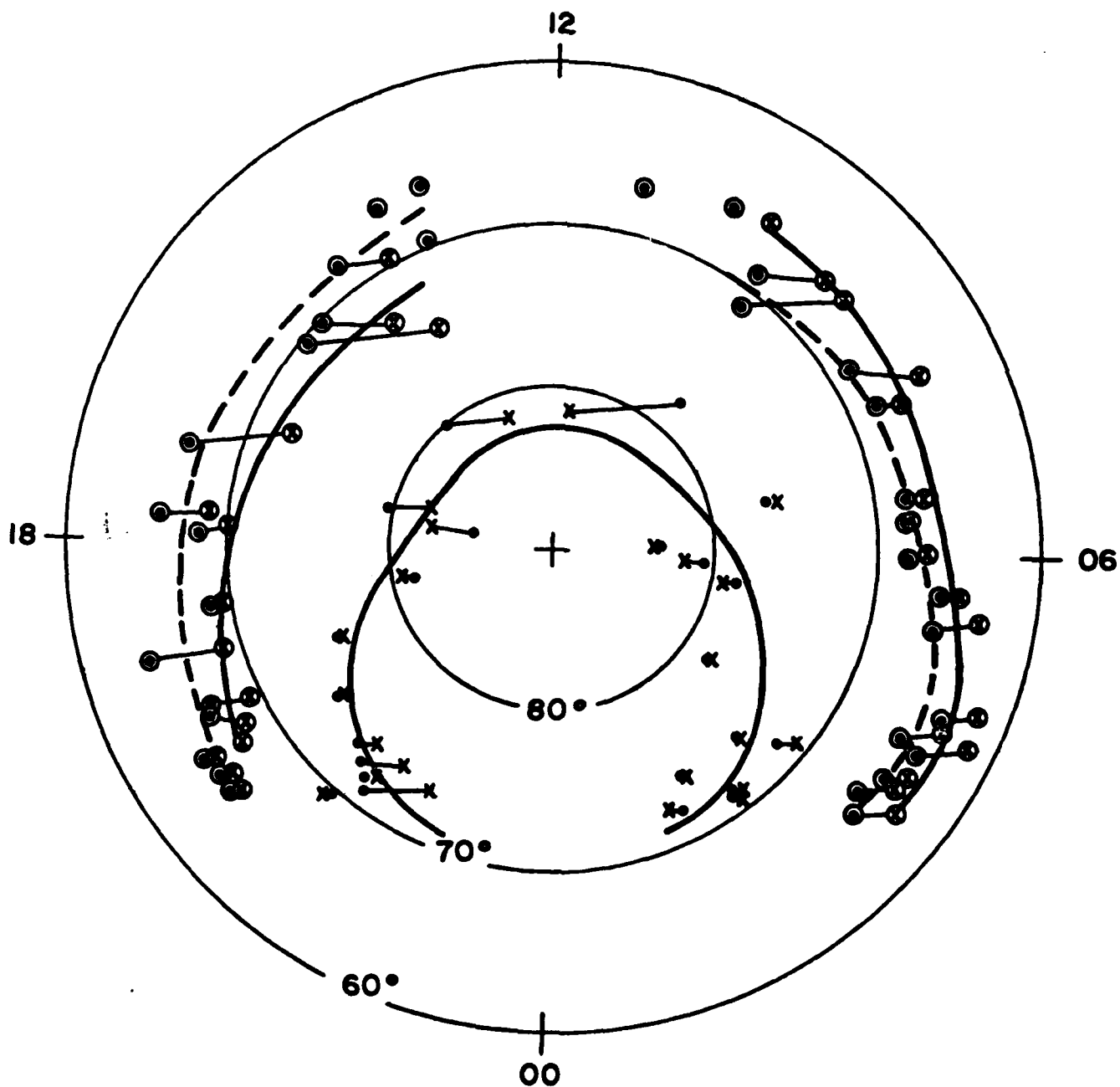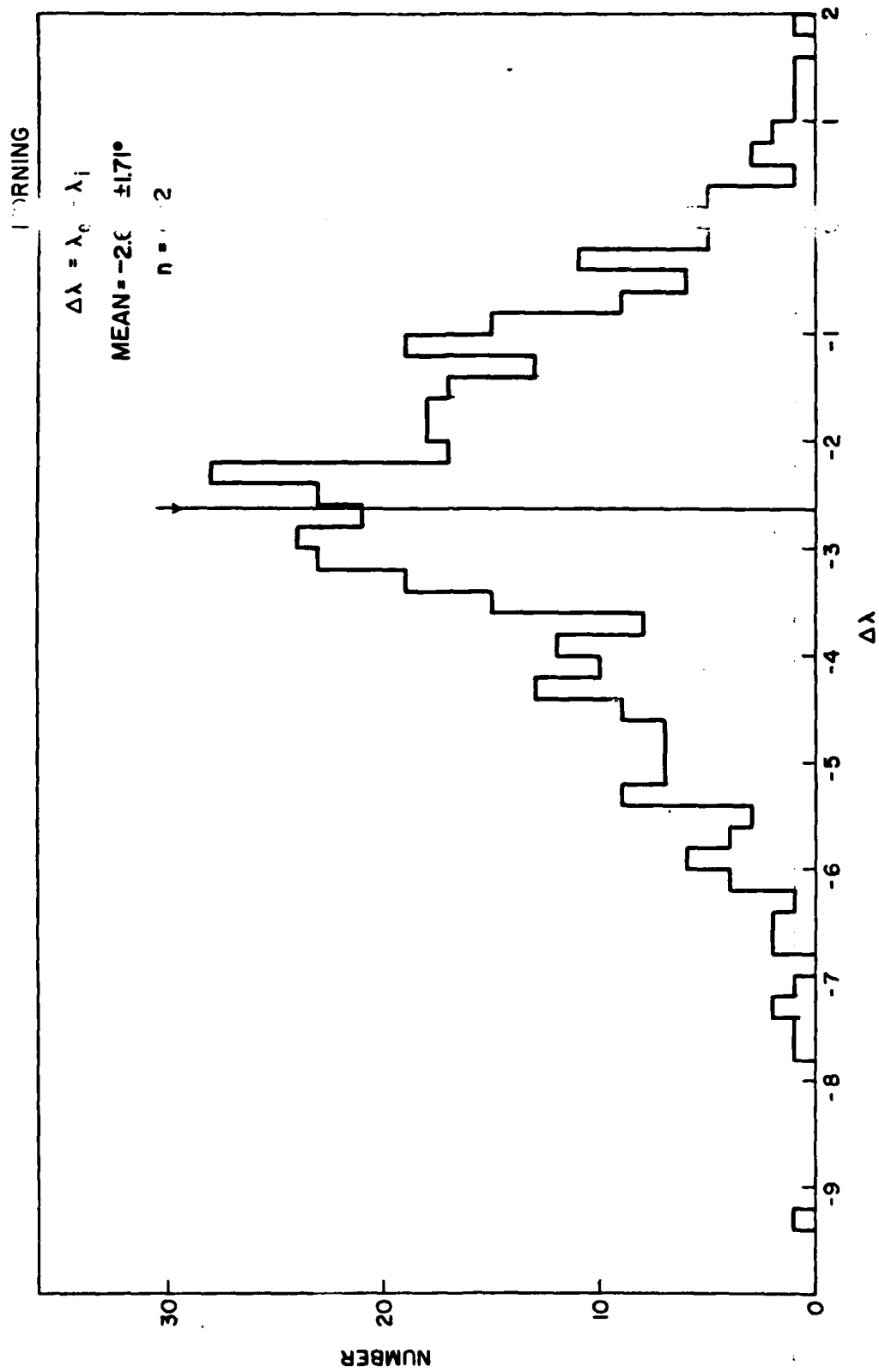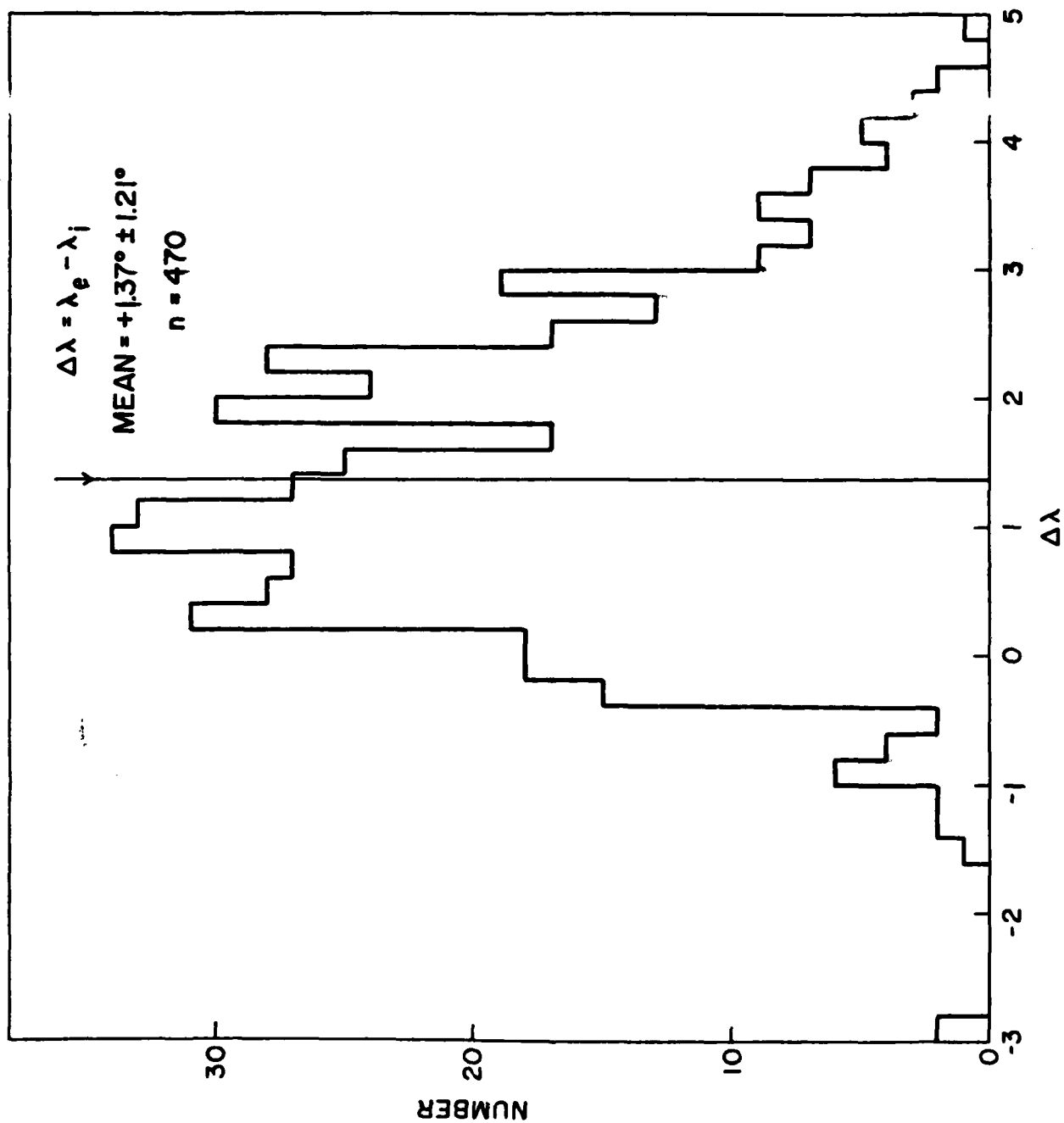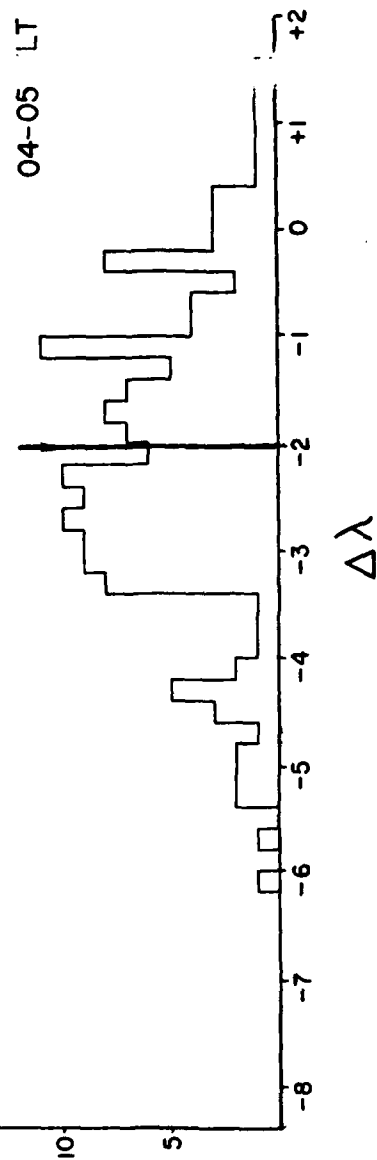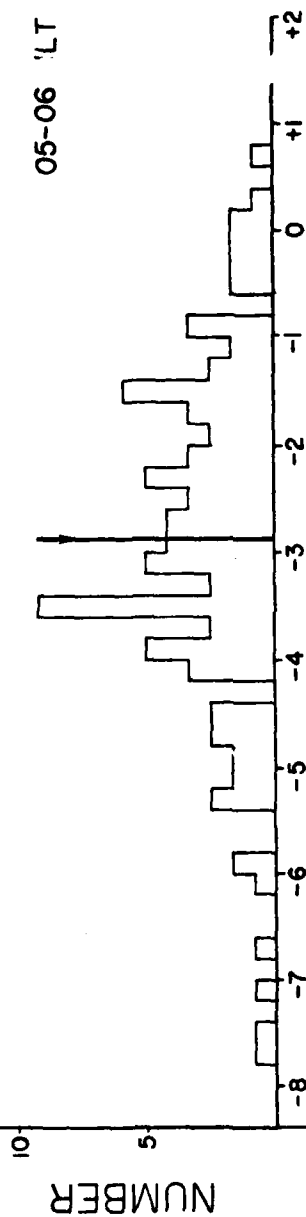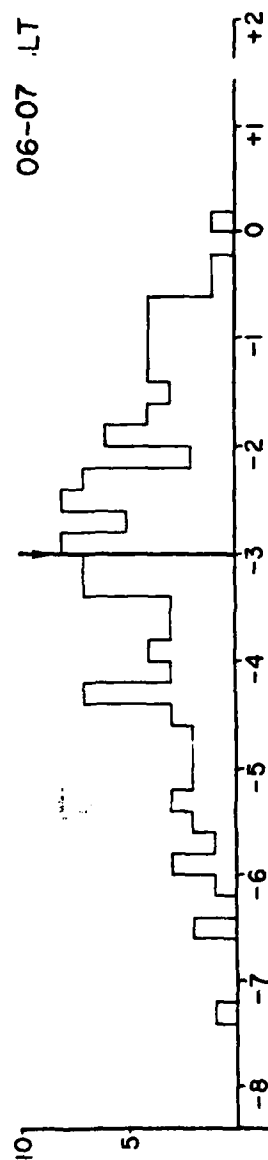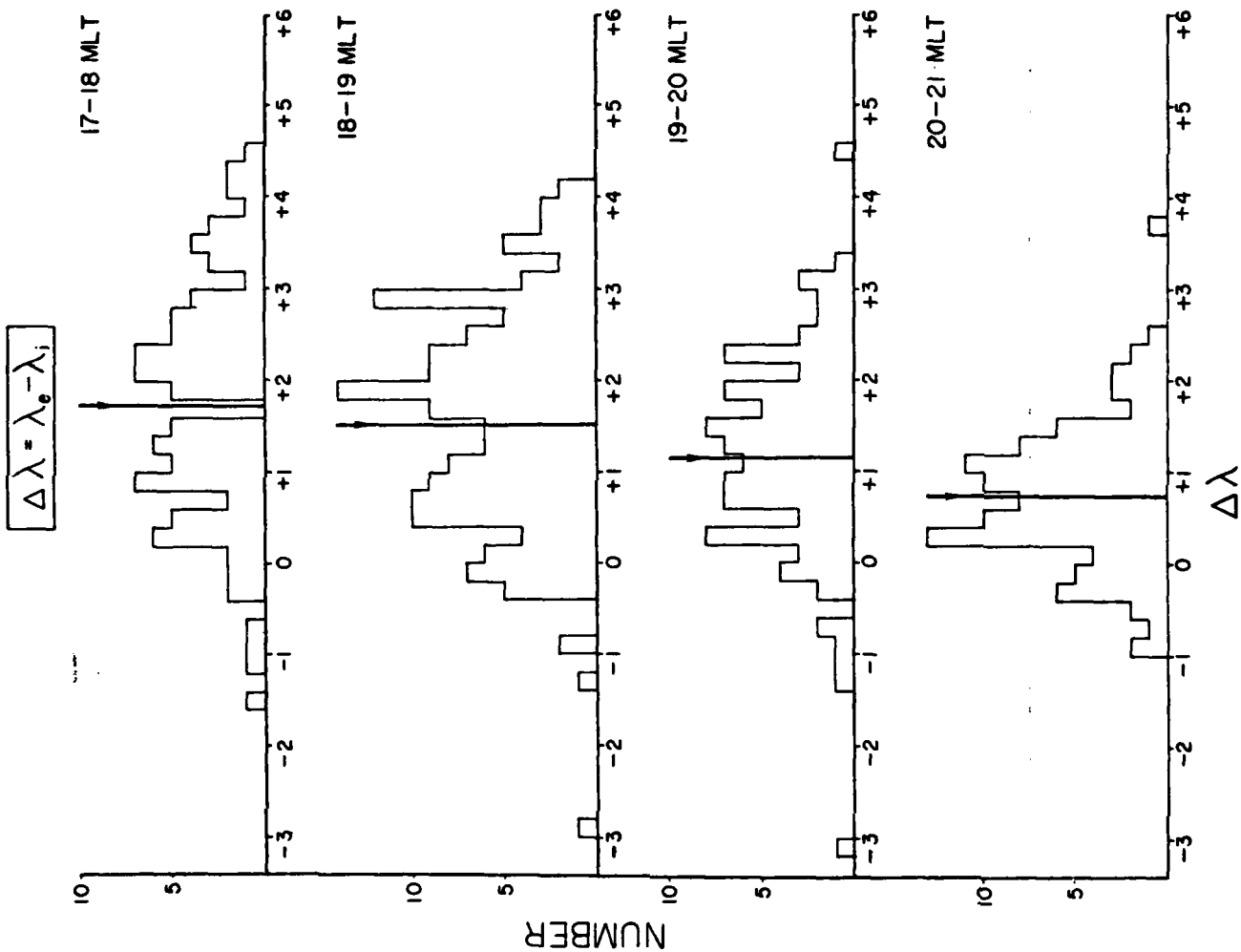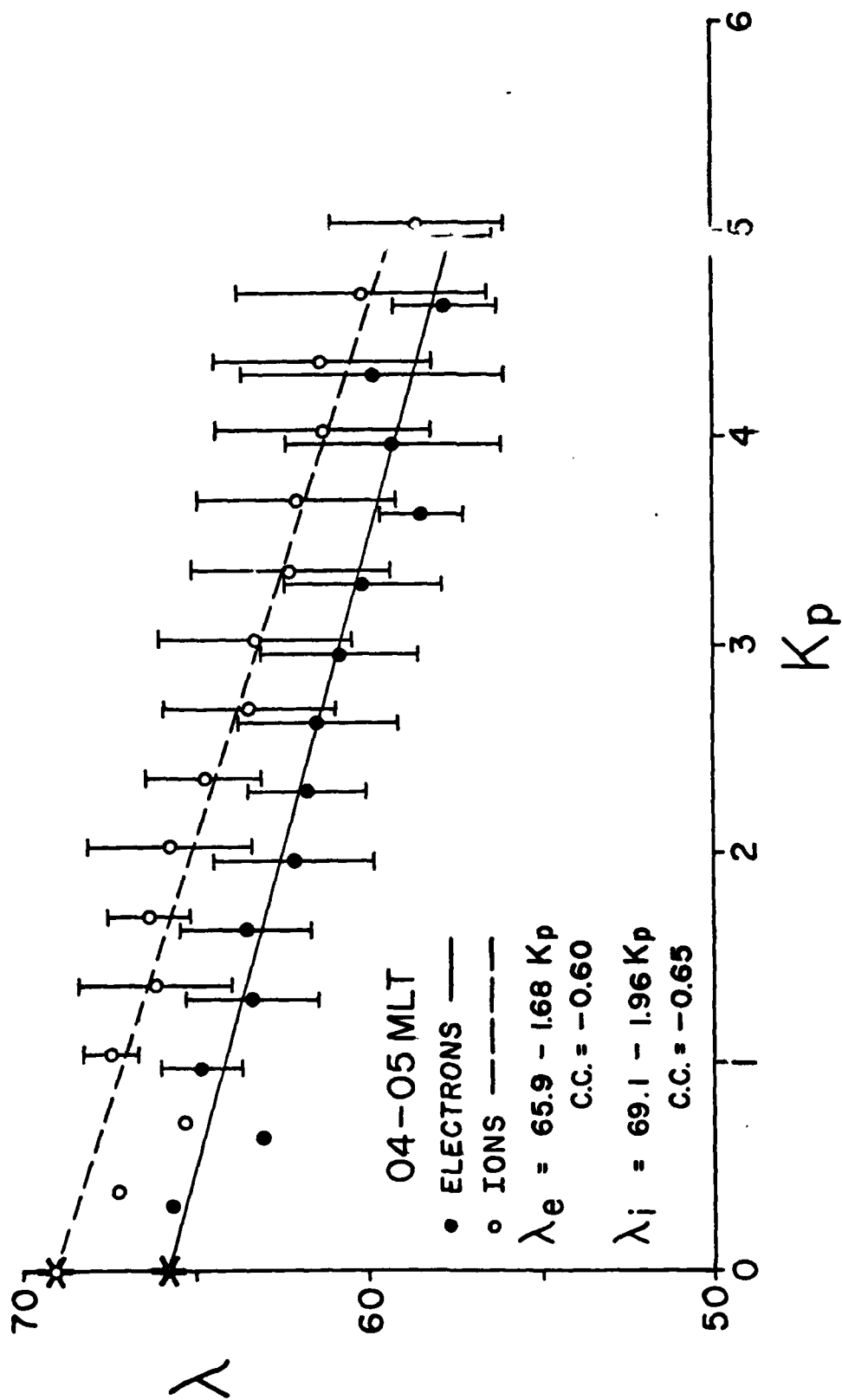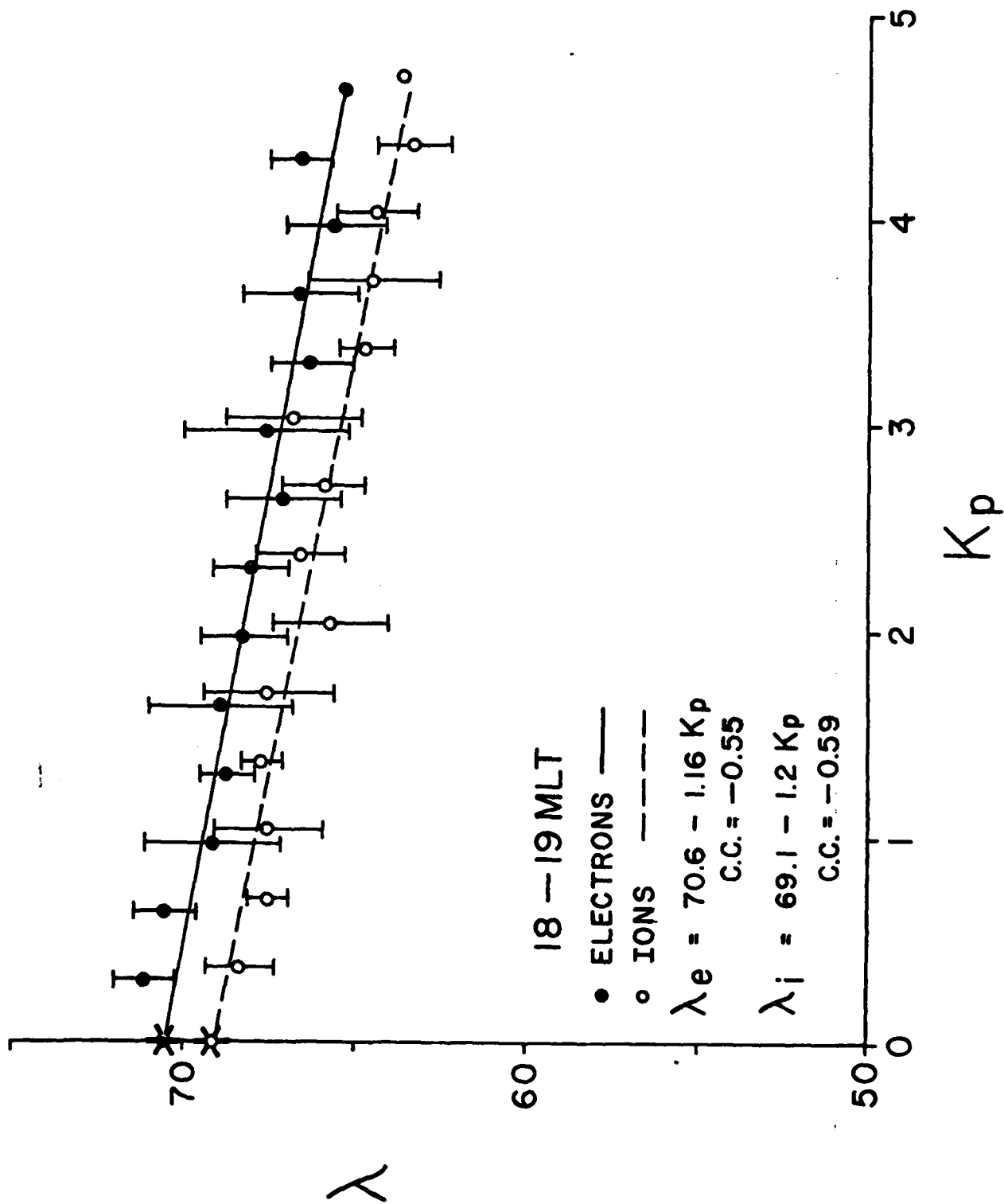
III. LARGE-SCALE PROPERTIES OF PRECIPITATING ELECTRONS MEASURED AT LOW ALTITUDES

See also: "Average electron precipitation in the polar cusps, cleft and cap," M.S. Gussenhoven, D.A. Hardy, and R.L. Carovillano, to be published in Proceedings of the Conference on the Morphology and Dynamics in the Polar Cusp, Lillehammer, Norway, 7-11 May 1984, D. Reidel, 1985.

"Requirements for validating system models," M.S. Gussenhoven, in Proceedings of the Air Force Geophysics Laboratory Workshop on Natural Charging of Large Space Structures in Near Earth Polar Orbit; 14-15 September 1982, R.C. Sagalyn, D.E. Donatelli, and I. Michael, eds., Rep. AFGL-TR-83-0046, Air Force Geophysics Laboratory, Hanscom AFB, MA, 1983, ADA134894.

THE BASELINE MAGNETOSPHERE: EMPIRICAL CONTRIBUTIONS

M.S. Gussenhoven
Physics Department, Boston College
Chestnut Hill, MA 02167

An obvious choice for a baseline magnetosphere is a strictly theoretical
one: a dipole field and the absence of a solar wind. This magnetosphere
cannot be related to measurements except very near the Earth's surface.
Except for this limiting case, one is faced with the question of whether there
is any solar wind-magnetosphere interaction which is not a dynamic one; which
can exist in a steady state. Solar wind parameters measured at 1 A.U. are
highly variable. When the large-scale variations are clearly structured, as
during solar minimum, they have a cyclic dependence in solar rotation,
organized by magnetic field sector structure. Prior to the crossing of a
sector boundary and an attendant shock structure, a region in the solar wind
often exists in which the speed, density, temperature, and magnetic field
magnitude reach minimal values (less than 350 km/sec, $10/cm^3$, 25×10^3 °K,
5 nT). While variation in the solar wind parameters still exist here the
absolute variations are small since the values are small. Such regions can be
large, requiring times on the order of days to flow past the Earth. During
these days, the various pressures exerted by the solar wind on the magneto-
sphere reach their minimum values (typically $< 10^{-8}$ dynes/cm^2 for solar
maximum; and $< 2 \cdot 10^{-8}$ dynes/cm^2 for solar minimum), and the magnetosphere
assumes its most inflated or dipolar configuration (with a subsolar dayside

107

dimension typically greater than 12 R_E). In addition, the quietest days in a solar rotation, as determined by the daily sum of Kp, are often found clustered together at these times. They also contain the highest concentration of Kp = 0, 0+ 3-hour intervals. Such periods of extended quiet are chosen as appropriate ones for the study of a baseline magnetosphere. It should not be inferred that such periods are more stable than periods of higher magnetic activity. The dynamical processes that operate during extended periods of quiet are to be part of the inquiry. Two additional points concerning the occurrence of baseline conditions are: 1) For statistical studies, it is more feasible and consistent to designate periods of extreme quiet by 0, 0+ Kp values. This increases the statistical sample over that of using Q1 days and gives a sample with greater uniformity in magnetic activity. The percentage of a solar rotation with Kp 0, 0+ is found to vary between 1%-15%, with uninterrupted Kp 0, 0+ intervals up to 24 hours. 2) Extended periods of quiet are not necessarily periods for which the z-component of the IMF is positive (nor are the intervals of Kp 0, 0+). However, they characteristically have low values for the magnitude of B, which means that B_z, whether positive or negative, is also small.

The first question to be addressed in this discussion of a baseline magnetosphere concerns the morphology of electron precipitation during periods of Kp 0, 0+. The data bases that are used to examine this and other questions are taken principally from Air Force and joint Air Force/NASA satellites including the polar orbiting satellites DMSP F2 and F4, P78-1, S3-2, and the near geosynchronous satellite P78-2 (SCATHA).

A statistical picture of electron precipitation at high latitudes for Kp 0, 0+, obtained from binning the DMSP data for each 1/2 hour in local time and for each degree in magnetic latitude, and averaging within each bin, is shown

in Figures 1a,b,c. The data were acquired from September, 1977, to August, 1980, with uniform seasonal spread and yielding approximately 1500 polar passes with Kp 0, 0+. The DMSP satellites are sun-synchronous, three-axis stabilized satellites in circular polar orbits at 840 km. The data are organized by number flux, NF, in $(cm^2-s-sr)^{-1}$; energy flux, EF, in keV/cm^2-s-sr; and average energy, AVE, in keV. The average energy is derived as the ratio of EF to NF, and can give spurious results when either or both values fall near or below threshold. The data are plotted in magnetic local time and corrected geomagnetic latitude.

From the number flux, Figure 1a, the following observations are made:

a) The equatorward edge of the auroral oval can be well fit by a circle, offset from the magnetic pole toward midnight, and having a radius of approximately 21° CGL.

b) Small patches of increased fluxes occur within three hours of midnight centered at 70° CGL.

c) The majority of particle flux occurs in a thick band (> 5°) wrapped around the dayside at latitudes between 75°-85° CGL. The number flux here is greater than 10^8 $(cm^2-s-sr)^{-1}$.

d) Number fluxes characteristic of polar rain, $< 3 \cdot 10^6$ $(cm^2-s-sr)^{-1}$, are limited to an extraordinarily small area at the center of the polar cap.

e) A region of flux, between $0.3 - 1 \cdot 10^7$ $(cm^2-s-sr)^{-1}$, exists in the cap. It is highly asymmetric, occurring principally in the nightside of the magnetic pole.

From the energy flux and average energy maps, the above observations are interpreted as follows:

a) The central plasma sheet (average energy > .5 keV) maps into an approximately 5° band above the equatorward auroral boundary.

b) The central plasma sheet precipitation occurs principally near midnight but is not sufficient to produce visible aurora (EF > 10^8 keV/cm^2-s-sr).

c) Cold electrons (< .5 keV) with fluxes much enhanced over that of polar rain cover the remainder of the high latitude region.

d) The highest fluxes have the lowest energies and correspond to the statistical positions of the dayside cusp. Cold, high level fluxes are found both equatorward and poleward of the cusp region, reaching beyond the magnetic pole in the morning sector.

e) The region of enhanced cold flux in the midnight sector is continuous with that on the dayside. It becomes very thin near midnight.

f) From the energy flux map, the total power input from precipitating electrons is estimated to be between 1 - 4 • 10^9 watts.

The statistical picture is not unlike that proposed by Vasyliunas (1979), reproduced in Figure 2, in which the origins of the cold precipitating electrons are various magnetospheric boundary layers. It differs in the extent of the high latitude region pervaded by these particles.

Other questions that must be addressed regarding the baseline magnetosphere are the following: 1) How does the electron precipitation pattern change for Kp 1 conditions? What are the variations from the average and what controls them? What can be inferred from this pattern about the electric and magnetic fields in the magnetosphere? 2) What additional particle information is obtained by comparison with near-geosynchronous measurements? 3) What are the characteristics of the convection electric field during periods of extended quiet? Are the magnetospheric electric field models consistent with

110

geosynchronous and with low altitude polar cap particle and field measurements? 4) How good are the magnetosphere magnetic field models for periods of extended quiet?

REFERENCES

Vasyliunas, V.M., Interaction between the magnetospheric boundary layers and the ionsphere, Magnetospheric Boundary Layers, ESA SP-148, Paris, 1979, 387.

FIGURE CAPTIONS

Figure 1. Statistically constructed maps of the precipitating electron
a) number flux (NF) in $(cm^2$-s-sec$)^{-1}$, b) energy flux (EF) in
keV/$(cm^2$-s-sec$)^{-1}$, and c) average energy (AVE) in keV for
Kp 0, 0+.

Figure 2. Schematic representation of magnetospheric boundary layers and
their ionospheric projections (Vasyliunas, 1979).

5 CONTOURS. FACTOR = 3.2 BEGINNING AT 1.000E+06
LEVEL = 5
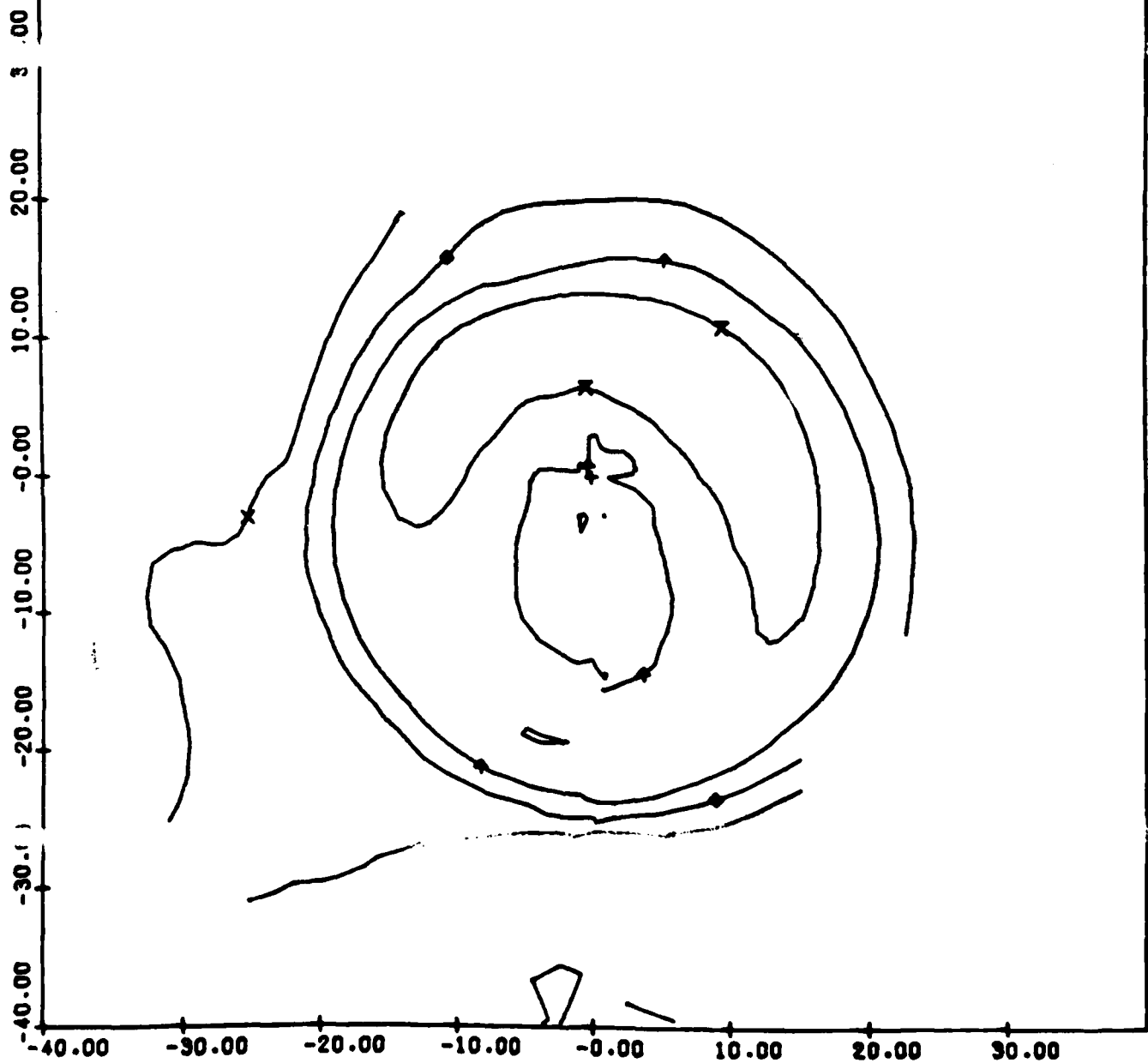
BOTH POLES POLAR PLOT FOR KP = 0. (IFLX)
⊙ ▲ + 100+4 X 316+4 ◇ 100+5
♦ 316+5 X 100+6

113

6 CONTOURS. FACTOR = 3.2 BEGINNING AT 3.162E+05

LEVEL = 5
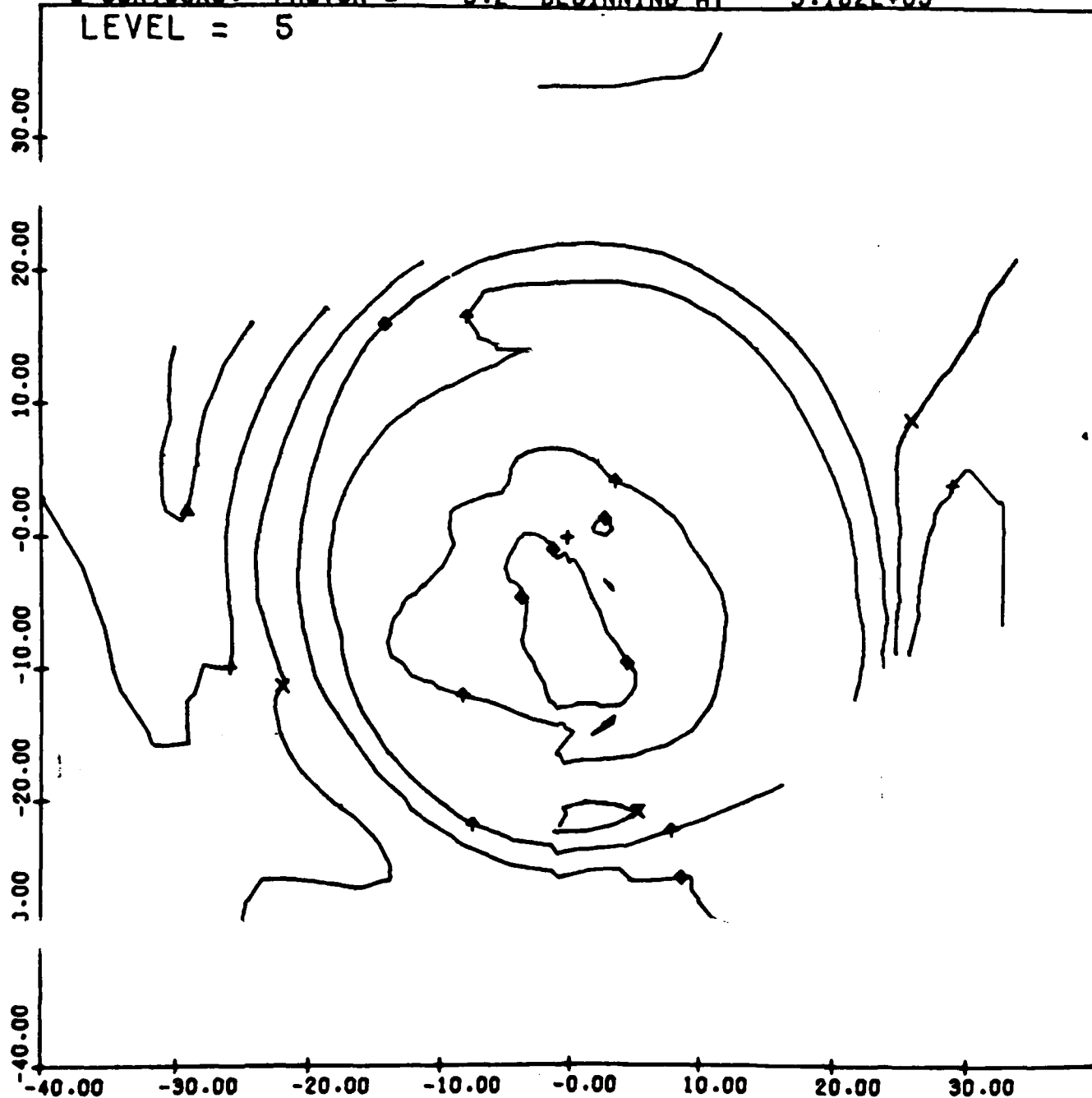
BOTH POLES POLAR PLOT FOR KP = 0. (EFLX)
⊙ ▲ 316+3 + 100+4 ✕ 316+4 ◈ 100+5
✦ 316+5 ✕ 100+6

114

11 CONTOURS. ADDEND = .5 FROM 5.000E-01

LEVEL = 5
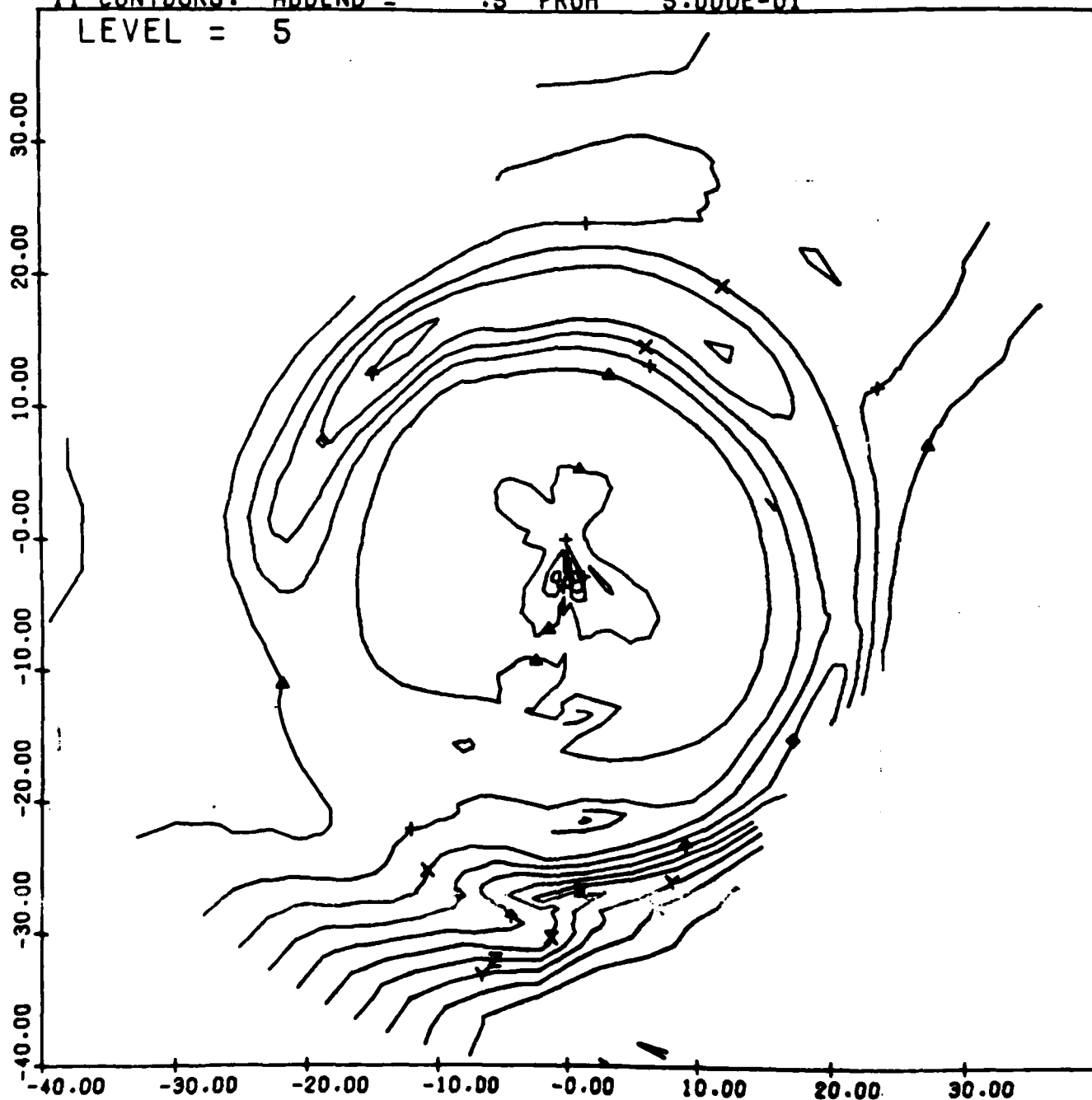
BOTH POLES   POLAR PLOT FOR KP =   0. (AEOY)

⊙	▲ .50	+ 1.00	X 1.50	◇ 2.00
♠ 2.50	X 3.00	Z 3.50	Y 4.00	X 4.50

PLASMA
MANTLE

INTERIOR
CUSP (EL)

LOW-LATITUDE
BOUNDARY
LAYER

PLASMA
BOUNDARY
LAYER

RING CURRENT
PLASMA SHEET
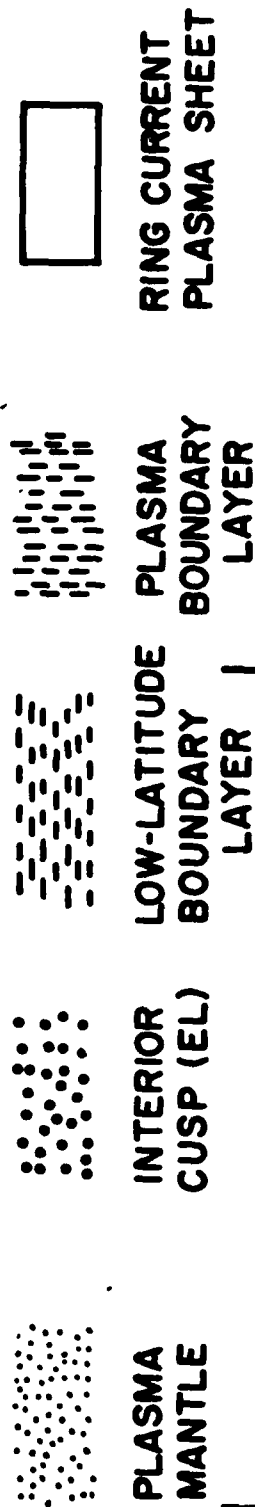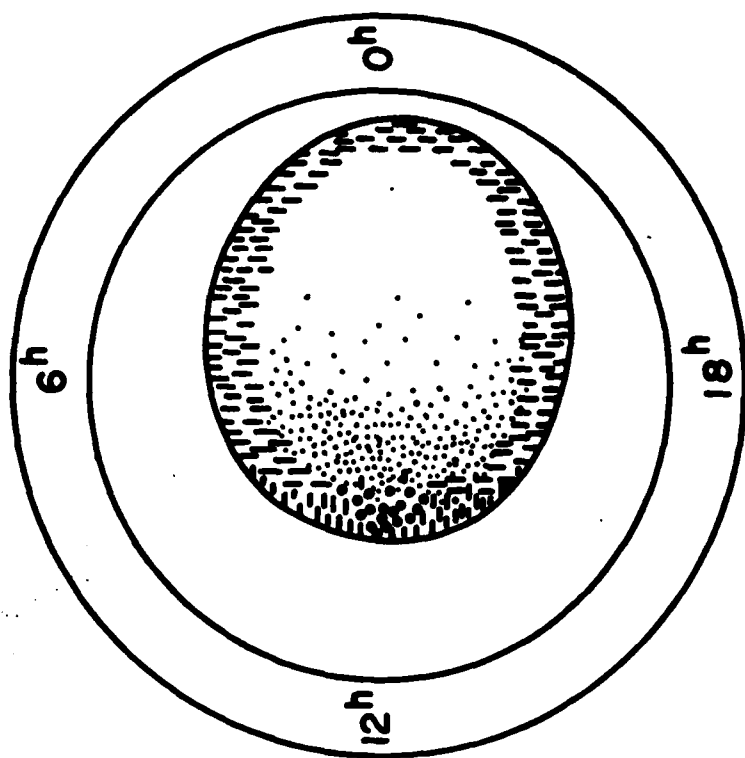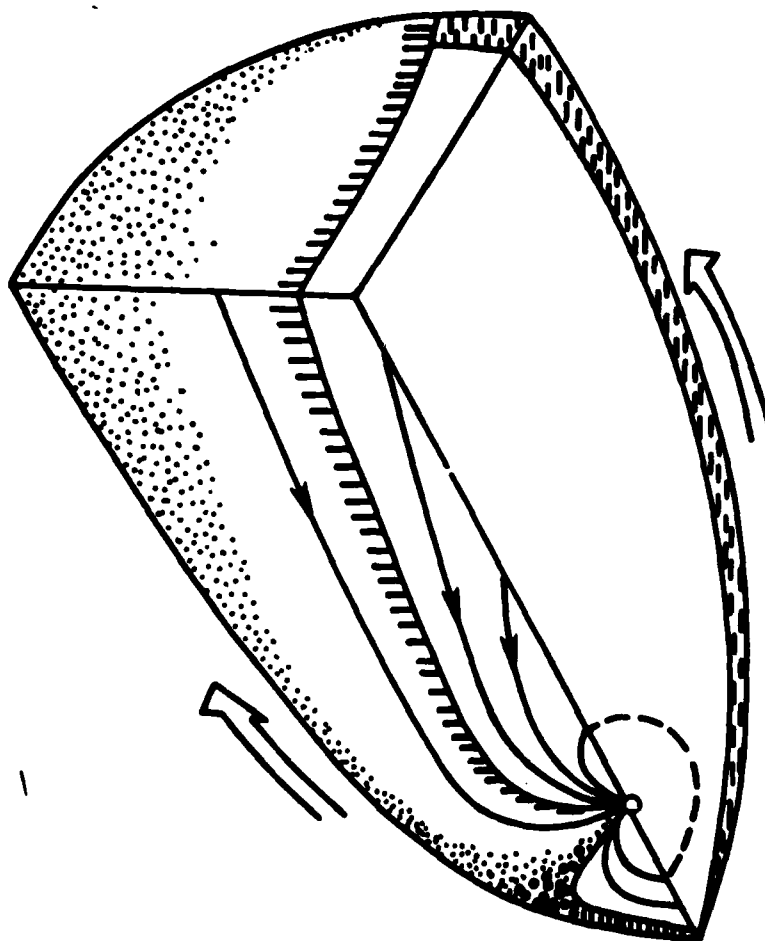
MAGNETOPAUSE BOUNDARY LAYERS

HIGH LATITUDE MAPS OF PRECIPITATING AURORAL ELECTRONS

D.A. Hardy
Air Force Geophysics Laboratory
Hanscom Air Force Base, MA 01731

M.S. Gussenhoven
Physics Department, Boston College
Chestnut Hill, MA 02167

and

E. Holeman
Physics Research, Emmanuel College
Lexington, MA 02173

ABSTRACT

Precipitating electron data from the SSJ/3 sensors on the polar orbiting DMSP/F2 and F4 and P78-1 satellites in the energy range, 50 eV - 20 keV are binned according to KP (each whole value: 0, 1, 2, ...), magnetic local time (48 zones) and corrected geomagnetic latitude (30 zones from 50° to 90°) for fifteen months (about 13 million spectra). In each zone of each KP matrix, the average and standard deviation of the counts in each of the sixteen channels of the sensor over all spectra in that zone were maintained. From the average spectra, contour plots of three quantities are prepared: integral flux, energy flux, and average energy. Systematic variations both in spatial dimensions and in magnetic activity are found. Dayside sources (cusp, entry layer, and low latitude boundary layer) and nightside sources (plasmasheet and boundary plasmasheet) are distinguishable when integral flux and average energy are examined together.

I. INTRODUCTION

In this paper, we present the results of a study of the global pattern of electron precipitation. Historically, there have been two approaches to such global specification. In the first of these, the researcher builds up a global or local time picture using a set of individual passes, each studied in detail. The advantage of such an approach is that all the details of each pass are considered in building up an overall picture. The major disadvantage in such studies is that, in order to keep both the analysis and data presentation manageable, the researcher must restrict the total number of passes studied either by spacing them widely in magnetic local time or in activity. In the second approach, the researcher builds up his global picture by dividing the region of interest into zones in magnetic local time, geomagnetic latitude, and activity and then using very large data sets to determine the average value of the quantity of interest in each zone (Feldstein, 1966; Eather and Mende, 1971; McDiarmid et al., 1975; Wallis and Budzinski, 1981; and Spiro et al., 1982). This approach has the advantage of providing real global maps. Its major disadvantage is that in the averaging process, all small spatial and temporal variations are smoothed out, of necessity. The number of such studies done in the past has additionally been restricted by the fact that they require very large data sets (millions of samples), and they require significant amounts of computer time.

In this study, we have taken the second of these two approaches using the data set from identical electrostatic analyzers flown on three Air Force satellites; the Defense Meteorological Satellite Program's F-2 and F-4 satellites and Satellite Test Program P78-1 satellite. This data set, due to its great size, is singularly suited to such a study since it allows very fine gridding in magnetic local time, latitude, and activity such that the global

118

pattern and its variation in activity can be studied in detail.

The paper is divided into five sections. Following the introduction, Section II deals with a description of the electrostatic analyzers that provided the data and the orbital coverage of the three satellites. Section III describes how the data were binned and what integral quantities were calculated. In Section IV, the global maps are discussed. This section is divided into two subsections, one dealing with the pattern of precipitation of cold electrons (average energies less than 600 eV) associated with the boundary plasma sheet and cusp, and one dealing with the precipitation pattern of hotter electrons associated with the diffuse auroras and central plasma sheet. Section V is then the discussion.

SECTION II. INSTRUMENTATION AND ORBIT

The data used in this study are from the cylindrical curved plate electrostatic analyzers flown on the F-2 and F-4 satellites of the Defense Meteorological Satellite Program and the P78-1 spacecraft of the Space Division, Space Test Program.

The detectors on the DMSP satellites, designated SSJ/3, consist of a pair of curved plate electrostatic analyzers, one covering the energy range from 50 eV to 1 KeV in eight semi-logarithmically spaced channels, and one covering the energy range from 1 KeV to 20 KeV, again also in eight channels. The two analyzers are stepped through the eight channels together such that a complete spectrum over the entire energy range is produced once per second. The DMSP satellites are three axis stabilized. The SSJ/4 detectors are oriented such that their look directions are always towards the local zenith. The detector on the P78-1 satellite, designated CRL-251, consists of a pair of SSJ/4 detectors mounted at right angles to each other with their look directions in

the spin plane of the satellite. The one difference between the CRL-251 and SSJ/3 detectors is that for CRL-251, the 16 channels are swept 4 times per second, as opposed to once per second for SSJ/3. The P78-1 satellite is spin stabilized with the spin plane in the orbit plane, and the spin axis orthogonal to the Earth-sun line. The satellite rotates at 11 rpm.

Both the F-2 and F-4 satellites were planned to be in circular sun synchronous orbit at an altitude of 840 kilometers and an inclination of 97.4° in the dawn-dusk and 1000-2200 meridians, respectively. F-4 achieved its orbit, but the F-2 orbit precessed approximately 2 hours toward the 0800-2000 meridian over its two and one-half years lifetime. The orbital coverage of the two satellites in a magnetic local time-corrected magnetic latitude coordinate system is shown in Figure 1. The P78-1 satellite was launched into a 600 kilometer circular sun synchronous orbit in the noon-midnight meridian. The three satellites clearly provide coverge of all latitudes and MLT except for a small region at low latitudes post-midnight and post-noon.

Data from the F-2 and F-4 satellites are available between September 1977 and February 1980 and April 1979 to August 1980. The SSJ/3 detectors were used as operational sensors on the satellite, and as such were operated continuously. Approximnately 80% of the data was recorded such that the data set consists of approximately 17000 northern or southern hemisphere passes for the F-2 satellite, and approximately 10000 for the F-4 satellite. The data from P78-1 were available for the time period from February 1979 to January 1980. The data set comprises approximately 1800 hemispheric passes.

SECTION III. DATA ANALYSIS PROCEDURES

In this study, we divided the high latitude region into zones in magnetic local time and corrected geomagnetic latitude. In MLT, the divisions were 48

120

one-half hour sections. In latitude, there were 30 divisions at 2° increments
between 50 and 60 degrees, 1° increments between 60 and 80 degrees, and 2°
increments from 80 to 90 degrees. Seven such matrices were created, one for
the Kp = 0, 0+ cases, one for Kp = 1-, 1, 1+ cases, and so on up to Kp = 5-,
5, 5+. The last matrix included all cases greater than Kp = 6-. Fifteen
months of data were used from the F-2 and F-4 satellites. The fifteen months
were chosen to give an even distribution of the data over the seasons of the
year and to provide sufficient coverage at high activity. Altogether, the 15
months of data provided 13.6 million spectra. All orbits of the P78-1
satellite in the interval from February 1979 to January 1980 were used. For
these orbits, only the zenith looking spectra were used. This comprised
approximately 1 million additional spectra. In each zone, the average and
standard deviation of the differential number flux for each of the 16 energy
channels of the detector were calculated using all spectra that fell within
that zone. The final product is, therefore, the average spectrum in each zone
at each level of activity.

For the purpose of display, we calculated integral quantities over the
entire energy range of the average energy spectrum. The three quantities
calculated were the integral number flux in units of e/cm^2-sec-ster defined as:

$$JTOT = j(E_1) \ (E_2 - E_1) + \sum_{i=2}^{15} j(E_i) \ \frac{E_i+1 - E_i-1}{2} + j(16) \ (E_{16} - E_{15})$$

The integral energy flux in units of keV/cm^2-sec-ster defined as:

$$JETOT = E_1 \ j(E_1) \ (E_2 - E_1) + \sum_{i=2}^{15} j(E_i) \ j(E_i) \ \frac{E_i+1 - E_i-1}{2} +$$

$$E_{16} \ j(E_{16}) \ (E_{16} - E_{15})$$

and the average energy in units of keV defined as:

$$EAV = \frac{JETOT}{JTOT}$$

where $j(E_i)$ = the average differential number flux in the i'th energy channel

E_i = the central energy of the i'th energy channel.

To eliminate effects due to a small amount of residual noise from the data in the average spectra, the integral quantities were smoothed slightly. The approach used was as follows: For any value in the matrix $\alpha_{i,j}$ where the subscripts refer to the i'th MLT zone and j'th latitude zone, the value was recalculated by the formula:

$$\alpha_{i,j}' = \frac{3\alpha_{i,j} + \alpha_{i-1,j} + \alpha_{i+1,j} + \alpha_{i,j+1} + \alpha_{i,j-1}}{7}$$

At the pole, the average was taken over all 48 MLT zones and at 50° $\alpha_{i,j-1}$ term was excluded and the sum was divided by six. In the plots shown in the next section, this procedure was repeated three times.

SECTION IV. GLOBAL MORPHOLOGY OF ELECTRON PRECIPITATION

In this section, we discuss the morphological features of the electron precipitation derivable from the global maps of the integral number flux, integral energy flux, and average energy. These maps are shown as contour plots in Figures 2a-d, 3a-d, and 4a-d, respectively for KP values 0, 2, 4, and 6. We divide this section into two parts. In the first part, we discuss the pattern of low energy electron precipitation (average energy < 600 eV) with special attention to the intense precipitation seen on the dayside half of the oval. In the second part, we discuss the pattern of high energy electron precipitation. In both parts, we limit ourselves to description of the various morphological features and a comparison to other observations. The

physical significance of the various features will be considered in Section V.

SECTION IV a. Low Energy Electrons

Referring to the maps of integral flux, one notes that up through Kp = 4, the maximum integral flux is observed on the dayside portion of the oval slightly pre-noon. Even in the Kp = 6 map, there is still at least a local maximum observed pre-noon although that level is met or exceeded elsewhere in the oval. At Kp's up through 4, this maximum is embedded in a crescent-shaped region of flux exceeding 10^8 electrons/cm^2-sec-ster. At a constant level of $\sim 2 \times 10^8$, this crescent is not symmetric about noon, but rather starts at ~ 0600 MLT and terminates ~ 1700 MLT. This asymmetry is clear in the Kp = 0 and 2 cases and less clear at higher activities. At the level of $\sim 2 \times 10^8$ electrons/cm^2-sec-ster, the crescent region extends from 75 to 80 degrees in geomagnetic latitude with only a 1 or 2 degree shift equatorward over the entire range in activity. Referring to the plots of average energy, one sees that in this entire region the average energy of the electrons is uniformly less than 600 eV with values as low as ~ 100 eV. The average energy is not uniform over the region. At Kp = 0, the average energy is roughly symmetric about noon. For Kp = 2, the region is clearly colder pre-noon than post-noon. At Kp = 4 and 6, the average energy becomes again more nearly symmetric about noon. In all cases, there is a clear region of minimum energy embedded in this cold regime. For Kp's up through 5 (not shown), this region of minimum energy is centered between 1/2 and one hour in MLT, pre-noon. Contours of constant energy near the minimum are approximately oval in shape being more extended in MLT than in latitude. The regions of minimum energy and maximum integral flux do not coincide. Table 1 gives the location, integral flux, and average energy for the two cases for Kp = 0 through 3.

	MAXIMUM INTEGRAL FLUX				AVERAGE MINIMUM ENERGY			
Kp	MLT	MLAT	JTOT	EAVE	MLT	MLAT	JTOT	EAVE
0	0800 → 0830	79°	3.04×10^8	249	1100 → 1130	80°	2.29×10^8	201
1	0800 → 0830	78°	3.23×10^8	268	1130 → 1200	80°	2.69×10^8	181
2	0930 → 1000	78°	3.31×10^8	255	1130 → 1200	79°	2.94×10^8	174
3	1100 → 1130	77°	3.81×10^8	190	1100 → 1130	79°	2.72×10^8	167eV

Going from low activity to high, the maximum integral flux region rotates towards noon and moves to slightly lower latitudes. The integral flux at the maximum increases slightly and the temperature decreases. For the temperature minimum, the location in MLT remains fixed between 1100 and 1200 hours MLT. The minimum moves equatorward less than the integral flux maximum; JTOT increases and the minimum average energy decreases. The energy flux in the cold morningside region is uniformly small. At the integral number flux maximum, the values of the integral energy flux are approximately .1 erg/cm^2-sec-ster. At the average energy minimum, the values are only approximately .07 ergs/cm^2-sec-ster.

The average energy plots show that the cold plasma region is roughly circular for Kp = 0 and 1 (not shown) with the center of the circle offset approximately 5 degrees towards magnetic midnight.

In the region extending in magnetic local time from approximately 0300 to 2000 hours for Kp = 0 and 0400 to 1830 hours for Kp = 1, the peak integral flux is enclosed within the cold region. In the rest of the oval, the peak lies just at or slightly equatorward of the cold electron region. For higher activity, the cold region contracts poleward particularly in the pre-midnight sector such that for a larger portion of the oval, the peak integral flux falls outside of the cold electron region.

SECTION IV b. <u>High Energy Electrons</u>

Referring to the plots of the energy flux, one notes that the location of the first maximum is seen to colocate with the region of maximum energy flux. Contours of constant energy flux have roughly a horseshoe shape symmetric about the 0200 - 1400 MLT meridian for Kp = 2 through 4. For Kp = 0, the contours are rotated such that they open in the pre-midnight sector. For Kp 5 and 6, the tendency is for the pattern to become more symmetric about the noon-midnight meridian. At all activity levels above Kp = 0, there is a strong negative gradient in the energy flux starting at approximately 1000 hours MLT. The location of this gradient is roughly coincident with the second region of maximum average energy. For Kp = 0 and 1, the maximum energy flux is found slightly pre-midnight. For all higher activities, the maximum is found post-midnight.

Referring again to the average energy plots, one notes that there is a region of minimum average energy within the auroral oval. For Kp = 0, this region is centered at approximately 2100 hours MLT. For higher activity, this region of minimum energy rotates towards noon. The average energy in this minimum is approximately the same as in the cold electron region. In the plots, it appears as a hole particularly evident in the Kp = 3 (not shown) and greater cases. It should also be noted that starting at the Kp = 3 case, the higher energy plasma is excluded from an increasing large portion of the morning sector with the hot plasma being confined almost completely to the nightside of the oval for the Kp = 6 case.

As part of our analysis, we calculated the total number flux and energy flux precipitating into each one-half hour MLT zone for each level of Kp. The results are shown in Figures 5 and 6 for the energy flux and number flux, respectively. The figures show that Kp orders the data well. Each level is

well separated from all others. The only exception is the Kp = 5 case for the energy flux. This most likely reflects the relatively low statistics used to construct this map. Figure 6 shows that for Kp = 0 and 1, the maximum energy flux is pre-midnight, and that for all higher activities, the maximum shifts post-midnight by between one-half and one and one-half hours. In the number flux, the values are seen to increase most near midnight and least near noon. Integrating over the entire oval, we calculated the total particle and energy input. The number flux has a roughly exponential rise from 1.51×10^{25} electrons/sec-ster at Kp = 0 to 1.02×10^{26} electrons/sec-ster at Kp = 6, i.e., less than an order of magnitude increase. For the energy flux, the values go from 1.35×10^{16} ergs/sec-ster at Kp = 0 to 2.27×10^{17} ergs/sec-ster at Kp = 6, i.e., approximately a factor of 16 increase. Again, as for the number flux, the energy flux shows roughly an exponential increase. In both cases, the Kp = 6 is above the trend defined by the lower Kp's reflecting the admixing of data from Kp's larger than six.

V. DISCUSSION

We have shown that at all levels of activity, there is a crescent-shaped region of cold electron precipitation on the morningside of the oval extending in magnetic local time from ~ 0600 to 1700 hours MLT at a level of 2×10^8 electrons/cm^2-sec-ster. The region spans 2° to 3° in latitude generally in the range from 76° to 80°. Such a region, if mapped in the equatorial plane, has an outer edge typically at approximately 12 earth radii, i.e., lying along the average position of the dayside magnetopause. Studies using magnetometer data have shown that the cusp has a conical shape only a few degrees across at 840 kilometers. It is therefore difficult to associate this broad region of cold electron precipitation with particles gaining direct access through the

126

cusp to the DMSP orbit. Rather, it is more reasonable to postulate that this region results from a diffusive process taking place at the magnetopause.

The asymmetry in the distribution in local time and the pre-noon maximum we explain as follows: We assume that electrons have equal diffusive access across the dayside magnetopause. In addition, plasma is convecting from the nightside towards noon. It has been well established that in the post-noon magnetosphere, the ionosphere sets up a charge separation electric field which shields this region from the convection electric field. The plasma convecting from the nightside would be diverted toward the magnetopause as it approached this region. The high energy plasma would simply convect out through the magnetopause and be lost. The low energy plasma would be caught up in the electric field near the magnetopause and recirculated to the tail. At the point where the cold plasma from the tail reaches the region near the magnetopause and is redirected towards the tail, both this cold plasma and the plasma that has diffused through the magnetopause are present such that the total density is higher resulting in the maximum observed at low altitudes. At later MLT, no cold plasma can convect due to shielding. At earlier MLT, the plasma has not convected to the magnetopause.

The region of minimum average energy we associate with the cusp since it has dimensions and shapes similar to those obtained from the magnetic field data. For the high energy plasma, the maximum in average energy and energy flux in the midnight sector results from plasma convected in from the tail. Hot electrons tend to drift to the east. The sharp gradient in energy density reflects the combined effects due to depletion of the particles on a flux tube from loss into the atmosphere and the fact that shielding is preventing the plasma from convecting any further in magnetic local time. The fact that the

second maximum in average energy occurs where this gradient begins strongly suggests it is tied to one or both of these processes.

REFERENCES

Eather, R.H. and S.B. Mende, Airborne observations of auroral precipitation patterns, J. Geophys. Res., 76, 1746, 1971.

Feldstein, Y.I., Peculiarities in the auroral distribution and magnetic disturbances distribution in high latitudes caused by the asymmetric form of the magnetosphere, Planet. Space Sci., 14, 121, 1966.

McDiarmid, I.B., J.R. Burrows, and E.E. Budzinski, Average characteristics of magnetospheric electrons (150 eV to 200 keV) at 1400 kilometers, J. Geophys. Res., 80, 73, 1975.

Spiro, R.W., P.H. Reiff, and L.J. Maher, Jr., Precipitating electron energy flux and auroral zone conductances -- an empirical model, J. Geophys. Res., 87, 8215, 1982.

Wallis, D.D. and E.E. Budzinski, Empirical models of height integrated conductivities, J. Geophys. Res., 86, 125, 1981.

FIGURE CAPTIONS

Figure 1   Combined coverage of the DMSP F2 and F4 satellites in a corrected
            geomagnetic latitude - magnetic local time coordinate system.

Figure 2   Contours of constant total number flux in e/cm^2 sec ster for KP
            values   a) 0,   b) 2,   c) 4, and d) 6.

Figure 3   Contours of constant total energy flux in keV/cm^2 sec ster for KP
            values   a) 0,   b) 2,   c) 4, and d) 6.
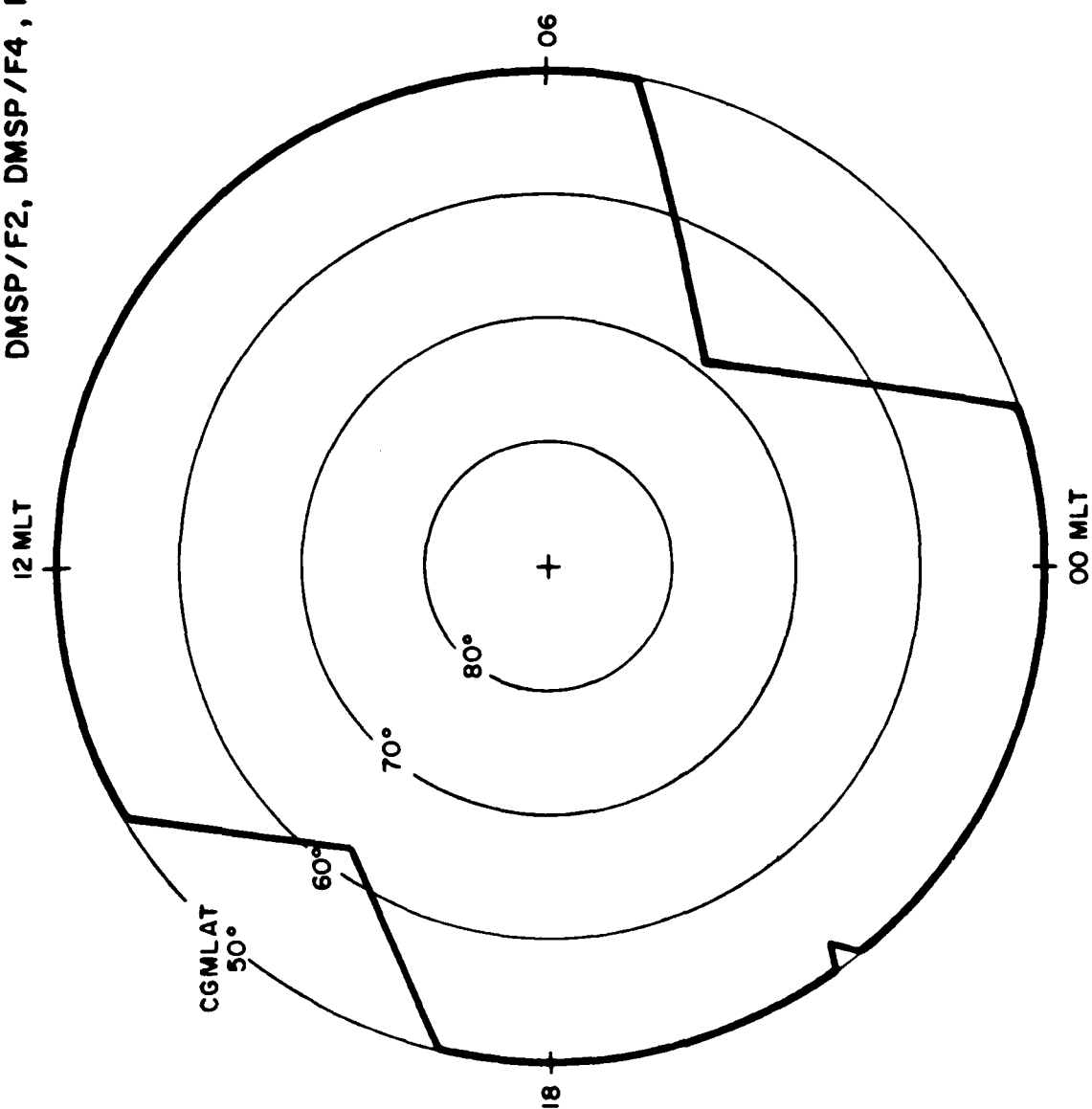
Figure 4   Contours of constant average energy in keV for KP values   a) 0,
            b) 2,   c) 4, and d) 6.

Figure 5   The average integral number flux integrated over latitude as a
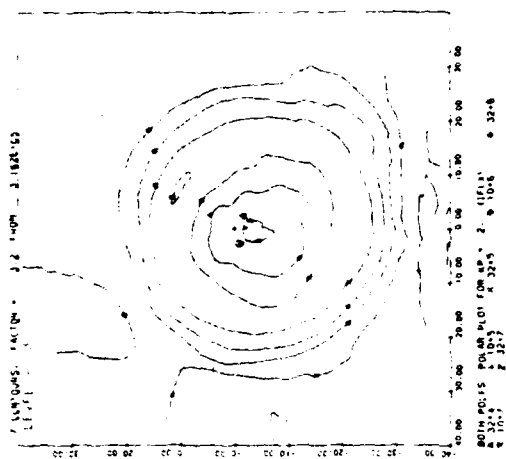   function of magnetic local time for each KP level.

Figure 6   The average integral energy flux integrated over latitude as a
            function of magnetic local time for each KP level.

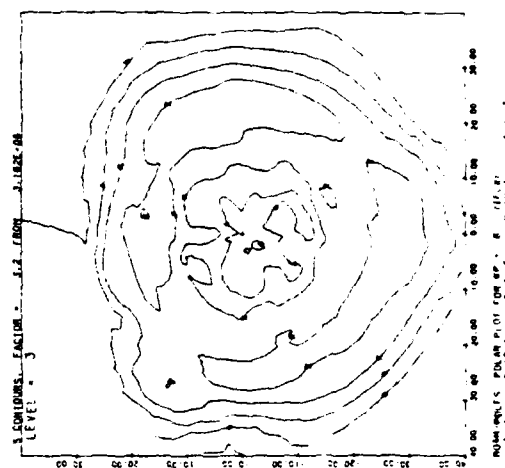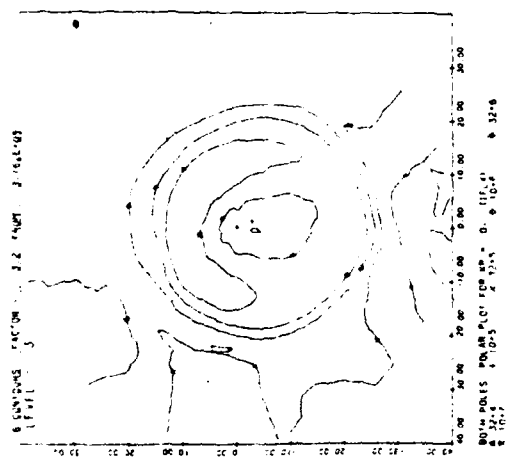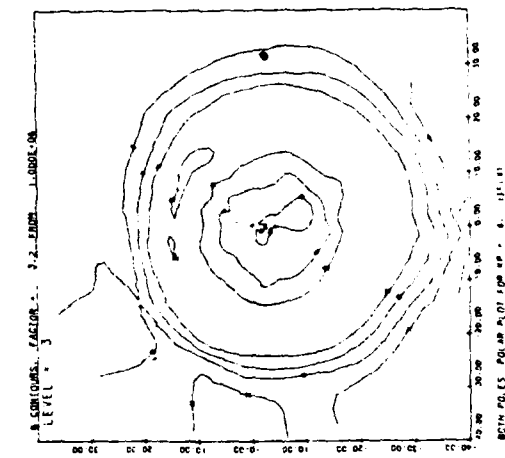# COMBINED ORBITAL
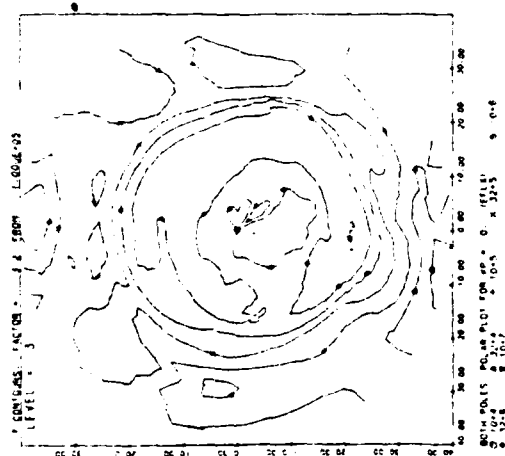## COVERAGE
DMSP/F2, DMSP/F4, P78-1

B

D

A

C

NUMBER FLUX (electrons /sec-ster)

NUMBER FLUX

Kp = 6
Kp = 5
Kp = 4
Kp = 3
Kp = 2
Kp = 1
Kp = 0

ENERGY FLUX

Kp=6
Kp=5
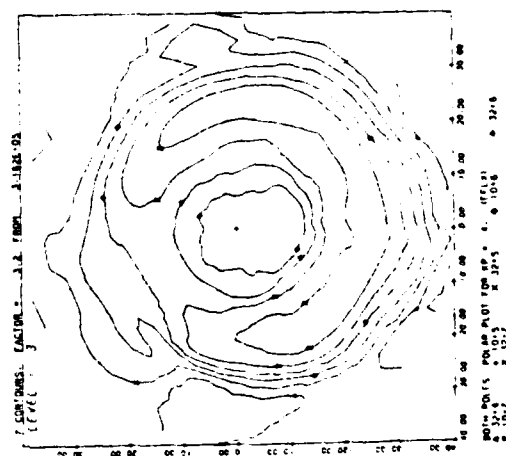Kp=4
Kp=3
Kp=2
Kp=1
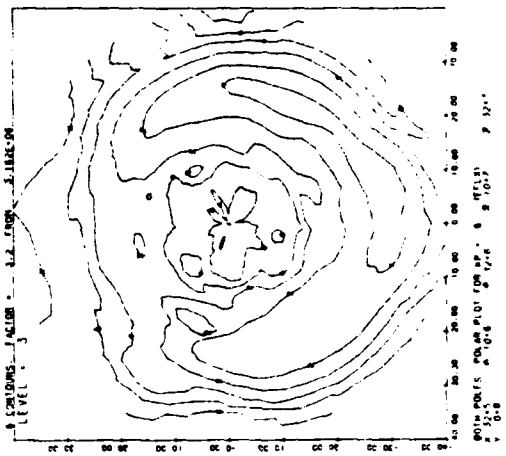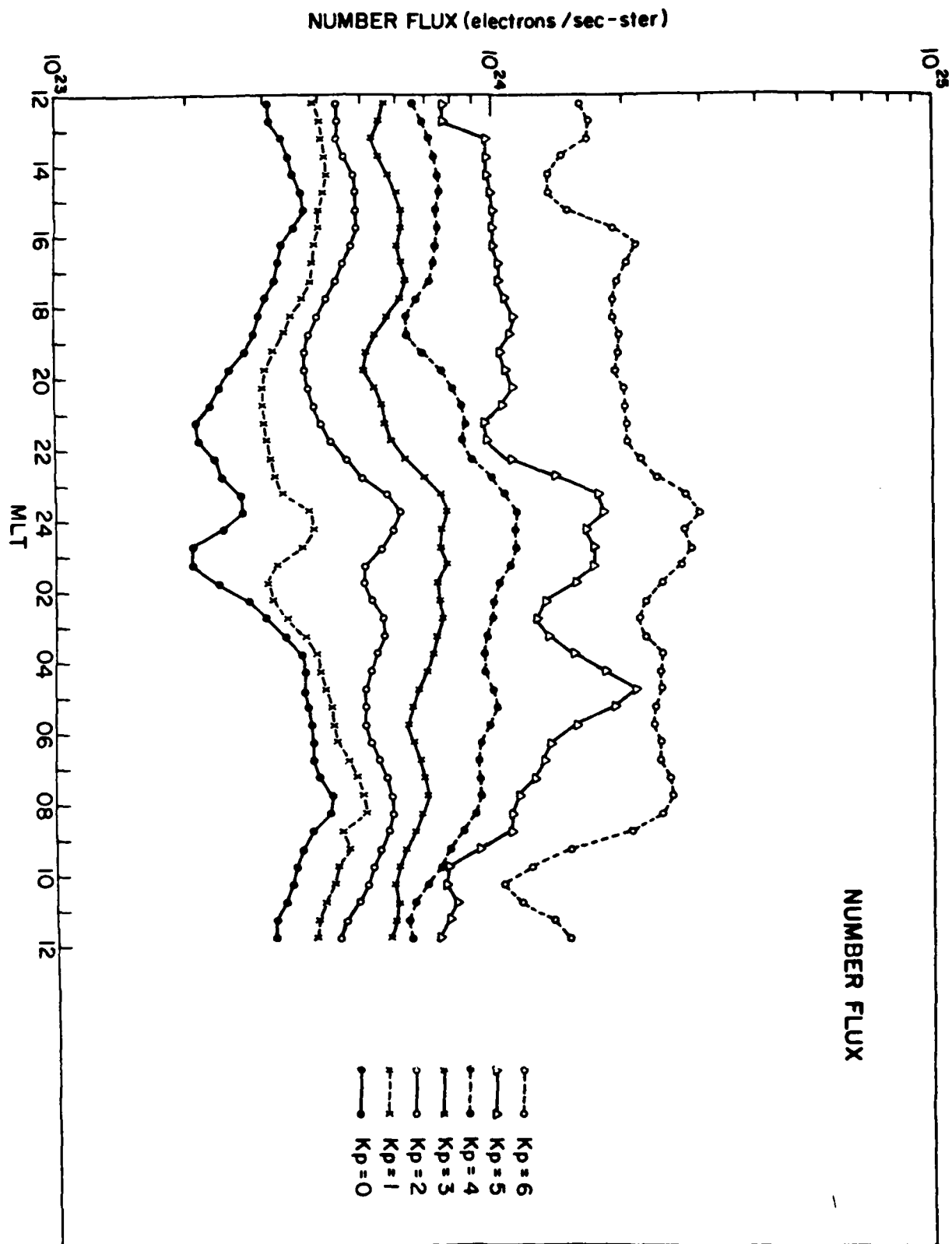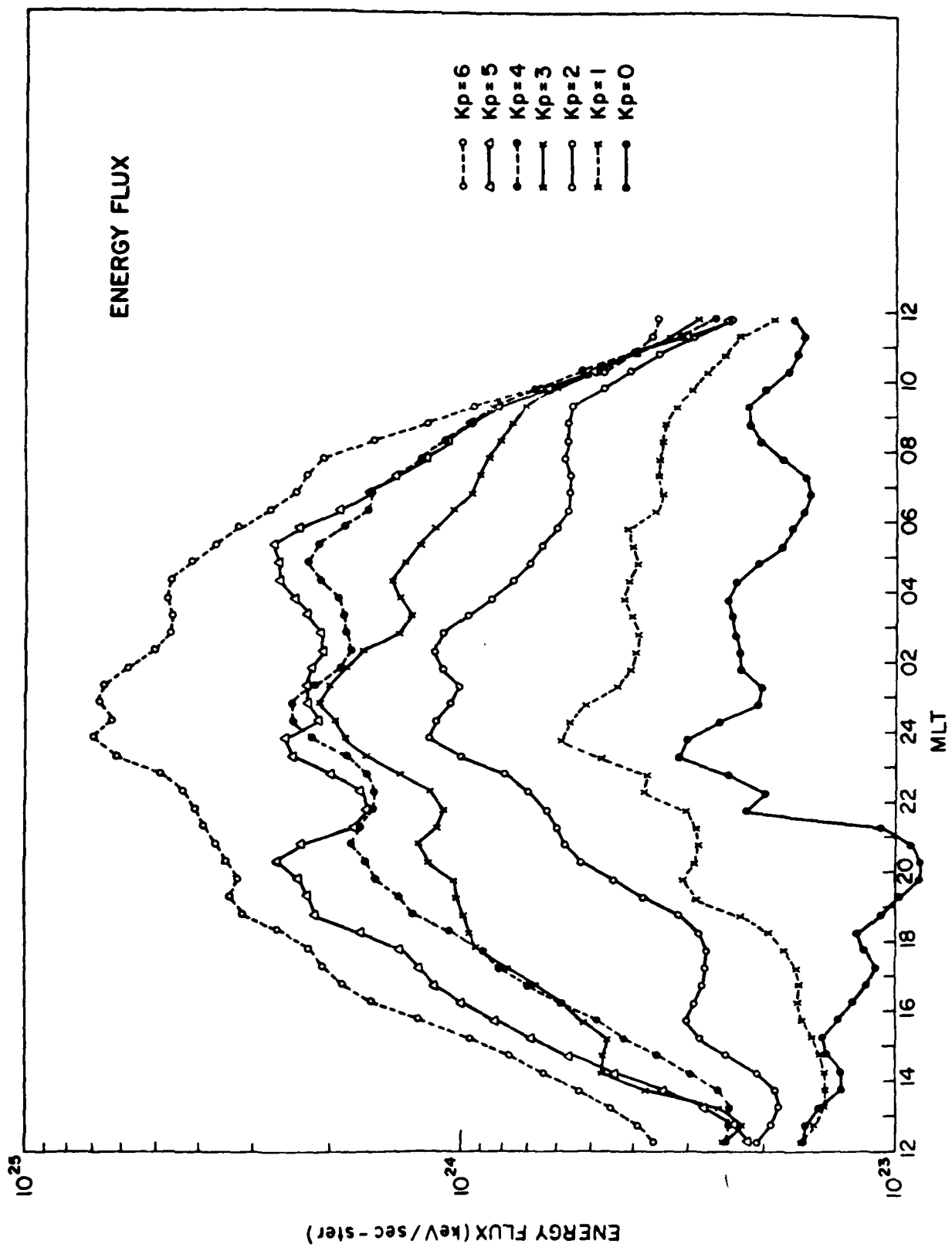Kp=0

ENERGY FLUX (keV/sec-ster)

MLT
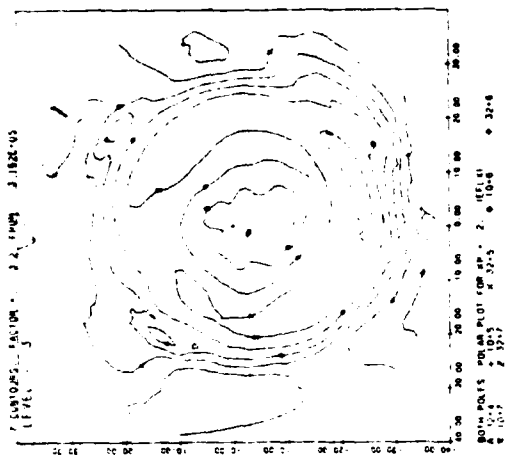
Extremely High Latitude Auroras

M. S. GUSSENHOVEN

Physics Department. Boston College. Chestnut Hill. Massachusetts 02167

Over 1600 Defense Meteorological Satellite Program north polar images from the winters 1972-1973, 1974-1975 were studied for the occurrence of auroral arcs at corrected geomagnetic latitudes greater than 80°. Auroras at these latitudes are designated extremely high latitude auroras and are categorized by the local time sectors in which they occur and their relationship to discrete oval arcs. A data base of ~300 cases of cap auroras was formed for correlation studies with geomagnetic activity indices and solar wind parameters. By far the greatest number of extremely high latitude auroras occur in the morning sector and appear to be expansions of the system of morning oval arcs poleward. The remaining categories include evening arcs expanding into the cap; single, sun-aligned arcs; and midnight sector oval auroras expanding into the cap. Except for the last category the auroras occur for similar magnetospheric conditions: moderate values of Kp and Dst, but comparatively low values of AE. They also occur preferentially for high solar wind speed and for positive B_z. While far less clear, their location in the cap shows a dependence on B_y. Morning (evening) arcs occur with greater frequency for negative (positive) B_y.

INTRODUCTION

Observations of auroral arcs near the magnetic poles have been reported in the literature for many years. Often the reports were of individual sightings, fortuitously made from ground, airplane, or rocket, and limited by the motion of the observer, or the arcs, or both, and also by the infrequency of occurrence and lifetime of the arcs. Nevertheless, in the composite of auroral studies, polar cap arcs have come to mean weak, sun-aligned arcs occurring poleward of the auroral oval during quiet times and occurring rarely [*Davis*, 1960, 1962*a, b; Denholm,* 1961; *Denholm and Bond,* 1961; *Akasofu,* 1963, 1968, 1972; *Gustaffson,* 1967; *Lassen,* 1968, 1972; *Eather and Akasofu,* 1969; *Whalen et al.,* 1971; *Romick and Brown,* 1971; *Akasofu et al.,* 1972].

There is disagreement on the lifetimes of polar cap arcs. They are sometimes referred to as short lived, but have been recorded in all-sky camera pictures taken at 1-min intervals as lasting for more than an hour (J. A. Whalen, private communication, 1977). In addition, they are found to occur more often in the morning. However, in the morning sector, sun alignment and oval alignment are nearly the same, as pointed out by *Lassen* [1973], and it is unclear whether polar cap arcs are distinguishable from a collection of morning oval arcs expanding poleward [*Meng,* 1981]. *Akasofu* [1968] and *Pike* [1975] show the occurrence of these arcs as characteristic of the recovery phase of substorms.

In one of the earliest statistical studies of auroras at high latitudes, *Davis* [1963] found the occurrence of morning arcs observed from Thule (86.8° corrected geomagnetic latitude) to anticorrelate with magnetic activity. More recently, *Lassen and Danielsen* [1978] constructed mass plots of arcs recorded by all-sky cameras at high latitude stations for times of no substorm activity. They ordered the plots according to the interplanetary magnetic field components to show contraction of the auroral oval and greater definition of a polar cap system of arcs with increasing B_z. The polar cap arc system is, however, quite clearly present in the morning for all but the most negative values of B_z. Thus ground-based

observations show an asymmetric, but systematic involvement of the polar cap which is related to magnetic activity and the IMF z component.

Imaging devices on the polar orbiting ISIS and Defense Meteorological Satellite Program (DMSP) satellites have greatly increased the extent of polar cap and auroral zone coverage and have prompted several studies of polar cap arcs. Focus has been on the most dramatic of auroras in high latitude regions: the single, well-defined arc directly crossing the cap, passing near the magnetic pole and sun aligned. Excellent examples of these, obtained from the DMSP satellites, are shown by *Meng and Akasofu* [1976]. Studies made from the ISIS data for approximately 50 cases of polar cap arcs demonstrated that the arcs occur for interplanetary conditions of northward B_z and magnetospheric conditions in which AE has a local minimum [*Berkey et al.,* 1976; *Ismail et al.,* 1977]. These findings are consistent with ground observations. *Ismail et al.* [1977] also point out that while the occurrence of sun-aligned polar cap arcs is low, they have been observed on successive passes, possibly indicating persistence on the order of hours.

The work presented here is a statistical study of the occurrence conditions for arcs recorded in DMSP images at extremely high latitudes: ≥80° corrected geomagnetic latitude (CGL). The 80° boundary is chosen to minimize the problems associated with defining a polar cap boundary. The region within 10° of the magnetic pole is generally conceded to be within the cap, but even if this is not always the case, the region is well defined. The study is the first of three companion pieces concerning polar cap arcs. The principal motivation for examining polar cap arcs, statistically and in detail, is an understanding of the mechanism(s) of energy, mass, and momentum transfer to the polar cap. The arcs are indicators of such mechanisms since they imply increased particle fluxes and particle acceleration. The second paper, by *Hardy et al.* [this issue], is concerned with electron precipitation in and near polar cap arcs; and the third, by *Burke et al.* [this issue], with the relationship of arcs to electric fields and currents. Therefore, to avoid repetition, the scope of analysis and discussion in this paper is strictly limited to a determination of the most favorable conditions under which visible arcs are found in the cap regions.

DATA BASE AND CATEGORIZATION OF EXTREMELY HIGH LATITUDE AURORAS

Images from satellites in the Defense Meteorological Satellite Program (DMSP) are the basis of the study. The program routinely places sun synchronous satellites into circular polar orbits at altitudes ~800 km, such that there are two satellites in orbit at a time. One satellite orbit is in the dawn-dusk meridian, the other in the noon-midnight meridian. Auroral images are made by means of scanning radiometers on board the satellites and are now familiar research tools. Their properties have been extensively discussed [*Akasofu*, 1974; *Pike and Whalen*, 1974; *Rogers et al.*, 1974; *Snyder et al.*, 1974; *Carovillano*, 1975; *Sheehan and Carovillano*, 1978; *Eather*, 1979].

The DMSP images from 1972 to 1976 were surveyed. The group of DMSP images that were found to be most appropriate for the study were those obtained during the winters of 1972–1973 and 1974–1975. For the two winters chosen good coverage of the polar cap region was consistently obtained in the images of both satellites. In addition, good coverage in supporting data was available. Only northern hemisphere images were used. All images for the winter months chosen were gridded in corrected geomagnetic local time (MLT) and corrected geomagnetic latitude (CGL) coordinates. The class of auroras that occurs above 80° CGL was determined. A member of this class is called an extremely high latitude aurora. No aurora that reached these latitudes was excluded.

Some comments on the limitations of the data base should be made. A single DMSP image shows only a portion of the polar cap region. The region surveyed changes systematically in a 24-hour period as the earth rotates under the satellite orbit stationary with respect to the sun. Good coverage of a given local time sector of the cap occurs at the same universal time each day, leading to apparent, but nonphysical, variations with universal time. Since part of the cap is an unknown quantity, the data cannot be used directly for a frequency of occurrence study. In addition, knowledge of the coexistence of extremely high latitude arcs in more than one local time sector is limited. It should also be noted that very little information in the noon sector is obtained since daylight and the scattering of daylight into the radiometer obscures arcs occurring there. On occasion the noon-midnight and dawn-dusk satellites crossed the polar regions within a few minutes of one another. For these times excellent coverage of the total cap was achieved, as well as better time resolution for arc movement. These periods are appropriate to case studies, one of which is presented by *Hardy et al.* [this issue].

Examples of auroras occurring at extremely high latitudes in various local time sectors are shown in four DMSP images: Figures 1a through 1d. Midnight is near the bottom of each image. Figures 1a and 1d show the midnight sector. Figure 1b is an image of the central cap; local morning is on the right. Figure 1c shows the evening sector.

Because it is difficult to reproduce weak features in DMSP images, and in order to show position of the arcs with respect to the magnetic pole, separate representations of the images in corrected geomagnetic local time–corrected geomagnetic latitude coordinates are shown in Figures 2a through 2d. Emphasis is placed on reproducing the form and position of the arcs. An attempt to reproduce brightness by the density of cross-hatching or line width is also made.

However, it is best to consider the reproductions as cartoons of the original rather than exact representations.

Each example in Figure 1 (Figure 2 also) was chosen to represent a class of extremely high latitude arcs. Each example will be discussed. The class of arcs of which the example is representative will be defined. Finally, a summary of the classes of extremely high latitude arcs will be given.

Figure 1a (2a) is an image made by the noon-midnight DMSP satellite 8531 on November 17, 1974. The polar crossing was ~1115 UT. The oval consists of quiet arcs, a confined active region near midnight, and diffuse aurora extending to 65° CGL. The most poleward quiet oval arc in the premidnight region turns sharply toward the magnetic pole near midnight and extends into the cap to 83° CGL. (The bright patch in the upper part of the image is a light streak.) The arc, though weak, has a great deal of structure. At the time of the image $Kp = 2+$ and the hourly averaged value of AE was 218 nT (nanotesla). Figure 1a is the example of a class of arcs for which the term 'polar cap arc,' as used in the literature, most certainly applies. These arcs occur singly or at most in pairs or triplets. They are sun aligned. They can be weak or have considerable brightness and definition. They can have a great deal of structure (swirls, etc.) or the appearance of none. They can appear to be attached to (continuous with) an oval arc at one end (as in Figure 1a) or completely discontinuous with oval arcs. This class of arcs is designated $P(1)$.

Figure 1b (2b) shows a good portion of the polar cap at latitudes >75° CGL. The image was made by the dawn-dusk DMSP satellite 9532 on November 20, 1974. The polar crossing is ~0715 UT. Kp was 3, AE was 118 nT. The portion of the oval shown is very quiet. All arcs are weak and multiple. The diffuse aurora is weak. Although very difficult to discern in the image reproduction, arcs reach to >80° CGL on both the morning and evening sides of the cap, as is shown in Figure 2b. Here, however, we will be concerned primarily with the morning arcs. The morning arcs that lie in the region above 80° CGL are clearly continuous with the arcs below 80° CGL. They appear as a single collection that extends from the diffuse aurora poleward. The arcs are weak and thin, often short, and branching from other arcs. Figure 1b (2b) exemplifies extremely high latitude morning arcs, designated $P(2)$. The collection of arcs thus designated can have the following additional properties: The arcs can be found in several consecutive passes, expanding poleward or contracting equatorward. The arc system can have gaps. The most poleward arc in the system can be comparatively quite bright and for given image orientations indistinguishable from the single arcs of $P(1)$. The arc system can extend across the magnetic pole into the dusk sector in a continuous fashion.

Figure 1c (2c) is an example of an extremely high latitude arc in the evening sector. The image was made on December 13, 1974, by the dawn-dusk DMSP satellite 7529. The polar crossing was at ~0820 UT. Again, the surrounding oval arcs and the diffuse aurora are weak. $Kp = 2$, and $AE = 160$ nT. The arc that extends >80° CGL is weak and patchy. It is very obliquely aligned with respect to the oval. Evening extremely high latitude arcs, designated $P(3)$, occur less frequently than those in the other categories. While the evening oval can consist of a collection of weak arcs as in Figure 1b (2b), the collection differs from similar morning arcs by being more concentrated and rarely extending to 80°

CGL. Thus the evening arcs reach high latitudes both by expansion of the system of oval arcs poleward, as with those in category $P(2)$, and by abrupt transistion from oval alignment, as with those in category $P(1)$.

Finally, a fourth type of extremely high latitude aurora was found to occur. An example of this is given in Figure 1d (2d). The image was made by the noon-midnight DMSP satellite 8531 on November 22, 1974. The time of polar crossing was ~0620 UT. $Kp = 3+$; $AE = 342$ nT. The local time sector is midnight. Here arcs fill the midnight region of the cap up to 86° CGL, and are clearly part of a very active oval that has expanded poleward. Multiple arcs, continuous with the oval in the midnight sector, which extend to 80° CGL are designated category $P(4)$.

Figures 1a–1d reveal why polar cap auroras are difficult to define. Auroras can reach extremely high latitudes in a wide variety of ways and in all local time sectors. They can appear to be continuous with oval aurora at lower latitudes and 'attached' there; or they can be 'attached' to the oval but emerge from it at large, oblique angles. On the other hand, they can be 'detached' from the oval arcs and not apparently associated with any specific part of the oval. Arcs at extremely high latitudes can be long or short, weak or bright, structureless as are the quiet oval arcs, or made up of a series of distinct swirls. They can have considerable lifetimes.

Even with the extended coverage of DMSP images it is difficult to specify unambiguously categories of arcs in the polar caps. Nevertheless, four categories are defined, principally indicating the portion of the cap in which they are found, although each category possesses other distinguishing characteristics. In summary, they are:

1. $P(1)$: One or two long, individual arcs appearing or actually seen to originate (or terminate?) in midnight sector oval auroras. These arcs can range from very faint with little structure to bright and sharp and interiorly convoluted.

2. $P(2)$: Extremely high latitude morning auroras. The discrete arcs that appear in the local time range of 0400–0900 MLT are characteristically fine and multiple. Their orientation is difficult to establish. They appear sun aligned, but the oval itself is sun aligned near 0600 MLT. When this array of short weak arcs moves to latitudes ≥80°, they are identified as belonging to the $P(2)$ category.

3. $P(3)$: Arcs principally in the evening sector. This category includes patches and arc fragments that can extend across the cap to morning hours, but are distinguishable from the morning arc system. It also includes well-defined high-latitude arcs attached to the evening sector (1600–2000 MLT).

4. $P(4)$: Extremely high latitude midnight oval auroras. This type of aurora occurs when the oval expands poleward to extremely high latitudes.

For the winters of 1972–1973 and 1974–1975, over 300 cases of extremely high latitude auroras were identified in nearly 1600 DMSP images. They are distributed according to category as follows: $P(1)$—19%; $P(2)$—51%; $P(3)$—9%; $P(4)$—21%.

Of the 317 cases of extremely high latitude auroras shown in the satellite images, 135 (42.5% of the total) were followed within 100 min by another case. While true persistence of the arcs cannot be determined by a single satellite, there were times when two satellites passing within 5 to 10 min of the same polar region showed the arcs to remain in nearly the

same position with near identical features. Of the 135 cases of 'persistence,' 94 or 29.6% of the total (317) occurred with the same satellite, or with a 100 min interval. Further, the maximum interval of successive passes in which extremely high latitude auroras was seen in excess of 10 hours.

RELATIONSHIP TO MAGNETIC ACTIVITY

In order to determine the type of magnetic activity with which extremely high latitude auroras are associated, the cases identified by the images were sorted according to category and distributed by: Kp, indicating mid-latitude magnetic activity; hourly averaged values of AE, indicating the strength of the auroral electrojets, or substorm activity; and the hourly averaged value of Dst, indicating ring current strength, or storm activity.

Dependence on Kp. Figure 3a shows the distribution according to Kp. The high-latitude morning and evening arcs, $P(2)$ and $P(3)$, respectively, have approximately the same characteristics, peaking at Kp values of 3 and 4, and showing very few cases at low Kp. In addition, they occurred very infrequently for $Kp > 4$. The distribution for category $P(4)$ is peaked at $Kp = 4$ and occurs for higher Kp values than the other categories. This confirms the impression obtained from the image survey that this category consists of poleward expansion of the midnight oval during active times. The single $P(1)$ arcs occurred at lower values of Kp than the rest, the maximum in the distribution being $Kp = 2$ (although a considerable number of cases exist for $Kp = 3$ and 4). It is the occurrence of this type of auroral arc at extremely high latitudes that has led to the often expressed belief that polar cap arcs occur in quiet times.

Although the survey presented here covers approximately 6 months of data, it is possible that the long length of the Kp interval (3 hours) or a period of unusual activity could bias the data. In addition, we know that moderate levels of activity ($Kp = 2$–4) are the most common. Therefore all images surveyed to obtain the sample of extremely high latitude auroras were binned according to Kp. The nearly 1600 images are distributed as follows:

Kp	Percentage of Total
0	4.5
1	14.7
2	18.6
3	23.7
4	22.9
5	10.9
6	4.0
7	0.5

The distribution is near Gaussian peaking at $Kp = 3$. For each category of extremely high latitude aurora, the percentage of the total number of images surveyed was calculated for each Kp bin. This gives, at best, a lower bound on the occurrence frequency. The results are shown in Figure 3b, from which essentially the same conclusions may be drawn as from Figure 3a. Two changes of note are that the sun-aligned arcs, $P(1)$, now have a greater distribution for low Kp values; and the midnight oval expansions, $P(4)$, are shifted to even higher Kp values. The evening arc distribution, $P(3)$, shows more clearly the effect of small sample size. Finally, it should be noted that not including midnight oval expansions Figure 3b suggests that arcs occurred at magnetic latitudes

Fig. 1a

Fig. 1c
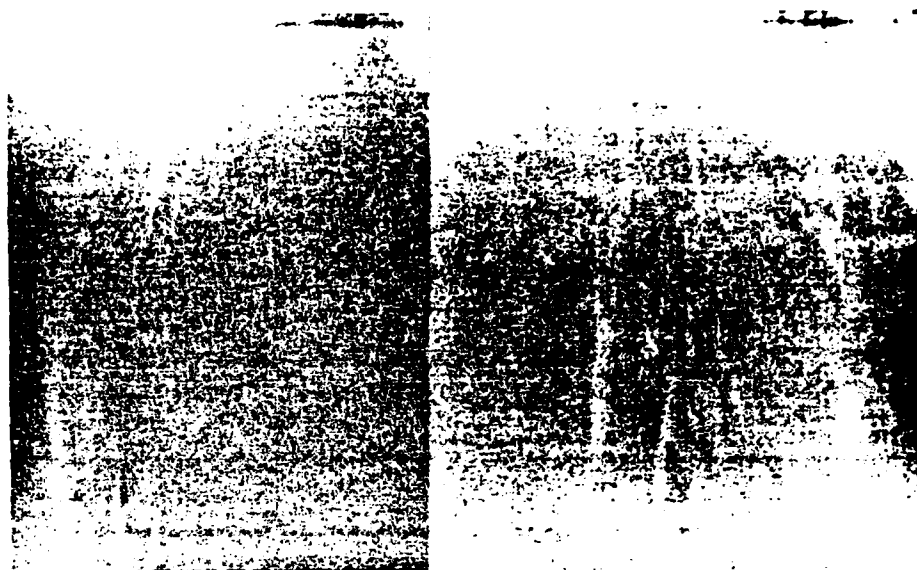
Fig. 1b

Fig. 1d

Fig. 1. North polar DMSP images exemplifying the four categories of extremely high latitude auroras. In each midnight is toward the bottom of the image, and noon toward the top. (a) An example of single arcs across the central cap, P(1); taken on November 17, 1974, at ~1115 UT. (b) An example of multiple arcs continuous with the morning oval arcs, P(2); taken on November 20, 1974, at ~0715 uT. (c) An example of arcs extending into the cap from the evening sector, P(3); taken on December 13, 1974, at ~0820 UT. (d) An example of midnight oval expansions into the cap, P(4); taken on November 22, 1974, at ~0620 UT.

Fig. 2. Cartoons of the DMSP images in Figure 1, plotted in corrected geomagnetic latitude and magnetic local time. The density of cross-hatching is representative of the brightness of the auroras. The categories of extremely high latitude auroras which the cartoons represent are (a) $P(1)$, (b) $P(2)$, (c) $P(3)$, (d) $P(4)$.

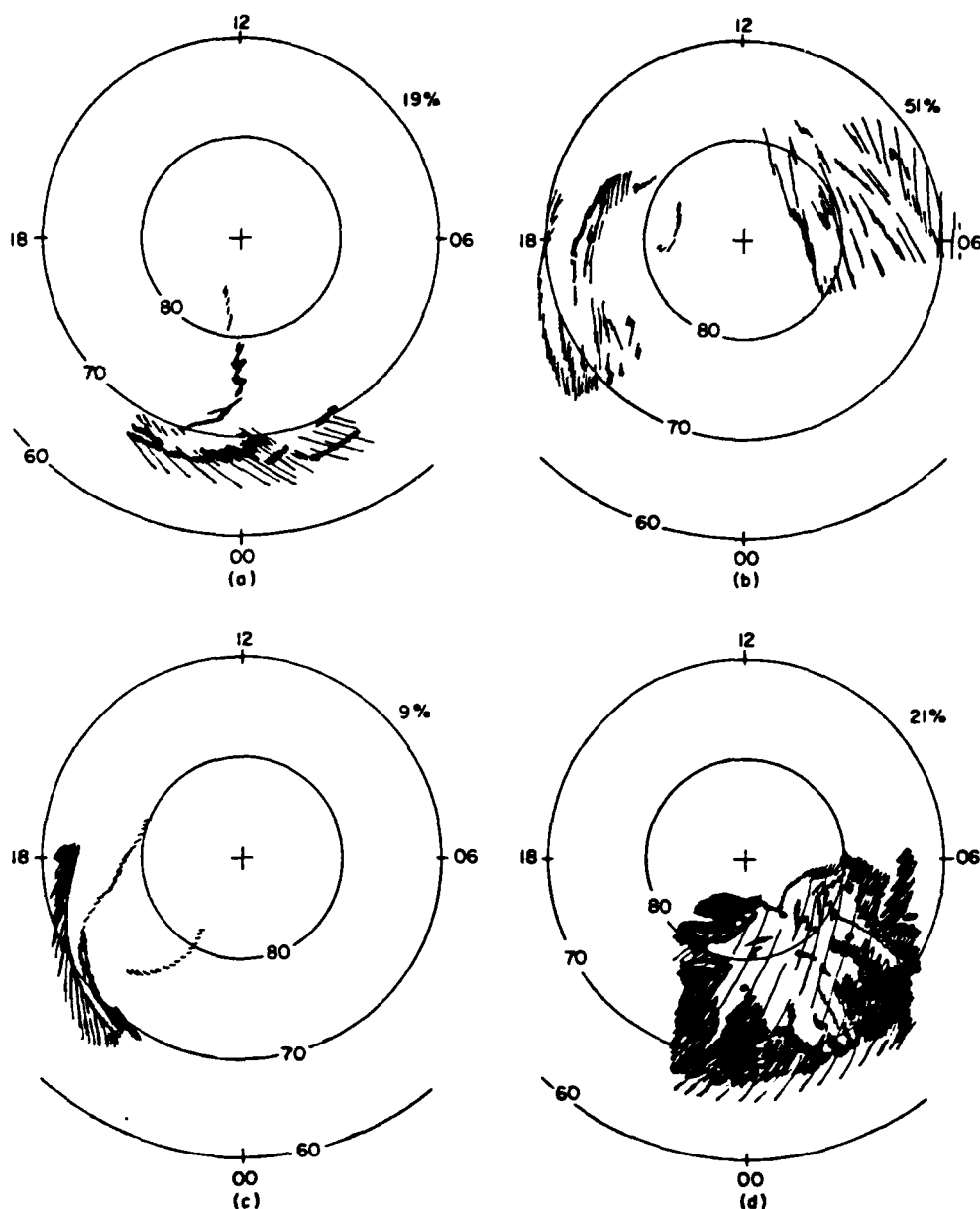greater than 80° at least 24% of the time when $Kp = 3$, and 23% of the time for $Kp = 4$. In conclusion, this sample shows that extremely high latitude auroras occurred when world-wide magnetic activity (indicated by the Kp index) was moderate. The activity was somewhat less for single arcs across the central cap, and greater for oval expansion into the cap in the midnight sector.

Dependence on AE. Figure 4 shows the distribution of cases of extremely high latitude auroras for 50-nT AE bins when separated by category. Comparing categories it can be seen that:

1. All cases for $AE > 500$ nT occur in categories $P(2)$ and $P(4)$, with by far the greater number occurring for $P(4)$: midnight oval expansions.

2. The midnight oval auroras, $P(4)$, are much more broadly distributed over variations in AE than are the other categories; the peak distribution for this category is considerably higher (300–400 nT) than for the other three categories.

3. The three categories $P(1)$, $P(2)$, and $P(3)$ have distributions with peak values in the 0- to 150-nT range.

4. $P(1)$ and $P(3)$ occur, on the whole at less active times than the morning auroras, $P(2)$. These are primarily times of $AE < 250$ nT. The two distributions are not dissimilar.

5. For $P(1)$ a significant portion of the distribution (~27%) occurs for AE between 0 and 50 nT. The reverse is also true: the majority of cap auroras at the lowest AE values fall within category $P(1)$.
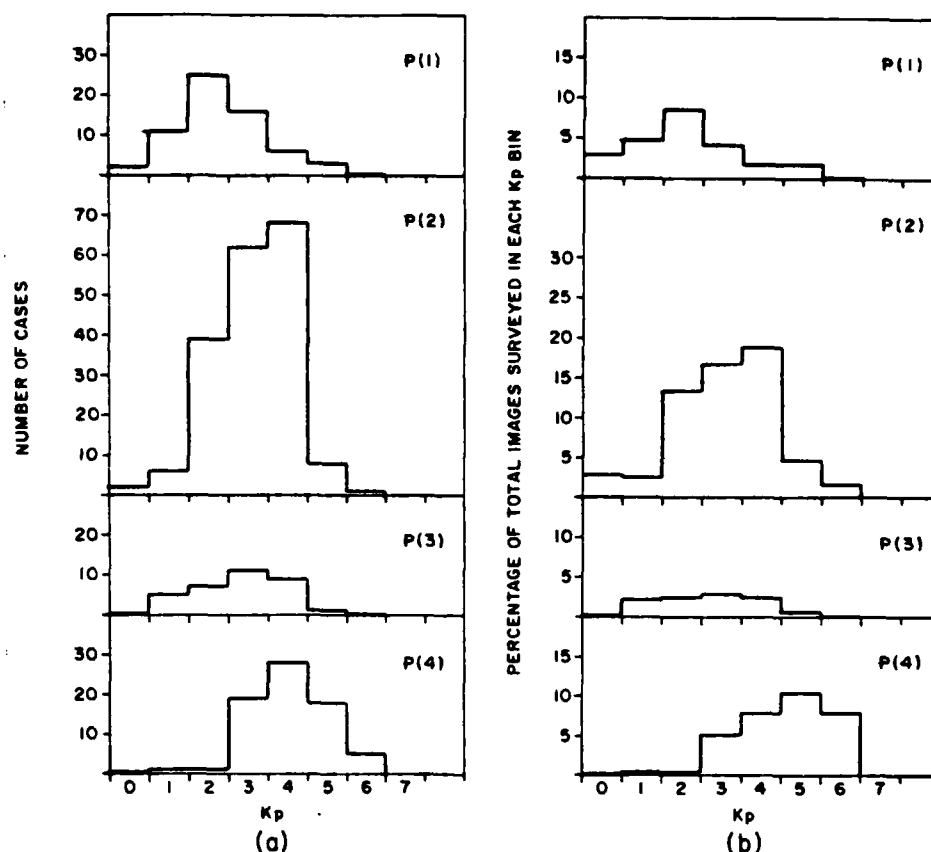
141

Fig. 3. (a) The distribution of extremely high latitude auroras, by category, according to Kp. (b) The distribution in Kp of the percentage of cases of extremely high latitude auroras in each Kp bin with respect to the number of images in the total survey for that bin. The distribution is separated by category.

Dependence on Dst. The dependence of the occurrence of extremely high latitude auroras on *Dst* did not appear to have much additional significance and is not shown here. (Plots of the distribution may be found in the work of *Gussenhoven* [1977].) The occurrence frequency of *Dst* values for the periods surveyed decreases in an exponential manner from slightly positive values (+10 nT) to negative values up to −100 nT, with approximately 60% of the time having values between +10 and −20 nT. The distribution of the entire class of extremely high latitude auroras over *Dst* shows somewhat more than 60% of the cases to occur between 0 and −30 nT, or shifted from the total distribution by −10 nT to higher ring current activity. In addition, very few cases (9%) occurred for *Dst* > 0. As would be expected from the *Kp* and *AE* distributions according to category, the sun-aligned arcs and evening auroras in categories *P*(1) and *P*(3) have distributions shifted toward lower negative *Dst* values than those of categories *P*(2) and *P*(4). Of the latter, the midnight oval auroras, *P*(4), have greater association with higher ring current values, although both midnight and morning auroras occurred for *Dst* values to −70 nT.

RELATIONSHIP TO SOLAR WIND CONDITIONS

A distribution of cases of extremely high latitude auroras was made for each of the following solar wind parameters: velocity, density, temperature, the magnitude of the interplanetary magnetic field (IMF) and each of its components. For all parameters the value assigned to the DMSP image is
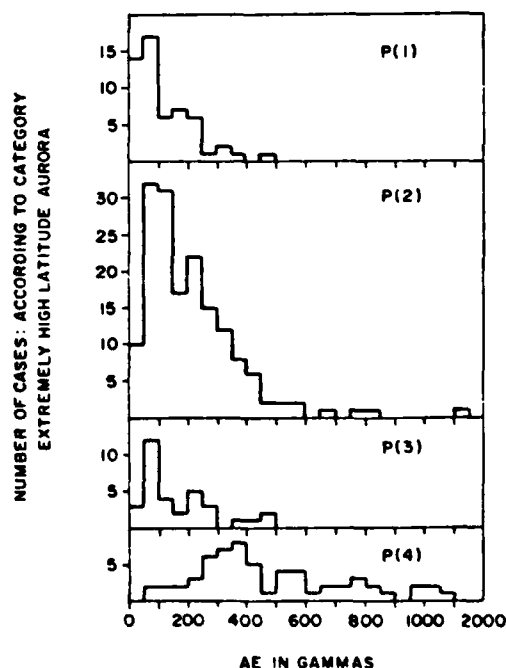

Fig. 4. The distribution by category of extremely high latitude auroras according to *AE* in 50-nT bins.
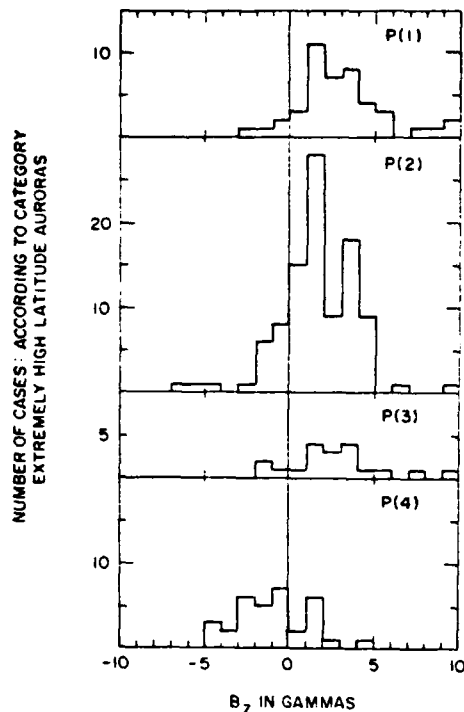
142

Fig. 5. The distribution of extremely high latitude auroras, by category, according to B_z.

Such is not the case for B_x and B_y whose sign variations are on the same order as the time intervals of missing data. Further, the number of sectors in the six months surveyed is, itself, small. For the two winters when both DMSP images and interplanetary magnetic field measurements were available, roughly 64% of the surveyable data occurred during toward sectors (as determined by the sign of B_x). Or, there are twice as many surveyable images in toward sectors as in away sectors.

The distribution of the total number of cases of extremely high latitude auroras in B_x and B_y were found to be nearly equal for positive and negative values when the number of toward sector cases were given half the weight of the away sectors. A slight bias exists for occurrence in toward sectors (53%); a bias to which it is difficult to attach much significance.

In looking at the dependence of extremely high latitude auroras upon the direction of the interplanetary magnetic field another approach is taken, one that appears to have growing success in ordering high-latitude magnetospheric data. The cases of auroras are distributed for each category according to the direction of the IMF in the y-z plane. The distribution is made in 10° bins.

Figure 6 shows the four distributions for given categories.

the hourly average (or occasionally, for velocity, temperature and density, 3-hourly average) as listed in the work of *King* [1977], taken in the hourly interval before the arc occurred. The coordinate system used for the magnetic field components is solar magnetospheric.

The interplanetary magnetic field. The occurrence of auroras in the polar cap is sensitive to the direction of the interplanetary magnetic field. Figure 5 shows the distribution of extremely high latitude auroras according to B_z, the north-south component, for each category. All categories except P(4) show very strong preference for occurrence during times of B_z northward (positive). For P(1) and P(3), 91% and 84% of the cases occur for positive B_z, respectively. The distribution for morning arcs, P(2), shows a significant number of occurrences for negative B_z (18%); however, nearly all of these occur for $B_z > -3$ nT. The midnight oval auroras, in P(4), show the opposite trend: 70% of the distribution occurs for B_z southward.

In examining the data set for variations in B_x and B_y, or more generally for toward (B_x positive, B_y negative) and away (opposite signs) sectors, it was quite evident that the sample w...

time interv... ... ... dominated by sector structures which persist for days. Thus in the survey of DMSP images over two winter periods, it could be anticipated that near-equal cases for B_z positive and B_z negative would occur, the scale of the variation being much smaller than the time surveyed. In addition, there are large gaps in the interplanetary magnetic field data as the measuring satellite enters and remains in the magnetosphere. This too should have no effect in biasing the B_z sample, since again, the missing data occur for time intervals on the order of days.
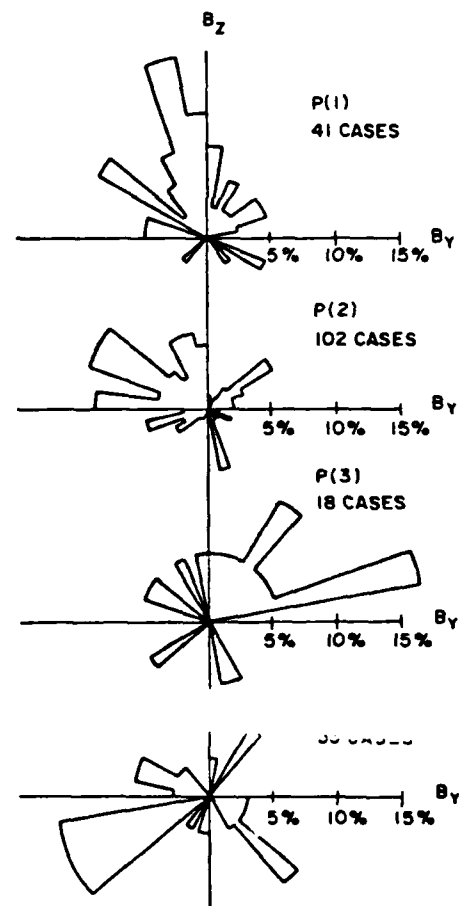

Fig. 6. The distribution of extremely high latitude auroras, by category, according to the direction of the interplanetary magnetic field in the y-z plane. The percentage of the total in each category is plotted in bin widths of 10°.

Here are plotted the percentage of the total number of cases within a given category, instead of the actual number plotted in Figure 5. The number of cases in each category is listed. In comparing categories $P(1)$, $P(2)$, and $P(3)$, there is a definite trend to rotate the major portion of the distribution from positive B_z and negative B_y for morning aurora to positive B_z and positive B_y for evening aurora, with single arcs occurring when the projected B is pointing northward (for small B_y).

Because the hourly averaged values of the components of the magnetic field are often only a rough indicator of the state of the magnetic field, a selection was made of the cases of extremely high latitude auroras for which B_y and B_z stayed in the same quadrant for 2 hours before the time of the DMSP image. If the effect of the direction of the IMF in the y-z plane is real, it should be more pronounced for a magnetosphere subjected a longer time to the same condition. The distributions according to category are shown in Figure 7. Again, the percentage of the total is plotted, this time for each 30° interval in the direction of B projected on the y-z plane. The number of cases in each catgory is listed. The bin size is increased because the sample size is so greatly reduced. The distributions show the same trend found above: extremely high latitude auroras tend to occur in local time preferentially with the direction of the interplanetary magnetic field in the y-z plane. Assuming B_z positive, they occur in the morning for B_y negative, (or for toward sectors) and in the evening for B_y positive (away sectors).

The solar wind velocity. In examining the occurrence of

Fig. 8. The distribution of extremely high latitude auroras, by category, according to the solar wind speed.

cap auroras in relation to other solar wind parameters: number density, velocity, temperature, and magnetic field magnitude; only correlation with velocity (v_{sw}) appeared to have obvious significance. Figure 8 shows the distribution in v_{sw} for each category of cap aurora. Each distribution has a maximum for v_{sw} between 650 and 750 km/s, that is, at very high solar wind velocities. With the exception of the first category, $P(1)$, the major part of each distribution occurs for v_{sw} greater than 550 km/s; 87% in $P(4)$ and 74% in $P(2)$. The single arc category, $P(1)$, has a bimodal structure, with peaks at 450–500 km/s and at 650–700 km/s.

The solar wind variation for 1974, and to a lesser extent for the winter months 1972–1973, had developed, with the approach of solar minimum, into a stable structure with two high speed streams per solar rotation. Gosling et al. [1976] show that the statistical distribution of v_{sw} varies from one with a single peak near 400 km/s for years near solar maximum, to a broad distribution with a flat peak between 400 and 600 km/s and a high-speed (>650 km/s) tail, reflecting the high speed–low speed structure near solar minimum. The great majority of cap auroras in all categories are shown by Figure 8 to occur for velocities characteristic of high-speed streams, or for the faster portion of the low-speed streams (i.e., above 450 km/s). They do not show distributions characteristic of either type of solar wind speed distribution, or of a combination of the two. Therefore it can be concluded that extremely high latitude auroras occur prefer-
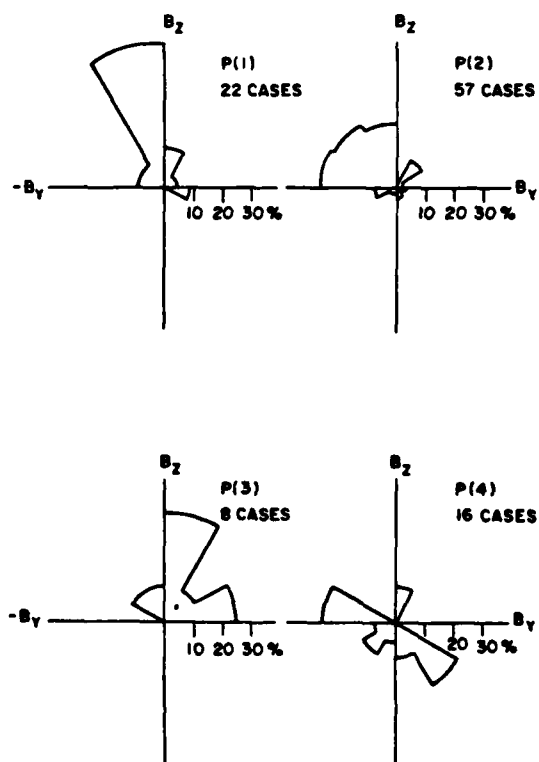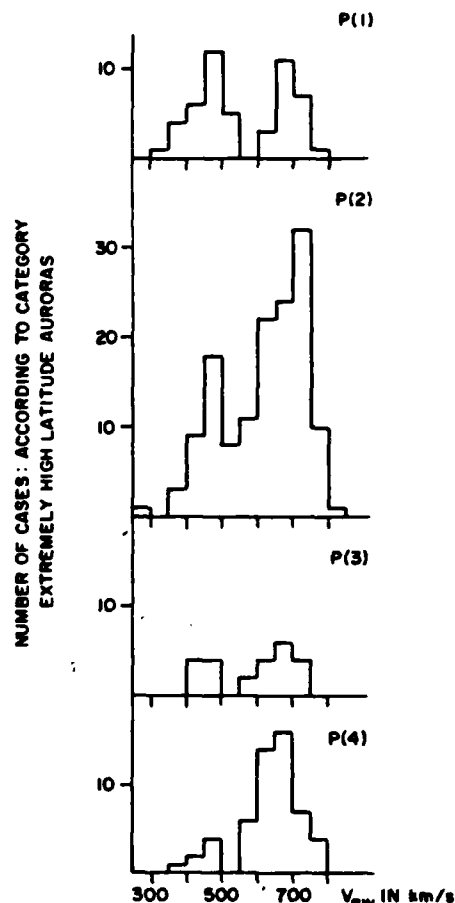

Fig. 7. Same as Figure 6. except that the cases of extremely high latitude auroras chosen for these plots occurred during times when the IMF was in the same quadrant in the y-z plane for the 2-hour period prior to the occurrence of auroras (as determined by the hourly averaged values).
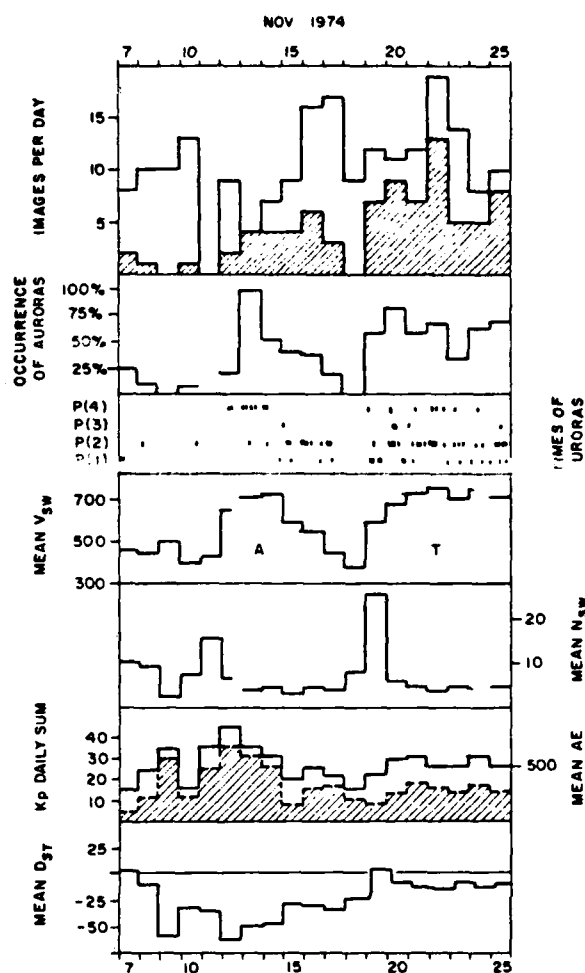
NOV 1974

Fig. 9. A composite of the occurrence of extremely high latitude auroras and the pertinent magnetospheric and solar wind parameters for November 1974. The top panel shows the number of DMSP images per day that gave good cap coverage (unshaded histogram) and the number that showed extremely high latitude auroras in all categories (shaded histogram). The second panel shows the percentage occurrence of auroras (the ratio of the values in the top panel times 100). The third panel marks the times auroras occurred in each category. The fourth panel gives the daily averages of the hourly solar wind speed. and the fifth panel gives the daily averages of the solar wind density. The two bottom panels give the daily sum of Kp (unshaded), the average of hourly values of AE (shaded), and Dst.

entially for high v_{sw}. It should be noted that since a large part of this study is made up of cases of cap auroras occurring in the winter of 1974–1975, the apparent high frequency of occurrence of auroras at extremely high latitudes may be characteristic only of periods near solar minimum.

To more clearly show the dependence of the occurrence of all types of auroras on v_{sw}. a summary of the occurrence of cap auroras and the variation of average values of magnetic indices and solar wind parameters for November 1974 is shown in Figure 9. In the top panel the unshaded histogram gives the number of DMSP images for each day on which the correct latitudes and proper gains appear so that polar cap arcs could be seen if they had been above the radiometer threshold. The brightness of the moon at the beginning and end of the month obscured all auroras. The shaded histogram in the same panel gives the number of DMSP images

that do show extremely high latitude auroras. All categories are included. The percentage of cases that occur for the number possible is given in the second panel. The third panel shows how the number of extremely high latitude auroras (the shaded histogram in the top panel) is distributed by category. The fourth panel shows the daily average of the hourly values of v_{sw}. The two high-speed streams are apparent: the one that occurred from November 12 to 16 was in an away sector; the second, from November 19 to 25, was in a toward sector. The three bottom panels show: the average solar wind density, n_{sw}; the sum of Kp (solid line) and the daily average of AE (dashed line); the daily average of Dst. Finaly, B_z can be characterized as having been essentially positive on November 7, 8; negative from November 9 to 12; unmeasured from November 13 to 20; and positive from November 20 to 25.

The percentage occurrence of cap auroras (the second panel) and that of v_{sw} are strikingly similar. Few cap auroras occurred in the low-speed stream on November 7, 8, even though B_z had large positive values for most of the period. The beginning of the magnetic storm on November 9 was coincident with a large negative excursion of B_z and a sector change. The magnetic activity continued into and maximized in a high-speed stream, still in the away magnetic sector. In the first high-speed stream, with high magnetic activity on the leading edge. the extremely high latitude auroras were mainly midnight oval expansions into the cap. As the magnetic activity and the velocity decreased, morning auroras and single arcs were found in the cap. The occurrence of extremely high latitude auroras dropped to zero as v_{sw} reached a minimum between the two high-speed streams. In the second high-speed stream. in a toward sector with many positive excursions of B_z, auroras of all types were found continuously in the cap.

The mid-latitude magnetic activity, measured by Kp, also followed v_{sw}, although to a lesser extent than the percentage of arcs in the cap. Of the two sectors, the greater activity occurred during the away sector, when B_z was predominantly negative. The lopsided profiles of AE and Dst also reflect greater auroral activity and ring current activity in the away sector.

SUMMARY AND DISCUSSION

One category of extremely high latitude auroras is distinctly different from the rest: the oval auroras that expand poleward in the midnight sector, $P(4)$. These occur for conditions that are characteristic of substorms: moderate to high Kp, and AE; B_z southward and v_{sw} large. Dependence, if any, on B_y is undetermined. At this point it is not possible to identify the relationship of this class of active auroras to the entire spectrum of substorm events. It is quite clear, however, that the poleward boundary of the oval can have very large fluctuations even in the midnight sector and for large magnetic activity.

Consider the three remaining categories of extremely high latitude auroras: $P(1)$, $P(2)$, and $P(3)$, differentiated primarily by their dawn-dusk location. All three have maximum occurrence for similar magnetospheric and solar wind conditions. These are: (1) the interplanetary magnetic field has a northward component; (2) the solar wind speed is high; (3) moderate mid-latitude activity, as measured by Kp; (4) low auroral zone magnetic activity, as measured by AE. The categories show the following difference in occurrence: (5)

arcs are preferentially located in the cap by the sign of the y component of the interplanetary magnetic field: (6) the occurrence of extremely high altitude auroras in the morning sector, type P(2), greatly exceeds occurrence in other sectors.

There is good agreement with previous studies in conditions 1 and 4. Berkey et al. [1976] and Ismail et al. [1977] found that all cases of sun-aligned polar cap arcs which they selected from the ISIS data for study (approximately 50 cases) occurred for B_z northward (or undetermined). The criterion used to select cases in the study presented here is more inclusive than theirs and gives a sample similar in more respects to that of Lassen and Danielsen [1978]. The latter showed that it is possible for arcs in the morning sector to reach latitudes greater than 80° for all values of B_z to -7 nT, although the arc density plots are increasingly denser for increasing values of B_z. Here, as well, the great majority of cases of extremely high latitude auroras in the first three categories occurred for B_z positive, but there is a substantial scatter into negative values of B_z. The scatter is prevalent for morning arcs (corresponding to the morning arcs of Lassen and Danielsen) but also exists for arcs across the central cap (corresponding to the arcs in the studies of the ISIS data) and for evening arcs.

The finding that extremely high latitude auroras in these categories occurred principally for low AE is consistent with the generally held notion that occurrence of polar cap auroras anticorrelates with magnetic activity [Davis, 1963; Ismail et al., 1977]. The finding that peak occurrence obtains for moderate Kp is not consistent with this notion. A strong correlation between AE and negative values of B_z was first shown by Arnoldy [1971] and Foster et al. [1971] and has been extended to include effects of the solar wind speed, v_{sw}, and other components of B [see Akasofu, 1980; Holzer and Slavin, 1978, and references therein]. The relationship between the two is most easily explained as the consequence of energy transfer to high latitudes by means of magnetic merging [Kan et al., 1980]. For B_z positive the amount of energy transferred by this process is small, possibly zero. The dependence of energy transfer on the entire range of B_z has been described in terms of a half-wave rectifier [Burton et al., 1975; Crooker, 1979 a, b]. Thus conditions 1 and 4 are not independent. However, it cannot be assumed that Kp and AE vary in the same manner. The differences in their variation were convincingly shown by Maezawa [1978]. He showed that the ratios of the subauroral magnetic activity index, A_m, to the auroral zone activity indices, AU and AL (comparable to the ratio of Kp and AE) increase as B_z becomes more strongly northward. He interpreted the ratio increase to the fading away of auroral zone activity (decrease of AE) with increasing B, so that lesser subauroral effects become apparent.

Even more pertinent to the study of high-latitude arcs is Maezawa's clear demonstration that all magnetic indices (A_m, AL, AU) increase with the solar wind speed, although not in the same manner. Thus the preferred conditions for extremely high latitude auroras, 2 and 3, namely, high v_{sw} and moderate Kp, are also causally linked.

The third solar wind variable that is at least statistically related to the process of arc formation at extremely high latitudes, is B_y. When the solar wind magnetic field direction was maintained (in the average sense) for at least 2 hours it was found that arcs occurred preferentially in the morning (evening) sector for B_y negative (positive). Lassen and Danielsen [1978] presented mass plots of arcs (their Figure 3) which show that for B_z positive large concentrations of arcs occur in the central cap for all separations in B_y. Even though arcs occur on both sides of the cap for either sign of B_y (as is also seen to be the case in the data presented here), they extend in a concentrated fashion through to the oval aligned arcs on the morning side for B_y negative but have a well-defined gap in this region for B_y positive. More recently, Lassen [1979] has related his auroral arc patterns in the cap to regions of sunward convection measured [Burke et al., 1979] or predicted by antiparallel field line merging [Crooker, 1979 a, b] during conditions of B_z northward. The preferred location of arcs in the sample presented here is also in the cap region where sunward convection would be predicted.

In conclusion, this statistical study indicates that energy transfer mechanisms and auroral arc processes that are pertinent to extremely high latitude auroral arc formation must depend on B_z, B_y and v_{sw} as primary independent variables.

REFERENCES

Akasofu, S.-I., The dynamical morphology of the aurora polaris, *J. Geophys. Res., 68.* 1667, 1963.

Akasofu, S.-I., *Polar and Magnetospheric Substorms,* Springer, New York, 1968.

Akasofu, S.-I., Midday auroras and polar cap auroras, *Geofys. Publ., 29,* 73, 1972.

Akasofu, S.-I., A study of auroral displays photographed from the DMSP-2 satellite and from the Alaska meridian chain of stations, *Space Sci. Rev., 16,* 617, 1974.

Akasofu, S.-I., The solar wind–magnetosphere energy coupling and magnetospheric disturbances, *Planet. Space Sci., 28,* 495, 1980.

Akasofu, S.-I., D. S. Kimball, J. Buchau, and R. W. Cowell, Alignment of auroral arcs, *J. Geophys. Res., 77,* 4233, 1972.

Arnoldy, R. L., Signature in the interplanetary medium for substorms, *J. Geophys. Res., 76,* 5189, 1971.

Berkey, F. T., L. L. Cogger, S. Ismail, and Y. Kamide, Evidence for a correlation between sun-aligned arcs and the interplanetary magnetic field direction, *Geophys. Res. Lett., 3,* 145, 1976.

Burke, W. J., M. C. Kelley, R. C. Sagalyn, M. Smiddy, and S. T. [...] etary magnetic field, *Geophys. Res. Lett., 6,* 21, 1979.

Burke, W. J., M. S. Gussenhoven, M. C. Kelley, D. A. Hardy, and F. J. Rich, Electric and magnetic field characteristics of discrete arcs in the polar cap, *J. Geophys. Res.,* this issue.

Burton, R. K., R. L. McPherron, and C. T. Russell, An empirical relationship between interplanetary conditions and Dst, *J. Geophys. Res., 80,* 4204, 1975.

Carovillano, R. L., Unified model of auroral substorm development, *Rep. AFRCL-TR-0558,* Air Force Cambridge Res. Lab., Bedford, Mass., Aug. 31, 1975.

Crooker, N. U., Antiparallel merging, the half-wave rectifier response of the magnetosphere, and convection, in *Proceedings of the Magnetospheric Boundary Layers Conference, Rep. SP-148,* p. 343, European Space Agency, Paris, 1979a.

Crooker, N. U., Dayside merging and cusp geometry, *J. Geophys. Res., 84*, 951, 1979b.

Davis, T. N., The morphology of the aurora, *J. Geophys. Res., 65*, 3497, 1960.

Davis, T. N., The morphology of the auroral displays of 1957–1958, 1, Statistical analyses of Alaska data, *J. Geophys. Res., 67*, 59, 1962a.

Davis, T. N., The morphology of the auroral displays of 1957–1958, 2, detailed analyses of Alaska data and analyses of high-latitude data, *J. Geophys. Res., 67*, 75, 1962b.

Davis, T. N., Negative correlation between polar cap visual auroral and magnetic activity, *J. Geophys. Res., 68*, 4447, 1963.

Denholm, J. V., Some auroral observations inside the southern auroral zone, *J. Geophys. Res., 66*, 2105, 1961.

Denholm, J. V., and F. R. Bond, Orientation of polar auroras, *Aust. J. Phys., 14*, 193, 1961.

Eather, R. H., DMSP calibration, *J. Geophys. Res., 84*, 4134, 1979.

Eather, R. H., and S.-I. Akasofu, Characteristics of polar cap auroras, *J. Geophys. Res., 74*, 4794, 1969.

Foster, J. C., D. H. Fairfield, K. W. Ogilvie, and T. J. Rosenberg, Relationship of interplanetary parameters and occurrence of magnetospheric substorms, *J. Geophys. Res., 76*, 6971, 1971.

Gosling, J. T., J. R. Asbridge, S. J. Bame, and W. C. Feldman, Solar wind speed variations: 1962–1974, *J. Geophys. Res., 81*, 5061, 1976.

Gussenhoven, M. S., Study of characteristics of polar cap auroras in DMSP images from 1972–1976, *Final Rep. F49620-77-C-0050*, Air Force Office of Sci. Res., Washington, D.C., 1977.

Gustaffson, G., On the orientation of auroral arcs, *Planet. Space Sci., 15*, 277, 1967.

Hardy, D. A., W. J. Burke, and M. S. Gussenhoven, DMSP optical and electron measurements in the vicinity of polar cap arcs, *J. Geophys. Res.*, this issue.

Holzer, R. E., and J. A. Slavin, Magnetic flux transfer associated with expansions and contractions of the dayside magnetosphere, *J. Geophys. Res., 83*, 3831, 1978.

Ismail, S., S. S. Wallis, and L. L. Cogger, Characteristics of polar cap sun-aligned arcs, *J. Geophys. Res., 82*, 4741, 1977.

Kan, J. R., L. C. Lee, and S.-I. Akasofu, The energy coupling function and the power generated by the solar wind–magnetosphere dynamo, *Planet. Space Sci., 28*, 823, 1980.

King, J. H., *Interplanetary Medium Data Book*, National Space Science Data Center, NASA Goddard Space Flight Center, Greenbelt, Md., Sept. 1977.

Lassen, K., Polar cap emissions, in *Proceedings of Aurora and Airglow Conferences*, edited by B. M. McCormac, Reinhold, As, Norway, 1968.

Lassen, K., On the classification of high latitude auroras, *Geophys. Pap. R-28*, Dan. Meteorol. Inst., Copenhagen, 1972.

Lassen, K., Orientation of auroral arcs and precipitation pattern of auroral particles, *Geophys. Pap. R-33*, Dan. Meteorol. Inst., Copenhagen, 1973.

Lassen, K., The quiet-time pattern of auroral arcs as a consequence of magnetospheric convection, *Geophys. Res. Lett., 6*, 777, 1979.

Lassen, K., and C. Danielsen, Quiet time pattern of auroral arcs for different directions of the interplanetary magnetic field in the y-z plane, *J. Geophys. Res., 83*, 5277, 1978.

Maezawa, K., Dependence of geomagnetic activity on solar wind parameters: A statistical approach, *Solar Terr. Environ. Res. Jpn., 2*, 103, 1978.

Meng, C.-I., Polar cap arcs and the plasma sheet, *Geophys. Res. Lett., 8*, 273, 1981.

Meng, C.-I., and S.-I. Akasofu, The relation between the polar cap auroral arc and the auroral oval arc, *J. Geophys. Res., 81*, 4004, 1976.

Pike, C. P. (Ed.), Defense Meteorological Satellite Program auroral-ionospheric interpretation guide, *Rep. AFCRL-TR-75-0191, Air Force Surv. in Geophys. 306*, Air Force Cambridge Res. Lab., Bedford, Mass., 1975.

Pike, C. P., and J. A. Whalen, Satellite observations of auroral substorms, *J. Geophys. Res., 79*, 985, 1974.

Rogers, E. H., D. F. Nelson, and R. C. Savage, Auroral photography from a satellite, *Science, 183*, 951, 1974.

Romick, G. J., and N. B. Brown, Midday auroral observations in the oval, cusp region, and polar cap, *J. Geophys. Res., 76*, 8420, 1971.

Sheehan, R. E., and R. L. Carovillano, Characteristics of the equatorward auroral boundary near midnight determined from DMSP images, *J. Geophys. Res., 83*, 4749, 1978.

Snyder, A. L., S.-I. Akasofu, and T. N. Davis, Auroral substorms observed from above the north polar region by a satellite, *J. Geophys. Res., 79*, 1393, 1974.

Whalen, B. A., J. R. Miller, and I. B. McDiarmid, Sounding rocket observations of particle precipitation in a polar cap electron aurora, *J. Geophys. Res., 76*, 6847, 1971.

147

DMSP Optical and Electron Measurements in the Vicinity of Polar Cap Arcs

D. A. HARDY AND W. J. BURKE

Air Force Geophysics Laboratory, Hanscom Air Force Base, Massachusetts 01731

M. S. GUSSENHOVEN

Boston College, Chestnut Hill, Massachusetts 02167

We have completed an extensive analysis of the electron and optical data from the DMSP satellites for an extended period of polar cap arc occurrences on December 12, 1977. The polar cap arcs are observed in three distinct intervals in a period of quieting after a time of intense substorm activity. Each interval occurs when the IMF B_y is less than 0 and follows a northward turning of the IMF B_z. The intervals are separated by periods of southward B_z and weak substorm activity during which no enhanced precipitation is seen in the polar cap. The polar cap arcs persist for periods of more than an hour with only gradual variation in position and intensity. At the time of our study the highest-energy flux and average energy for electrons precipitating into the polar cap are seen in the northern polar cap. The observation of polar cap arcs is associated with the admittance of large and variable fluxes of low-energy electrons into a major portion of both the northern and southern hemisphere polar caps. These fluxes fall into the following categories: First, nearly Maxwellian distributions of electrons with temperatures between 50 eV and 200 eV and number densities varying from $0.03/cm^3$ to $4/cm^3$. The highest densities are found at the poleward boundary of the diffuse aurorae and near the visible polar cap arcs. The lowest densities are associated with the polar rain. Second, distributions of electrons peaked between 50 eV and 200 eV. These distributions result from acceleration of the cold Maxwellian distribution through a potential of 50 to 200 V without any heating of the electrons. Third, distributions of electrons displaying two populations: an intense low-energy component with a temperature of ~ 20 eV and a much weaker high-energy component with a temperature of 180 eV. We interpret such distributions as evidence of direct admittance of magnetosheath electrons into the polar cap. Fourth, distributions of electrons peaked at ~ 1 keV. These distributions produce the visible arcs. They result from the acceleration of a two-component electron population with temperatures of 100 and 350 eV through a potential drop of ~ 750 V.

INTRODUCTION

For a variety of reasons, discrete auroral arcs in the polar cap have been studied far less extensively than their counterparts in the auroral oval. Most of the currently existing information concerning polar cap arcs comes from ground-based [*Davis*, 1960; *Lassen and Danielsen*, 1978], aircraft [*Eather and Akasofu*, 1969], and satellite-borne [*Berkey et al.*, 1976; *Ismail et al.*, 1977; *Meng and Akasofu*, 1976; *Gussenhoven*, this issue] optical instrumentation. In recent years, this information has been supplemented by direct measurements of electrons bombarding the polar cap [*Burch*, 1968; *Hoffman and Evans*, 1968; *Winningham and Heikkila*, 1974; *Foster and Burrows*, 1976; *Burch et al.*, 1979]. Measurements by *Whalen et al.* [1971], *Meng and Akasofu* [1976], and *Ismail et al.* [1977] include simultaneous observations of electron fluxes into and visible emissions from polar cap arcs.

Arcs in the polar cap are generally aligned close to the sunward-antisunward direction but occasionally deviate from this direction in the midnight sector to follow the boundary of the auroral oval [*Meng and Akasofu*, 1976]. They tend to appear during periods of magnetic quieting [*Starkov and Fel'dshteyn*, 1971; *Gussenhoven*, this issue] when the IMF has a northward component [*Berkey et al.*, 1976]. A northward IMF B_z does not appear to be a strictly necessary condition [*Lassen and Danielsen*, 1978] and certainly is not a sufficient one. Although the most dramatic example is the single, sun-aligned arc stretching from noon toward midnight, polar cap arcs are usually multiple and occur twice as often on the dawn side as on the dusk side of the polar cap [*Ismail et al.*, 1977]. Recently, *Meng* [1981a] has cautioned that many sun-aligned arcs at high latitudes may really be auroral oval rather than polar cap arcs.

The high intensity ratios of 6300 $\mathring{A}$/4278 $\mathring{A}$ [*Eather and Akasofu*, 1969] and 5777 $\mathring{A}$/3914 $\mathring{A}$ [*Ismail et al.*, 1977] emissions indicate that electrons with typical energies ≤ 1 keV are the sources of visible polar cap arcs. *Weber and Buchau* [1981] have identified a class of subvisual arcs at F layer altitudes which are caused by electrons with energies of a few hundred eV. Direct measurements of particles entering the quiet time polar cap reveal two types of precipitation: (1) a uniform flux of low-energy (~ 200 eV) electrons with energy fluxes of 10^{-2} to 10^{-3} erg/cm^2 s sr known as 'polar rain' and (2) narrow regions of more intense keV electron fluxes known as 'polar showers' [*Winningham and Heikkila*, 1974]. Polar shower electron fluxes are probably the same as the bursts of keV electrons measured by OGO 4 instrumentation [*Hoffman and Evans*, 1968]. Rocket measurements by *Whalen et al.* [1971] over a polar cap arc showed electron energy distributions similar to 'polar showers' and to those reported by Hoffman and Evans but they were isotropically distributed over the downcoming hemisphere. A recent study by *Burch et al.* [1979] has shown that during periods when the IMF is in an away ($B_y < 0$), northward ($B_z > 0$) sector, structured precipitation of electrons that have been accelerated along magnetic field lines

are found over the northern polar cap. Despite these accelerations the primary electrons did not appear to be highly field aligned in their pitch angle distributions. It is interesting that Eather and Akasofu could explain their spectroscopic measurements if the precipitating electrons were field aligned but not if they were isotropic over the downcoming hemisphere. Finally, we note that all experimenters with the capability of measuring proton fluxes above polar cap arcs report their absence.

In this and a companion paper [Burke et al., this issue] we present observations from the USAF DMSP and S3-2 satellites dealing with the detailed phenomenology of polar cap arcs and the geophysical context in which they occur. Both papers are in the forms of case studies. Simultaneous optical and electron flux measurements were taken during 12 passes of two DMSP satellites between 0400 and 2300 UT on December 12, 1977. This day was marked by alternating periods of weak substorm activity in the auroral oval and discrete arcs in the polar cap. The companion paper focuses on measurements of electric fields and Birkeland currents taken during several dawn-dusk passes of S3-2 over the polar cap when the IMF had a northward component. Due to the small geometric factor of the S3-2 spectrometer only the most intense polar cap fluxes were significantly above instrument background. No visible imagery is available. However, the spectral similarity of downcoming electrons to those reported here and elsewhere assure us that, at least in some instances, S3-2 passed over visible polar cap arcs.

In the following section, we describe the DMSP instrumentation and the mode of electron data presentation. The data observations section is divided into three parts: (1) the geomagnetic and IMF conditions on December 12, 1977; (2) the nearly simultaneous measurements of visual emissions from DMSP satellite near the moon-midnight (DMSP/F1) and the dawn-dusk (DMSP/F2) meridians; and (3) fluxes of electrons measured in 16 energy channels between 50 eV and 20 keV by a zenith-looking electron spectrometer. The discussion section contains a comparison of DMSP observations with previously reported results and some comments on possible source mechanisms for the observed electron fluxes.

INSTRUMENTATION AND DATA PRESENTATION

Each DMSP satellite is three-axis stabilized in a nearly sun synchronous, circular orbit, the orbital altitude is 840 km, the period is 101 min, and the nominal inclination is 98.75°. The orbital plane of DMSP F1 is approximately the noon-midnight meridian. The orbital plane of DMSP/F2 was centered near the 0700–1900 meridian at launch but was subject to a very slow precessional drift toward later local times. Owing to the offset between the earth's spin axis and magnetic axis, each orbit has significant diurnal and seasonal variations in the magnetic local time (MLT) and magnetic latitude frame, more than might be assumed from its restriction in geographic local time.

Each DMSP satellite carries a scanning radiometer, as the principal weather-monitoring experiment, which produces the now familiar DMSP images. The spectral characteristics of the radiometers are well documented [Eather, 1979] The time for a DMSP satellite to cross the auroral zone is approximately 10 min. Throughout December 12, the two satellites passed over the same polar region within about 15 min of each other. Therefore excellent coverage of the

auroral and polar cap region is obtained by forming a composite image from the two satellites. This technique is valid so long as the phenomena of interest change slowly on time scales longer than 10 min. The DMSP images do not reproduce well, especially during quiet times. Instead of reproducing the images taken on December 12, by the two satellites, the format we choose for presenting the optical data in the following section is the 'cartoon' form developed by Gussenhoven [this issue]. The cartoon representations are drawn in corrected geomagnetic latitude and MLT coordinates (Figure 2), giving a uniform orientation and allowing composite imaging on the same scale. In addition, the cartoons eliminate scan-induced geometric distortions and roughly compensate for instrument gain changes.

In addition, the DMSP/F2 satellite carries a precipitating electron detector. The detector consists of two curved plate electrostatic analyzers that measure the fluxes of electrons in 16 energy channels between 50 eV and 20 keV once per second. The aperture of the analyzers always faces vertically upward so that at auroral and polar cap latitudes precipitating rather than backscattered and/or trapped electrons are detected. One analyzer covers the energy range from 50 eV to 1 keV with a geometric factor of 4×10^{-4} cm^2 sr and a $\Delta E/E$ of 10%. The other analyzer covers the energy range from 1 keV to 20 keV with a geometric factor of 10^{-3} cm^2 sr and a $\Delta E/E$ of 12%. The large geometric factors insure that the flux level from the electrons in the polar rain is well above the detector's sensitivity. A detailed description of the detector is given by Hardy et al. [1979].

Electron data presented in the following section have three formats. In the first format (Figures 3–5), data are plotted as JTOT, the directional integral flux (cm^2 s sr)$^{-1}$ in the bottom panel; JETOT, the directional energy flux (keV/cm^2 s sr) in the middle panel; and EAVE, the average energy in keV in the top panel. The scale for EAVE is linear. These quantities are plotted as functions of universal time, corrected geomagnetic latitude and longitude, geographic latitude and longitude, and magnetic local time. A common feature in these plots is a hump observed in JTOT, JETOT, and EAVE equatorward of the auroral oval. Such humps are produced by penetrating radiation that directly stimulates channeltrons and as such do not represent real fluxes. The second format gives time sequences of electron differential number flux spectra (Figures 7, 10, 11, and 13). The third format shows the logarithm of the electron distribution function as a function of energy on a linear scale (Figures 8, 9, 12, and 14). It should be noted when comparing particle and optical data that conjugate electron fluxes can lag or lead substatellite imagery by up to 25 s because of tilt of magnetic fields lines [Meng et al., 1978].

AURORAL ACTIVITY AND SOLAR WIND CONDITIONS

Geomagnetic and IMF Conditions

The interplanetary and magnetospheric conditions prior to the time interval 0400–2300 UT on December 12 were as follows: From December 6 to 9 the IMF was in a 'toward' sector and the magnetospheric activity, as measured by Kp, was minimal. The ΣKp for these days was 9, 6-, 3, 6-. A change to an 'away' sector occurred in the last 2 hours on December 10. The transition was accompanied by an hourly average B_z of +11.3 nT, followed by 30 hours of large and persistent negative B_z values (up to -13.1 nT), on December 11 and into December 12. At the sector transition the solar
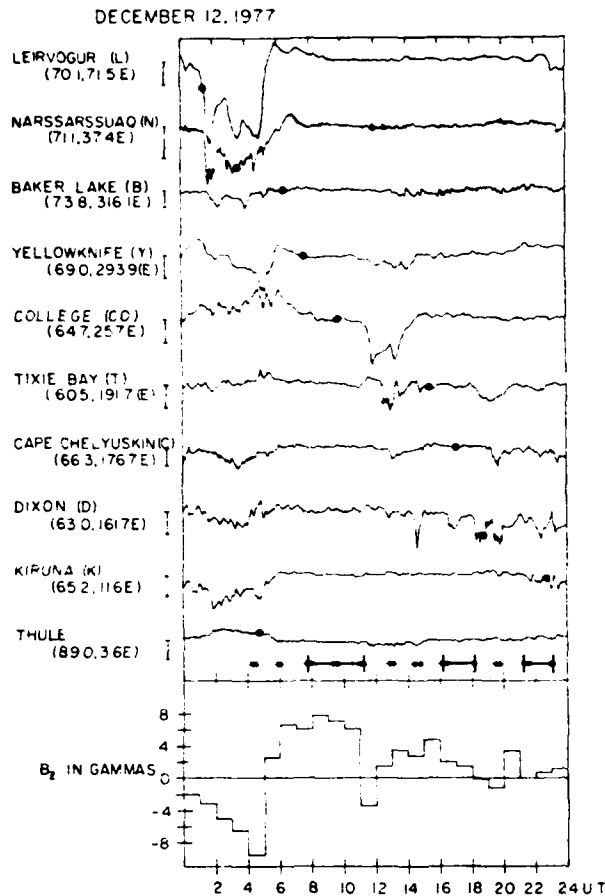
DECEMBER 12, 1977

Fig. 1. Survey of geomagnetic activity for December 12, 1977. The *H* component measured at 10 high-latitude stations is given as a function of universal time. The stations are arranged in magnetic longitude. The solid bar represents a 200-nT deflection in *H*. Asterisks below the Thule magnetogram give the times of DMSP north polar passes, with solid bars indicating times when polar cap arcs were present in the imagery. The bottom panel gives the hourly averaged value of IMF B_z.

wind speed rose from 310 to 480 km/s, after which it remained high. The density rose from 8 cm^{-3} to 45 cm^{-3} and fell back to an ~10 cm^{-3} level [*King*, 1979]. On December 11, $\Sigma Kp = 36-$. The period following this activity, on December 12, is presented here. The *Kp* values for December 12 were: 4+, 6−, 3, 3−, 2−, 2+, 3−. Throughout the period of interest on December 12 the solar wind speed was moderate (482 ± 8 km/s) and density was high (11.1 ± 2.2 cm^{-3}).

Magnetic activity as observed at selected high latitude stations on December 12 is given in Figure 1. The stations are ordered according to longitude with their magnetic latitudes and longitudes given in parentheses. The times at which the stations passed through midnight are marked by circles. Asterisks show the times of DMSP north polar passes; the bars indicate the presence of polar arcs. The hourly averages of B_z given in the bottom trace show that the IMF had a southward component for the first 5 hours of the day. This was accompanied by strong substorm activity at Leirvogur, Narssarssuaq, and Yellowknife. Southward turnings of the IMF between 1100 and 1200 UT and between 1800 and 2000 UT were also accompanied by substorms. From

the distribution of asterisks and bars, we note that polar cap arcs were observed only during periods of northward IMF. However, there were periods with $B_z > 0$ during which no polar cap arcs were discernible in the DMSP imagery.

DMSP Visual Imagery

Optical images taken by the F1 and F2 DMSP satellites over the northern hemisphere during the last 20 hours of December 12, 1977, are synopsized in Figures 2a and 2b. The coordinate system is corrected geomagnetic latitude versus magnetic local time. Portions of the F2 trajectories for which electron data are available are represented by solid lines. Tick marks along the trajectories denote electron precipitation boundaries. The universal times that the satellites passed closest to the magnetic pole, the solar geomagnetic YZ projections of the IMF, and the locations of the auroral zone magnetic stations (Figure 1) are provided for reference.

The sequence of events shown in Figure 2a is as follows:

~0400 UT. B_z is large and negative. The auroral oval near midnight extends from 62° to 78°; bright, discrete arcs border the polar cap which is empty. (Note that the particle boundaries show much greater dawn-dusk symmetry than might be deduced from visual features.)

~0600 UT. B_z has a small positive value. The diffuse oval boundary has moved poleward ~3° in the dawn-dusk meridian but remains essentially constant near midnight. The system of bright, discrete arcs has also moved considerably poleward, by almost 8° in the dusk sector. The empty polar cap has shrunk to about 12° diameter.

~0800 UT. B_z is northward; the B_y component is small. The diffuse auroral boundary near midnight and in the morning sector has moved only slightly poleward (~1°); the diffuse aurora has thinned considerably. An arc system, composed in the main of two long, structureless arcs, extends from near midnight, across the magnetic pole, and into the noon sector.

~0930 UT. B_z remains northward. The morning oval boundary has moved poleward by 1°, the midnight boundary equatorward by 1°. The double arc system persists across the cap with the following changes: it is more elongated and more closely approaches the midnight oval; it is more intense and highly structured. Additional sun-aligned arcs flank either side of the two-arc system.

~1100 UT. B_z remains northward. The auroral boundaries (visual only) remain the same. The polar cap arcs are shorter, weaker, and more uniformly distributed. They are no longer strictly sun-aligned. On the evening side they extend into the weak discrete arcs of the oval.

~1300 UT. B_z has an excursion southward from 1100 to 1200 UT and is weakly northward from 1200 to 1300 UT. The auroral boundaries move equatorward by ~1°-2°. There is auroral oval activity in the midnight sector: a poleward bulge and evidence of weak westward surge. The cap is empty.

Four major points summarize the first sequence of events: (1) polar cap activity occurs after B_z turns and remains northward; the time delay appears to be greater than 1 hour; (2) polar cap activity ceases when B_z has a southward excursion; (3) the evolution of the polar cap arc system is slow; features can persist for at least tens of minutes; and (4) the equatorward boundary of the visual auroral oval varies less than 3° through the process that produced the empty cap–polar arcs–empty cap dynamic.

DECEMBER 12, 1977

F1 1935
F2 1948

F1 2116
F2 2130

F1 2258
F2 2312

F1 1430
F2 1444

F1 1612
F2 1625

F2 1807

B

F1 0925
F2 0939

F1 1102
F2 1120

F1 1249
F2 1302

DECEMBER 12, 1977

F1 0419
F2 0434
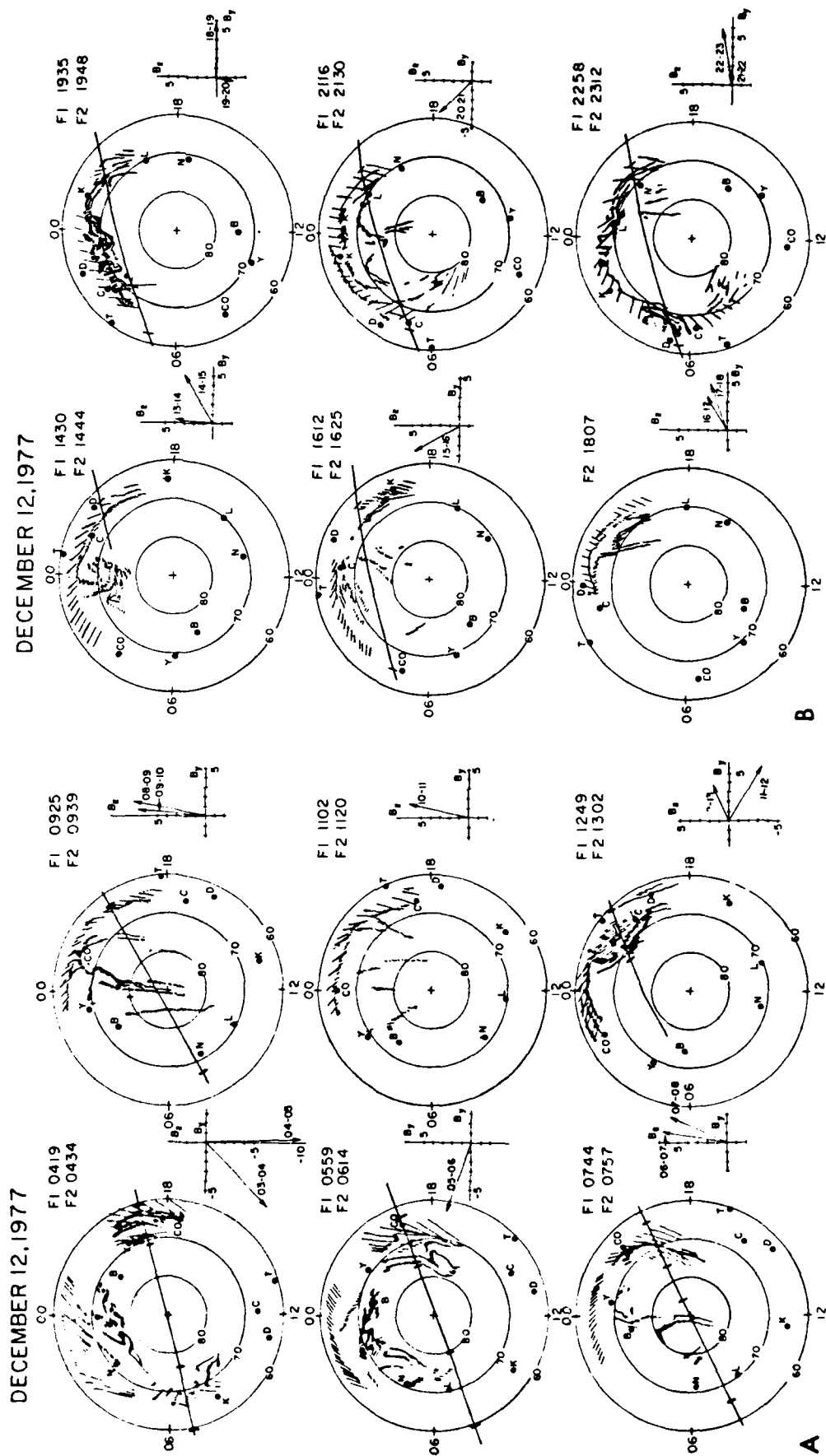
F1 0559
F2 0614

F1 0744
F2 0757

A

Fig. 2. Synoptic cartoons of DMSP F1 and F2 imagery in corrected geomagnetic latitude–magnetic local time coordinates (*a*) from 0400 to 1400 UT and (*b*) from 1400 to 2400 UT on December 12, 1977.

151

In Figure 2*b* the same type of process occurs two more times. B_z turns northward from 1200 to 1300 UT, and by 1600 UT arcs appear in the cap. (At 1800 UT only the F2 image is available, and there are no particle data; thus the information is limited.) B_z turns slightly negative from 1900 to 2000 UT and the cap is empty. A northward turning from 2000 to 2100 UT produces polar cap arcs by 2116 UT. These persist until the end of the day. The equatorward auroral boundary has a persistent poleward movement throughout this interval.

A comparison of the images with the magnetograms in Figure 1 shows that a high level of magnetic activity preceded the occurrence of polar cap arcs. The first and longest period of cap activity occurs when there is almost no magnetic activity at the auroral latitude stations. The second period follows a weak substorm from 1100 to 1400 UT. The third period occurs during persistent, weak ($\sim$100 nT) magnetic activity at Cape Chelyuskan, Dixon Island, and Kiruna. This activity results from electrojets in the vicinity of the intense, discrete arcs near midnight and in the morning sector, shown in Figure 2*b*.

ELECTRON OBSERVATIONS

In this section, attention is confined to measurements of precipitating electrons from the period prior to and during the first sequence of polar cap arcs, from $\sim$0500 to 1100 UT. At this time the electron data coverage is most complete and the satellite orbits pass very near to the magnetic poles. The section itself is divided into two parts. The first part deals with large-scale characteristics of electron precipitation. The second deals with detailed spectral characteristics from a single pass.

Large-Scale Characteristics

In Figure 3 we show the data from the south and north pole passes of DMSP/F2 prior to the observation of the polar cap arcs. The south pole pass, from 0513 to 0538 UT, occurs at the end of the large negative bay seen at Leirvogur and Narssarssuaq and during the hour in which the IMF turns strongly northward. The north pole pass from 0604 to 0629 UT occurs when the midnight magnetograms show no substorm activity and after the IMF has been northward for $\sim$1 hour. In both cases the equatorward boundary of the auroral oval is at low magnetic latitudes: $\sim$−61° and 63° on the evening side and $\sim$−57° and 59° on the morning side. The poleward edge of the oval is confined to geomagnetic latitudes below 80°. A contraction of the poleward boundary of the oval occurs between the southern and northern passes (refer also to Figure 2*a*). In the northern pass the poleward contraction is marked by the appearance of highly variable fluxes of electrons with average energies $\leqslant$1 keV. Within the polar cap, precipitation is nearly uniform polar rain.

Figure 4 shows four consecutive south pole and north pole passes of DMSP F2 during the first period of polar cap arc activity. No electron data are available for the $\sim$1120 UT pass shown in Figure 2*a*. The four passes show a clear and asymmetric contraction of the oval following the northward turning of the IMF. The equatorward boundary of the oval moves poleward by 10° on the morning side but only by $\sim$4° on the evening side.

There are five large-scale characteristics of polar cap electron precipitation evident in Figure 4 to which we direct attention:

1. Electrons with characteristics other than the polar

rain have access to magnetic latitudes up to the geomagnetic pole. In the present case, for both northern and southern hemispheres electrons with an integral flux exceeding 10^8 el/cm² s sr are observed up to the maximum magnetic latitude crossed by the satellite ($\sim$−86° and −88° for south pole passes and $\sim$90° and 87° for north pole passes). Indeed, in all four passes the distance along the satellite track during which the polar rain is observed is a small fraction of the distance between the equatorward boundaries of electron precipitation. The pattern of electron precipitation differs in one respect between northern and southern hemispheres. The extent over which the polar rain is observed is larger in the south pole than in the north pole.

2. Outside the regions of visible polar cap arcs the electrons observed at magnetic latitudes above $\sim$75° have average energies below 200 eV. Even for visible arcs the average energy of the associated electrons is only $\sim$1 keV. Only near the equatorward boundary of the oval does the average energy exceed 1 keV. The DMSP pictures show that this region of higher-energy electrons is associated with the discrete and diffuse visual forms within the normal location of the auroral oval.

3. The low-energy electrons in the polar cap exhibit large variations in intensity along the satellite track. Changes in the intergral flux of precipitating electrons by as much as a factor of 100 are observed on time scales of 5 s or less, corresponding to distance scales of $\leqslant$35 km. Whether such variations represent spatial or temporal effects cannot be determined from observations of a single satellite.

4. The low-energy electrons occupy a significant portion of the region above $\sim$70° geomagnetic latitude during the entire period in which polar cap arcs are observed, in this case 2 or more hours. This implies that the two phenomena are most likely related, i.e., that the presence of low-energy electrons at high latitudes is a necessary condition for the observation of polar cap arcs. It is also of note that once the pattern of low-energy electrons and polar cap arcs is established, it undergoes little change in intensity for periods of an hour or longer.

5. Although the low-energy electrons reach high latitudes in both hemispheres, the average energy and the energy flux are larger in the northern cap. The energy flux and average energy in the north pole at high latitudes reach values of 5 ergs/cm² s sr and 1.5 keV, respectively, while in the south pole they are confined below 1 erg/cm² s sr and 500 eV. In addition, the regions of polar rain appear to be larger in the southern hemisphere. The importance of orbital effects in determining the extent of polar rain regions is not known. No imagery exists for the south pole passes so whether the energy flux into the south pole is sufficient to produce visual forms cannot be determined.

Spectral Characteristics

In this subsection we examine the spectral characteristics of the precipitating electrons in the north pole pass shown in Figure 4*b*. The orbit crosses the magnetic pole at $\sim$0756 UT. At approximately this time there are two well-defined enhancements in the electron average energy and peaks in the electron energy flux. These correspond to the two visible arcs that extend across the central cap in a sun-aligned manner, as shown in the composite DMSP image. A third enhancement in the average electron energy at $\sim$0758 UT is not seen in the DMSP images. There are two types of steady
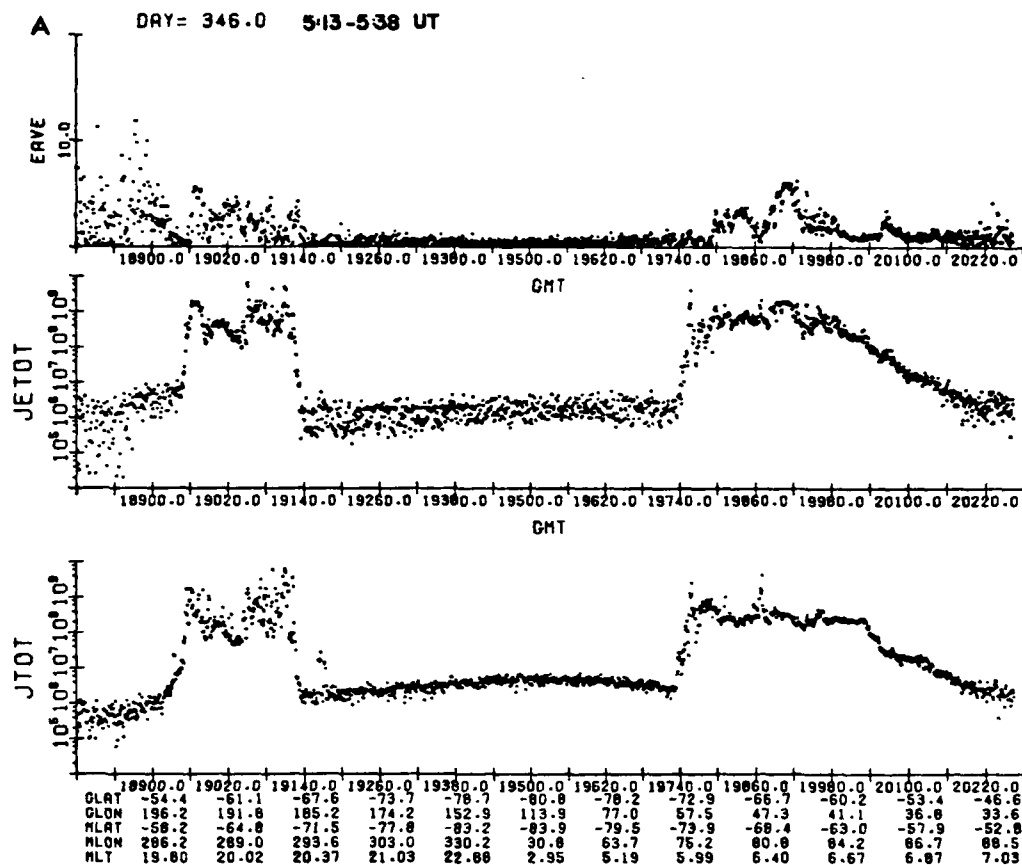
Fig. 3. The electron data for passes of the DMSP F2 satellite over the northern and southern hemisphere auroral zones and polar caps prior to the first occurrence of polar cap arcs. In the three panels from top to bottom we have plotted the average energy (EAVE) on a linear scale in keV, the integral energy flux (JETOT) in keV/cm² s sr, and the integral number flux (JTOT) in el/cm² s sr. The bottom is annotated with the universal time in seconds, the geographic latitude and longitude of the satellite (GLAT and GLON), the geomagnetic latitude and longitude of the satellite mapped along magnetic field line to 110 km (MLAT and MLON), and the magnetic local time at 100 km (MLT).

electron precipitation within the auroral oval in this pass: the morning and evening diffuse aurora, and a small segment of polar rain in the cap. For discussion purposes we define, somewhat arbitrarily, two additional regions between the morning diffuse aurora and the polar rain; a transition region between the morning diffuse aurora and the first polar cap arc; and a region of polar cap arcs, ending at the polar rain. Figure 5 is an expanded plot of the electron precipitation in which the four regions (morning diffuse aurora, transition region, polar cap arc region, and polar rain) are clearly marked. The scales for EAVE in Figures 5a and 5b are different, but it is clear that the average energies in the transition region, in much of the arc region, and in the polar rain are less than several hundred eV. A 'baseline' has been drawn for JTOT in the transition region. The baseline decreases continuously across the transition region until it reaches a minimum value equal to that of the polar rain just before the first polar cap arc.

The electrons outside the diffuse auroral region can be categorized by a relatively small number of types, defined in relationship to the polar rain spectrum. The types are shown schematically in Figure 6, in which the logarithm of the distribution functions is plotted versus energy. In this format a Maxwellian distribution appears as a straight line with a slope proportional to the negative inverse of the temperature

and an intercept proportional to the number density. The polar rain is a Maxwellian with low density and temperature. The Type I spectrum, also labeled 'baseline' spectrum, has the same temperature (same slope) as polar rain, but a higher density (larger intercept). The density of 'baseline' electrons varies by 2 orders of magnitude with polar rain as the low-density limit. The Type II spectrum is a weakly accelerated Maxwellian spectrum. The acceleration peak, here at ~100 eV, indicates the potential difference through which the primary spectrum has been accelerated. Electrons below this peak are backscattered and secondary electrons. The electrons with energies above the acceleration peak are shifted uniformly by the potential drop. In Figure 6 the Type II spectrum results from the acceleration of a primary Maxwellian population with the same temperature and a lower density than the Type I baseline distribution shown. The Type III population has two components: a high-density cold population and a higher-temperature baseline population. The Type IV spectrum is characteristic of polar cap arcs and shows a high degree of acceleration with a peak at ~700 eV.

The diffuse auroral region. In Figure 5a it is seen that the integral flux rises smoothly from background starting at ~0749:20 UT, reaching a relatively stable level of 10⁸ el/cm² s sr by 0750 UT. The energy flux and average energy show a

B DAY= 346.0   6:40-6:29 UT

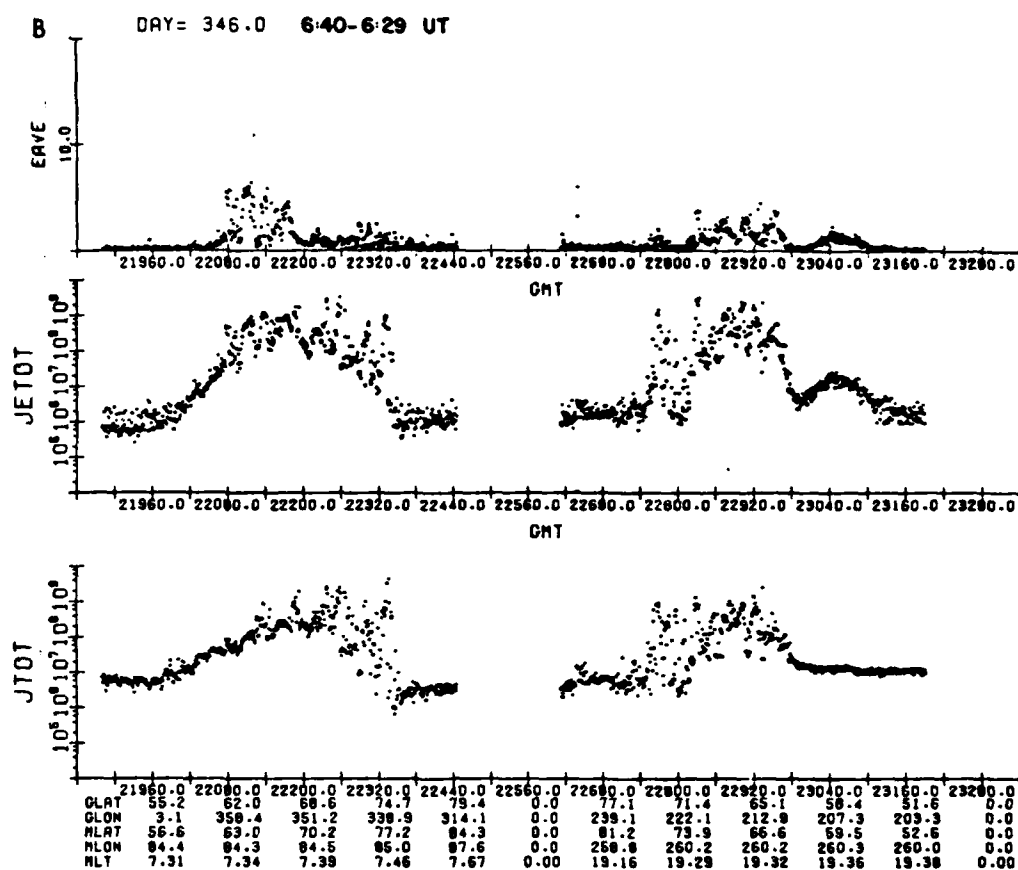|											
GLAT	55.2	62.0	68.6	74.7	79.4	0.0	77.1	71.4	65.1	58.4	51.6	0.0
GLON	3.1	358.4	351.2	338.9	314.1	0.0	239.1	222.1	212.8	207.3	203.3	0.0
MLAT	56.6	63.0	70.2	77.2	84.3	0.0	81.2	73.9	66.6	59.5	52.6	0.0
MLON	84.4	84.3	84.5	85.0	87.6	0.0	258.8	260.2	260.2	260.3	260.0	0.0
MLT	7.31	7.34	7.38	7.46	7.67	0.00	19.16	19.29	19.32	19.36	19.38	0.00

Fig. 3. (continued)

similar rise but exhibit greater variability fluctuating between 10^7 and 5×10^8 keV/cm² s sr and 1 and 7 keV, respectively. These characteristics of the electrons are consistent with passage of the satellite over the morning side diffuse auroral region.

Electron characteristics change abruptly at ~0750:50 UT, when average energies abruptly decrease from several keV to a few hundred eV (marked 'Transition' in Figure 5a). The details of the exit from the diffuse aurora and entry into the transition region are given in Figure 7, where we have plotted the 20 electron differential flux spectra spanning the region crossing as well as two differential flux spectra taken before and after the crossing. One notes that the electron spectrum softens appreciably. The flux of electrons above 1 keV decreases by at least an order of magnitude while the flux below 500 eV increases. The transition between the two spectral shapes is smooth and the shape is stable on both sides of the crossing. The entire change in electron characteristics takes place in the 5 s from 0750:47 to 0750:52.

The transition region. Electrons in the transition region show many rapid fluctuations in JTOT. Their spectra are mainly Type I and Type II, that is, Maxwellians with varying density or weakly accelerated Maxwellians. The baseline spectra are Type I. Figure 8 shows two baseline distribution functions in the transition region: Figure 8a, taken near the diffuse auroral crossing, and Figure 8b, taken 6° poleward of the crossing (and similarly marked in Figure 5a). These distributions are compared with Figure 8c, a time average of the baseline distributions in the polar cap arc region between

0756:30 and 0757:00 UT and marked Type I in Figure 5b, and Figure 8d, a time average of the polar rain distribution. None of the distribution functions shows a clear acceleration peak. All are Maxwellian and have temperatures of ~100 eV. The number density, calculated by assuming an isotropic flux outside the upcoming loss cone of width ~60° at 840 km, varies over 2 orders of magnitude. The distributions of Figures 8a and 8b shown here have the same temperature as the average polar rain. An examination of all baseline distributions shows a range in temperature from 50 to 200 eV.

The JTOT excursions from the baseline in the transition region are made up almost entirely (~85%) of electrons with Type II spectra. Two examples of these excursions (solid lines) are given in Figure 9, with their nearest baseline distribution functions (dashed lines). While the baseline distributions are slightly non-Maxwellian, it is clear that the accelerated spectra have, in addition to well-defined acceleration peaks, a uniform shift in energy of the baseline spectrum. Since there is no change in spectral shape, we infer that no heating accompanies the acceleration. In the first example, from 0752:53 and 0752:56 UT, the accelerating potential difference (distribution shift) is 100 eV; in the second, from 0752:37 and 0752:38 UT, the accelerating potential is 70 eV.

In approximately 80% of the cases the peaked distributions are observed last from 1 to 4 s, or for distances of ~7 to 30 km. The extent of these acceleration regions could be larger. Since the lowest-energy channel of the DMSP detec-
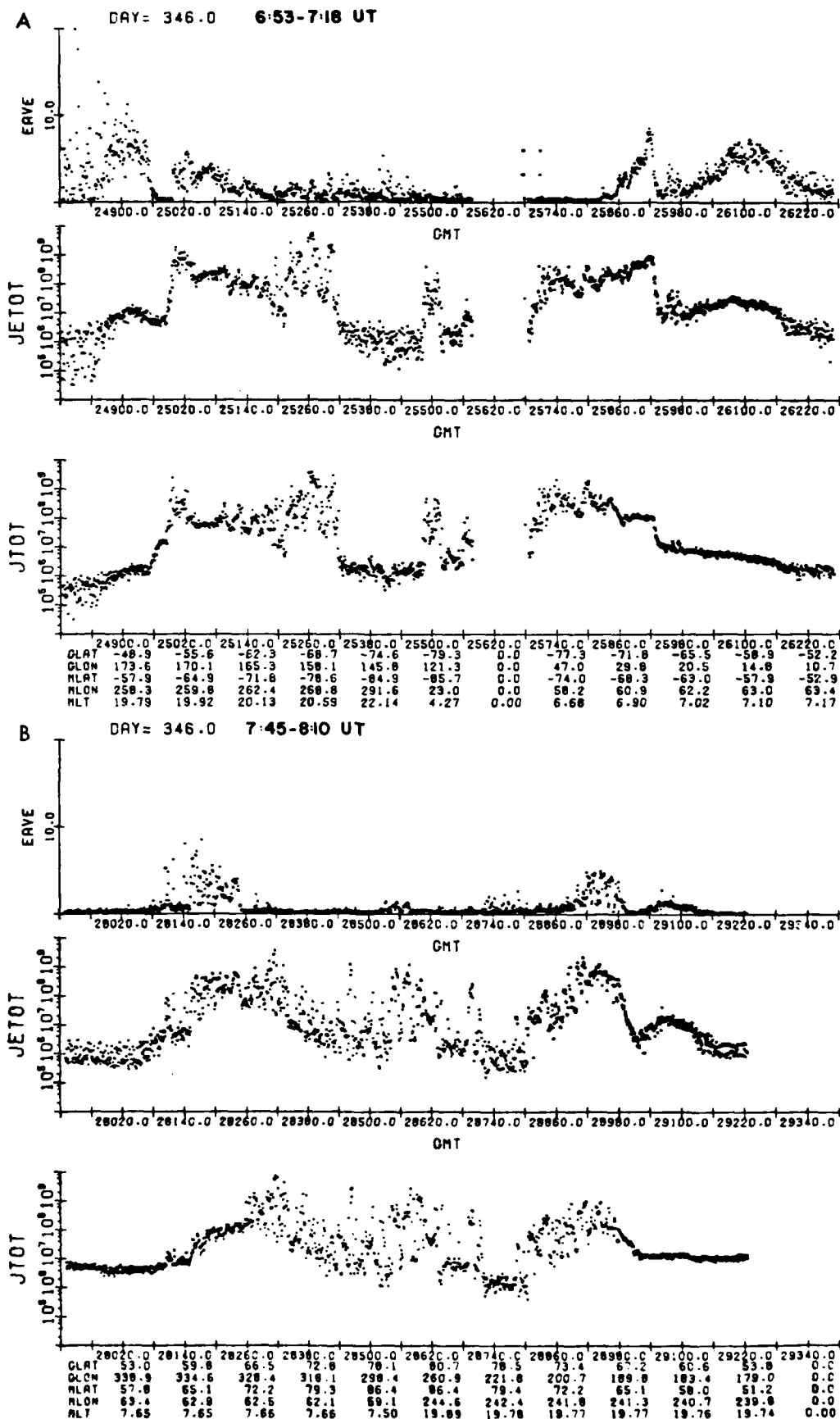
Fig. 4. The electron data from four passes of the DMSP F2 satellite over the auroral zone and polar cap plotted in the same format as Figure 3.

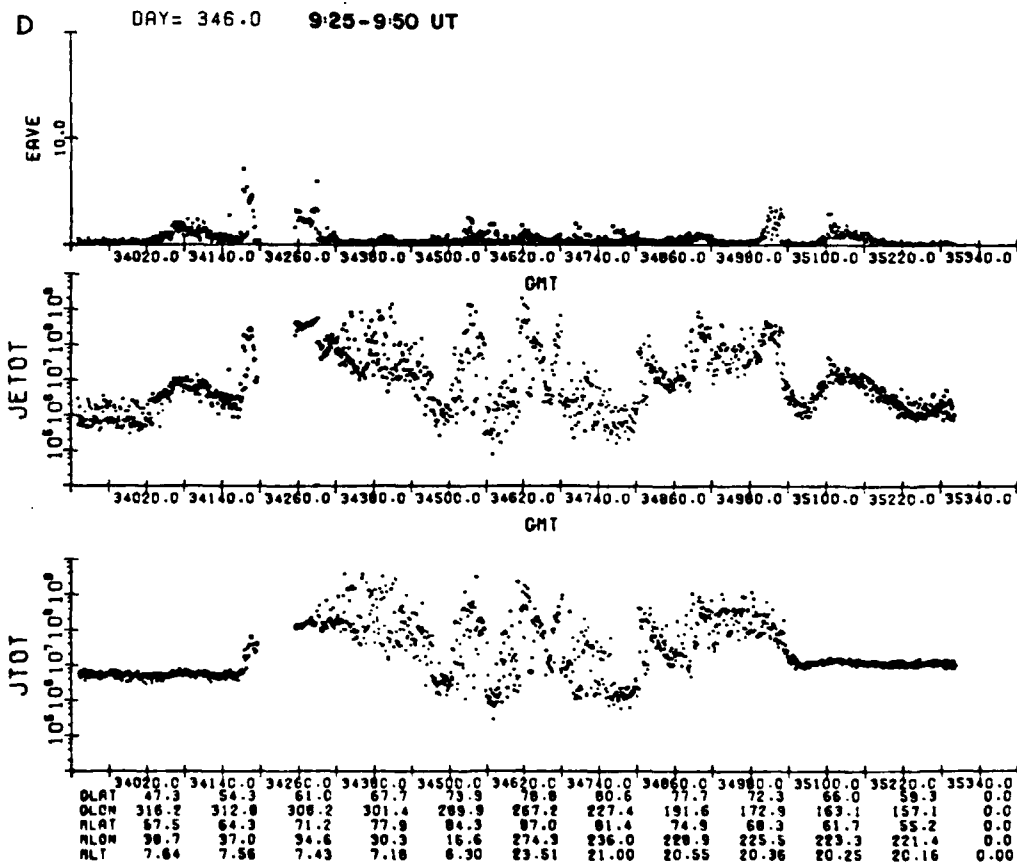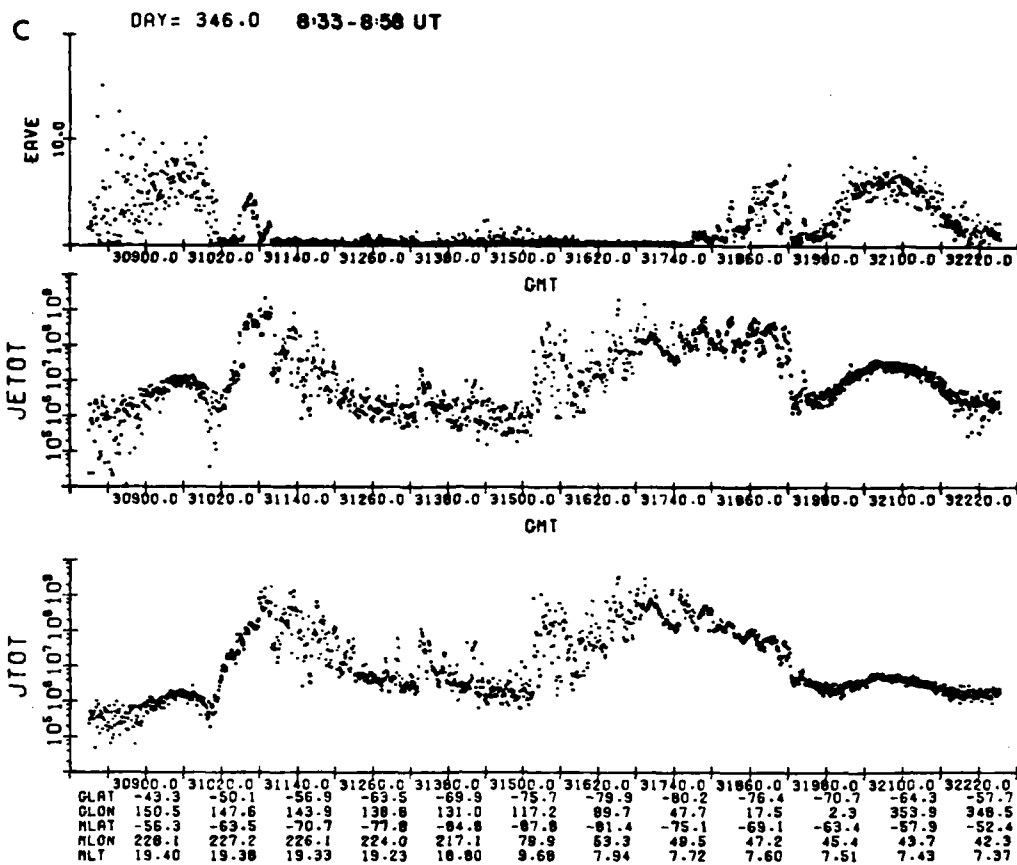Fig. 4. (continued)

156
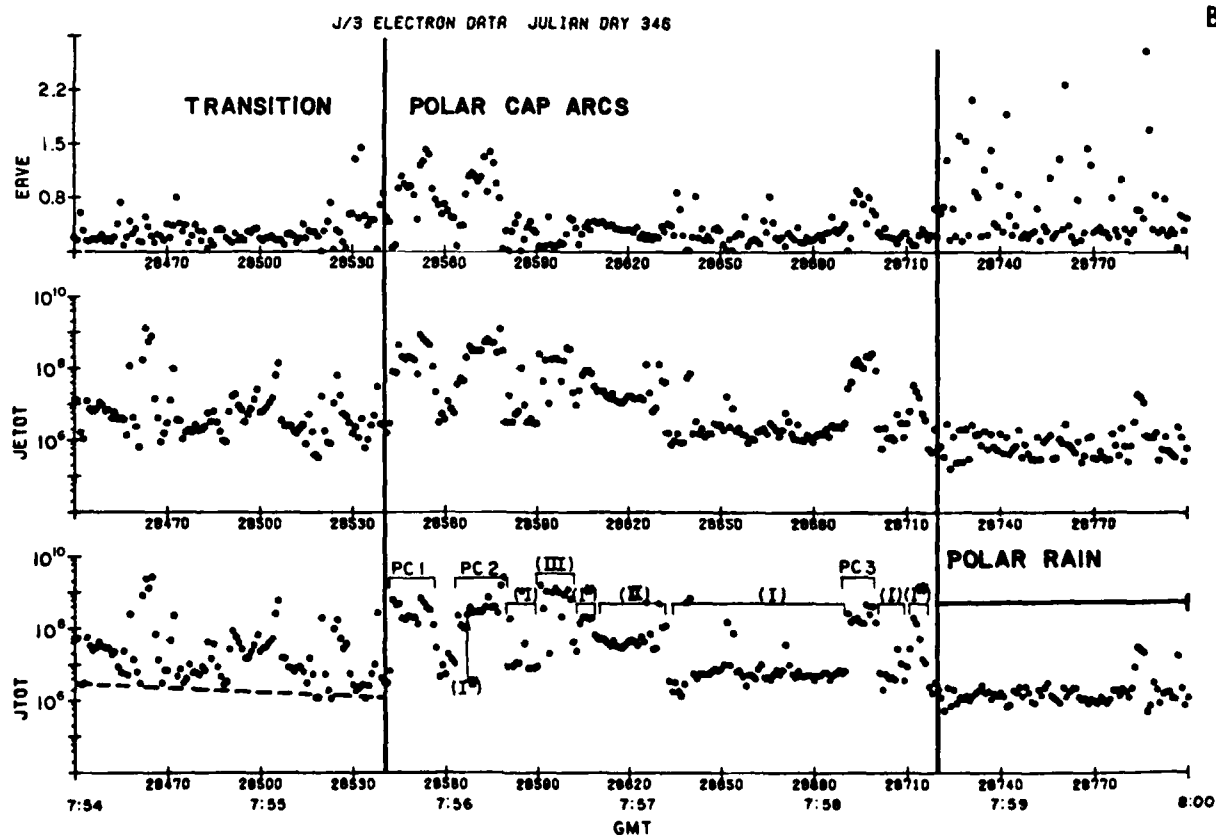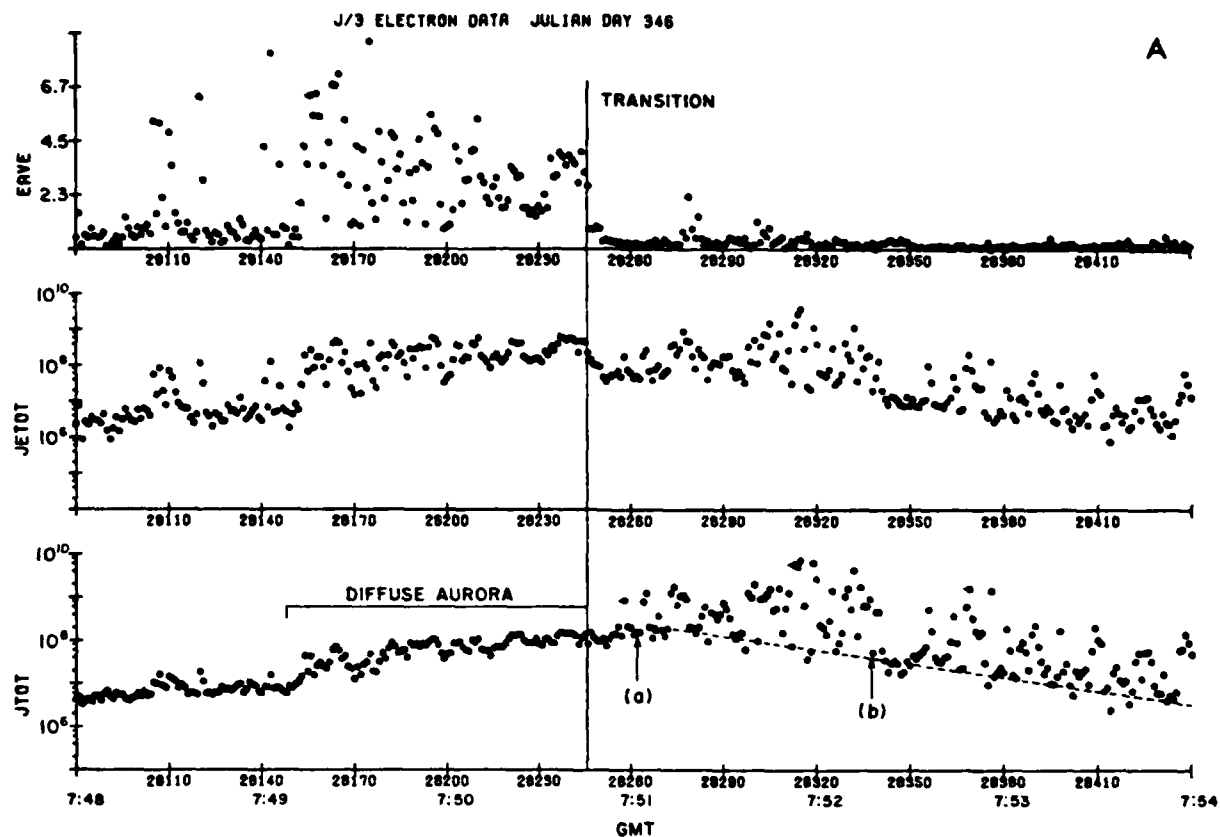
Fig. 5. An expanded plot of Figure 4b. The arrows labeled a and b show the points at which spectra a and b of Figure 7 were taken. Brackets labeled PC1, PC2, and PC3 show the location of the three polar cap arcs. Brackets labeled by roman numerals I through IV show the locations in the central polar cap of the four types of plasma precipitation discussed in the text.

157

tor is 50 eV, electrons that have been accelerated by potential drops of 50 V or less are difficult to pick out. Although 1 to 4 s is a typical span for observing these spectra, they are seen for periods of up to 15 to 20 s (0753:57 to 0753:13 and 0754:51 to 0755:08). In both short and longer events we have been unable to detect any systematic modulation in the peak energy as observed in an 'inverted V' event.

Polar cap arc region. Figure 5b shows three intervals, each 15 to 20 s in duration, in which the electron average energy is greater than 700 eV and which are labelled polar cap arcs PC1–PC3. The first two enhancements are associated with the visible arcs in Figure 2a. Between PC1 and the polar rain, electron spectral Types I–III, shown in Figure 6, can be identified. The extent over which each spectral type is observed is marked in Figure 5b. In this region, Type I electrons have temperatures ~100 eV and densities ~0.1 cm^{-3} which are a factor of 3 greater than the polar rain density. They are found on either side of all three arcs. JTOT for these electrons is ~10^7 $(cm^2 s sr)^{-1}$. In addition, Type I spectra with much higher densities (>2 cm^{-3}) occur during three brief periods: before and after passage over the second arc and after passage over the third arc (0756:07, 0756:43–0756:48 UT and 0758:33–0758:36 UT). We label these Type I* in Figure 5b to differentiate them from the lower-density Type I population. JTOT for Type I* electrons exceeds 10^8 $(cm^2 s sr)^{-1}$. These electrons are spectrally indistinguishable from the high-density baseline electrons found in the transition region just after exit from the diffuse aurora. A compari-
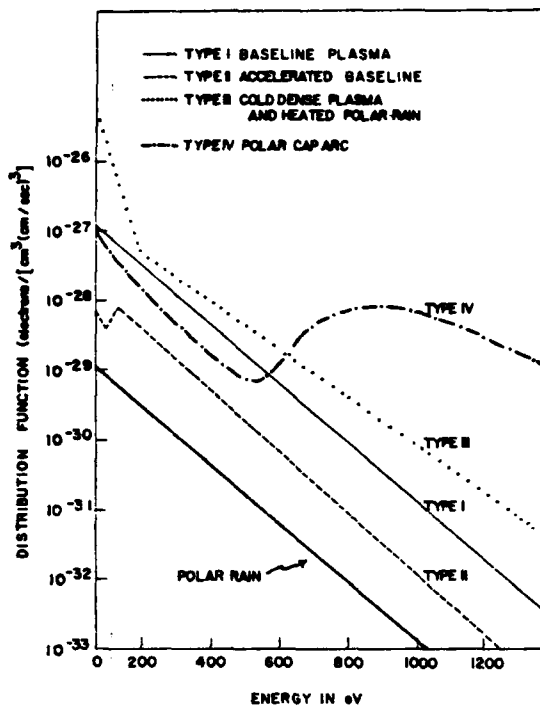

Fig. 6. The logarithm of the electron distribution functions as a function of energy for the various classes of electron distribution found in the polar cap.
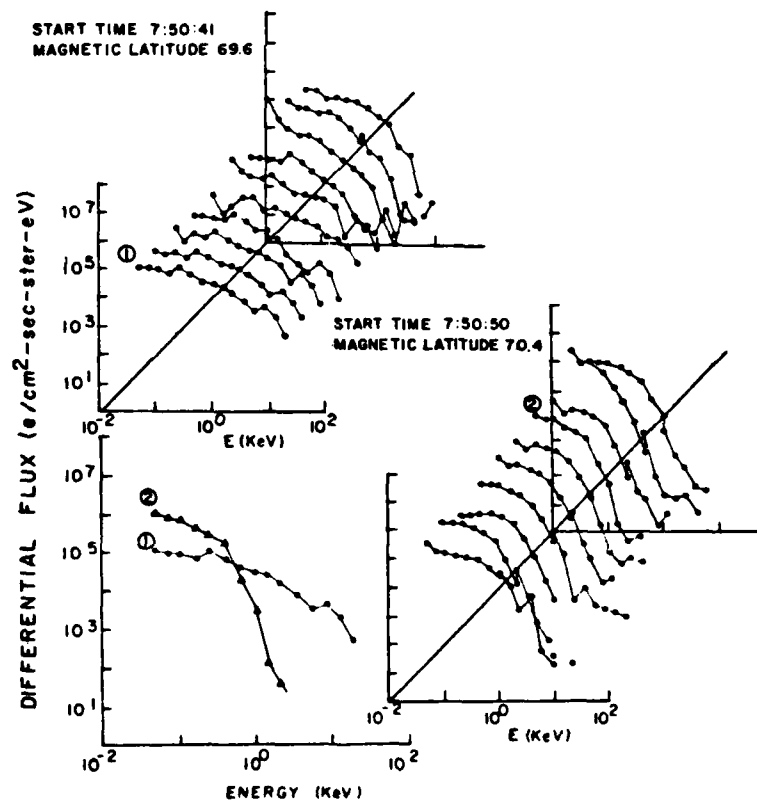

Fig. 7. A time sequence plot of the 20 differential flux spectra spanning the transition in electron characteristics at approximately 0750:50 UT. Two individual spectra have been drawn in the left corner to show more clearly the change in shape. The numbers 1 and 2 show where the spectra were taken from the set of 20 spectra.
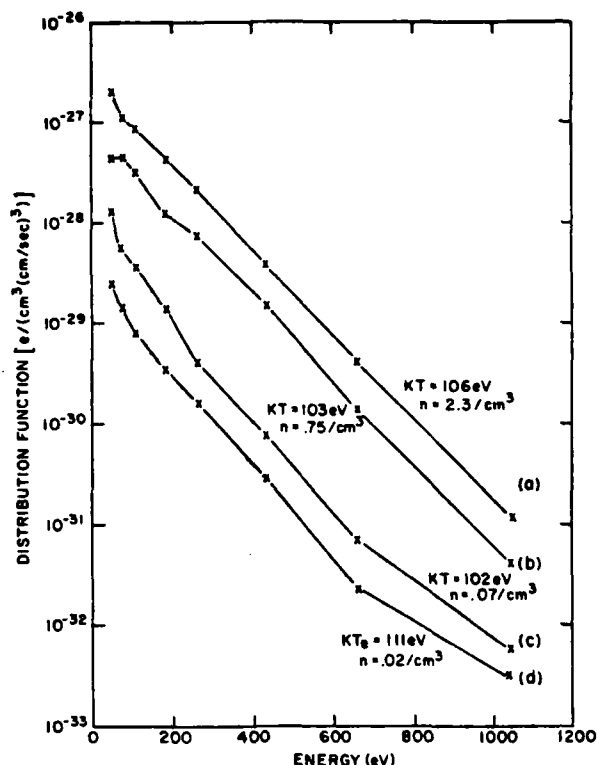
Fig. 8. The electron distribution function plotted as a function of energy for four points in the DMSP pass centered at 0757 UT. The four curves represent (a) a single spectrum measured at 0751:02, (b) a single spectrum measured at 0752:18 (c) a time average of the spectrum from 9756:20 to 0757:00, and (d) a time average of the spectrum after 0758:40. The number density and temperature are calculated from the linear regression on the points assuming a 60° wide loss cone.

son of Type I* electrons in the transition region and near the polar cap arcs is given in Figure 10. In this figure, two sets of 10 spectra are plotted. One set starts at 0751:01 UT just after the satellite crossed into the transition region (71° magnetic latitude). The second set starts at 0756:41 UT after the satellite had passed over the second polar cap arc (88° magnetic latitude). In the lower left-hand corner a single spectrum from each 10-s period is plotted. It is clear that the precipitating electrons in the two regions are almost identical. Indeed, if they differ in any particular, it is that the plasma at the higher latitude has a slightly higher intensity.

Type II spectra, weakly accelerated Maxwellian, similar to those in the transition region are also found in the polar cap arc region between PC2 and PC3 (0756:49–0757:05 UT). For these electrons, JTOT is ~6 × 10⁷ (cm² s sr) and EAVE is in the 200 to 300-eV range. The distribution functions during this period (not shown) are similar to those shown in Figure 9, produced by field-aligned accelerations. We estimate that the unaccelerated electrons had temperatures of ~150 eV and densities of 0.2 cm⁻³. These parameters are close to the levels of the unaccelerated polar rain in which the arcs are embedded.

Double-Maxwellian Type III electrons were found in the central polar cap, from 0756:30 to 0756:41 UT, shortly after passage over PC2. Figure 5b shows that in this period JTOT was ~10⁹ (cm² s sr)⁻¹ and JETOT was ~0.5 erg/(cm² s sr), with EAVE varying between one and several hundred eV. The spectral charactertisics of electrons observed in this interval, as well as similar electrons found intermittently in the transition region, are shown in Figure 11. The two sets of spectra in this figure start at 0752:01 UT (magnetic latitude = 74.5°) and 0756:30 UT (magnetic latitude = 88.3°), respectively. In both regions the two-component population alternates with spectra in which only the hotter, Type I population is present.
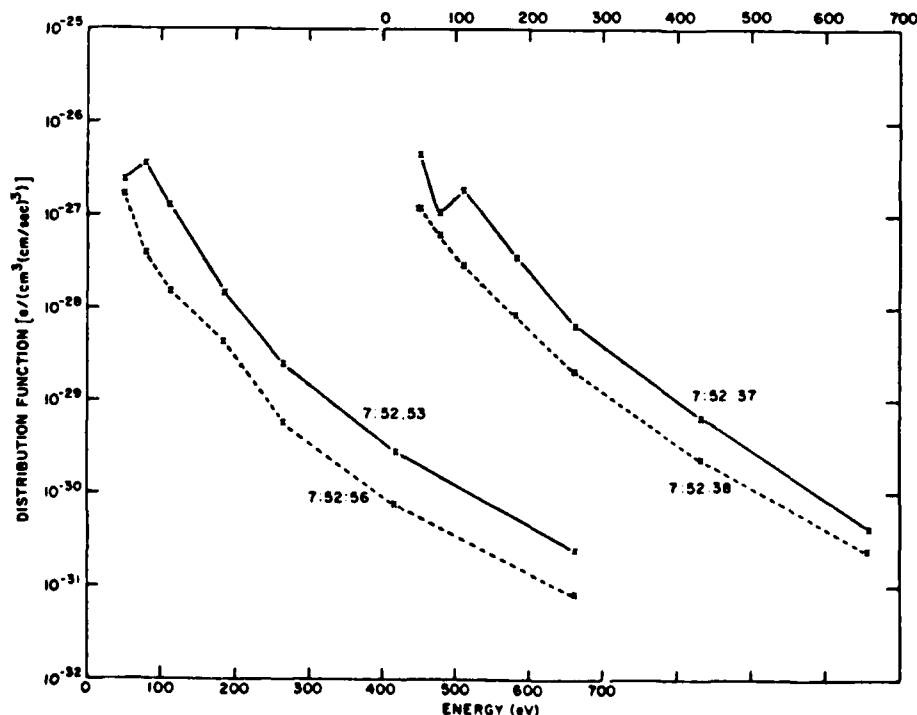
Fig. 9. Two examples of accelerated (solid line) and unaccelerated (dashed line) electron distributions observed poleward of the transition from the diffuse aurorae.

159
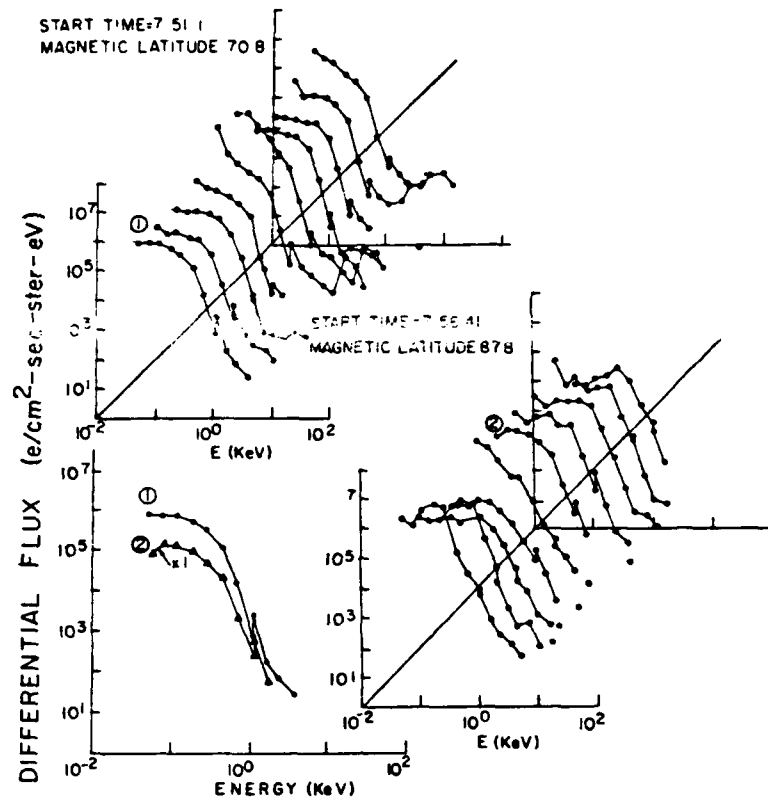
Fig. 10. Two sets of 10 differential flux spectra each, showing the similarity of the cold electron spectra in the region just poleward of the transition and in the central polar cap near the polar cap arc. Each set of ten spectra is annotated with the time and geomagnetic latitude at the beginning of the interval. A single plot in the low left corner shows a comparison of single spectra from the two intervals. The numbers 1 and 2 denote the origin of the two spectra from the two sets of 10 spectra.
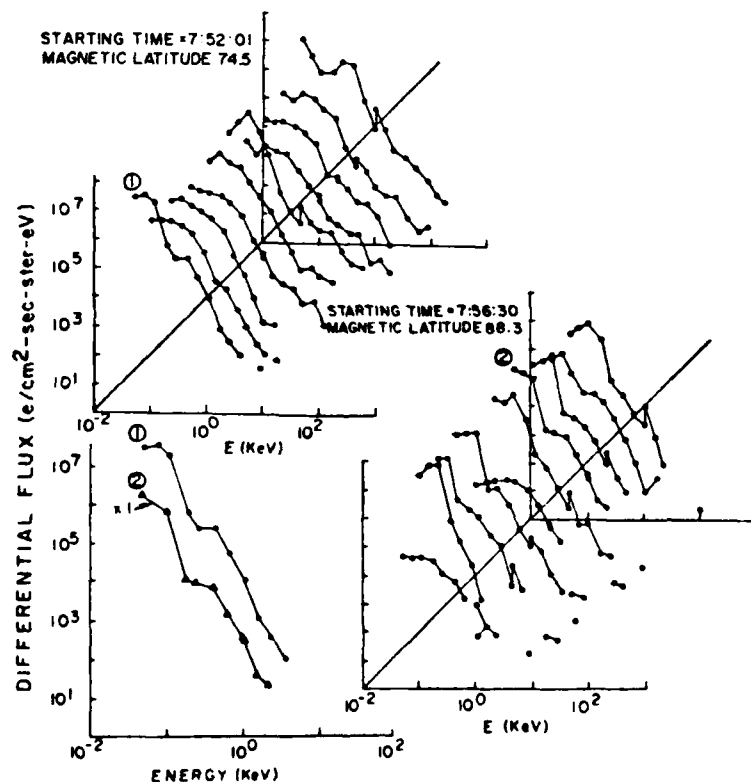
Fig. 11. A comparison of spectra in the region poleward of the transition on the morning side and in the central polar cap. The format is the same as in Figure 9.

Fig. 12.   The logarithm of the distribution function versus energy for the two-component and one-component electrons seen in the central polar cap. The number density and temperature are calculated as for Figure 7.

The distribution functions of electrons measured at 0756:34 and 0756:36 UT (spectrum 2 in Figure 11) are plotted in Figure 12. The temperatures of the 'hot' components are approximately the same. The density calculated for the single-component plasma, assuming isotropy outside the upcoming loss cone, is 0.2 cm^{-3}. From their slopes the hot and cold components of the two-population distribution have temperatures of 176 eV and 21 eV respectively. Assuming

Fig. 13.   Ten differential flux spectra as the satellite passes into the region of the polar cap arcs.

isotropy outside of the upcoming loss cone, densities of 0.6 cm^{-3} and 80 cm^{-3} are obtained for the hot and cold components, respectively. As we show below, the isotropy assumption at least for the cold component is probably not justified.

Finally, we consider the characteristics of TYPE IV electrons, detected above the three arcs. The arcs were encountered from 0755:47 to 0755:57 UT, from 0756:06 to 0756:20 UT, and from 0758:13 to 0758:21 UT corresponding to spatial extents between 0.5° and 1°. From Figure 5b we note that in these three intervals JTOT was in the range 3 to 9 × 10^8 (cm^2 s sr)$^{-1}$; JETOT in the range 0.1 to 1.5 ergs/(cm^2 s sr), and EAVE in the 500- to 1500-eV range. In considering spectral details we restrict ourselves to measurements taken above the second arc as representative of all three.

Figure 12 is a plot of the consecutive spectra beginning at 0756:01 UT (magnetic latitude = 89.4°) 4 s prior to entering the arc. The first four spectra are Type I enhanced polar rain. The next two spectra have peaks below 1 keV (Type II). These are followed by a single unpeaked spectrum that is much more intense than those observed in the first 4 s (Type I*). The final three spectra are peaked at ~1 keV. For the sake of direct comparison the spectra of the enhanced polar rain and the arc electrons are plotted in the bottom portion of Figure 12.

A further analysis of electron measurements from the 0756:01 to 0756:10 UT interval suggests that the simple Maxwellian representation of electron spectra near the arcs is insufficient and that both enhanced particle entry and field-aligned acceleration play significant roles in visible polar cap arc formation. Figure 13 provides electron distribution functions measured at 0756:03, 0756:07, and 0756:10 UT. These correspond to: (1) the enhanced polar rain spectrum, (2) the single, intense unpeaked spectrum at the edge of the arc, and (3) the peaked spectrum 2 within the arc of Figure 12. The distribution functions measured at 0756:03 and 0756:07 UT have at least two components: a cooler population with temperature of 110 eV and densities of 0.31 and 1.5 cm^{-3}, respectively; a warmer population with a temperature of ~350 eV and densities of 0.05 and 0.13 cm^{-3}.

Fig. 14. The logarithm of the distribution function versus energy for the unaccelerated (solid lines) and accelerated (dashed line) electron distribution seen in the region of the first polar cap arc in the interval from 0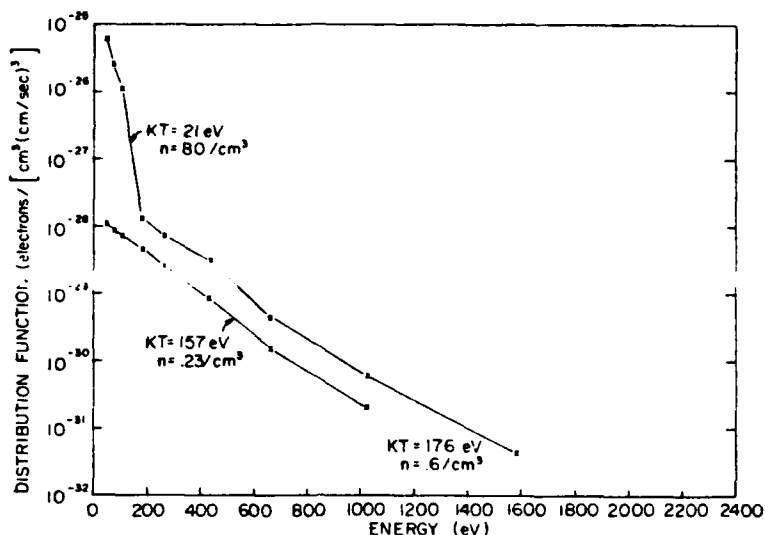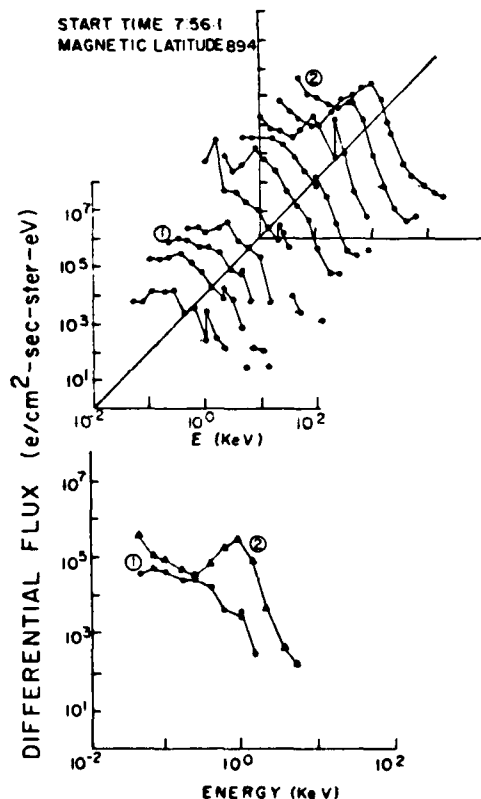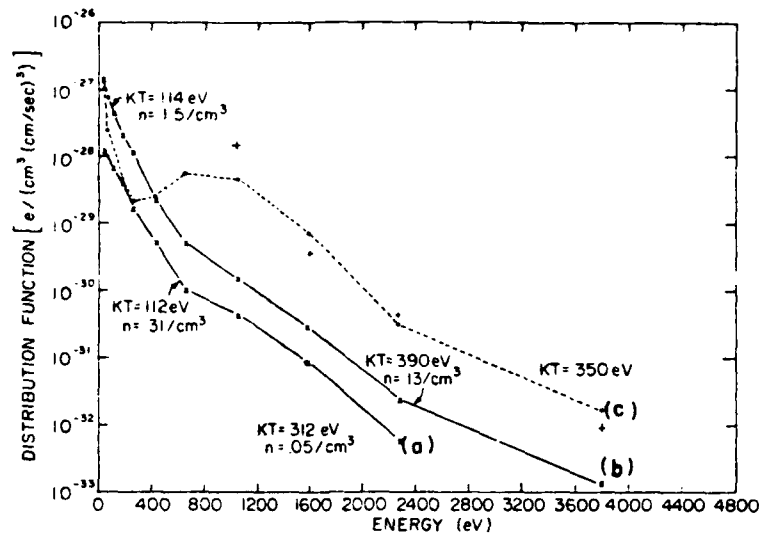756:01 to 0756:10. The number density and temperature are calculated as in Figure 7. Crosses mark the values of the distribution function for the denser of the unaccelerated electrons if they fell through a potential of ~800 V.

respectively. The cooler population has the characteristics of Type 1 particles: enhanced polar rain or baseline electrons. As one nears the arc the differences in the spectra (comparing 1 to 2) are principally in density. No acceleration peak is seen.

A comparison of the distributions 2, measured at 0756:07, and 3 in the arc, at 0756:10 UT, for energies >1keV shows the slopes to be identical. The separation in energy between the high-energy portion of the distributions suggests that the peaked distribution has fallen through a potential drop of ~750 V. The crosses in Figure 13 give the distribution that would be measured by the DMSP electron detector had the distribution measured at 0756:07 UT been shifted in energy by 800 eV. The low-energy component would pass largely undetected due to the small values of $\Delta E/E$ for the detector (0.10 and 0.12). For a potential drop of 800 V the accelerated cold component would be energized beyond the 660-eV channel. Only the portion of the cold distribution originally in the 220- to 350-eV range would be seen in the 1045-eV channel. The agreement between the crosses and the measured distribution at 0756:10 UT is reasonably good, indicating that polar cap arcs are produced by the acceleration of low-energy, relatively dense electrons. In this interpretation the electrons with energies below the peak are secondaries trapped between the field-aligned potential barrier and their magnetic mirror points [Evans, 1974]. The very low energy component has been shown by Burch et al. [1979] to be highly field aligned and is made up of ionospheric electrons that have been both thermalized and accelerated through a potential drop.

SUMMARY AND DISCUSSION

The immediate goal of the present study is to describe clearly the various electron populations found at high magnetic latitudes during a period of polar cap arc activity. A more long-range goal of this and the companion observational studies is to provide a base of information for a comprehensive understanding of how the open field line portion of

the earth's magnetosphere interacts with the solar wind and the IMF to change the characteristics of polar cap electron precipitation so as to produce polar cap arcs. At this writing there is no coherent theory to explain increased electron precipitation and sun-aligned arcs in the polar cap. In this section we first summarize the salient features of the rather complex data set reported here. In commenting on the DMSP observations we point out: (1) how they relate to other reported measurements, (2) what further observations are needed, and (3) what constraints the observations placed on a comprehensive model of the polar magnetosphere.

The DMSP measurements show the following:

1. During the initial period of substorm activity and southward IMF only uniform polar rain precipitation was found in the polar cap. Within an hour of the first northward turning of the IMF electron precipitation in the polar caps of both hemispheres increased dramatically, and visible arcs appeared in the northern, winter cap. The average energy of the accelerated electrons was observed as high as ~1 keV in the northern polar cap but only as high as a few hundred eV in the southern polar cap. Following a brief period of southward excursion of the IMF, visible arcs and enhanced precipitation vanished from the polar caps. They returned soon after the IMF regained its northward orientation. The process of arc formation in the cap for B_z northward and disappearance for B_z southward occurred three times on December 12.

2. After the northward turnings of the IMF, large-scale electron precipitation was characterized by: (1) persistent fluxes of unaccelerated keV electrons only in the diffuse auroral region; (2) rapidly varying fluxes of low-energy electrons in a region poleward of the morning and evening side diffuse aurorae called the transition region; the fluctuations in number and energy flux resulted from field-aligned accelerations, with no heating, of cold 'baseline' electrons through potential drops of between 50 and 200 V (Type II spectra); (3) 'baseline' electron fluxes that decrease smoothly from ~10^8 (cm^2 s sr)$^{-1}$ at the poleward boundary of the

162

morning side diffuse aurorae, to polar rain fluxes of $<10^7$ (cm^2 s sr)$^{-1}$ in the evening flank of the polar cap (Type I spectra); no systematic change in temperature is observed.

3. Within the polar cap arc region the precipitation producing the visual arcs is embedded in a 'baseline' flux of 10^7 (cm^2 s sr)$^{-1}$ identified as high-density polar rain (Type I). In the region in and near the polar cap arcs, precipitation consists of: (1) unaccelerated 'baseline' electrons (Type I)* with densities similar to those seen just poleward of the diffuse aurorae; (2) extremely dense, cold electrons with temperatures of 20 to 30 eV superimposed on the 100-eV baseline distribution (Type III); (3) baseline electrons that have been accelerated through potential drops of ~100 V (Type II); (4) visible arc electrons which result from the acceleration of a two-component electron population with temperatures of 100 and 350 eV, through potential drops of 750 V (Type IV).

The general features of DMSP observations summarized above, under point I, are in agreement with many previously reported detections of visible sun-aligned arcs in the central polar cap during periods of magnetic quieting when the IMF has a northward component [Berkey et al., 1976; Ismail et al., 1977; Lassen and Danielsen, 1978; Gussenhoven, this issue.] In addition, we show here that when conditions are favorable for the production of polar cap arcs, the process can be interrupted by B_z turning southward. Arcs then reappear in the cap for B_z turning again northward. The time delay for the IMF to affect the cap is somewhat greater than 1 hour. We have not determined here the full temporal extent of the favorable conditions for polar cap arcs, but on December 12 it was in excess of 16 hours. During this time the solar wind velocity varied between 470 and 515 km/s, the magnetic sector was 'away,' and B_y had both negative and positive values. No clear dependence of arc position on B_y could be seen in the DMSP images corresponding to the statistical dependence found by Lassen [1979] and Gussenhoven [this issue]. The arcs were, however, more sun aligned during the first sequence when $B_y \ll B_z$.

The fact that polar cap arcs most frequently appear during periods of magnetic quieting is consistent with either an intramagnetospheric or an extramagnetospheric source for the particles and energy involved. A model of an intramagnetospheric source would require that at the time of northward turning of the IMF, potential energy stored in the magnetotail and particles in the plasma sheet would be transmitted in some as yet unspecified way to the polar cap rather than to the auroral ionosphere. In time the stored energy would be dissipated, ... features would vanish from the polar cap. An extramagnetospheric source model requires that arcs result from a nearly direct interaction between the magnetosheath plasma and the polar ionosphere. The words 'nearly direct' allow for some field-aligned acceleration between the magnetopause and ionosphere. With northward IMF such a model must allow, in a way not yet specified, for the admission of a variable amount of magnetosheath particles onto field lines connected to the polar ionosphere. If the amount of plasma admitted to the polar cap is related only to the level of the solar wind flux, and if there is no threshold for the particle admission mechanism, then structured precipitation should be found in the polar cap whenever B_z is northward. For extended quiet periods, however, the intensity of precipitation would be only sufficient to produce subvisual arcs. A

recent study by Meng [1981b] shows cases of extreme quiet in which structured low-energy electron precipitation occurs throughout the cap. He attributes the precipitation to a much expanded plasma sheet causing the auroral oval to reach very high latitudes. We, however, find these precipitations to be more indicative of a 'nearly direct' magnetosheath plasma entry mechanism.

Turning now to the second point of the summary of DMSP observations, namely, the large-scale characteristics of electron precipitation for B_z north, we focus on the problem of magnetic topologies. The diffuse auroral region needs little comment. It is well accepted that the diffuse auroral region maps to the central plasma sheet, a region of closed magnetic field lines, and that electron temperatures are elevated during the recovery phase of substorms [Hones et al., 1973]. Thus our observations of electrons with average energies of several keV in the diffuse aurora during northward B_z periods is not surprising.

Somewhat more surprising is the presence of relatively high fluxes of much lower energy electrons in the region poleward of the diffuse aurora but prior to the polar cap arcs which we have called the transition region. This region is characterized spectrally by fluctuations in JTOT and JETOT of an ~100-eV population and occurs on both the morning and evening sides. This morphology is similar in structure to the mapping into the polar ionosphere of the interior cusp, the low-latitude boundary layer and the plasma boundary layer proposed by Vasyliunas [1979]. In this picture the transition region maps along closed magnetic field lines that pass close to the magnetopause [Crooker, 1977] and the electrons originate in the magnetosheath. How they gain entry to the magnetosphere in such relatively high numbers, as shown in Figure 8, or how they undergo the modest field-aligned accelerations shown in Figure 9 is not known.

The third point of the summary concerns observations in the polar cap arc region. Three distinct spectral types were found in addition to those of the polar cap arcs themselves: the three types (I-III) are defined in relation to the average spectrum found in the polar rain region. The characteristics of polar rain have been discussed adequately by Winningham and Heikkila [1974]. It is curious, however, that the density of polar rain (lowest-density Type I electrons) found in the polar cap arc region in the vicinity of the arcs was a factor of 3 higher than near the evening flank of the polar cap. Whether this is a common feature of polar cap arc environments requires further study. The very high density baseline (Type I, I*) and accelerated baseline (Type II) electrons found a have characteristics identical to the electrons in the transition region. Most likely this similarity reflects a common particle source, i.e., the magnetosheath. It does not, however, require that the entrance mechanisms are the same for the electrons in the two regions. Indeed, if the field lines of the transition region are closed and those of the polar cap arc region are open then particle dynamics may be quite different.

The third spectral type (Type III) consists of an extremely cold electron distribution superimposed on a 'baseline' distribution. They occur over a relatively broad region and are not embedded in an accelerated primary population. Therefore we do not identify them as the highly field aligned cold electrons reported by Burch et al. [1979] in the polar cap electron acceleration regions. Assuming that the Type III electrons were unaccelerated and isotropic outside the up-

Burch, J. T., Low-energy electron fluxes at latitudes above the auroral zone. *J. Geophys. Res., 73*, 3585, 1968.

Burch, J. T., S. A. Fields, and R. A. Heelis, Polar cap electron acceleration regions, *J. Geophys. Res., 84*, 5863, 1979.

Burke, W. J., M. S. Gussenhoven, M. C. Kelley, D. A. Hardy, and F. J. Rich, Electric and magnetic field characteristics of discrete arcs in the polar cap, *J. Geophys. Res.*, this issue.

Crooker, N. U., The magnetospheric boundary layers: A geometrically explicit model, *J. Geophys. Res., 82*, 3629, 1977.

Davis, T. N., The morphology of the polar aurora, *J. Geophys. Res., 65*, 3497, 1960.

Eather, R. H., DMSP calibration, *J. Geophys. Res., 84*, 4134, 1979.

Eather, R. H., and S.-I. Akasofu, Characteristics of polar cap auroras, *J. Geophys. Res., 74*, 4794, 1969.

Evans, D. S., Precipitating electron fluxes formed by a magnetic-field-aligned potential difference, *J. Geophys. Res., 79*, 2853, 1974.

Foster, J. C., and J. R. Burrows, Electron fluxes over the polar cap, 1, Intense keV fluxes during poststorm quieting, *J. Geophys. Res., 81*, 6016, 1976.

Gussenhoven, M. S., Extremely high latitude auroras, *J. Geophys. Res.*, this issue.

Hardy, D. A., M. S. Gussenhoven, and A. Huber, The precipitating electron detectors (SSJ/3) for the block 5D/flights 2-5 DMSP satellites: Calibration and data presentation, *Rep. AFGL-TR-79-0210*, Air Force Geophys. Lab., Hanscom Air Force Base, Mass., 1979.

Hoffman, R. A., and D. S. Evans, Field-aligned electron bursts at high latitudes observed by OGO 4, *J. Geophys. Res., 73*, 6201, 1968.

Hones, E. W., Jr., J. R. Asbridge, S. J. Bame, and S. Singer, Substorm variations of the magnetotail plasma sheet from $X_{SM} = -6 R_E$ to $X_{SM} \approx -60 R_E$, *J. Geophys. Res., 78*, 109, 1973.

Ismail, S., D. D. Wallis, and L. L. Cogger, Characteristics of polar cap sun-aligned arcs, *J. Geophys. Res., 82*, 4741, 1977.

King, J. H., *Interplanetary Medium Data Book Supplement 1, 1975-1978, NSSDC/WDC-A-R&G-79-08*, NASA Goddard Space Flight Center, Greenbelt, Md., 1979.

Lassen, K., The quiet-time pattern of auroral arcs as a consequence of magnetospheric convection, *Geophys. Res. Lett., 6*, 777, 1979.

Lassen, K., and C. Danielsen, Quiet time patterns of auroral arcs for different directions of the interplanetary magnetic field in the Y-Z plane, *J. Geophys. Res., 83*, 5277, 1978.

Lemaire, J., The magnetospheric boundary layer: A stopper region for a gusty solar wind, in *Quantitative Modelling of Magnetospheric Processes*, edited by W. P. Olson, p. 412, AGU, Washington, D. C., 1979.

Lyons, L. R., Generation of large-scale regions of auroral currents, electric potentials, and precipitation by the divergence of the convection electric field, *J. Geophys. Res., 85*, 17, 1980.

Lyons, L. R., Discrete aurora as the direct result of an inferred high-altitude generating potential distribution, *J. Geophys. Res., 86*, 1, 1981.

Meng, C.-I., Polar cap arcs and the plasma sheet, *Geophys. Res. Lett., 8*, 273, 1981a.

Meng, C.-I., The auroral electron precipitation during extremely quiet geomagnetic conditions, *J. Geophys. Res., 86*, 4607, 1981b.

Meng, C.-I., and S.-I. Akasofu, The relationship between the polar cap auroral arc and the auroral oval arc, *J. Geophys. Res., 81*, 4004, 1976.

Meng, C.-I., A. L. Snyder, Jr., and H. W. Kroehl, Observations of auroral westward traveling surges and electron precipitations, *J. Geophys. Res., 83*, 575, 1978.

Reiff, P. H., and D. L. Reasoner, The magnetosheath electron population at lunar distance: General features, *J. Geophys. Res., 80*, 1232, 1975.

Starkov, G. V., and Ya. J. Fel'dshteyn, Substorms in auroras, *Geomagn. Aeron., 11*, 478, 1971.

Vasyliunas, V. M., Interaction between the magnetospheric boundary layer and the ionosphere, in *Proceedings of Magnetospheric Boundary Layers Conference, ESA SP-148*, p. 387, European Space Agency, Neuilly, France, 1979.

Weber, E. J., and J. Buchau, Polar cap F-layer auroras, *Geophys. Res. Lett., 8*, 125, 1981.

Whalen, B. A., J. R. Miller, and I. B. McDiarmid, Sounding rocket observations of particle precipitation in a polar cap electron aurora, *J. Geophys. Res., 76*, 6847, 1971.

Winningham, J. D., and W. J. Heikkila, Polar cap auroral electron fluxes observed with ISIS 1, *J. Geophys. Res., 79*, 949, 1974.

164

Morphology of the Polar Rain

M. S. GUSSENHOVEN AND D. A. HARDY

Space Physics Division, Air Force Geophysics Laboratory, Hanscom Air Force Base, Massachusetts

N. HEINEMANN

Physics Department, Boston College, Chestnut Hill, Massachusetts

R. K. BURKHARDT

Physics Research Division, Emmanuel College, Boston, Massachusetts

Results of a statistical study of the occurrence and characteristics of the polar rain (Winningham and Heikkila, 1974) are reported. Precipitating electron data in the energy range from 50 eV to 20 keV from the SSJ 3 sensor on the polar-orbiting DMSP/F2 satellite were used for the study. Intervals of clear polar rain were identified in all orbits in the 1-year interval September 1977 to August 1978. The spectra from the intervals were binned in a two-dimensional spatial array in geomagnetic latitude and magnetic local time. Separate arrays were maintained for different levels of magnetic activity, values of the components of the interplanetary magnetic field (IMF), and season. The average spectra were determined in each bin and were used to calculate the integral flux and average energy. Two-dimensional maps of average energy and integral flux show significant large-scale spatial variations that are roughly symmetric about an axis running prenoon to premidnight. Integral flux (average energy) decreases (increases) from the dayside to the nightside along this axis by a factor of almost 15 (3). This basic variation was maintained in all separations by magnetic activity, season, intensity of the polar rain, and sector structure, although small rotations in magnetic local time of the symmetry axis could be seen in some cases. The second most prominent variation is one that has been noted previously (Yeager and Frank, 1976; Meng and Kroehl, 1977); polar rain occurs preferentially in the northern (southern) cap for away (toward) IMF sectors. In the preferred cap the precipitation is stronger in the morning. Approximately 70% of the spectra occurred for B_z negative. The overall intensity of the polar rain increases and cools with increasing magnetic activity. The occurrence of polar rain falls within a circular region whose center is offset toward premidnight and whose radius increases with magnetic activity.

1. INTRODUCTION

Polar rain, the weak (~ 0.01 cm^{-3}), structureless, near-isotropic flux of electrons precipitating in the polar caps and having temperatures in the 100-eV range, was discovered and named by *Winningham and Heikkila* [1974]. Field lines on which polar rain is found map back into the tail lobes of the magnetosphere. They either close at such great distance down tail that their particle populations and processes remain distinct from neighboring field lines of the auroral oval, or they are open, merging with solar wind field lines, and contiguous to closed field lines of the oval.

Whether extremely high latitude field lines are open or closed and what is the relationship of the high-latitude plasma populations to the boundary plasma sheet are questions of great importance, particularly during times for which the interplanetary magnetic field (IMF) B_z component (in geocentric solar magnetospheric coordinates) is northward. At such times the polar rain is interrupted throughout the cap by bursts of high-intensity (up to solar wind densities) electron fluxes of approximately the same temperature as the polar rain [*Hardy et al.*, 1982; *Hardy*, 1984]. *Winningham and Heikkila* [1974] called these structures "polar showers." It is also at these times that more or less spectacular polar cap arcs occur [*Berkey et al.*, 1976; *Gussenhoven*, 1982; *Frank et al.*, 1982]. Activity in the polar caps, then, has variations which apparently are in

opposite phase to those of the oval and which can be thought of as proceeding from and returning to a quiet state characterized by the widespread occurrence of polar rain.

Two conceptual frameworks for explaining electron precipitation in the caps are in the literature. The first was developed shortly after the discovery of polar rain. It takes polar rain as evidence that the cap field lines are open and directly accessed by the solar wind. In this view, polar rain is the backscattered component of the solar wind with unimpeded entry along the connected field lines [*Fennell et al.*, 1975; *Meng and Kroehl*, 1977; *Mizera and Fennell*, 1978]. The main evidence here is that the precipitation is hemisphere-selective according to IMF sector. Greater polar rain flux is found in the north (south) pole when the IMF is in an away (toward) sector. The difference in fluxes precludes the notion of any effective closing of field lines from the two hemispheres. In addition, the field lines from the cap with the greater electron flux have a sharper discontinuity with the B_x component of the IMF. Much of this method of describing the polar rain entry mechanism is made by analogy to relativistic solar particle entry. (See *Paulikas* [1974] for a review.)

The second approach to the cap dynamics attempts to explain phenomena when the IMF B_z component is northward: the active cap. The suggestion has been made by several [*Meng*, 1981; *Winningham and Gurgiolo*, 1982; *Akasofu et al.*, 1984; *Akasofu and Roederer*, 1984] that for B_z northward a substantial modification is made in the magnetospheric magnetic field configuration: field lines open (or greatly extended down tail) when the IMF is southward close when the IMF reverses. Polar caps defined by regions of open field lines.

165

then, shrink to nothing as the closure becomes complete. In this view, "polar cap arcs" occur on closed field lines, and their source is the boundary plasma sheet expanded poleward. The ion composition and particle spectra of polar cap arcs and neighboring auroral oval arcs would be expected to be similar in this picture, as they have been found to be on at least one occasion [Peterson and Shelley, 1984].

While these views give a pleasing asymmetry in the magnetic field behavior between the B_z-northward and the B_z-southward states, we question whether the understanding of the behavior of particle populations on high-latitude field lines is sufficient to distinguish between a major change in magnetic field morphology and variations in particle dynamics caused by changes in electric fields and currents. Several other facts also need to be considered in this problem: (1) There are other sources for polar rain and polar cap arcs besides the solar wind and the boundary plasma sheet, namely, the cusp mantle and the polar ionosphere. Even if not sources, these particle populations occupy the same field lines as polar rain and polar cap arcs and also vary with IMF conditions. (2) Systematic measurements of electrons at altitudes between 5 and 10 R_E have been made by Yeager and Frank [1976], and of ions and electrons at 60 R_E by Hardy et al. [1979b, c] on field lines connecting to the cap. These measurements show sector structure dependences similar to those of the polar rain, although no distinction was made between times of B_z north or south. (3) Polar rain and polar cap arcs can occur alternately across the cap [Hardy et al., 1982], implying a complex magnetic field configuration if the one occurs on open and the other on closed field lines. (4) There is evidence for the existence of parallel electric fields or potential barriers having broad extent across the cap with values larger than the few electron volts anticipated for polar wind expansion [Winningham and Heikkila, 1974; Foster and Burrows, 1976, 1977; Winningham and Gurgiolo, 1982].

All of these measurements indicate that the phenomena in the polar caps, while occurring with relatively long time scales and comprising weak energy exchanges, are still extremely complex and, in fact, if properly modeled, could have a substantial impact on our understanding of neighboring, more dynamic processes. It is in this spirit that we have reexamined the statistical properties of the polar rain using precipitating electron measurements from the DMSP F2 satellite. In particular, we have identified the large-scale variations across the two horizontal dimensions of the cap as a function of auroral activity, IMF conditions, and season. This study also gives a more precise evaluation of the contribution that precipitating electrons in the polar rain make to the energy and mass budget of the magnetosphere. Section 2 describes the satellite instrumentation; section 3 describes the method of binning and averaging the data. In sections 4–6 we present results from separations by variables Kp, IMF, and season. Finally, in section 7 we discuss the results and their implication for polar cap models.

2. INSTRUMENTATION

DMSP F2, a three-axis stabilized satellite, was launched into a near-sun-synchronous, circular orbit at an altitude of 840 km in June 1977. Its orbital period was 101 min; the nominal inclination was 98.75. At launch the orbit was centered near the 0700–1900 local time meridian, but was subject to a very slow precession toward later local times. Because of the offset between the earth's spin axis and magnetic axis, the orbit had significant diurnal and seasonal variations in the

magnetic local time-magnetic latitude frame of reference. Thus for corrected geomagnetic latitudes (CGL) above 75, full local time coverage is obtained in each 24-hour period; for latitudes above 70 CGL, full local time coverage is obtained throughout the first year of operation in all but the midnight sector (~2300 to 0300). To obtain full local time coverage, the north and south pole data must be combined. South pole coverage is principally on the dayside, while north polar passes lie nearly entirely on the nightside. The region of overlap is a dawn-dusk band, ~7 wide, on the nightside (83 –90 at midnight). A plot of the DMSP F2 orbital coverage is given by Gussenhoven et al. [1983, Figure 1].

A detailed description of the particle detector on DMSP F2 is given by Hardy et al. [1979a]. Briefly, it consists of two curved plate electrostatic analyzers that measure the fluxes of electrons in 16 energy channels between 50 eV and 20 keV, once per second. The apertures of the analyzers always face in the local zenith direction such that at auroral and polar cap latitudes they detect precipitating rather than backscattered and/or trapped electrons. One analyzer covers the energy range from 50 eV to 1 keV with a geometric factor of 4 × 10^{-4} cm² sr and a $\Delta E/E$ of 13%. The other analyzer covers the energy range from 1 keV to 20 keV with a geometric factor of 10^{-3} cm² sr and a $\Delta E/E$ of 9%. The large geometric factors ensure that the flux level for electrons in the diffuse and discrete auroras is well above the detector's sensitivity. In the polar rain, counts in each channel below several hundred electron volts are generally only of the order of 10 or less above background for an accumulation period of 0.1 s; and in channels measuring energies greater than several hundred electron volts, counts must be averaged over considerable time intervals to obtain a signal which is only a fraction of a count per second. Nevertheless, the uniformity of the polar rain gives validity to averaging procedures.

3. SELECTION, CORRECTION, AND BINNING OF DATA

The electron data for each pass of the DMSP F2 satellite are routinely processed at the Air Force Geophysics Laboratory to produce survey plots giving the directional integral flux in (cm² s sr)$^{-1}$, JTOT; the directional energy flux in keV cm² s sr, JETOT; and the ratio of the two, the average energy in keV, EAVE.

These quantities are plotted as functions of universal time in seconds of the day, the geographic and corrected geomagnetic latitudes and longitudes, and the magnetic local time of the satellite all projected to an altitude of 110 km. Typically, the satellite passes through the auroral region on the dawnside (duskside) in the north (south) pole, across the polar cap, and through the auroral region on the duskside (dawnside). High-latitude regions of low-average energy (hundreds of electron volts and low particle flux (10^4 10^5 particles cm² s sr eV) in the 50- to 200-eV range are easily recognized as regions of polar rain in these plots. In order to eliminate regions with highly variable low-energy flux characteristic of the B_z-north state, we imposed a severe uniformity restriction on polar rain intervals selected for the study: the integral flux on time scales of a few seconds could not vary by more than a factor of 5. The variation was generally less than a factor of 2. In polar showers, variations over a few seconds are typically more than an order of magnitude. Additionally, the uniform fluxes were required to persist for a minimum time interval of 2 min (120 spectra and ~800 km).

Examples of intervals of polar rain chosen for study are illustrated by three polar passes shown in Figures 1a, 1b, and
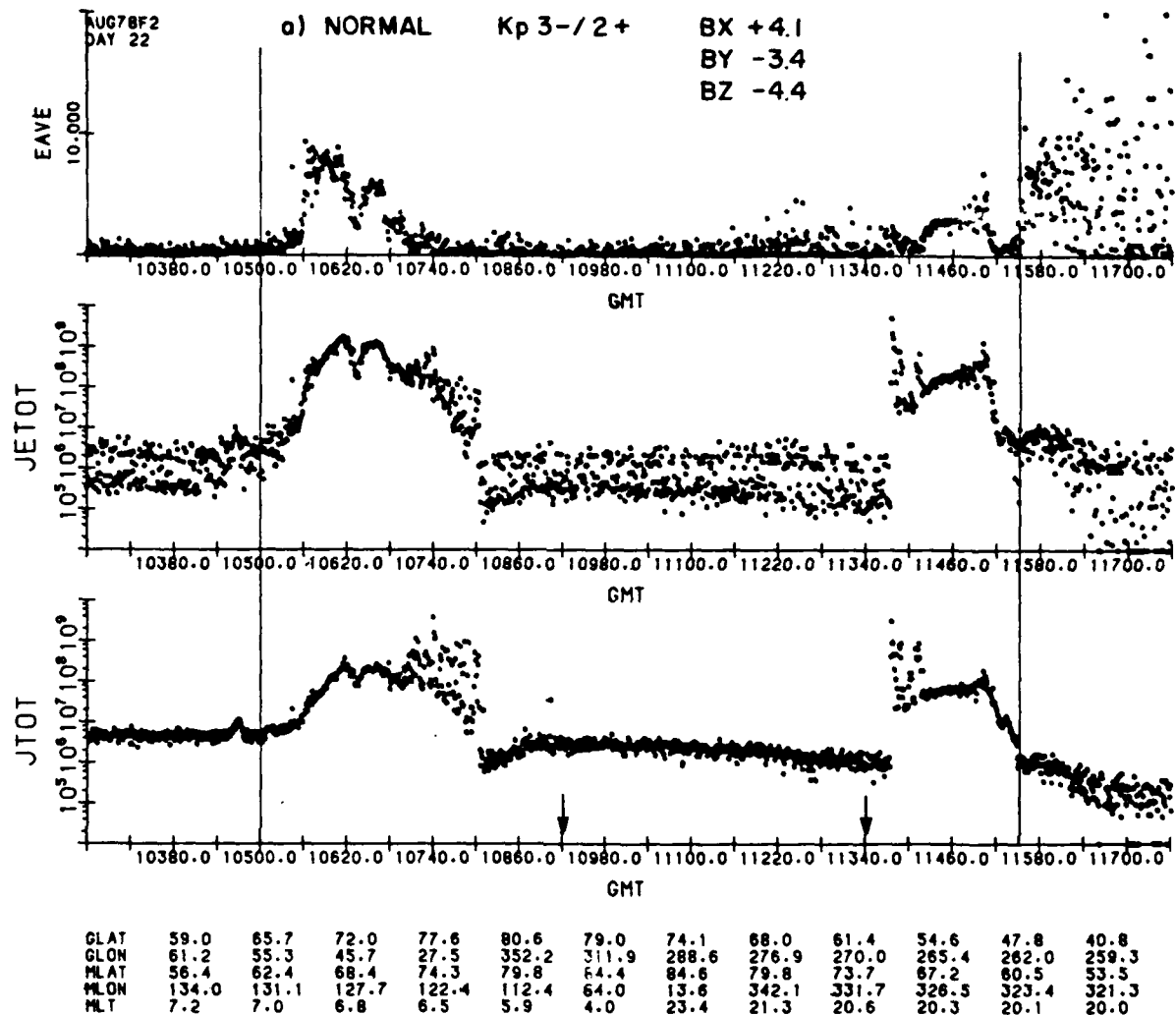
AUG78F2
DAY 22   a) NORMAL   Kp 3-/2+   BX +4.1
                                          BY -3.4
                                          BZ -4.4

EAVE
10.000

GMT
10380.0 10500.0 10620.0 10740.0 10860.0 10980.0 11100.0 11220.0 11340.0 11460.0 11580.0 11700.0

JETOT

GMT
10380.0 10500.0 10620.0 10740.0 10860.0 10980.0 11100.0 11220.0 11340.0 11460.0 11580.0 11700.0

JTOT

GMT
10380.0 10500.0 10620.0 10740.0 10860.0 10980.0 11100.0 11220.0 11340.0 11460.0 11580.0 11700.0

GLAT	59.0	65.7	72.0	77.6	80.6	79.0	74.1	68.0	61.4	54.6	47.8	40.8
GLON	61.2	55.3	45.7	27.5	352.2	311.9	288.6	276.9	270.0	265.4	262.0	259.3
MLAT	56.4	62.4	68.4	74.3	79.8	84.4	84.6	79.8	73.7	67.2	60.5	53.5
MLON	134.0	131.1	127.7	122.4	112.4	64.0	13.6	342.1	331.7	326.5	323.4	321.3
MLT	7.2	7.0	6.8	6.5	5.9	4.0	23.4	21.3	20.6	20.3	20.1	20.0

Fig. 1. Examples of occurrence of polar rain in DMSP/F2 polar crossings. The integral flux, JTOT, in (cm² s sr)⁻¹, the energy flux, JETOT, in keV/cm² s sr, and the average energy, EAVE, in keV are plotted as functions of universal time in seconds, geographic and corrected geomagnetic latitudes and longitudes, and magnetic local time all projected to an altitude of 110 km: (a) Normal polar rain occurring in the north pole on August 22, 1978. (b) High-intensity polar rain occurring in the south pole on the same day. (c) Polar rain contaminated by high-energy solar protons occurring in the south pole on May 1, 1978. Arrows mark intervals of polar rain included in the study. IMF and Kp values are given for each pass.

1c. Figures 1a and 1b are successive passes over the north and south pole, respectively, on August 22, 1978, and Figure 1c is a south pole pass on May 1, 1978. Vertical lines show entry into and exit from the diffuse aurora on either side of the oval. Increases in integral flux equatorward of the vertical lines that have high, but noisy average energies are a result of increased background from high-energy protons in the radiation belts that penetrate the detector casing and directly stimulate the channeltrons. All three examples occur during Kp moderate and B_z negative. The first two passes occur in a toward sector; the third pass occurs in an away sector. Arrows mark the intervals of polar rain selected for use in the study.

The three passes in Figure 1 also illustrate three divisions made in the data set. Figure 1a shows "normal" polar rain for which the total integral flux of the polar rain is below 10⁷ particles/cm² s sr. Passes in this category had integral fluxes as low as ~4 × 10⁵ particles cm² s sr. Of the cases used, 73% fell in this category. A "high" level of polar rain is shown in

Figure 1b and is a pass in which the integral flux reaches (or exceeds) ... found in one polar cap only and is often the high end of a steep gradient, as is the case here. We point out that the requirement of uniformity in the flux level does not extend over the large spatial domain of this example. High levels of polar rain were found in 19% of the selected intervals.

Figure 1c is an example of increased instrumental background from high-energy solar protons in polar cap absorption (PCA) events, a phenomenon similar to the radiation belt background mentioned previously. Cases of contamination of the low-energy data by the background are usually easy to recognize in the survey plots because of the high average energy that results (here about 5 keV) and because they are long lived (of the order of days). They also exhibit selection by pole as is expected of high-energy particle entry. At the beginning and end of such periods, however, and during weak events, such contamination is not so evident. For this reason

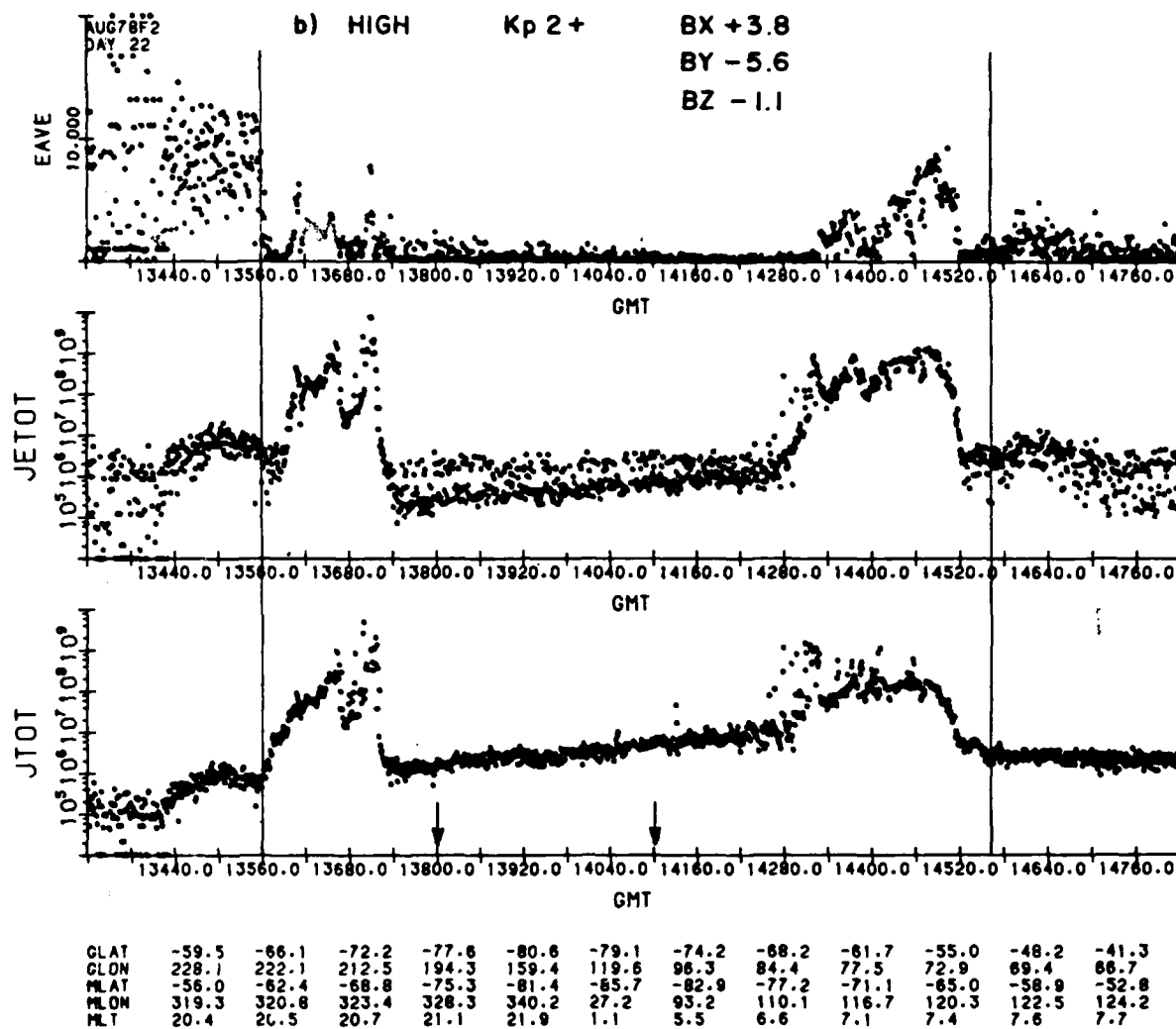| GLAT	-59.5	-66.1	-72.2	-77.6	-80.6	-79.1	-74.2	-68.2	-61.7	-55.0	-48.2	-41.3
GLON	228.1	222.1	212.5	194.3	159.4	119.6	96.3	84.4	77.5	72.9	69.4	66.7
MLAT	-56.0	-62.4	-68.8	-75.3	-81.4	-85.7	-82.9	-77.2	-71.1	-65.0	-58.9	-52.8
MLON	319.3	320.8	323.4	328.3	340.2	27.2	93.2	110.1	116.7	120.3	122.5	124.2
MLT	20.4	20.5	20.7	21.1	21.9	1.1	5.5	6.6	7.1	7.4	7.6	7.7

Fig. 1. (continued)

we established a procedure for eliminating background in all the data. Figure 2 shows individual 1-s spectra for each of the passes in Figure 1. The normal and high polar rain spectra fall to below threshold by 1 keV. The contaminated spectrum has a high-energy tail that falls as $\sim E^{-1}$. This is the expected spectral shape for this detector when an equal number of counts occur in each channel (background from high-energy protons). A correction for such background is made by using as a background count, the count in the highest-energy channel for the higher-energy detector (1–20 keV), and the count times the ratio of the cross-sectional areas of the channeltrons of the two detectors for the lower-energy detector (50 eV to 1 keV). We apply this correction routinely to all cases of polar rain. While in theory the correction should give reasonable results for all passes, we chose to eliminate the contaminated cases (8% of the total) from our statistical study.

Data were obtained from a survey of all DMSP F2 passes in the 1-year interval September 1977 to August 1978. Each 1-s spectrum of polar rain was assigned a value of magnetic activity, Kp; a value of corrected geomagnetic latitude (CGL); and a value of magnetic local time (MLT). In order to bin the spectra in zones of equal area, the CGL-MLT coordinate

system at 110 km was treated as planar, and a Cartesian coordinate system of 1 (along the noon-midnight axis) by 1 (along the dawn-dusk axis), or ~ 110 km $\times$ 110 km, was superimposed. Separation by two levels of Kp was made: 0 to 2+ (designated henceforth as Kp 02), and 3– to 5+ (Kp 35); as well as by pole. Separation by the sign of the IMF B_x and B_y component was made using hourly averaged values listed in supplement 1 of the Interplanetary Medium Data Book [King, 1979]. No time delay was used in assigning values. More than 380,000 spectra in all were used. This number is reduced by approximately one half when assignment of IMF data is required. The distribution of the whole data set by season is summer, 24%; winter, 24%; spring and fall, 52%. The distribution of data with B_z is as follows: 32% of the data occur for positive B_z, the majority at values less than 4 nT, trailing off up to 12.5 nT; the remaining 68% of the data occur for negative values of B_z up to −19.5 nT. The distribution in B_z is in agreement with the results of Hardy [1984] which show that for B_z north, electron precipitation other than polar rain occurs in the polar cap. In sorting the data set by B_x and B_y, we use the findings of Yeager and Frank [1976] and Meng and Kroehl [1977] and group the north (south) pole toward sector with the south (north) pole away sector; we find
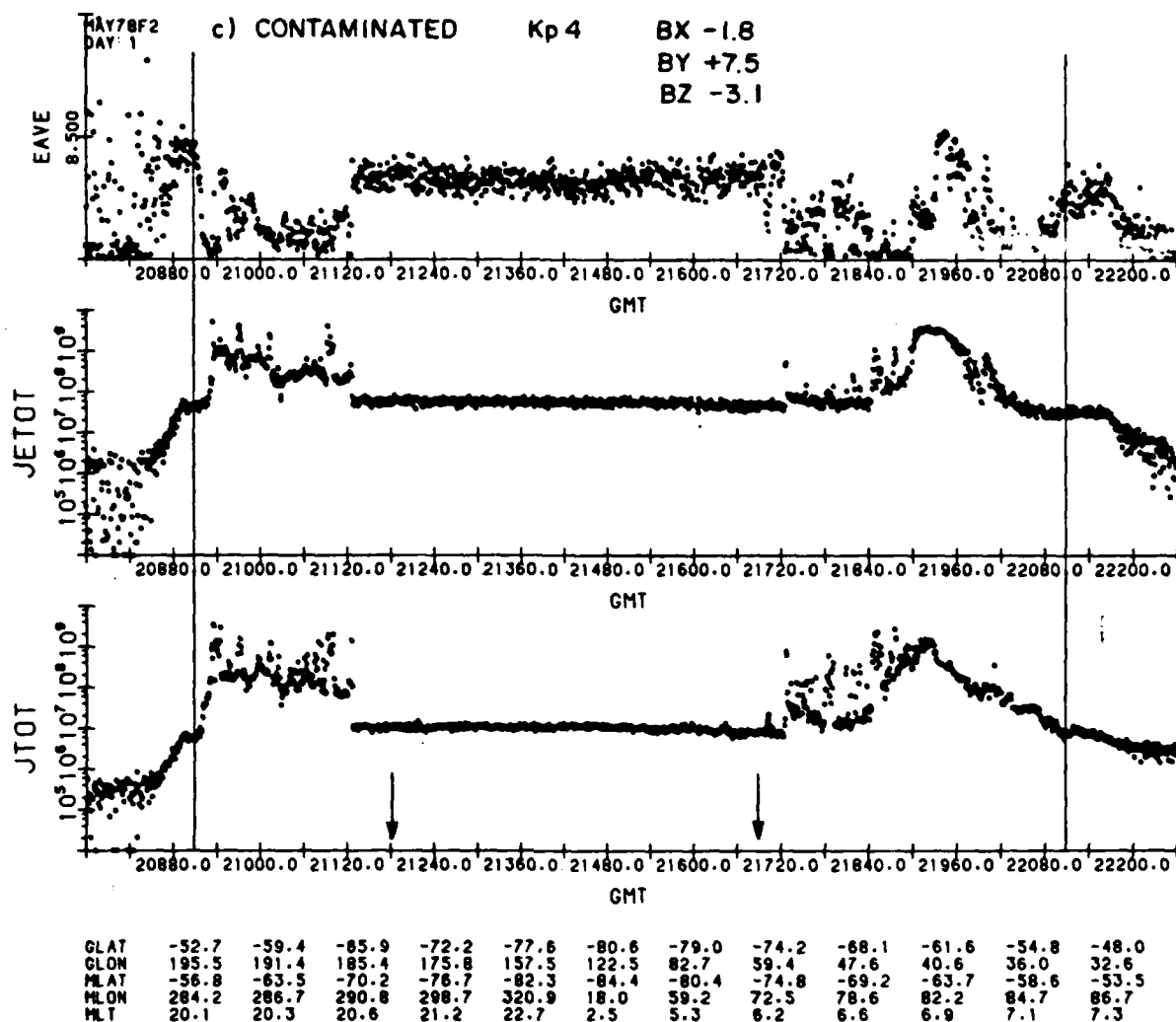
MAY78F2
DAY 1

c) CONTAMINATED   Kp 4   BX -1.8
                                      BY +7.5
                                      BZ -3.1

EAVE
8.500

20880|0 21000.0 21120.0 21240.0 21360.0 21480.0 21600.0 21720.0 21840.0 21960.0 22080|0 22200.0

GMT

JETOT
$10^5 10^6 10^7 10^8 10^9$

20880|0 21000.0 21120.0 21240.0 21360.0 21480.0 21600.0 21720.0 21840.0 21960.0 22080|0 22200.0

GMT

JTOT
$10^5 10^6 10^7 10^8$

20880.0 21000.0 21120.0 21240.0 21360.0 21480.0 21600.0 21720.0 21840.0 21960.0 22080.0 22200.0

GMT

GLAT	-52.7	-59.4	-85.9	-72.2	-77.6	-80.6	-79.0	-74.2	-68.1	-61.6	-54.8	-48.0
GLON	195.5	191.4	185.4	175.8	157.5	122.5	82.7	59.4	47.6	40.6	36.0	32.6
MLAT	-56.8	-63.5	-70.2	-76.7	-82.3	-84.4	-80.4	-74.8	-69.2	-63.7	-58.6	-53.5
MLON	284.2	286.7	290.8	298.7	320.9	18.0	59.2	72.5	78.6	82.2	84.7	86.7
MLT	20.1	20.3	20.6	21.2	22.7	2.5	5.3	6.2	6.6	6.9	7.1	7.3

Fig. 1. (continued)

59% (41%) of the spectra in the combined grouping. In addition, 38% (62%) of the spectra occurred in the south (north) pole, reflecting the lesser high-latitude orbital coverage in the southern hemisphere.

A corrected average spectrum was calculated for each grid point binned by Kp and IMF sector. Typically, the standard deviation for each spectral point was 50–100% of the average value. Deviations of this size are normal in large statistical studies of magnetospheric parameters. From the average spectrum, the average integral flux, energy flux, and average energy were calculated.

4. VARIATIONS IN THE AVERAGE
ENERGY AND INTEGRAL FLUX:
NO SEPARATION BY IMF

Plates 1a and 1b are color spectrograms of the total number of spectra (number), the average integral number flux (IF), and average energy (AE) for the two Kp bins, Kp 02 (Plate 1a, top, and Plate 1b, left column) and Kp 35 (Plate 1a, bottom and Plate 1b, right column). No separation other than by Kp was used (except exclusion of contaminated spectra, as stated earlier). The spectrograms are plotted in CGL-MLT coordinates. The CGL coordinates measured from the magnetic pole along

the noon-midnight and the dawn-dusk axes are shown on the sides of each spectrogram. Local noon is at the center top of each plot: dawn is middle right. A key to the color coding is given at the right-hand side of each spectrum. The color separations are equal linear steps for number and average energy (in keV) and in equal logarithmic steps for the integral flux (in (cm² s sr)⁻¹). Maximum and minimum color values are given. (The log of IF is given: other values are integral.)

The spectrograms of the number of cases (Plate 1a) show that the largest sampling of polar rain occurs in the center of the cap where south pole orbits (covering dayside to midcap) and north pole orbits (covering midcap to nightside) cover the same latitude-local time area. The poorest sampling is on the dayside and at the equatorward edges of the cap, where particle enhancements above the level of the polar rain are often continuous with the cusp region or the oval. To avoid including such enhancements, we have been extremely conservative in choosing intervals of polar rain near the oval (see Figure 1) leading to the poorer sampling rate there. The high sampling rate at the midnight region boundary and the sameness of this boundary for the two Kp bins results from the lack of orbital coverage below the boundary, as mentioned in section 2. A consequence of the selection method and the orbital coverage
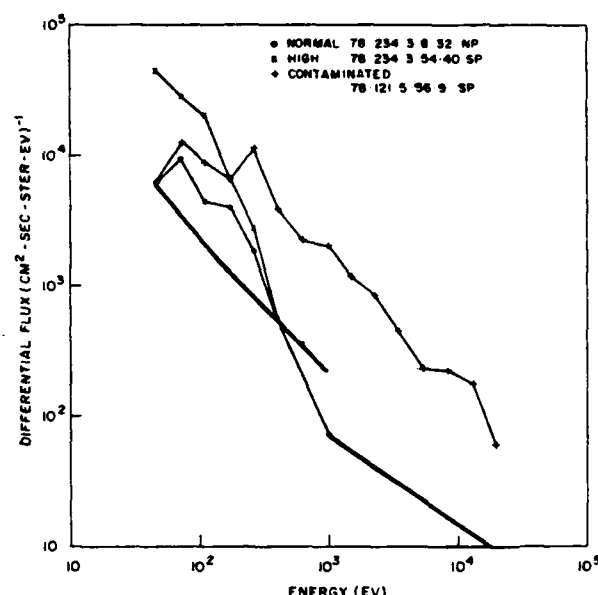
Fig. 2. Polar rain spectra from the examples shown in Figure 1: normal polar rain (circles) from August 22, 1978, 0303:32 (11012 s) UT; high polar rain (crosses) from August 22, 1978, 0354:40 (14080 s) UT; contaminated polar rain (pluses) from May 1, 1978, 0556:09 (21369 s) UT.

is that the distribution of number of cases does not represent frequency of occurrence. Nevertheless, we can use the edges of the sample as an indication of the approximate size of the polar cap. A rough circular fit to the limits of each sample (not taking into account the spherical curvature of the earth and ignoring the artificial midnight region boundary) is shown in Plate 1a. The circle is offset toward 2300 MLT by ~5° (~3°) and has a radius of 15 (16.5°) for Kp 02 (35). The polar cap becomes larger and more spherically symmetric about the geomagnetic pole as magnetic activity increases.

In the integral flux and average energy (Plate 1b, top and bottom), systematic local time–latitude variations are evident. The axis of symmetry of the variations (or the axis of maximum gradient in the variations) is prenoon to premidnight. Along this axis the variations are bandlike. The integral flux decreases from day to night, while the average energy increases. The overall range of average values for the two quantities is approximately the same for both Kp bins. Integral flux varies from 10^6 to 2×10^7 electrons/cm^2 s sr, and average energy varies from 150 eV to 600 eV. For higher Kp values a larger portion of the cap is filled with the more intense, cooler fluxes than for quieter periods.

A prenoon to premidnight gradient appears to be the fundamental variation in polar rain morphology. For all separations of the data (by season, by components of the IMF, for normal and for high polar rain) a noon-midnight variation in the same sense emerges. In some cases there is a slight rotation of the axis of symmetry (see section 5). Often the noon-midnight variation is less regular than in Plate 1, primarily because of reduced statistics caused by additional separations. In such separations the bandlike nature of the variation generally persists in the noon sector (where the fluxes are highest), but breaks up into patches in the midnight sector, leaving an extension of low midnight fluxes along the edges of a substantial portion of the cap. When only normal polar rain cases are used, the gradients are much reduced and confined more to

the edges of the polar caps. For these cases, large sections of the center of the cap have near-uniform values of flux and average energy.

The total cap area, total number flux, and total energy flux are given in Table 1 for the two Kp separations. Also given are the percent differences between the two cases. Assuming that the flux is isotropic over the downcoming hemisphere, the total number of electrons entering the cap in the polar rain is 1.0×10^{24} s^{-1} (2.1×10^{24} s^{-1}), and the energy flux into the cap is 4.7×10^7 W (8.7×10^7 W) for Kp 02 (Kp 35). Although the cap size varies by only 21% between quiet and moderate activity, the particle flux and energy flux increase by about 50%.

5. VARIATIONS IN THE AVERAGE ENERGY AND INTEGRAL FLUX: SEPARATION BY B_y

We present here separation of the polar rain data by B_y, maintaining the separation in Kp. Separation of the data by B_x was found to be indistinguishable from B_y separations (comparing separations of opposite sign). In the separation, north pole B_y positive (away sector) data are grouped with south pole B_y negative (toward sector) data; and vice versa. In the text we refer to the above groupings only by north pole assignments: B_y positive and B_y negative, respectively. The availability of IMF data and the separation by B_y reduced the total spectra used to produce each map to approximately one quarter of the total available in the separation by Kp alone. Plates 2 and 3 are plots of the integral flux and the average energy for Kp 02 and Kp 35 with the B_y separation. The integral flux (average energy) is shown in the top (bottom) row; and B_y positive (negative) in the left (right) column. Because of the smaller sample the polar cap boundaries are higher, more irregular, and harder to interpret than those for the total.

As was the case for the total distribution, the low and high Kp distributions in the B_x and B_y separations differ principally by flux intensity. Therefore our focus will be on the high Kp range (high intensities) shown in Plate 3. The range in integral flux for B_y positive (away sector) is a factor of 2 greater than that for B_y negative (toward sector), $(2.8–20) \times 10^6$ electrons/cm^2 s sr as compared to $(1–11) \times 10^6$ electrons/cm^2 s sr. The distribution of the flux range across the cap is quite different in the two cases. For B_y positive the polar rain intensity is highest on the dayside, prenoon, and lowest on the nightside, premidnight, which is similar to the bandlike structure without the B_y separation. For B_y negative the flux for most of the cap falls below the lowest levels of the B_y positive cap: $(1–3.9) \times 10^6$ particles cm^2 s sr. Higher fluxes are limited to a small region on the dayside, presumably just poleward of the cusp. Overall, the B_y negative cap is more symmetric dawn to dusk than the B_y positive cap. In Figure 3 we have plotted the average number flux along the noon-midnight meridian for each separation in B_y and for Kp 35. The averages were performed over 5 square bins on either side of the noon-

TABLE 1. Polar Cap Integrated Quantities: Total Sample

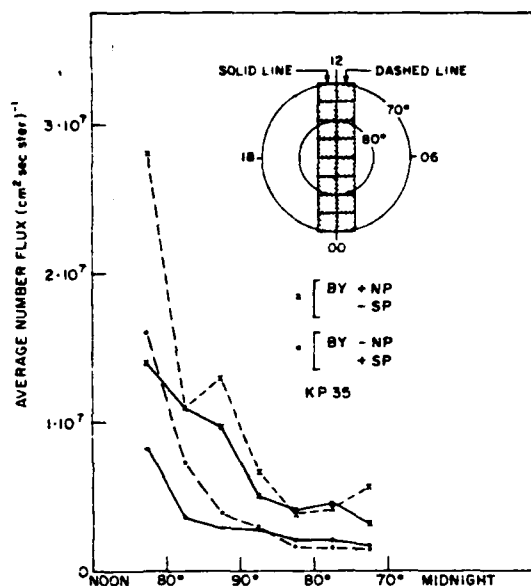|	Area, cm^2	IF, (s sr)$^{-1}$	EF, keV s sr
Kp 02	0.86×10^{17}	3.3×10^{23}	0.94×10^{23}
Kp 35	1.09×10^{17}	6.7×10^{23}	1.73×10^{23}
% difference	21	51	46

IF is integral flux. EF is energy flux.

Fig. 3. Polar rain number flux in (cm² s sr)⁻¹ averaged over 5 square bins on either side of the noon-midnight meridian, plotted as a function of latitude, for Kp 35. The cases for B_y positive (negative) in the north (south) pole are represented by circles, and the opposite IMF signature by pluses.

energy data corresponding to the integral flux data in Figure 3 are plotted by latitude across the noon-midnight meridian.

The anticorrelation between the integral flux and the average energy is remarkably consistent for all separations and for all parts of the cap. Averages of these quantities in the large 5 bins across the whole cap are plotted against one another in Figure 5. Here circles (triangles) represent low-activity (high-activity) bins for B_y positive; and crosses (pluses) represent the low-activity (high-activity) bins for B_y negative. No points were excluded, even though the number of samples was small in some bins. The results show a clear linear relationship between the parameters. A linear regression gives a correlation coefficient of -0.86. For the integral flux in (cm² s sr)⁻¹ and the average energy in electron volts the linear regression equation is $\log IF = 7.51 - EAVE/357$.

Average spectra at extreme ends of the noon and midnight meridian in the cap are plotted for the two B_y separations and Kp 35, in Figure 6. Compared to the dayside spectra, the midnight spectra have decreased fluxes at low energies (by more than an order of magnitude for B_y positive) and increased fluxes above 1 keV. Further, the lower fluxes in the B_y negative cases are harder than comparable spectra in the B_y positive cases. That is, low-level fluxes, whether within a given cap (i.e., in the midnight region) or in a given hemisphere, appear to be accompanied either by energization or by admixtures of higher-energy fluxes.

Integrated values of the average quantities for separations of the data by B_y and Kp are given in Table 2. As in the total distribution, the increase in magnetic activity from Kp 02 to Kp 35 increases the number flux and energy flux by approximately a factor of 2, with a somewhat larger increase in the B_y positive cap. For higher activity the difference between the B_y positive and the B_y negative cap is greater: 56% (43%) for the
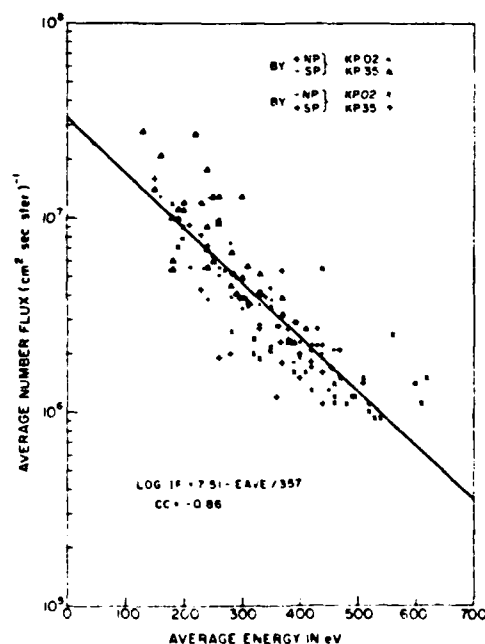
midnight meridian as shown in the inset. We note that at lowest latitudes in the midnight and noon sectors the difference for fluxes in the two sectors for B_y positive and negative is uniform, at about a factor of 2. The ratio of fluxes of B_y positive to those of B_y negative increases, however, as one approaches the magnetic pole, reaching values as high as 5.

The variations in average energy follow the flux in an inverse sense, as in the total distributions. For both signs of B_y the average energy for Kp 35 ranges from 100 to 150 eV on the dayside and from 400 to 600 eV on the nightside. The rotation of the axis of symmetry between B_y positive and B_y negative is clearly seen in the average energy distributions. The gradients in average energy are greater for B_y negative than for B_y positive, as is shown in Figure 4. Here the average

Fig. 4 Polar rain average energy in electron volts plotted as a function of latitude on either side of the noon-midnight meridian, in the same format as Figure 3

Fig. 5 Average number in (cm² s sr)⁻¹ plotted against the corresponding average energy in electron volts for MLT-CGL bins of 5 square. For B_y positive (negative) in the north (south) pole the data points are represented by circles (triangles) for Kp 02 (35). For B_y negative (positive) in the north (south) pole the data points are represented by crosses (pluses) for Kp 02 (35).
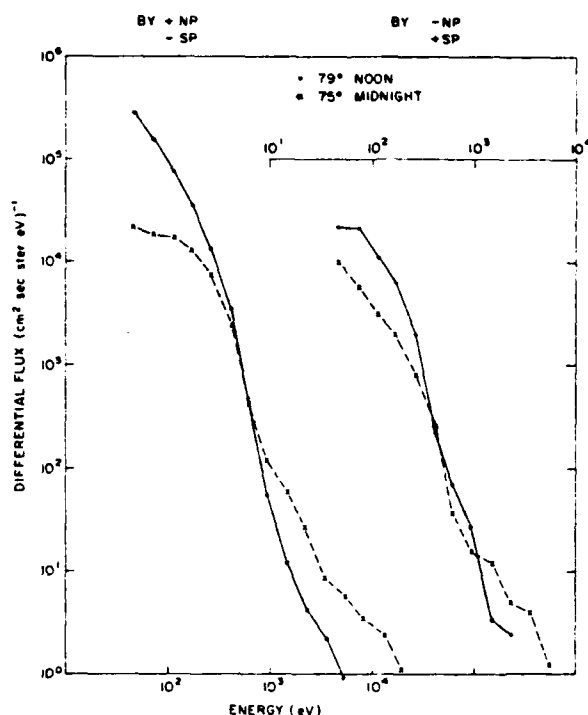
171

Fig. 6. Average polar rain spectra at 79 CGL, noon (circles) and at 75 CGL, midnight (crosses) for B_y positive (negative) in the north (south) pole (left-hand side) and for B_y negative (positive) in the north (south) pole (right-hand side). Kp is 35; the lower (upper) energy scales are appropriate to the spectra on the left-hand (right-hand) side.

number flux (energy flux) as compared to 36% (32%) at Kp 02.

Finally, there appears to be a difference in the cap shape, or difference in the polar rain access region for the two signs of B_y. The cap extends to lower latitudes in the postnoon region for B_y negative. There is a less well-defined move of the cap boundary to lower latitudes in the prenoon region for B_y positive. Little difference exists between the two states in the midnight region.

In summary: (1) There is strong hemispheric selection of polar rain by sector. (2) Polar rain fluxes are always greater on the dayside. (3) Polar rain fluxes are greater on the morning flank for north pole (south pole) away sectors or B_y positive (toward sectors or B_y negative). There does not appear to be reciprocal asymmetry, giving higher fluxes in the evening sector, for the reversed IMF configuration. (4) The average energy of the polar rain varies inversely with the log of the number flux (5) The shape of the cap is lopsided on the dayside according to the sign of B_y.

6. ADDITIONAL SEPARATIONS

Separations of the polar rain data were made with parameters other than Kp and B_y. We summarize the results of the separations here without presenting the data.

Separation by B_z. The data were divided into three, near-equal parts: $B_z < -2.5$ nT; $-2.5 < B_z < 0$ nT; and $B_z > 0$ nT. No correction was made in assigning B_z values to the polar rain data for propagating the IMF data from their measured position to the cap, or for the observed high-latitude magnetospheric response time to changes in the IMF [*Hardy et al.*, 1982] For B_z weakly negative ($-2.5 < B_z < 0$ nT) the

	Area, cm^2	IF, (s sr)$^{-1}$	EF, keV/s sr
Kp 02			
$B_y + NP (B_y - SP)$	0.59×10^{17}	2.2×10^{23}	0.62×10^{23}
$B_y - NP (B_y + SP)$	0.68×10^{17}	1.4×10^{23}	0.47×10^{23}
Kp 35			
$B_y + NP (B_y - SP)$	0.75×10^{17}	5.9×10^{23}	1.38×10^{23}
$B_y - NP (B_y + SP)$	0.82×10^{17}	2.6×10^{23}	0.78×10^{23}

IF is integral flux. EF is energy flux. NP is north pole. SP is south pole.

variations in integral flux, energy flux, and average energy were indistinguishable from the results for $B_z > 0$, and both, in turn, were nearly identical to the Kp 02 results (Plate 1). One difference is that in both B_z separations, values of the average energy were higher by between 50 and 100 eV in the nightside cap than for the Kp 02 separation. For $B_z < -2.5$ nT, the results were very similar to those for Kp 35. Comparing these two cases in detail showed that the average energy was somewhat lower (~ 50 eV) in the nightside cap for the B_z separation.

Separations by pole, B_z, and B_y. A separation by north and south pole, positive and negative B_z, and positive and negative B_y was made for the following reasons: to check the validity of combining north and south pole data of opposite sectors and to uncover obvious correlations between B_y and B_z. North and south pole data overlap only in the midcap. Thus separation by pole does not affect the individual bin sample size except in the midcap where the best sampling occurred. (See Plate 1.) These same orbital characteristics limit comparison of day-night trends in both caps to the midcap region where the gradients are not large.

For the four separations (B_z positive, negative; B_y positive, negative) the midcap overlap values of integral flux and average energy were very nearly the same. Further, in all cases, the trends of decreasing flux and increasing average energy toward midnight are clear in each hemisphere taken separately: from day (midcap) to midcap (night) in the south (north) pole.

No obvious combined B_z-B_y effects could be seen. However, the dependence of the shape of the polar cap (access region of polar rain) on B_y, discussed in section 5, was again observed. For B_z positive the access region is additionally confined almost entirely to the nightside. Sketches of the outlines of the polar rain data sample regions for the B_z-B_y combinations are shown in Figure 7. The dashed (solid) lines show polar rain regions in CGL-MLT coordinates for B_z negative (positive) and for each sign of B_y. As before, for B_z negative there is a small, but clear indentation in an otherwise near-symmetric cap which lies either prenoon or postnoon depending on the sign of B_y. For B_z positive the cap is even more strongly lopsided in the same sense, and, in addition, there is very little extension of the cap into the dayside region below ~ 85 CGM.

Separation by season. The data were separated by season and by Kp. The seasons are defined as the three months centered on the equinoxes and the solstices. Corresponding seasons in opposite hemispheres were combined. The percentage occurrence by season is given in section 3. There is a regular variation in the polar rain integral flux with season. This is true for both low and moderate Kp separations. For Kp 35, which has the stronger variation of the two activity separations, intense fluxes ($>6 \times 10^6$ (cm^2 s sr)$^{-1}$) fill almost the
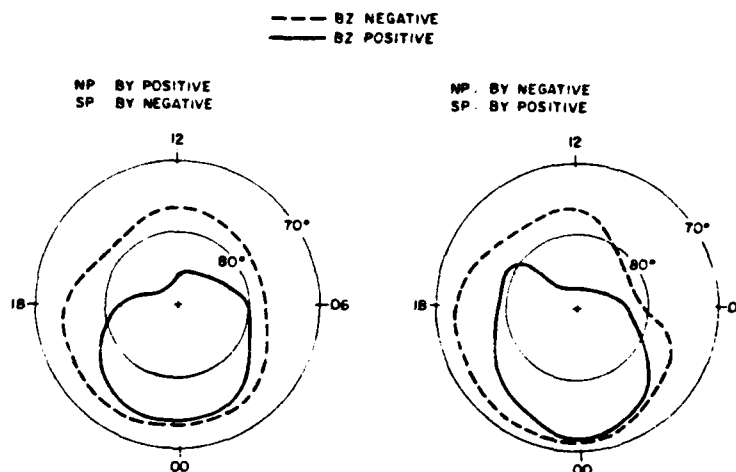
Fig. 7. Regions of polar rain accessibility in corrected geomagnetic latitude and magnetic local time polar plots. The dashed (solid) lines are for cases of B_z negative (positive). The left-hand (right-hand) plot is for B_y positive (negative) in the north pole and the opposite sign of B_y in the south pole.

entire summer cap, are confined mostly to the dayside for equinoctial seasons, and occur only in the prenoon sector in the winter. The average energy variations, however, are increasing from day to night in approximately the same way from season to season. It should also be noted that the band-like variations in number flux and average energy seen in the total distribution (Plate 1) are far more regular across the whole cap for equinoctial seasons than for those centered on the solstices.

7. DISCUSSION

The observational results may be summarized as follows:

1. In all separations of the data, polar rain fluxes are highest on the dayside of the cap.

2. The average polar rain number and energy flux increases with magnetic activity (or equivalently with increasing negative B_z), as does the size of the polar rain precipitation region.

3. In all cases the average precipitation is much weaker than in the auroral oval. However, because the precipitation occurs over such a large area, the total contribution to the polar ionosphere of $\sim 10^{24}$ electrons/s and $\sim 10^8$ W is only 1–2 orders of magnitude less than the rates into the auroral oval [Hill, 1974; Spiro et al., 1982].

4. The polar rain fluxes are higher in the north (south) pole for away (toward) sectors in which B_y is positive (negative). This is in agreement with previously published results [Fennell et al., 1975; Meng and Kroehl, 1977; Yeager and Frank, 1976]. For the IMF configuration resulting in higher polar rain fluxes the day/night variation is reasonably symmetric about an axis running across the cap slightly prenoon to premidnight. For the alternate case, where polar rain fluxes are lower, the axis is oriented more from noon to midnight, but does not rotate such that the eveningside fluxes are higher than the morningside fluxes. This latter finding is significantly different from the dawn-dusk, B_y-dependent polar rain asymmetry proposed by Meng et al. [1977].

5. The average energy and number flux of the polar rain vary together in a consistent manner. Regions of high (low) flux are regions of low (high) average energy. The anticorrelation between number flux and average energy is quite high and exists over all local times and both poles, for all IMF separations, and for all geomagnetic activities.

6. Higher average number and energy fluxes occur in the sunlit cap (summer) than in the darkened cap (winter).

The primary purpose of this report is presentation of observational results. Nevertheless, we wish to make some comments on the relationship of our observations to others and to suggest what additional information is necessary to model these weakest of high-latitude plasma interactions.

To explain the morphology of polar rain precipitation, we require knowledge of (1) the source of electrons and ions in the tail lobes, (2) the mechanisms by which the plasma is transported (and, possibly, heated) from the sources, through the lobes, and out, and (3) the means by which the electrons are precipitated, and, in particular, the mechanism for pitch angle diffusion if diffusion is required.

A schematic representation of the tail lobe and its adjoining regions is shown in Figure 8. In Figure 8 we note the four possible sources of lobe plasma: (1) the ionosphere, at low altitudes, (2) the magnetosheath over the top lobe surface, (3) the boundary plasma sheet near the equatorial surface, and (4) direct solar wind access far down tail where the magnetopause and magnetosheath have lost their identity.

In some instances, plasma from these various sources has been measured. At the position marked 1 in Figure 8, the polar wind has been theoretically predicted [Banks and Holzer, 1968, 1969; Axford, 1968] and experimentally observed [Hoffman and Dodson, 1980; Gurgiolo and Burch, 1982]. Light ions with low-altitude temperatures of $O[0]$ eV (where $O[n]$ indicates order of magnitude n) are measured to have supersonic velocities $O[1]$ km/s at altitudes of $O[3]$ km with outward fluxes of $O[8]$ (cm^2 s)$^{-1}$. Sharp et al. [1981] and Shelley et al. [1982] have reported outward flows of O+ comparable to or exceeding that of H+ in the tail lobes at <20 R_E and at the DE orbit (<5 R_E), respectively. While these ions have fluxes similar to those predicted by polar wind theory, $O[6]$ (cm^2 s)$^{-1}$ at 5 R_E and $O[3]$ (cm^2 s)$^{-1}$ at 20 R_E, they are considerably warmer than polar wind hydrogen [Gurgiolo and Burch, 1982], and their escape from the ionosphere, not predicted by polar wind theory, is currently unexplained.

At the position marked 2, the dayside cusp and magnetosheath populations have easy access to the lobes and form the mantle [Schopke and Puschmann, 1978; Rosenbauer et al., 1975]. The mantle is characterized by a transition in the magnetic field from a variable magnetosheath field to the highly
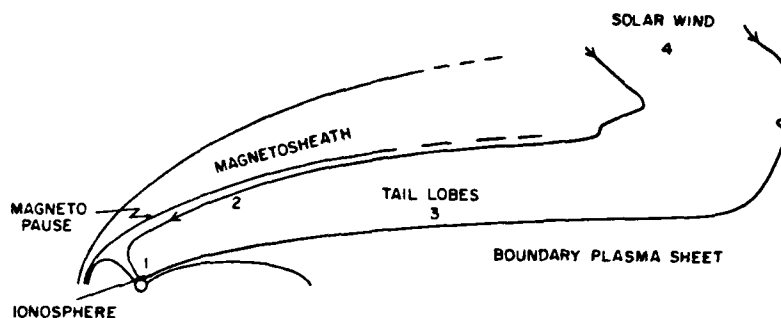
Fig. 8. Schematic illustration of the northern tail lobe and surrounding plasma populations: (1) the ionosphere, (2) the magnetosheath-cusp, (3) the boundary plasma sheet, and (4) the solar wind.

ordered lobe field. While the temperature of the ions in the mantle near the magnetosheath at $<15\ R_E$ is similar to that in the magnetosheath, the density falls from magnetosheath values, $O[1]$ cm^{-3}, by 2 orders of magnitude over mantle thicknesses that can be as large as several earth radii. The antisolar streaming velocity of mantle ions is reduced from that in the magnetosheath to ~ 100 km/s. At lunar distances (60 R_E), ion populations are measured streaming antisunward with velocities $O[2]$ km/s, densities from 0.01 to 5 cm^{-3}, and temperatures generally <30 eV [Hardy et al., 1979b]. While Hardy et al. [1979b] interpreted these plasma observations as arrival of mantle plasma through convection to the position of the moon (see also Pillip and Morfill [1978]), Sharp et al. [1981] have suggested that some of these observations may include the warm $O+$ flow seen by them at 20 R_E.

Evidence for solar wind or magnetosheath plasma entry across the magnetopause bordering the tail lobes has not been established for ions, although the very existence of polar rain has been taken to be such evidence for electrons [Fennell et al., 1975; Mizera and Fennell, 1978]. For low-energy plasma such entry is problematic. Although direct connection of magnetic field lines from the lobes and solar wind is generally assumed to occur to some degree [see Voigt, 1981; Stern, 1973, 1977; Heikkila, 1984], the polarization electric fields and currents at the magnetopause should strongly affect any low-energy plasma in the process of entering the magnetotail. We think it doubtful that there is any region down tail where the processes at the magnetopause would be sufficiently weak to allow the more energetic component of either the solar wind or the magnetosheath to have direct entry to the tail lobes. Nevertheless, the fact that higher levels of polar rain (and a cooler electron population) occur in the north (south) polar cap in an away (toward) sector, when compared to the opposite hemisphere, is an argument for this simple picture, since the preferred caps are those that would be more directly connected to the sun.

The remaining contiguous population is the boundary plasma sheet. This is also a doubtful source, since in order to populate the tail lobe this plasma would have to move, by diffusion or other processes, against the direction of convection by the large-scale magnetospheric electric field.

A comparison of the electron spectra observed in the tail lobes in the energy range from 40 eV to 1 keV is shown in Figure 9. Here we compare DMSP measurements with ISIS 1 measurements at 3000 km [Winningham and Heikkila, 1974], IMP 5 measurements between 5 and 10 R_E [Yeager and Frank, 1976], and observations at the lunar surface [Hardy et al., 1979c]. One notes that while the high-energy portion of

the electron spectrum becomes more prominent with distances down tail, the range in intensities for electrons at ~ 100 eV is quite similar throughout the lobes. This indicates that the electron density and pressure should be reasonably constant along the magnetic field lines on which polar rain occurs.

Two other points on polar rain measurements are important. First, at all altitudes the polar rain electrons are isotropic outside the atmospheric loss cone. This indicates either a continuous and uniform source for the entire tail lobes or maintenance of strong pitch angle diffusion across the loss cone with less restrictive requirements on the source. Second, in all measurements reported to date, no warm streaming ions have been observed in association with the polar rain. While the instrumental limitations of the measurement have been carefully discussed [Winningham and Heikkila, 1974; Yeager and
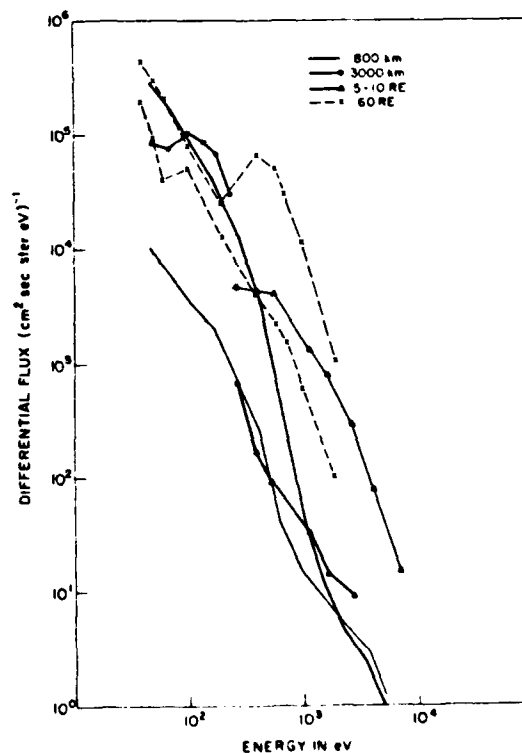

Fig. 9   Electron spectra at different altitudes in the polar cap-tail lobe region. Narrow-lined spectra are from the DMSP F2 satellite at 800 km, circles represent spectra from ISIS 2 at 3000 km, triangles from IMP 5 at 5-10 R_E, and crosses from the moon at 60 R_E.
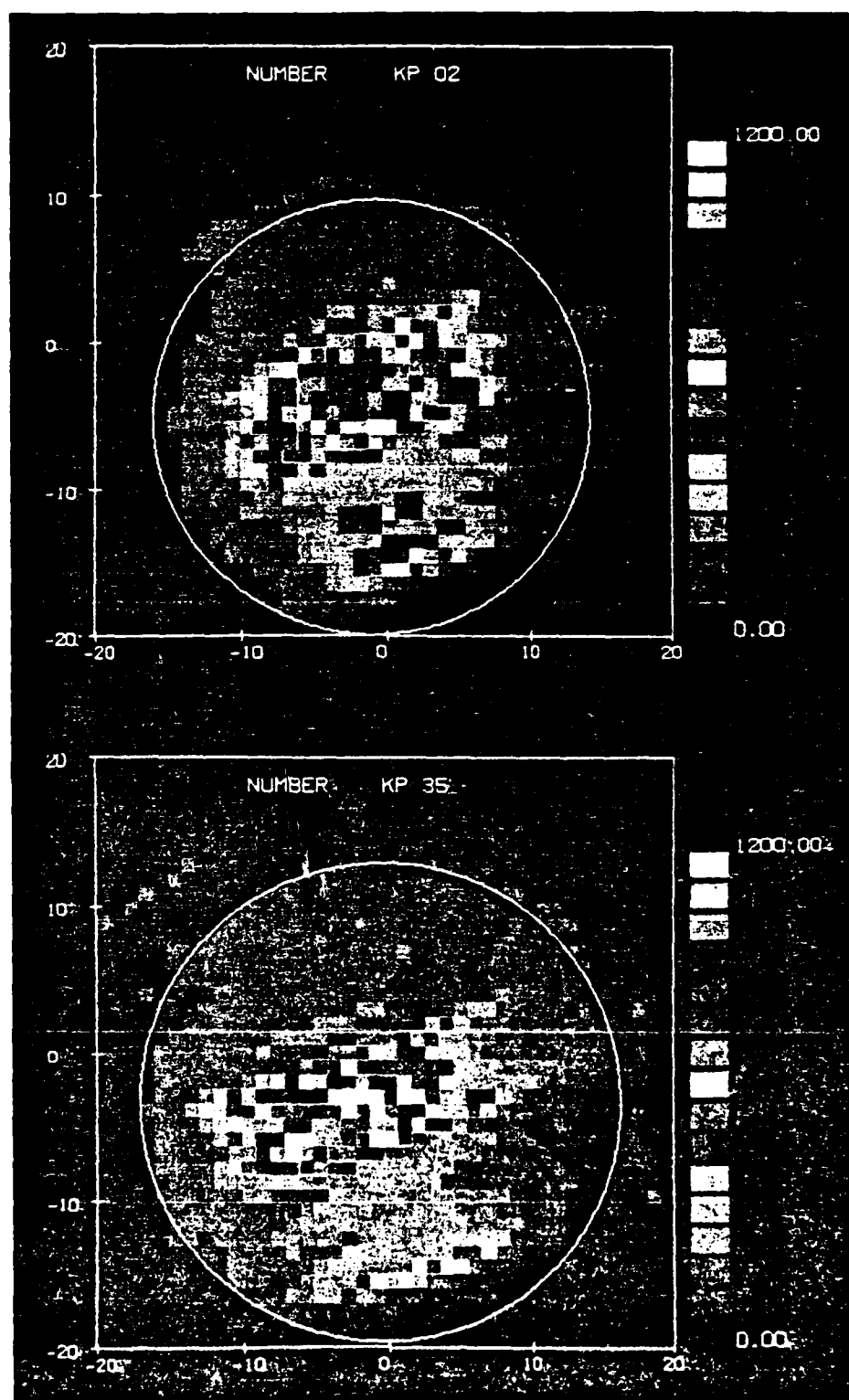
Plate 1a. (Top) Number of polar rain spectra used in each CGL-MLT bin in the total distribution for Kp 02, color coded in equal linear steps. (Bottom) Number of polar rain spectra for Kp 35. The axes are labeled by degrees along the noon-midnight (top to bottom) and dusk-dawn (left to right) meridians.
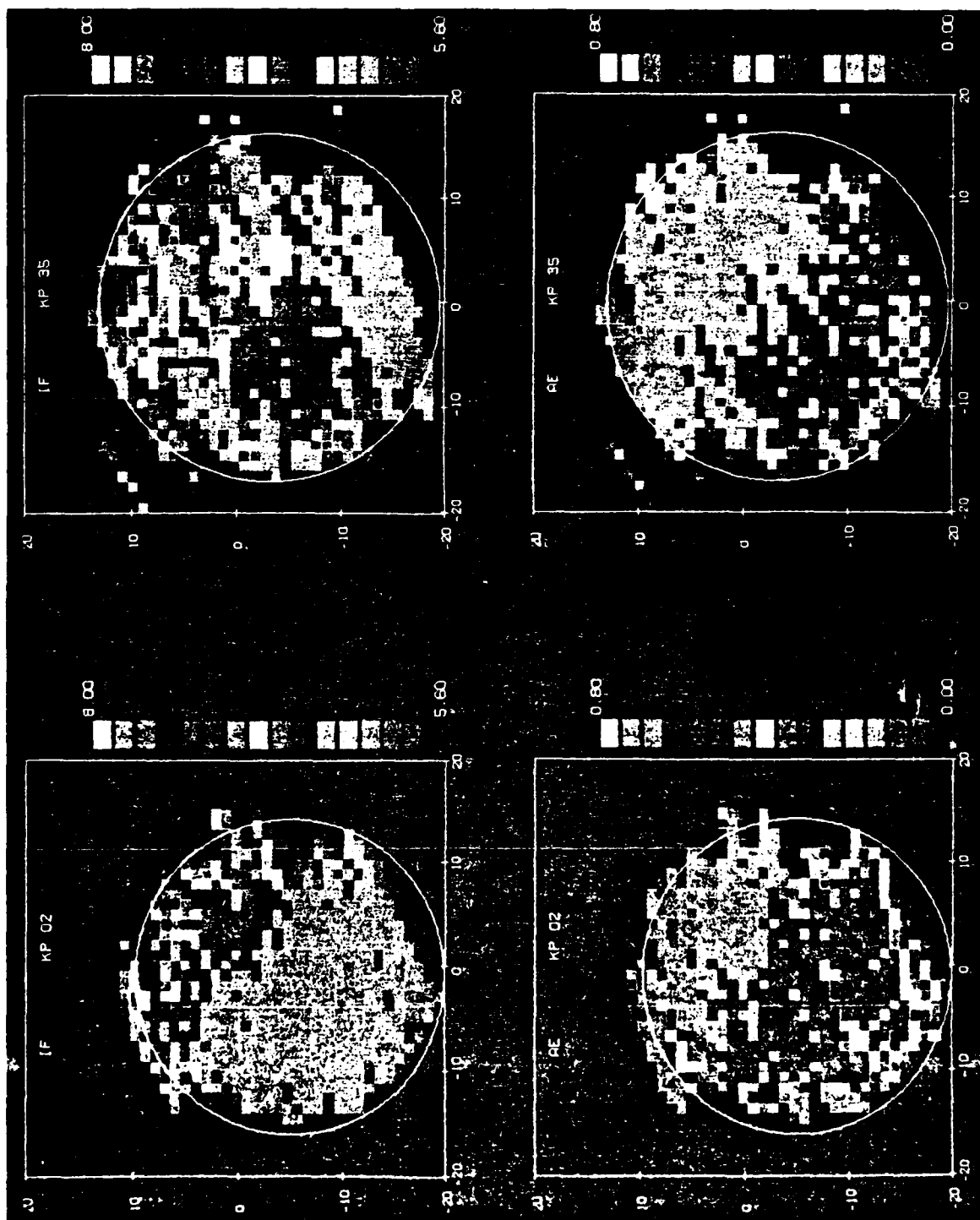
Plate 1b. (Top left) Average values of the log of the polar rain integral flux in (cm² sr)⁻¹ in the total distribution for Kp 02, color coded in equal logarithmic steps. (Top right) Integral flux for Kp 35. (Bottom left) Average energy for Kp 02 in keV, color coded in equal linear steps. (Bottom right) Average energy for Kp 35. The axes are labeled by degrees along the noon-midnight (top to bottom) and dusk-dawn (left to right) meridians.
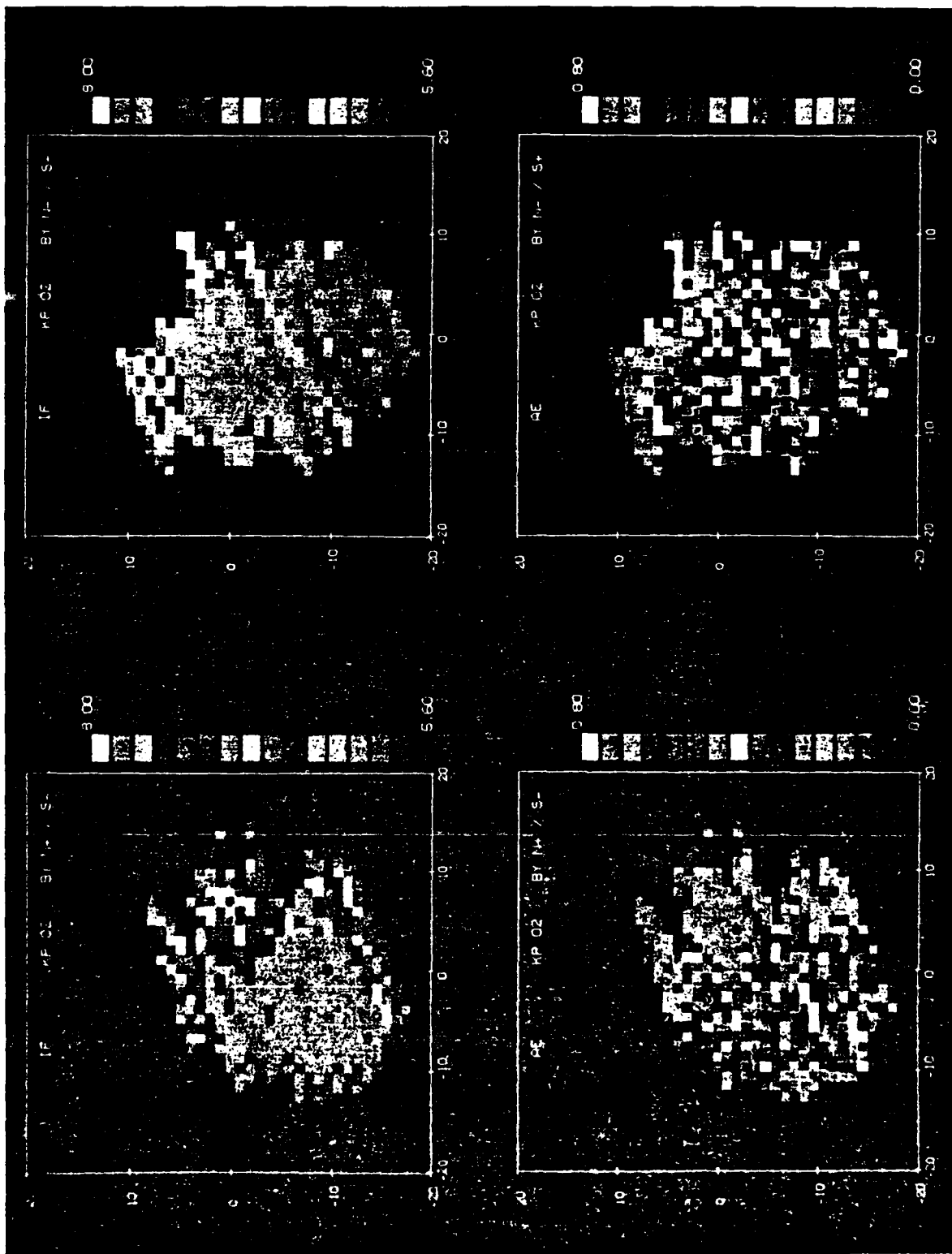
Plate 2. Average values of the polar rain integral flux (IF) in (cm² s sr)⁻¹ and average energy (AE) in keV for Kp02 when the polar rain samples were distributed by B_y positive (negative) in the north (south) pole (left-hand column) and by B_y negative (positive) in the north (south) pole (right-hand column). The format for each plot is the same as that for Plate 1
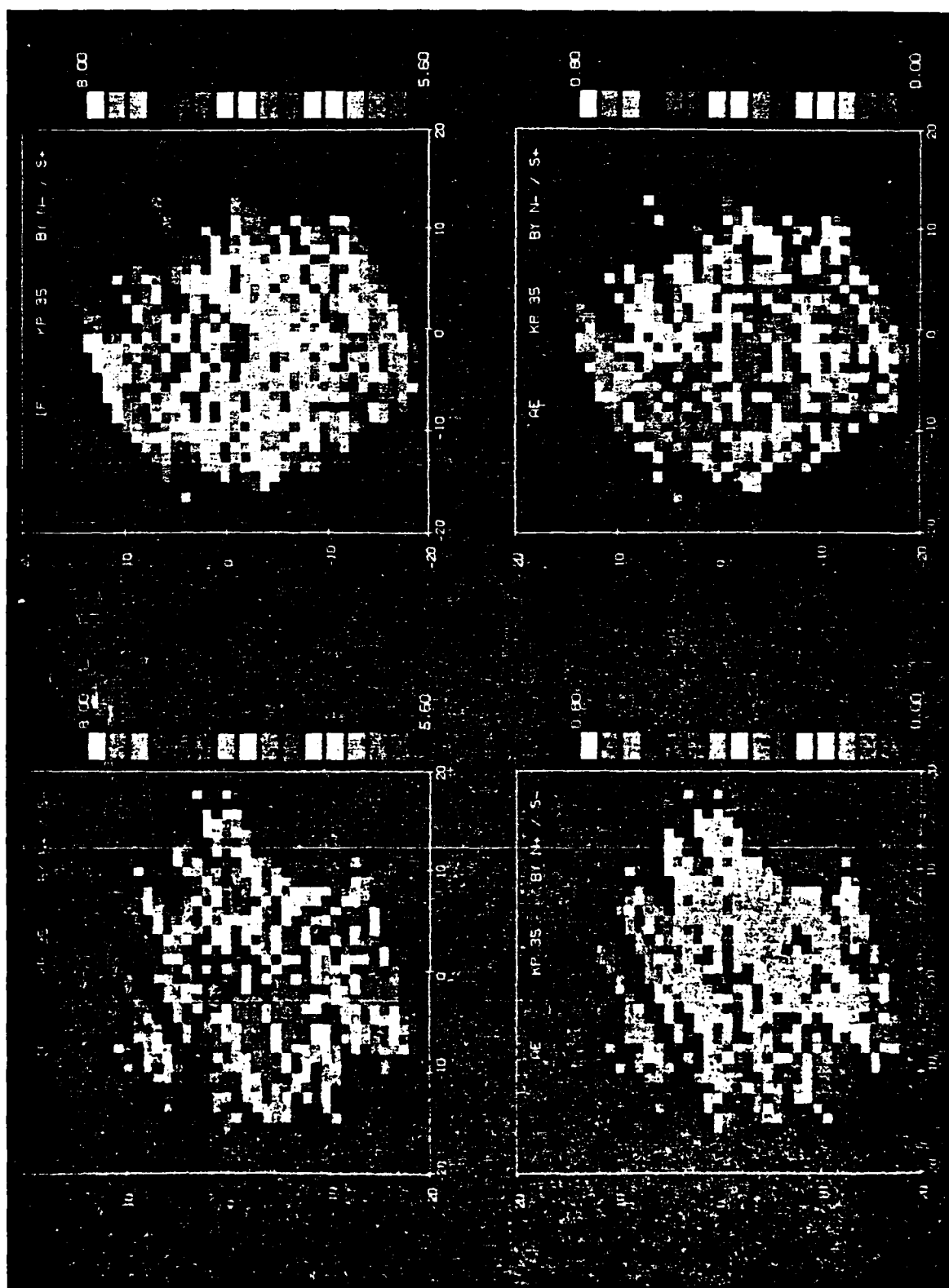
Plate 3. Same as Plate 2, but for Kp 35.

Frank, 1976], it is clear that the streaming ions of the plasma mantle are not present and some other ion source is required to maintain charge neutrality. Measurements of the cold plasma density in the tail lobes from approximately 2 to 5 R_E have recently been presented by *Persoon et al.* [1983]. Over this range they show that the average variation in density falls as $r^{-3.8}$ from about 30 cm^{-3} to 1 cm^{-3}. If the rate of decrease were extended, albeit questionably, to 10 R_E, the average density would be 0.06 cm^{-3}, which is comparable to polar rain densities.

On the basis of the above discussion we propose the following mechanisms for polar rain production and transport. The polar rain originates from the plasma mantle, since this is the plasma population that has the greatest access to the tail lobes. The mantle ions (with magnetosheath characteristics) are dominated by convection and stream from the dayside far down tail into the plasma sheet. Their energy is almost entirely directed along their convection path. Their thermal energies are small. The mantle electrons, having higher temperature and pressure than the ions, while also streaming, will tend to escape in both directions along the lobe field lines. The escape is prevented by a field-aligned electric field (or region of positive charge density) within the ion stream. The potential barrier traps some portion of the electrons between the converging magnetic field of the ionosphere and the region of the ion stream. The tenuous, trapped election population is neutralized by cold ions drawn out either from the ionosphere or out of the ion stream. Although involvement of the mantle in forming the electrostatic potential has not been considered in the literature, stable field-aligned potential drops have been proposed for mirror and half-mirror configurations by *Persson* [1963, 1966]. *Stern* [1981]. *Foster and Burrows* [1977], and *Winningham and Gurgiolo* [1982].

Two aspects of the polar rain morphology can be rationalized in this picture: the falling off of number flux, and the increase of average energy from noon to midnight. The trapped electron source is strongest where the magnetosheath particles enter the magnetosphere and become the mantle, namely, on field lines contiguous to the cusp. Many will precipitate immediately, but a continuously depleted population will convect toward the plasma sheet (or equivalently toward the nightside in the cap). The longer the electrons escape loss and continue to convect, the longer they are subject to processes which heat (or cool) them.

In this picture, as well, the polar rain intensity would be a reflection of IMF-induced changes in the mantle plasma observed down tail at the moon [*Hardy et al.*, 1979c]. Lobe plasma is seen in the morning quadrant in the north (south) pole for away (toward) sectors, and in the evening sector for the opposite configuration. Initial correspondence between the lobe plasma and preferred access of polar rain obtains. However, polar rain is not symmetrically distributed between morning and evening for preferred sectors, as it appears the lobe plasma is. Plasma mantle thickness at lower altitudes has not been found to have clear IMF dependence [*Schopke and Paschmann*, 1978]. Thus the asymmetry of plasma in the lobes may be a consequence of the unequal convection velocities and therefore strongly dependent on distance down tail.

Finally, we suggest that the polar rain fluxes to the ionosphere are balanced by polar wind and photoelectron expansion, since there is no comparable polar rain ion flux. If so, polar rain flux should be greater at times of enhanced photoelectron flux and polar wind flux, namely, on the dayside and in summer, as this study shows to be the case. At low altitudes

and on the dayside the polar rain flux can be within 1 order of magnitude of the polar wind flux. It is possible that all the mechanisms suggested here require, as well, instabilities that control the rate of pitch angle diffusion for polar rain, and that a full explanation of polar rain morphology requires the identification and the production mechanism of this instability.

REFERENCES

Akasofu, S.-I., and M. Roederer, Dependence of the polar cap geometry on the IMF, *Planet. Space Sci.*, *32*, 111, 1984.

Akasofu, S.-I., R. Williams, and M. Roederer, Effects of the passage of an IMF discontinuity on the polar cap geometry and the formation of a polar cap arc, *Planet. Space Sci.*, *32*, 119, 1984.

Axford, W. I., The polar wind and the terrestrial helium budget, *J. Geophys. Res.*, *73*, 6855, 1968.

Banks, P. M., and T. E. Holzer, The polar wind, *J. Geophys. Res.*, *73*, 6846, 1968.

Banks, P. M., and T. E. Holzer, High-latitude plasma transport: The polar wind. *J. Geophys. Res.*, *74*, 6317, 1969.

Berkey, F. T., L. L. Cogger, S. Ismail, and Y. Kamide, Evidence for a correlation between sun-aligned arcs and the interplanetary magnetic field direction, *Geophys. Res. Lett.*, *3*, 145, 1976.

Fennell, J. F., P. F. Mizera, and C. F. Croley, Low energy polar cap electrons during quiet times, *Proc. Int. Conf. Cosmic Rays, 14th, 4*, 1267, 1975.

Foster, J. C., and J. R. Burrows, Electron fluxes over the polar cap, 1, Intense keV fluxes during poststorm quieting, *J. Geophys. Res.*, *81*, 6016, 1976.

Foster, J. C., and J. R. Burrows, Electron fluxes over the polar cap, 2, Electron trapping and energization on open field lines, *J. Geophys. Res.*, *82*, 5165, 1977.

Frank, L. A., J. D. Craven, J. L. Burch, and J. D. Winningham, Polar views of the earth's aurora with Dynamics Explorer, *Geophys. Res. Lett.*, *9*, 1001, 1982.

Gurgiolo, C., and J. L. Burch, DE-1 observations of the polar wind—A heated and an unheated component, *Geophys. Res. Lett.*, *9*, 945, 1982.

Gussenhoven, M. S., Extremely high latitude auroras, *J. Geophys. Res.*, *87*, 2401, 1982.

Gussenhoven, M. S., D. A. Hardy, and N. Heinemann, Systematics of the equatorward diffuse auroral boundary, *J. Geophys. Res.*, *88*, 5692, 1983.

Hardy, D. A., Intense fluxes of low-energy electrons at geomagnetic latitudes above 85, *J. Geophys. Res.*, *89*, 3883, 1984.

Hardy, D. A., M. S. Gussenhoven, and A. Huber, The precipitating electron detectors (SSJ 3) for the block 5D flights 2-5 DMSP satellites: Calibration and data presentation, *Rep. AFGL-TR-79-0210*, Air Force Geophys. Lab., Hanscom Air Force Base, Mass., 1979a.

Hardy, D. A., H. K. Hills, and J. W. Freeman, Occurrence of lobe plasma at lunar distance, *J. Geophys. Res.*, *84*, 72, 1979b.

Hardy, D. A., P. H. Reiff, and W. J. Burke, Response of magnetotail plasma at lunar distance to changes in the interplanetary magnetic field, the solar wind plasma, and substorm activity, *J. Geophys. Res.*, *84*, 1382, 1979c.

Hardy, D. A., W. J. Burke, and M. S. Gussenhoven, DMSP optical and electron measurements in the vicinity of polar cap arcs, *J. Geophys. Res.*, *87*, 2413, 1982.

Heikkila, W. J., Magnetospheric topology of fields and currents, in *Magnetospheric Currents, Geophys. Monogr. Ser.*, vol. 28, edited by T. A. Potemra, p. 208, AGU, Washington, D. C., 1984.

Hill, T. W., Origin of the plasma sheet, *Rev. Geophys. Space Phys.*, *12*, 379, 1974.

Hoffman, J. H., and W. H. Dodson, Light ion concentration and fluxes in the polar regions during magnetically quiet times, *J. Geophys. Res.*, *85*, 626, 1980.

King, J. H., *Interplanetary Medium Data Book*, supplement 1, 1975–1978, *Rep. NSSDC WDC A-R&G-79-08*, NASA Goddard Space Flight Center, Greenbelt, Md., 1979.

Meng, C.-I., The auroral electron precipitation during extremely quiet geomagnetic conditions, *J. Geophys. Res.*, *86*, 4607, 1981.

Meng, C.-I., and H. W. Kroehl, Intense uniform precipitation of low-energy electrons over the polar cap, *J. Geophys. Res.*, *82*, 2305, 1977.

Meng, C.-I., S.-I. Akasofu, and K. A. Anderson, Dawn-dusk gradient of the precipitation of low-energy electrons over the polar cap and its relation to the interplanetary magnetic field, *J. Geophys. Res.*, *82*, 5271, 1977.

Mizera, P. F., and J. F. Fennell, Satellite observations of polar, magnetotail lobe, and interplanetary electrons at low energy, *Rev. Geophys. Space Phys.*, *16*, 147, 1978.

Paulikas, G. A., Tracing of high-latitude magnetic field lines by solar particles, *Rev. Geophys. Space Phys.*, *12*, 117, 1974.

Persoon, A. M., D. A. Gurnett, and S. D. Shawhan, Polar cap densities from DE 1 plasma wave observations, *J. Geophys. Res.*, *88*, 10,123, 1983.

Persson, H., Electric field along a magnetic field line in a low-density plasma, *Phys. Fluids*, *6*, 1756, 1963.

Persson, H., Electric field parallel to the magnetic field in a low-density plasma, *Phys. Fluids*, *9*, 1090, 1966.

Peterson, W. K., and E. G. Shelley, Origin of the plasma in a cross-polar cap auroral feature (theta aurora), *J. Geophys. Res.*, *89*, 6729, 1984.

Pillip, W. G., and G. Morfill, The formation of the plasma sheet resulting from plasma mantle dynamics, *J. Geophys. Res.*, *83*, 5670, 1978.

Rosenbauer, H., H. Grünwaldt, M. D. Montgomery, G. Paschmann, and N. Sckopke, HEOS 2 plasma observations in the distant polar magnetosphere: The plasma mantle, *J. Geophys. Res.*, *80*, 2723, 1975.

Sckopke, N., and G. Paschmann, The plasma mantle: A survey of the magnetotail boundary layer observations, *J. Atmos. Terr. Phys.*, *40*, 261, 1978.

Sharp, R. D., D. L. Carr, W. K. Peterson, and E. G. Shelley, Ion streams in the magnetotail, *J. Geophys. Res.*, *86*, 4639, 1981.

Shelley, E. G., W. K. Peterson, A. G. Ghielmetti, and J. Geiss, The polar ionosphere as a source of energetic magnetospheric plasma, *Geophys. Res. Lett.*, *9*, 941, 1982.

Spiro, R. W., P. H. Reiff, and L. J. Maher, Jr., Precipitating electron energy flux and auroral zone conductances: An empirical model, *J. Geophys. Res.*, *87*, 8215, 1982.

Stern, D. P., A study of the electric field in an open magnetospheric model, *J. Geophys. Res.*, *78*, 7292, 1973.

Stern, D. P., Large-scale electric fields in the earth's magnetosphere, *Rev. Geophys. Space Phys.*, *15*, 156, 1977.

Stern, D. P., One-dimensional models of quasi-neutral parallel electric fields, *J. Geophys. Res.*, *86*, 5839, 1981.

Voigt, G.-H., A mathematical magnetospheric field model with independent physical parameters, *Planet. Space Sci.*, *29*, 1, 1981.

Winningham, J. D., and C. Gurgiolo, DE-2 photoelectron measurements consistent with a large-scale parallel electric field over the polar cap, *Geophys. Res. Lett.*, *9*, 977, 1982.

Winningham, J. D., and W. J. Heikkila, Polar cap auroral electron fluxes observed with ISIS 1, *J. Geophys. Res.*, *79*, 949, 1974.

Yeager, D. M., and L. A. Frank, Low-energy electron intensities at large distances over the earth's polar cap, *J. Geophys. Res.*, *81*, 3966, 1976.

R. K. Burkhardt, Physics Research Division, Emmanuel College, Boston, MA 02115.

M. S. Gussenhoven and D. A. Hardy, Space Physics Division, AFGL (AFSC), Hanscom AFB, MA 01731.

N. Heinemann, Physics Department, Boston College, Chestnut Hill, MA 02167.

IV. PARTICLE DYNAMICS ALONG MAGNETOSPHERIC FIELD LINES

COMPARISON OF STATISTICAL MAPS OF GEOSYNCHRONOUS PARTICLE POPULATIONS WITH LOW ALTITUDE PRECIPITATING ELECTRONS

M.S. Gussenhoven
Physics Department, Boston College
Chestnut Hill, MA 02167

D.A. Hardy and E.G. Mullen
Air Force Geophysics Laboratory
Hanscom AFB, MA 01731

ABSTRACT

An environmental atlas of the near-geosynchronous region (L = 5.5-8.5 RE) has been compiled from ~ 120 days of data taken aboard the AF SCATHA (P78-2) satellite in 1979, 1980. Moments of the ion and electron distribution functions, measured by the AFGL Rapid Scan Particle Spectrometer, are calculated for low energy (50 eV-20 keV) and high energy (20 keV-400 keV) ranges. The moments are binned in L-Shell, local time, and KP and averaged. Three-dimensional maps of the average quantities in the low energy range show good overall agreement with existing models of particle motion in combined magnetic and large-scale convection electric fields, with progressive particle loss along trajectories moving away from the midnight sector. Only small variations in average energy are found. The electrons precipitating out of this region should map to a significant portion of the diffuse auroral region at low altitudes. A comparison is made between the average population at geosynchronous and statistical maps of precipitating electrons made from measurements taken on the AF/DMSP/F2 and F4 and AF/P78-1 satellites in polar orbits at $\leq$ 800 km. The AFGL SSJ4 sensors\ on each satellite measure electrons from 50 eV-20 keV and return one spectrum every second. Over 14 million spectra are binned and averaged to give integral flux, energy flux, and

average energy mapped in a geomagnetic latitude-local time grid for each KP value. Significant similarities and differences are found between the electron patterns in the two regions.

\

The SCATHA satellite was launched in January, 1979, for the purpose of investigating satellite charging at high altitudes. The satellite is in near-geosynchronous orbit with altitude between 5.3 and 7.8 RE, inclination of 7.9°, a spin rate of ~ 1 rpm. The satellite drifts eastward approximately 5° per day.

The orbit and instrumentation of SCATHA were designed, in part, to provide data needed to make a statistical atlas of the near-geosynchronous environment.* For this purpose, 120 days of data from February, 1979, to July 1980, were used.

One of the instruments onboard SCATHA is the Air Force Geophysics Laboratory Rapid Scan Particle Spectrometer measuring electrons and ions, both perpendicular and parallel to the spin axis, in the energy range 50 eV to 400 keV. The detectors have high time resolution, returning a complete spectrum every second; and low energy resolution: $\Delta E/E \sim 1$. From these data, the first four moments of the electron and ion distributions were calculated, integrating over each complete spin. The moments were calculated in a low energy range, 50 eV to 20 keV; and a high energy range, 20 keV to 400 keV; the total moment being the sum of the two. The division at 20 keV was made to distinguish those particles which are strongly affected by the magnetospheric convection electric field from those which are not. (We had also found from other studies that the > 20 keV electron population is the driver of spacecraft charging, and we wanted to look separately at that population.) The moments were binned according to L-Shell in 1 RE units (using the quiet Olson-Pfitzer model to determine L), local time in hourly intervals, and

---

* Mullen, E.G. and M.S. Gussenhoven, SCATHA Environmental Atlas, AFGL-TR-83-0002, Air Force Geophysics Laboratory, Hanscom AFB, 1983.

184

KP in intervals: 0-1, 2-3, 4-5, >6-. The points in each bin were averaged.

The quietest conditions for which the SCATHA orbit reliably passes through the plasmasheet are for KP 2, 3, and are, therefore, conditions most appropriate for comparison with models of quasi-static processes. In this presentation, we show a) the spatial variations in number density and average energy of electrons and ions; b) the pitch angle anisotropy derived by relating fluxes with pitch angles of 90° to those of 45°; and c) a comparison of geosynchronous low energy electron fluxes and average energies with those of precipitating electrons at low altitudes. The distributions show evidence for large-scale convection electric fields and the importance of including loss processes in any global magnetospheric model.

Density. Figure 1 gives an overview of the density variations. Here are plotted the total density for ions (o) and electrons (+); and the density over the high energy range (20-400 keV) for ions (Δ) and electrons (x), when variations in local time, L-Shell and KP are looked at separately.

The variation in local time for the total ion population is small, between 1 and 2 cm^{-3}, and has a maximum in the midnight sector and minimum post-noon. On the other hand, the total electron variation with local time is significantly larger, a factor of 5. There is a near-steady decrease in electron density from 05-15 LT, from which an e-folding loss rate can be calculated to be between 5 and 10 hours, depending on L-Shell and magnetic activity. For the high energy contribution to the total density, the ions make a substantial contribution, while the high energy electrons do not, being more than an order of magnitude smaller. It can also be seen that the minimum for the high energy ions is significantly shifted toward morning compared to the total, indicating that the local time dependence for ions is highly energy dependent. This is not the case for electrons (except for the very highest

energies where contribution to the density is very small).

The L-Shell dependence is only unambiguous for the high energy ions, decreasing with increasing L.

An increase in density with increasing magnetic activity is clearly demonstrated in both ions and electrons and for the high energy populations. The high energy electron population appears to saturate at highest KP levels.

Perhaps the most striking feature of Figure 1 is the non-equality of electron and ion densities over the measured energy range (50 eV to 400 keV). Corrections for ion composition would only increase the differences. The two densities are more nearly the same in the midnight sector and for high KP. They differ the most on the dayside, for low L-values and for low activity. Since charge neutrality must maintain (at least to a degree much higher than achieved here), and since the electrons and ions are lost at different rates, low energy electron (backscattered, secondary, photoelectrons) from the ionosphere (or from other sources) must play an important role in maintaining neutrality.

A more detailed spatial display of the density variations in the high and low electron and ion populations for KP 2, 3 is shown in Figure 2. The number density is given in gray scale in approximately equal logarithmic steps (except for the lowest bin) and plotted as a function of local time and L-Shell. In the low energy ion case, a correction for ion composition is made using the statistical results of the Lockheed Ion Composition Experiment onboard SCATHA. Also, it should be noted that to use the same gray scale for all populations, the high energy electron densities must be reduced by 1/10.

In the low energy populations, we look for evidence of sources, convection, and loss. In a combined cross-tail and corotation electric field, kilovolt ions will move sunward from the midnight region on trajectories that

186

carry them earthward of the SCATHA regime, through the SCATHA regime in the
noon sector and out through the dayside magnetosphere. Figure 2c presents no
contradictory evidence to this picture. The maximum ion loss is 50% from
nightside to dayside. On the other hand, kilovolt electrons, whose source is
the midnight high L region, are, as they near the earth, deflected from sun-
ward motion toward dawn, moving in near-circular, counterclockwise paths
through noon, where they resume a sunward motion again. They are unable to
penetrate a teardrop-shaped region, centered on the earth and having its long
axis along the dusk meridian (where cross-tail and corotation electric fields
cancel producing a stagnation region for electron motion.) In Figure 2d there
is some evidence of the existence of an inner edge to the low energy electron
population between 18 and 03 LT in the night sector and a stagnation region at
dusk. However, the effect of loss from midnight through the dawn sector to
post-noon is so great (90% loss) that the convection pattern is overwhelmed by
it. Any quasi-static model of the electron population in this energy range
must include loss processes in order to make comparison with measured values.

The high energy electron and ion motions are dominated by the magnetic
field within the SCATHA regime, resulting in closed trajectories. If all
trajectories are circular and under conditions of no loss, there should be a
high degree of azimuthal symmetry in the high energy distributions. This
appears to be the case for high energy ions (Figure 2a), but not for electrons
(Figure 2b). A quasistatic cross-tail convection electric field that
increases with distance from the center of the earth can affect the high
energy particles at high L-values resulting in open trajectories on the
post-noon (pre-noon) side for electrons (ions). The trajectories should then
"pile-up" in the post-midnight (pre-midnight) region where the high energy
electron (ion) density is, in fact, seen to be greatest.

There are at least two other mechanisms by which high energy particles at high L-values can access the inner magnetosphere: diffusion and repeated application of short-lived induction electric fields. In the former, high energy particles move earthward across field lines leading to a hotter population at lower L-values. In the latter, in-place acceleration of the existing population occurs leading to an increase in the high energy population, but not necessarily a hotter one.*

Anisotropy. The nature of the dynamical processes occurring in the inner magnetosphere can also be revealed by the anisotropies in the particle populations. We define an anisotropy index for a given energy channel by using the ratio of fluxes measured at 90° pitch angle to those measured at 45°. The index is made symmetric about the isotropic case by the following definition of the anisotropy index:

$$AI \equiv J_{90}/J_{45} - 1, \text{ for } J_{45} > J_{90};$$

and

$$AI \equiv -(J_{45}/J_{90} - 1), \text{ for } J_{90} > J_{45}.$$

Thus, for normal or pancake distributions ($J_{90} > J_{45}$), AI is positive. For butterfly distribution or broad streaming along field lines ($J_{45} > J_{90}$), AI is negative. In general, we expect distributions to be isotropic or preferentially aligned along the field line in regions of particle entry or in injection regions or wherever particles have not been subject to loss. On the other hand, trapped configurations develop for particles which are long-lived.

---

*An additional stipulation is required for acceleration by induction electric fields and that is that the strength of the accelerations accumulated over many events is greater than the strength of the decelerations. If the induction electric field results from the changes in the magnetic field, this requires that, say, the formation of a tail-like configuration is slower than the recovery of a dipole configuration. There is evidence for this.

In addition, systematic changes in the anisotropy index of the trapped population of high energy particles should also be observed because of azimuthal asymmetries in the magnetic field configuration (drift shell splitting).

Figure 3 shows maps of average anisotropy indices in L-Shell, local time coordinates for sample energies which fall within the low (represented by 9 keV energies) and high (represented by 100 keV energies) energy populations. The sample energy anisotropy index variations are representative of the two populations. No separation by magnetic activity has been made in the data from which the averages were calculated.

The 9.2 keV electron anisotropies (Figure 3a) are consistent with the picture of a low energy electron source region at high L-values in the midnight sector (highest degree of isotropy), and near-circular electron trajectories through dawn to post-noon accompanied by continuous loss (the distribution becomes increasingly trapped). Two other points require comment. First, the low energy electrons also show a strongly trapped distribution at the lowest L-value (5.5 - 6 RE), for all local times. This is the trough region composed of trapped particles from old, active periods, and its outer boundary can be taken as the inner limit of open trajectories (Alfven boundary for 9 keV electrons). Second, there is a region of reasonably isotropic 9 keV electrons in the dusk sector at high L (8 RE). We postulate that this is the inner edge of the electron population that is convected directly to the dayside from the tail region without deflection toward dawn; that is, that it is a continuation of the midnight source region.

The 9.7 keV ions (Figure 3c) show a very broad region from midnight to dusk of near isotropy, with development of loss cone distributions on the dayside. Again, this is consistent with the density variations which indicate

that the low energy ions move sunward through the inner magnetosphere with little loss.

The anisotropy index variations of the 100 keV electrons and ions (Figures 3b and 3c) show that at least three separate transport mechanisms are operating. First, there is the overall pattern of drift loss cones expected for stably trapped high energy particles circulating in the combined dipolar and tail-like inner magnetospheric magnetic field and subject to drift shell splitting. The loss cones are perpendicular to the field near midnight, resulting in butterfly distributions, and parallel to the field near noon giving very flat pancake distributions. Second, in addition to regions of negative anisotropy index centered around midnight, there are also asymmetric regions on the dawn (dusk) side for ions (electrons) at high L-values. We postulate that these reflect entry regions for high energy particles which contain open trajectories to either flank of the magnetosphere. Third, the anisotropy index increases with decreasing L, which may, in part, result from inward diffusion.

Average Energy. The average energy for each population is defined as the ratio of the energy density for the population (second moment of the distribution function) and the number density. The average energy is used in place of temperature because the distribution functions are not well-described by Maxwellian distributions. Figure 4 shows the average energy variations for the high and low energy populations in L-Shell, local time plots. The first observation is that in all cases, the average energy variation is small. In order to show the variation, a linear scale had to be used. The second point is that the ions are hotter than the electrons, but only by at most a factor of two. The average energy of the high energy electrons (ions) is 20-30 keV (30-40 keV); and the low energy electrons (ions), 1-3 keV (2-4 keV).

The high energy ions (Figure 4a) show a reasonably symmetric increase in the average energy with decreasing L. This again indicates a process that conserves the second adiabatic invariant, such as inward diffusion. The high energy electron average energy distribution (Figure 4b) is asymmetric dawn to dusk, being hotter in the dusk sector, at lower L values. The explanation for this is not apparent in any of the processes discussed thus far.

We look for the convection electric field effects principally in the low energy ions, since their density distributions indicate smaller loss effects than for electrons. Figure 4c shows higher average energies in the dusk sector which is in the correct sense for a dawn to dusk electric field. There is also little change in average energy along the midnight-noon axis. The total cross-magnetosphere change in energy density is approximately 3 keV over 10 RE, which gives an average dawn to dusk electric field of .05 mV/m, which is smaller by about an order of magnitude than normally assumed.

From the SCATHA Atlas we draw the following conclusions concerning sources, losses, and convection (or transport) of the particles in the inner magnetosphere:

High energy electrons and ions (20 keV-400 keV): The region from 5-8 RE is a region which is principally occupied by stably trapped populations that strongly reflect drift shell splitting in their pitch angle anisotropies, are reasonably isothermal, and lie on the outer limits of inward diffusion. There is evidence of entry from the flanks of the magnetosphere on the dawn (dusk) side for ions (electrons). The high energy ion population is the major contributor to the energy density (pressure) of the total ion and electron population and is extremely stable to variations in density and average energy. The high energy electron population, by comparison, is far more

variable, both in density and in average energy, variations without ready explanation.

The low energy ion population (50 eV-20 keV) strongly reflects the existence of a quasi-static, large-scale dawn to dusk magnetospheric electric field. The density varies little from midnight to noon with only small increases in loss cone development. The ion population suffers, at most, a 50% loss in this regime. The average energy increases from dawn to dusk.

The low energy electron population (50 eV-20 keV) is far more variable, suffering losses from midnight to noon of more than 90%. The losses appear to be highly energy dependent since they obscure the effects of the convection electric field that are so clearly seen in the ion distributions. In order to model this population, an inclusion of the loss process must be made.

A comparison of the geosynchronous low energy electron population with the precipitation electrons over the same energy range at low altitudes (DMSP orbit) can be made as an initial attempt to describe the loss process in a global fashion. Figure 5 is a plot of the low energy electron number flux measured at SCATHA (o) (all L-values are included in the averages) as a function of local time, and those precipitating at low altitudes (., x) in a region which maps to the SCATHA regime by means of a dipole magnetic field. Again, we consider only KP levels of 2 and 3. The evening and midnight regions (where we have postulated sources for the low enegy population) show comparable number fluxes. Beyond about 4 LT to 15 LT, the precipitating electrons fall off much more sharply than those at geosynchronous, having their minimum value near noon, while the electrons at SCATHA minimize later, at about 17-18 LT.

A comparison of average energies at geosynchronous orbit and at low altitudes is shown in the same format in Figure 6. Here, the dusk to midnight
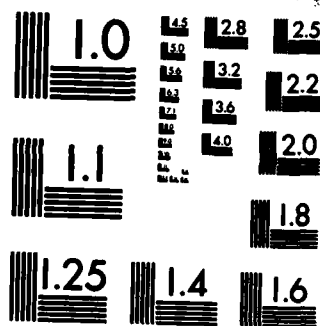
END

FILMED

DTIC

MICROCOPY RESOLUTION TEST CHART
NATIONAL BUREAU OF STANDARDS-1963-A

region (the source region at SCATHA) shows preferential precipitation of the low energy portion of the parent population; while beyond 4 LT, the precipitating electrons have average energies approximating, or greater than, the parent population. The region from noon to dusk shows erratic behavior in the precipitating average energies.

We tentatively conclude that the loss process for low energy electrons is characterized differently in three local time regimes:

1) From dusk through the midnight sector, the sources and losses of low energy electrons are comparable, and there is preferential selection of the lower energies in the loss process.

2) From 4 LT to noon, there are no sources, and the precipitation (or loss) is only a fraction of the parent population. Higher energy particles are preferentially precipitated in this region.

3) From noon to dusk, the precipitation is effectively quenched, although there is a substantial, albeit trapped, parent population.

FIGURE CAPTIONS

Figure 1   SC5 number densities for ions and electrons as determined from
spin-averaged moments for energy ranges 100 eV to 400 keV and 20 to
400 keV.   The average number densities are plotted vs (left) LT,
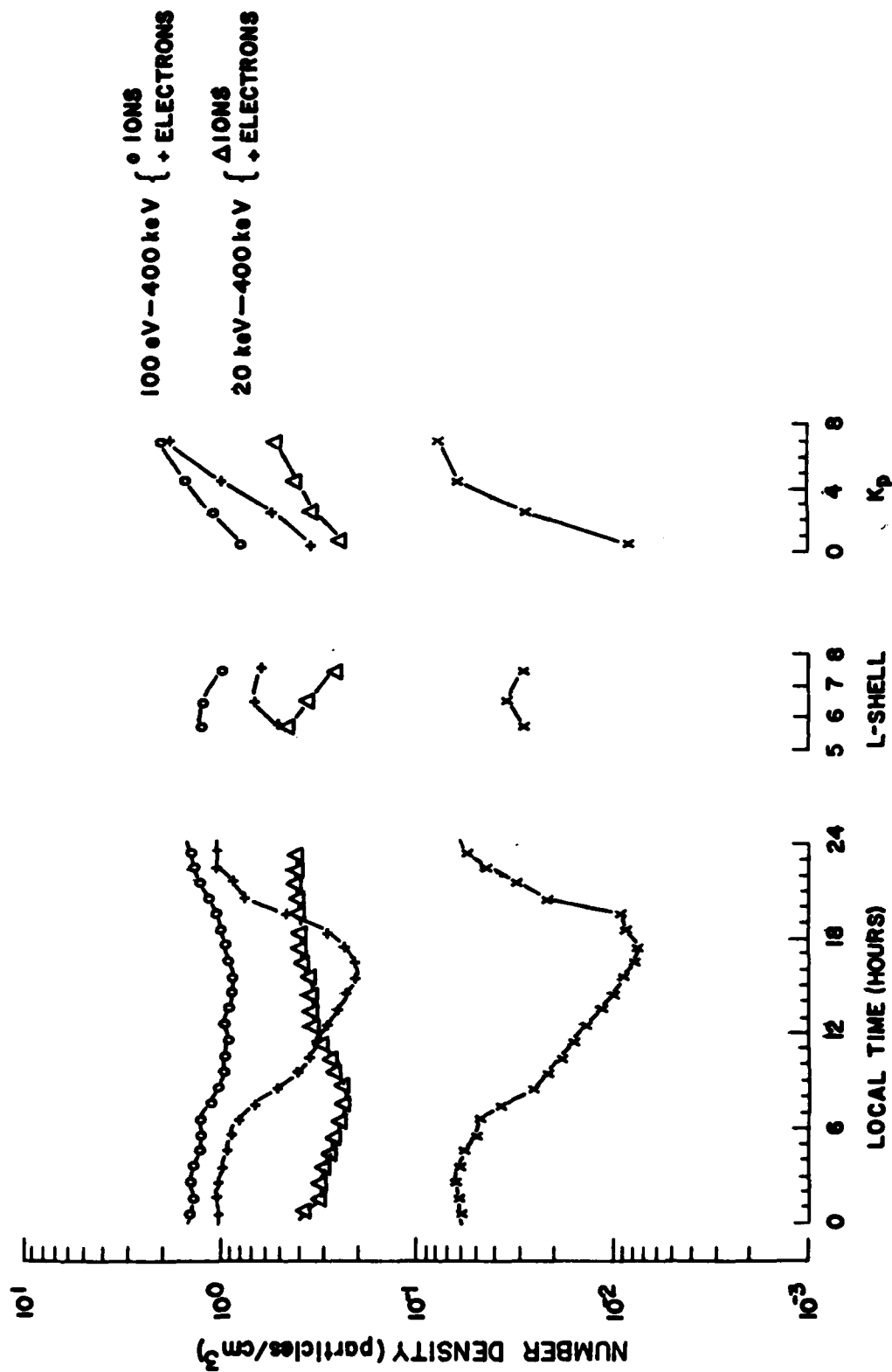(center) L-Shell, and (right) KP.

Figure 2   Variations in number density coded in polar coordinate LT and
L-Shell ranges.   The densities are for (a) high-energy ions, (b)
high-energy electrons, (c) low-energy ions, and (d) low-energy
electrons.   The code is in the center in particles/cm^3, and values
in (b) must be multiplied by 10^{-1}.

Figure 3   Variations in average energy coded in polar coordinate LT and
L-Shell ranges.   The average energies are for (a) high-energy ions,
(b) high-energy electrons, (c) low-energy ions, and (d) low-energy
electrons.   The code is in the center in keV, and values in (c) and
(d) must be multiplied by 10^{-1}.

Figure 4   Anisotropy indices averaged over all KP and plotted in polar
coordinate representations of LT and L-Shell for (a) 9-keV
electrons, (b) 96-keV electrons, (c) 10-keV ions, and (d) 126-keV
ions.   The codes represent ranges of the indices and are identified
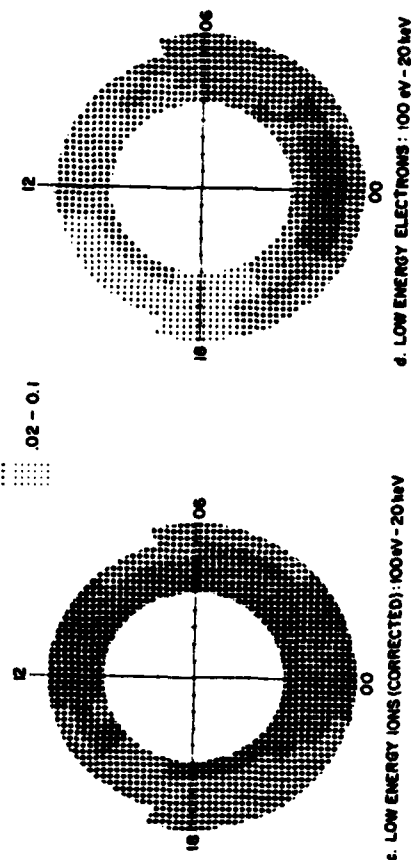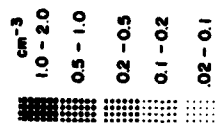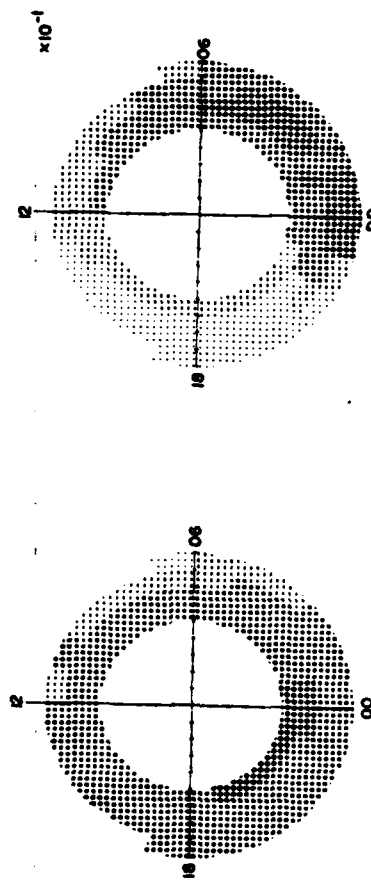in the center of the figure.

Figure 5   Comparison of local time variation of average number flux measured

near-geosynchronous by SCATHA, and at the low altitude latitudes

which lie on the same field lines measured by DMSP. The magnetic

activity of the averaged values is for KP 2-3.

Figure 6   Same as Figure 5, but for the average energy, defined as the ratio
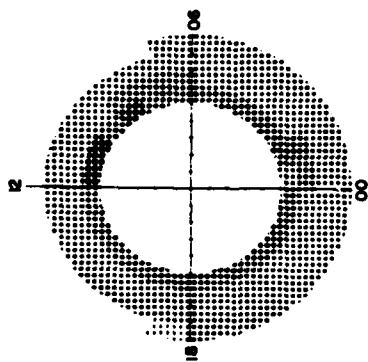
of the energy flux to the number flux.

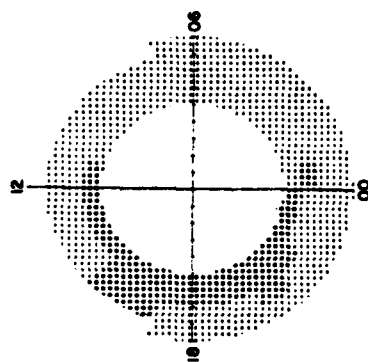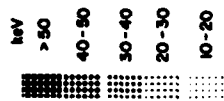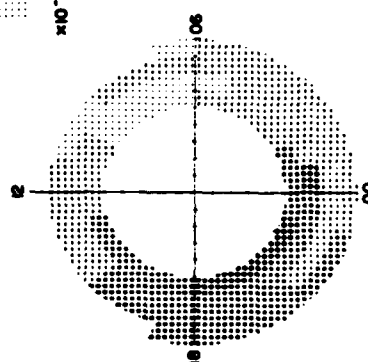SC5 MOMENT STATISTICS
(NUMBER DENSITY)

NUMBER DENSITY Kp 2,3

b. HIGH ENERGY ELECTRONS : 20 keV - 400 keV

d. LOW ENERGY ELECTRONS : 100 eV - 20 keV

a. HIGH ENERGY IONS (UNCORRECTED): 20 keV - 400 keV

c. LOW ENERGY IONS (CORRECTED): 100 eV - 20 keV

cm⁻³
1.0 – 2.0
0.5 – 1.0
0.2 – 0.5
0.1 – 0.2
.02 – 0.1

x10⁻¹

AVERAGE ENERGY (ED/N) Kp 2,3

b. HIGH ENERGY ELECTRONS: 20 keV - 400 keV

d. LOW ENERGY ELECTRONS: 100 eV - 20 keV

a. HIGH ENERGY IONS: 20 keV - 400 keV
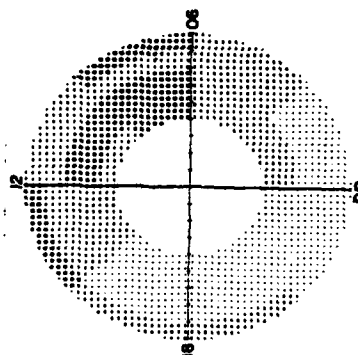
c. LOW ENERGY IONS: 100 eV - 20 keV
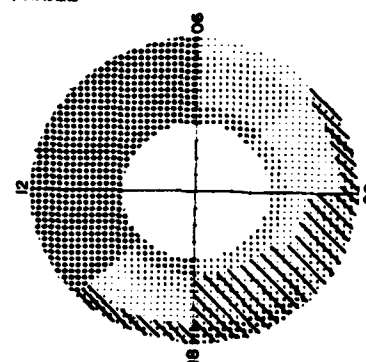
keV
> 50
40 - 50
30 - 40
20 - 30
10 - 20

198
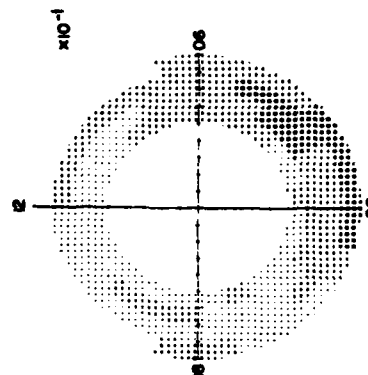
ANISOTROPY INDICES

ELECTRONS
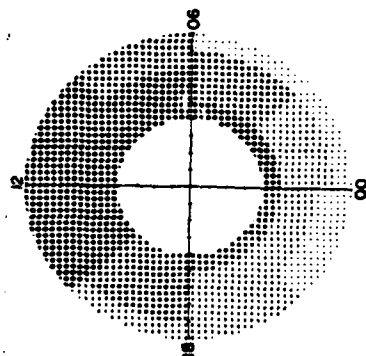
9.2 keV
(a)
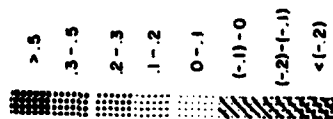
96 keV
(b)

IONS

9.7 keV
(c)

126 keV
(d)

> .5

.3 - .5

.2 - .3

.1 - .2

0 - .1

(-.1) - 0

(-.2) - (-.1)
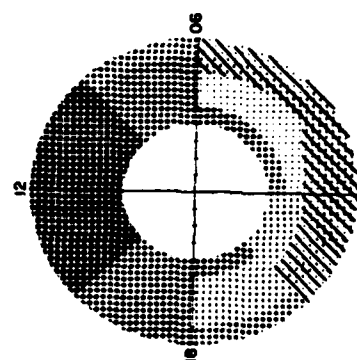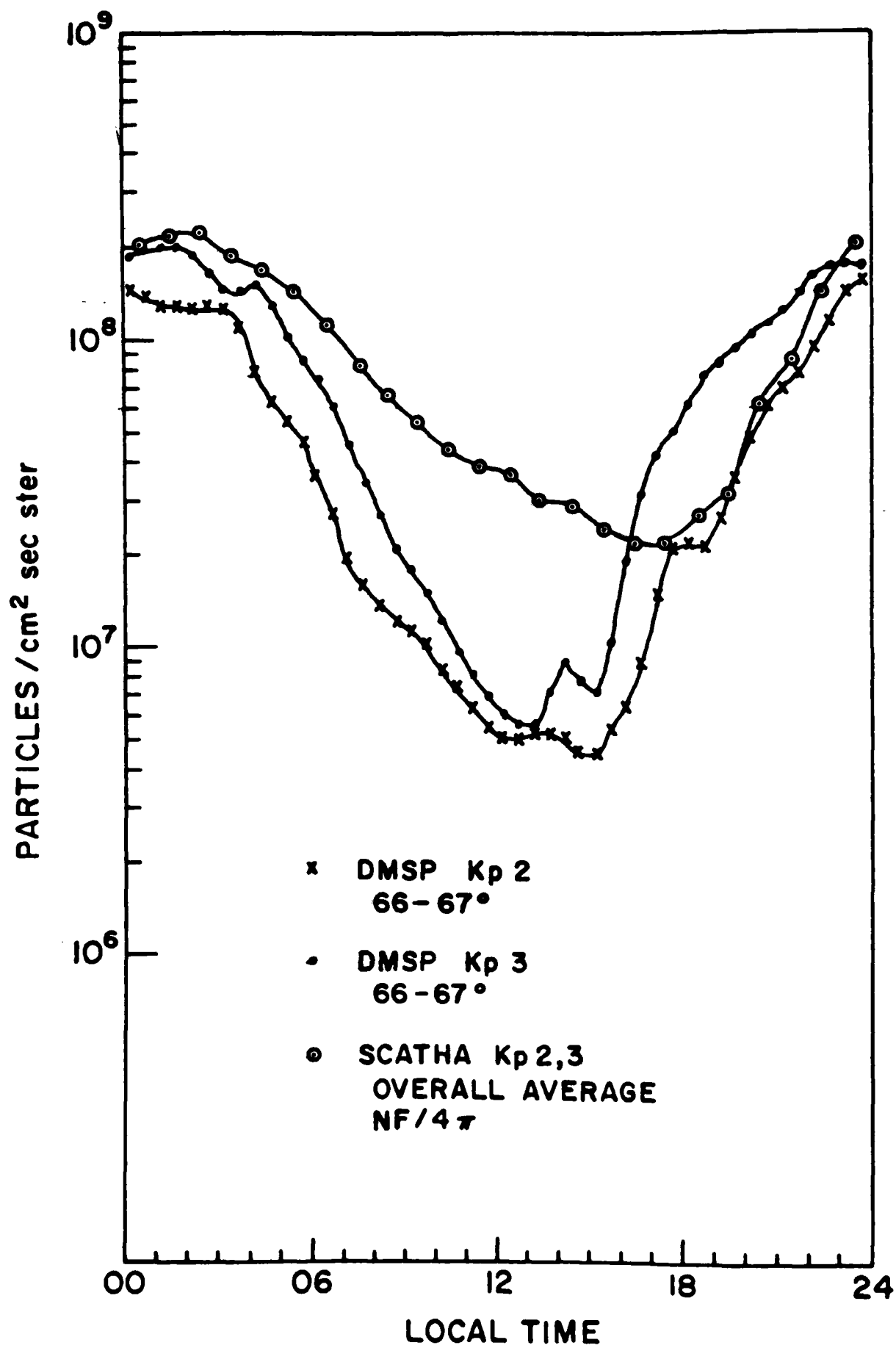
< (-2)
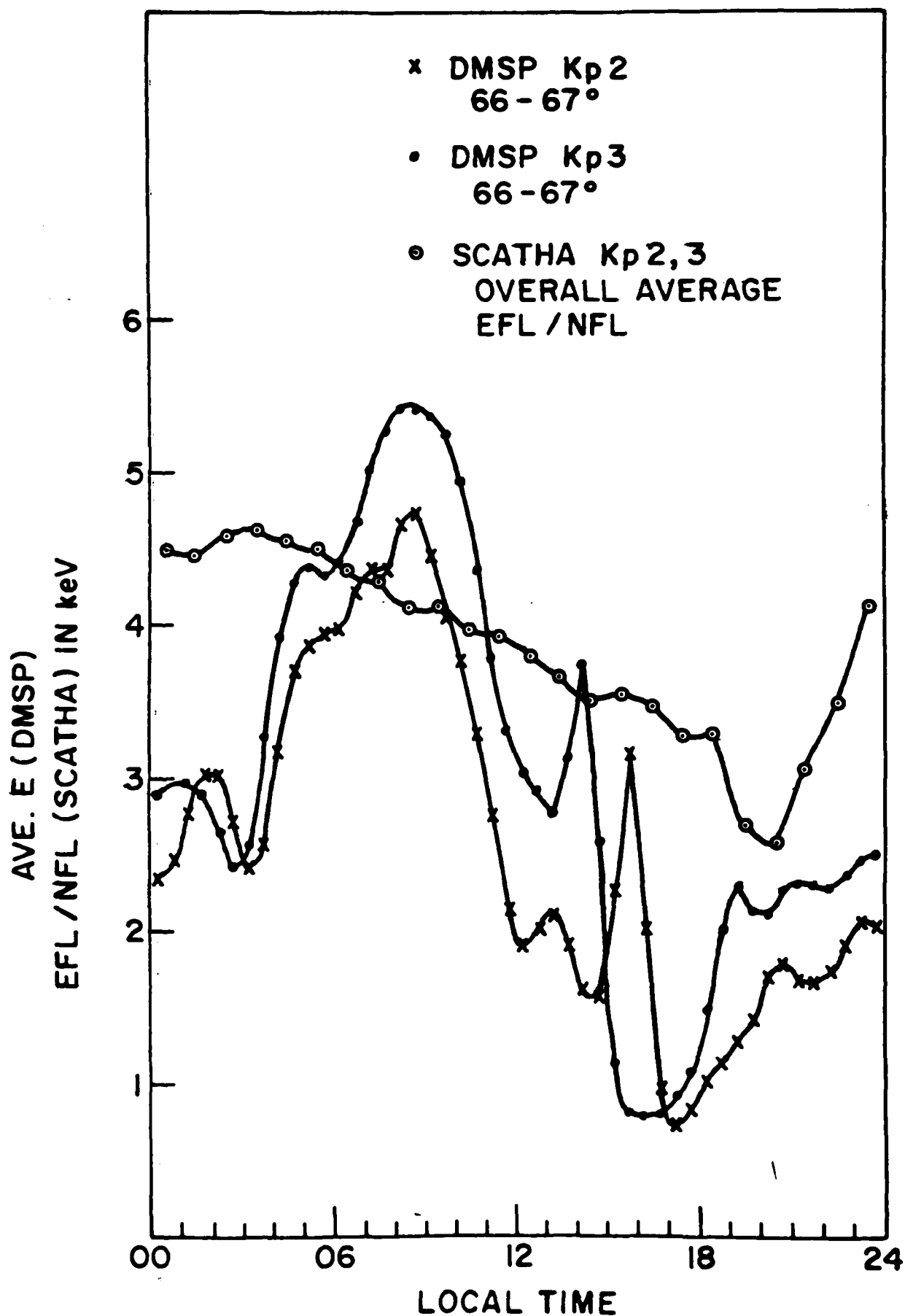
201

COMPARISON OF NEAR-SIMULTANEOUS ELECTRON POPULATIONS
AT GEOSYNCHRONOUS AND LOW ALTITUDE REGIONS

T.L. Schumaker and M.S. Gussenhoven
Boston College Physics Department
Chestnut Hill, MA 02167

and

D.A. Hardy
Air Force Geophysics Laboratory/PHG
Hanscom AFB, MA 01731

ABSTRACT

The relationship between auroral electron precipitation and its source region is explored by comparing electron data from the low altitude, polar orbiting P78-1 satellite and the near geosynchronous orbiting P78-2 (SCATHA) satellite when both are located near the same magnetic field lines. The IGRF model was used to determine the approximate time of magnetic conjugacy of the two satellites. A total of seven conjunctions were found in the period from April 1 through December 22, 1979, which satisfied the criteria that KP < 2, that the field lines near which the satellites are located thread the auroral oval, and that the electron spectra at the two satellites exhibit nearly identical shapes and differential fluxes. For these conjunctions, the electron distributions at low altitude were notably isotropic over the upper hemisphere. By contrast, the fluxes at geosynchronous displayed either "pancake" or "butterfly" distributions. The presence of these anisotropic distributions suggests weak pitch angle diffusion. The degree of anisotropy at geosynchronous, defined as the average ratio of parallel to perpendicular electron fluxes, ranged from approximately 2 to 20. Furthermore, the depth of the loss cone as a function of energy is not constant within a spectrum or

from case to case. Number densities and loss times within the loss cone at geosynchronous were calculated under the assumption that the flux level did not change appreciably within the loss cone.

\

We examine a series of magnetic field line conjunctions between a satellite located near the geosynchronous region of the equatorial plane and a low altitude, polar orbiting satellite. Using a number of case studies, we explore the relationship between electron populations as observed in the midnight regions of the diffuse aurora and their source region near the equatorial plane.

We find that:

1. From low altitude observations in the diffuse aurora, the particle distributions over the upper hemisphere are isotropic. Since these distributions map into the loss cone near geosynchronous, the electron flux across this loss cone is also isotropic. This is inconsistent with weak pitch angle diffusion which maintains that the electron distribution should be anisotropic at all pitch angles.

2. The electron distribution near the geosynchronous region of the equatorial plane, responsible for producing diffuse aurora, is highly anisotropic outside of the loss cone. This is inconsistent with strong pitch angle diffusion, which maintains that the electrons are isotropically distributed.

3. The e-folding loss times of these near-geosynchronous electron populations are much slower than loss times predicted from strong pitch angle diffusion.

The study is done by comparing electron data from the low altitude, polar orbiting P78-1 satellite and the near-geosynchronous orbiting P78-2 (SCATHA) satellite when both were located near the same field lines. The detectors aboard the spinning P78-1 satellite collect electrons in the energy range of 50 eV to 20 keV in 16 semi-logarithmic steps. The SC-5 detectors aboard the spinning SCATHA satellite, which were specifically designed to provide high

204

time resolution particle spectra, collect electrons in the energy range of 110 eV to 54 keV in 8 semi-logarithmic steps.

The IGRF field model is used to determine the time of magnetic conjugacy of the two satellites. Initially, 44 possible conjunctions were found from April 1 to December 22, 1979, which satisfied the criterion of Kp < 2. However, precipitation profiles from P78-1 revealed that the majority of these field lines did not map into the auroral oval. This, along with the fact that the SC-5 detectors aboard SCATHA were not continuously operating, narrowed the total number of possible conjunctions down to 11. For each of the 11 conjunctions, comparisons were then made between the SC-5 differential electron spectra (taken from the smallest pitch angle nearest the calculated "footprint" of the conjugate field line) and the P78-1 spectra (taken within ±3 detector spins from the field line). In 6 out of the 11 cases, nearly identical spectra were found. In the other 5 cases, they were not, possibly because of the presence of inverted V's, electric fields parallel to field lines, or other phenomena that prevent a one-to-one mapping of the distribution function.

Figure 1 shows a typical example of differential electron spectra, taken from day 242, which exhibit spectral similarity at the time of the conjunction. Differential flux is plotted as a function of energy on a log-log scale. The SCATHA spectrum (represented by the solid line) was taken at a pitch angle of 4.49° that was just outside the edge of the loss cone (~ 3°). The P78-1 spectrum (represented by the dashed line) was taken at a pitch angle of 176.52° where the observed electron fluxes are precipitating into low altitude southern latitudes from near geosynchronous.

Figure 2 shows another example of spectra that are nearly identical. This time the SCATHA spectrum was taken at a pitch angle of 3.22° which is

inside the loss cone ($\sim 4.5°$). The P78-1 spectrum was taken at a pitch angle of 8.02° where the observed electron fluxes are precipitating into low altitude northern latitudes from near geosynchronous.

Figure 3 shows plots of differential flux (linearly scaled) versus pitch angle that is characteristic for electrons viewed at low altitude by P78-1. It is evident that the fluxes shown here are isotropic over the upper hemisphere (between 0° and 90°). Flux data is compiled from approximately 3 detector spins in the conjunction regions, and averaged in bins spanning 5° in pitch angle. Included are data from days 299, 180, and 300 taken by 0.6, 1.5, and 3.6 keV energy channels, respectively. The scatter seen in the top and middle panels are within statistical error. Particle isotropy is evident near most of 7 conjunctions at low altitudes, except where strongly inverted V structures make the claim ambiguous.

Since the electron distributions seen at low altitudes map into the loss cone near geosynchronous, the electron distributions inside the loss cone are also isotropic. This implies that the electron populations near geosynchronous do not undergo weak pitch angle diffusion since weak pitch angle diffusion is associated with anisotropic distributions within the loss cone.

Since we don't see signs of weak pitch angle diffusion, we may then ask: "Do we see indications of strong pitch angle diffusion?" We examine electron distributions outside of the loss cone near geosynchronous for our answer.

Figure 4 shows plots of differential flux (linearly scaled) versus pitch angle that is characteristic of electrons viewed near geosynchronous orbit by SCATHA. The three panels show fluxes that directly correspond to the three panels in the previous viewgraph. Unlike the electron distributions observed at low altitudes by P78-1, the electron distributions observed near geosynchronous are typically anisotropic. The top and bottom panels show clear

indication of a "pancake" distribution (flux peaking at 90°), while the middle panel exhibits a "butterfly" distribution (flux peaking near 45° and 135°). Such anisotropic distributions were evident in all seven cases of magnetic conjugacy at geosynchronous. This implies that the electron population near geosynchronous does not undergo strong pitch diffusion since strong pitch angle diffusion demands isotropic distributions outside of the loss cone.

Even though the data appear to be inconsistent with both weak and strong pitch angle diffusion, we may make an estimation of the e-folding electron loss rates. Table 1 shows the number densities within the loss cone, total number densities, and the e-folding loss times within the loss cone as a function of energy at the conjunction point near geosynchronous on day 300.

The number density within the loss cone was readily calculated from a knowledge of the loss cone size, and electron flux information within the loss cone. The electron fluxes were found by linear extrapolation across the loss cone whenever the detector spins in such a manner that it does not look directly into the loss cone. The total number density was obtained by integrating the electron fluxes over all pitch angles for a complete satellite spin at the conjoint field line location. Note that the number density within the loss cone is approximately three orders of magnitude less than the total number density for each energy channel. This holds true for the other five conjunctions as well.

In column 4 of Table 1, the e-folding electron loss times within the loss cone were calculated using the observed electron distributions found near geosynchronous. In this specific case, as is generally true in the other conjunctions, the loss times are seen to decrease with increasing energy, from a value of 35 minutes at .11 keV to 5 minutes at 54 keV. Considering all cases, loss times ranged from approximately 0.5 to 3.5 hours for 100 eV

electrons, and from 4 to 11.5 minutes for 54 keV electrons.

The e-folding rates in column 5 of Table 1 were calculated as if isotropy had been maintained along the entire particle distribution at geosynchronous. These values range from 27 minutes at .11 keV to 1 minute at 54 keV. Strong pitch angle diffusion may be associated with these hypothetical electron distributions since isotropy is assumed both inside and outside of the loss cone. We see that the e-folding electron loss rates of the observed near-geosynchronous electron populations in column 4 are much slower than the loss rates associated with strong pitch angle diffusion in column 5.

The loss times calculated from measured electron fluxes are a factor of 1.5 to 10 times slower than those predicted by the limit of strong pitch angle diffusion.

From our study, we may conclude that in the midnight region, the diffuse aurora appears to be maintained by a slow dribble of particles originating at near-geosynchronous altitudes which do not seem to be undergoing either weak or strong pitch angle diffusion as defined in the literature.

\

REFERENCES

Ashour-Abdalla, M., and C.F. Kennel, Nonconvective and convective electron cyclotron harmonic instabilities, J. Geophys. Res., 83, 1531, 1978.

Ashour-Abdalla, M., and R.M. Thorne, Toward a unified view of diffuse auroral precipitation, J. Geophys. Res., 83, 4755, 1978.

Baker, D.N., P. Stauning, E.W. Hones, Jr., P.R. Higbie, and R.D. Belian, Strong electron pitch angle diffusion observed at geostationary orbit, Geophys. Res. Lett., 6, 205, 1979.

Burrows, J.R., and I.B. McDiarmid, Trapped particle boundary regions, in Critical Problems of Magnetospheric Physics, edited by E.R. Dyer, (National Academy of Sciences, Wash., D.C., 1972).

Hones, Jr., E.W., J.R. Asbridge, S.J. Bame, and S. Singer, Energy spectra and angular distributions of particles in the plasma sheet and their comparison with rocket measurements over the auroral zone, J. Geophys. Res., 76, 63, 1966.

Kennel, C.F., and H.E. Petshek, Limit on stably trapped particle fluxes, J. Geophys. Res., 71, 1, 1966.

Kennel, C.F., F.L. Scarf, R.W. Fredricks, J.H. McGehee, and F.V. Coroniti, VLF electric field observations in the magnetosphere, J. Geophys. Res., 75, 6136, 1970.

Lyons, L.R., Electron diffusion driven by magnetospheric electrostatic waves, J. Geophys. Res., 79, 575, 1974.

Meng, C.-I., B. Mauk, and C.E. McIlwain, Electron precipitation of evening diffuse aurora and its conjugate electron fluxes near the magnetospheric equator, J. Geophys. Res., 84, 2545, 1979.

O'Brien, B.J., Lifetime of outer-zone electrons and their precipitation into the atmosphere, J. Geophys. Res., 67, 3687, 1962.

Retterer, J.M., J.R. Jasperse, and T.S. Chang, A new approach to pitch angle scattering in the magnetosphere, J. Geophys. Res., 88, 201, 1983.

Sharp, R.D., D.L. Carr, R.G. Johnson, and E.G. Shelley, Coordinated auroral electron observations from a synchronous and polar satellite, J. Geophys. Res., 76, 7669, 1971.

Young, T.S.T., J.D. Callen, and J.E. McCune, High-frequency electrostatic waves in the magnetosphere, J. Geophys. Res., 78, 1082, 1973.

FIGURE CAPTIONS

Figure 1. Comparison of the differential spectra between electrons detected
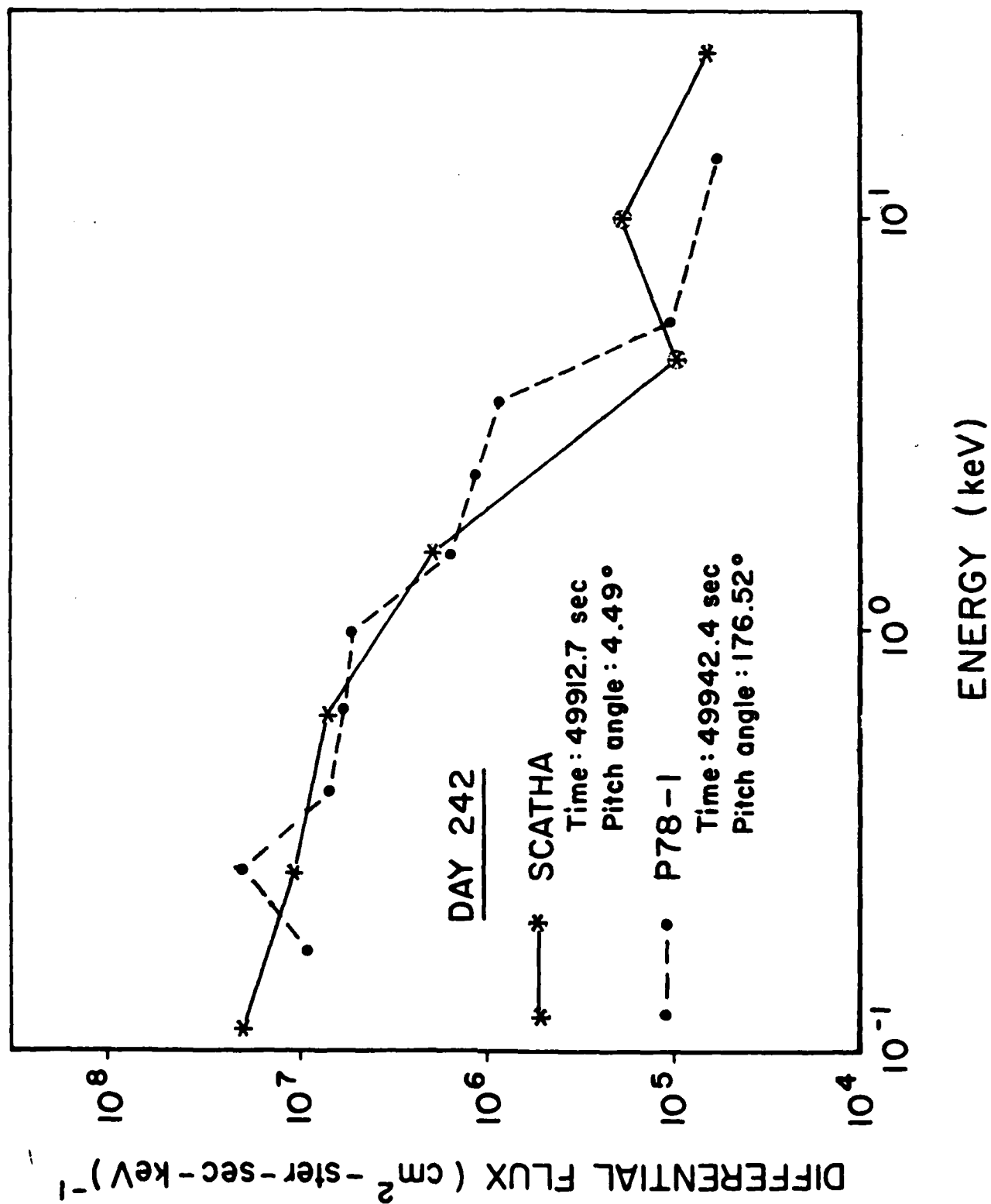by P78-1 and SCATHA on day 242 near the conjugate magnetic field
line.

Figure 2. Same as Figure 1 for day 300.

Figure 3. Differential flux as a function of pitch angle; determined from
electrons detected at P78-1, instrument 2, channel 7 (0.6 keV) on
day 299, channel 10 (1.5 keV) on day 180, and channel 12 (3.6 keV)
on day 299, compiled from approximately 3 detector spins within
the region of the conjugate field line.

Figure 4. Differential flux as a function of pitch angle, determined from
electrons detected at SCATHA by the 0.62 keV energy channel on day
299, the 1.57 keV energy channel on day 180, and the 4.4 keV
energy channel on day 300. The fluxes are averaged over a 200
second time interval around the conjugate field line.

\

TABLE 1

DAY 300 ENERGY CHANNEL	NUMBER DENSITY IN LOSS CONE (CM^{-3})	TOTAL NUMBER DENSITY (CM^{-3})	e-FOLDING LOSS RATE IN LOSS CONE (HR:MIN) (MEASURED DIST)	e-FOLDING LOSS RATE IN LOSS CONE (HR:MIN) (ISOTROPIC DIST)
0.11 KeV	4.4×10^{-4}	8.6×10^{-2}	00:35	00:27
0.26 KeV	5.1×10^{-4}	1.8×10^{-1}	00:23	00:17
0.62 KeV	6.4×10^{-4}	3.2×10^{-1}	00:18	00:10
1.57 KeV	8.5×10^{-4}	5.4×10^{-1}	00:15	00:07
4.40 KeV	7.0×10^{-4}	3.8×10^{-1}	00:10	00:04
9.20 KeV	2.9×20^{-4}	3.0×10^{-1}	00:10	00:03
24.0 KeV	3.2×10^{-5}	5.3×10^{-2}	00:11	00:02
54.0 KeV	5.5×10^{-5}	5.9×10^{-3}	00:05	00:01

DAY 242

SCATHA
Time : 49912.7 sec
Pitch angle : 4.49°

P78-1
Time : 49942.4 sec
Pitch angle : 176.52°

ENERGY (keV)

DIFFERENTIAL FLUX (cm²-ster-sec-keV)⁻¹

DAY 300

SCATHA
Time: 73389.4 sec
Pitch angle: 3.22°

P78-1
Time: 73382.8 sec
Pitch angle: 8.02°

ENERGY (keV)

DIFFERENTIAL FLUX (cm^2 - ster - sec - keV)$^{-1}$

P78-1 (600 km) 1979

DIFFERENTIAL FLUX (cm²-s-ster-eV)⁻¹
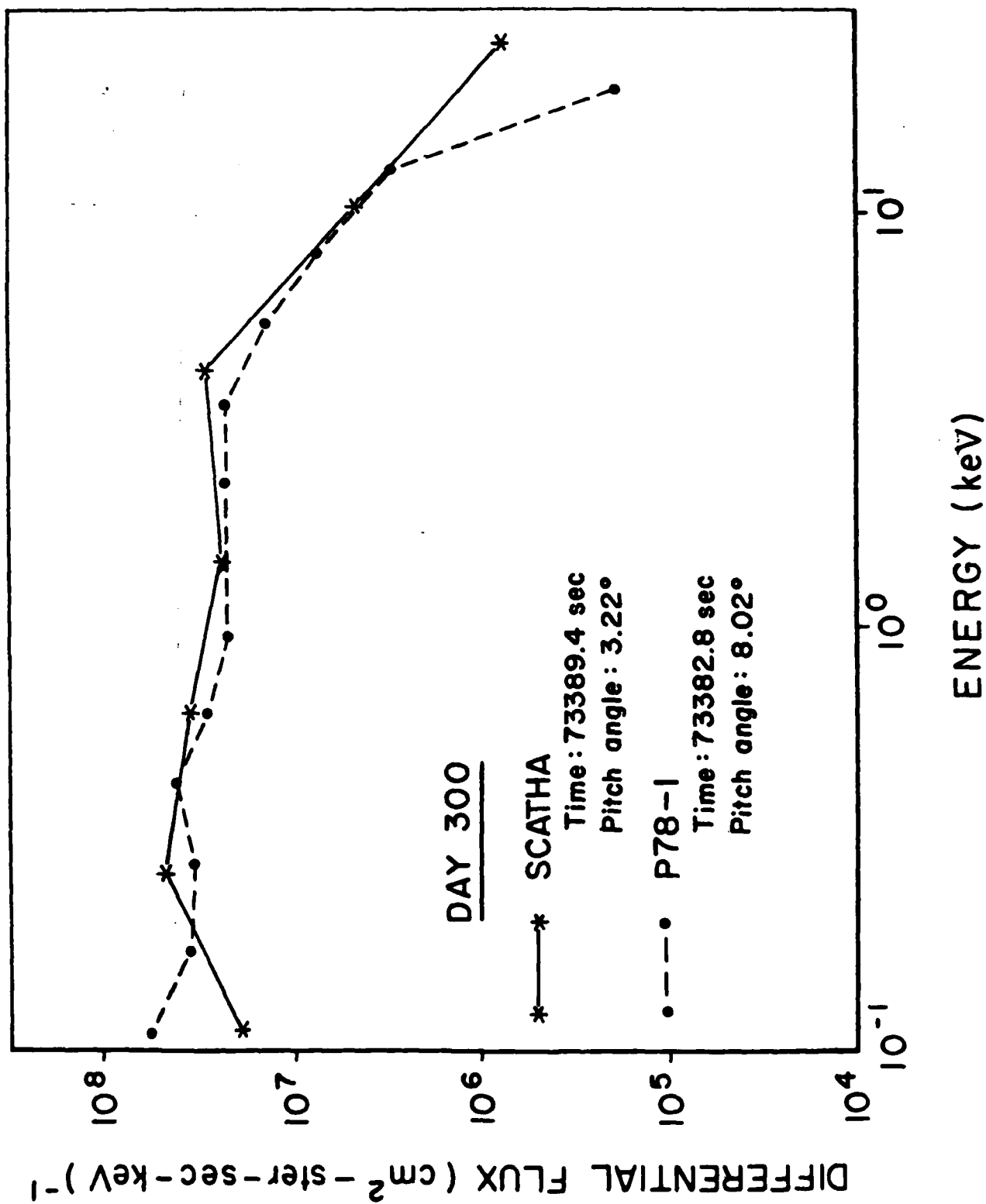
PITCH ANGLE

DAY 299
73165.5-731906 UT
Ē = 0.6 keV
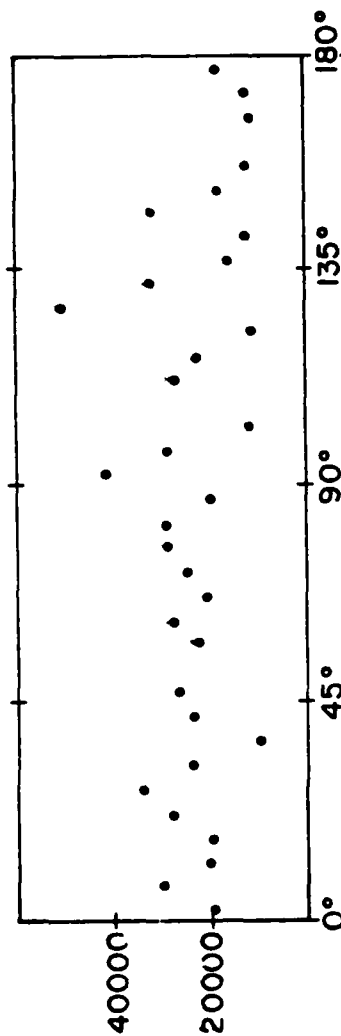
DAY 180
37510.1-37529.3 UT
Ē = 1.5 keV
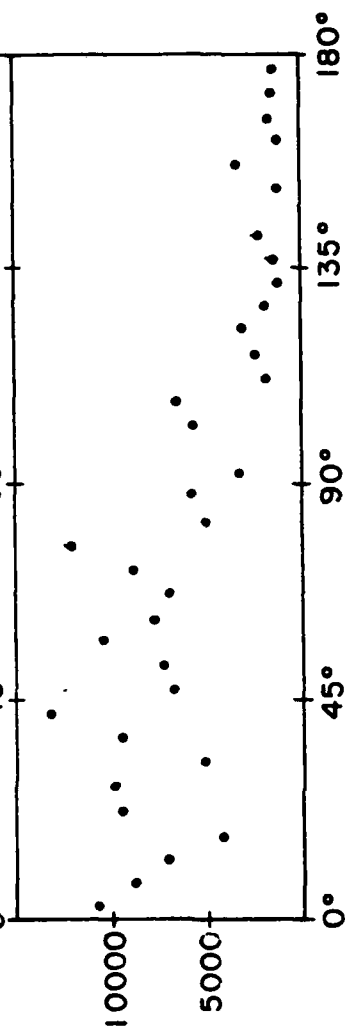
DAY 300
73350.1-73400.0 UT
Ē = 3.6 keV

215
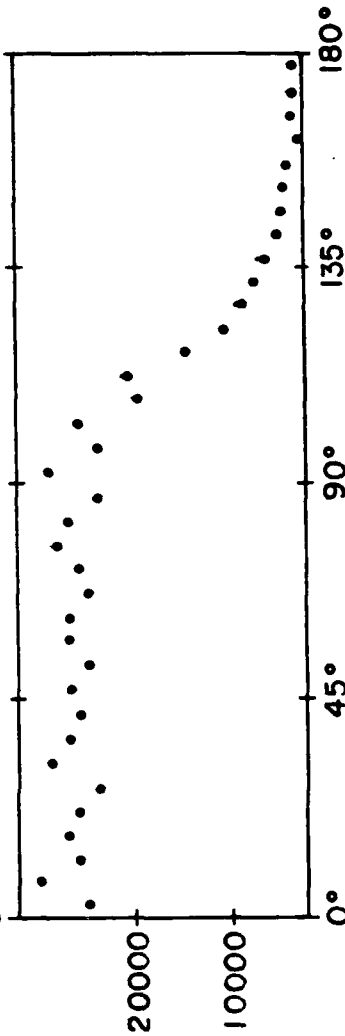
SCATHA (~GEOSYNC) 1979

DAY 299

73100.-73300. UT

$\bar{E}$ = 0.62 keV

DAY 180

37400.-37600. UT

$\bar{E}$ = 1.57 keV

DAY 300

73300.-73500. UT

$\bar{E}$ = 4.4 keV

DIFFERENTIAL FLUX (cm^2-s-ster-eV)$^{-1}$

PITCH ANGLE
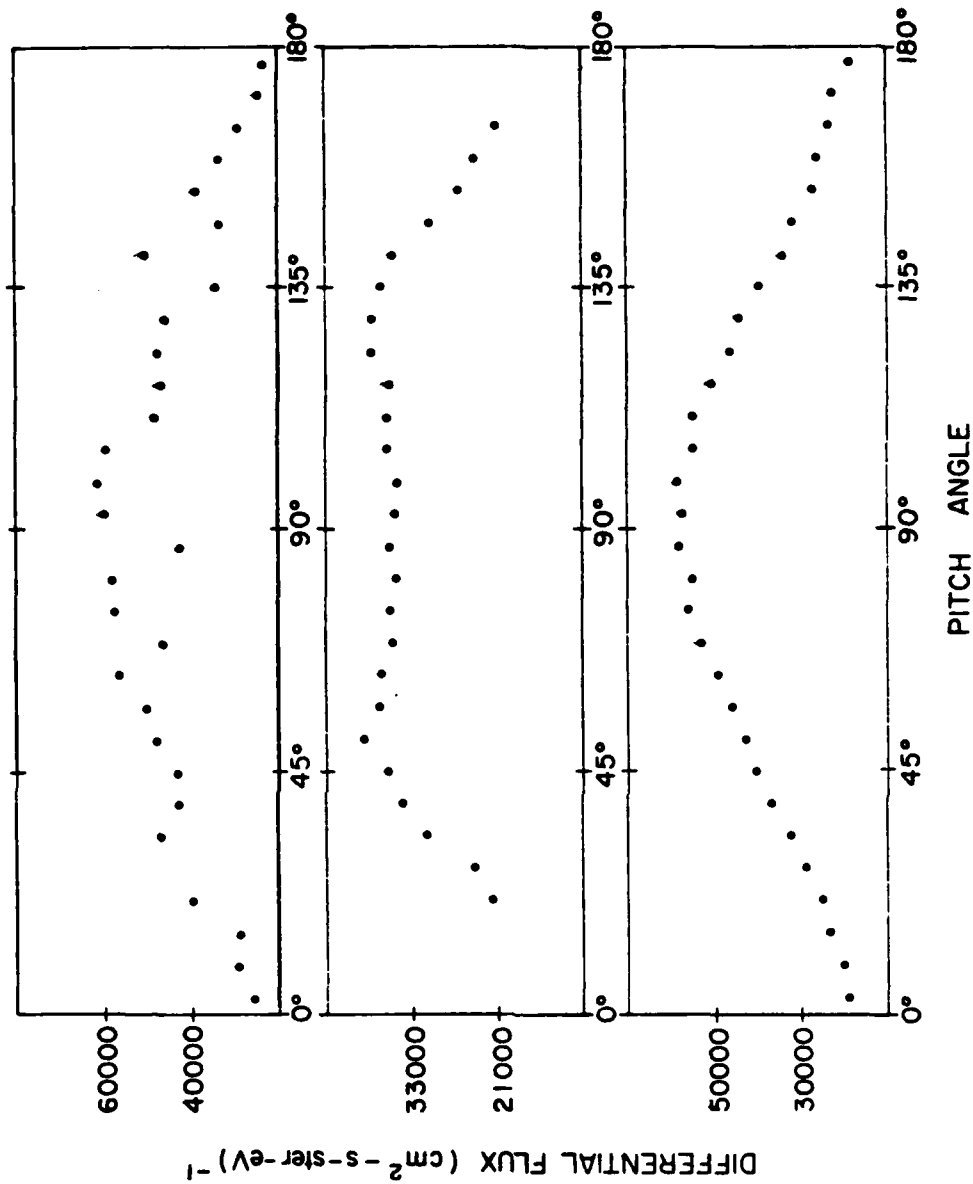
AFGL-TR-83-0085

ELECTRON BEAM-INDUCED
ELECTROMAGNETIC WAVES IN A
MAGNETOSPHERIC PLASMA

D. E. Donatelli
T. S. Chang

Department of Physics
Boston College
Chestnut Hill, MA 02167

Scientific Report No. 1

15 May 1983

217

INTRODUCTION

The question of whether or not electromagnetic cyclotron harmonic waves can be excited in the magnetosphere near geostationary altitude, was raised upon examination of the data from the VLF broadband measurements on the SCATHA satellite during a severe spacecraft charging event (Donatelli et al., 1983). During this event strong emission bands were detected at or near the first two harmonics of the 2 kHz electron gyrofrequency. These emission bands appeared on both the electric and magnetic wave field detectors. While the SCATHA electron gun was in operation at varying current/energy levels attempting to discharge the satellite, there were frequency shifts in the emission band and consistent magnetic field components. This observation prompted the present theoretical study to determine whether electromagnetic electron cyclotron harmonic waves could be generated in a plasma representative of local conditions.

Theoretical and observational studies to date have explained observations analogous to those of the SCATHA data in terms of electrostatic emissions. Using the Harris dispersion relation, Fredricks (1971) showed that non-resonant electrostatic waves could be excited in a plasma in which the electron perpendicular velocity distribution has a narrow region of positive slope, i.e. $\partial f_0/\partial v_\perp > 0$. The restriction on the velocity distribution was relaxed by Young et al. (1973) to the requirement that a distribution of cold and warm electrons have a velocity distribution that is non-monotonic in $V_\perp$. They showed that this provides sufficient free energy for driving instabilities. The ratio of cold to hot plasma density, above which instability will not occur, was established by Ashour-Abdalla et al. (1975). The non-

218

convective and convective nature of the instability is shown to be controlled by the temperature ratio of the cold to hot electron populations (Ashour-Abdalla and Kennel, 1978). Electrostatic upper hybrid waves observed on ISEE-1 have also been explained by this theory (Kurth, et al. 1979). Sentman et al. (1979) show examples of two-component electron distribution functions constructed from ISEE-1 observations of low energy magnetospheric electrons that occur simultaneous with the detection of electrostatic emissions between the electron cyclotron frequency and the upper hybrid resonance.

Electromagnetic emissions within this frequency range, with the exception of the whistler mode, have not been reported prior to the SCATHA observations. Ohnuma et al. (1981) have shown that electromagnetic cyclotron harmonic waves may be generated in a dense plasma; i.e. one in which $\omega_{pe} \gg \Omega_{ce}$, where ω_{pe} and Ω_{ce} are the electron plasma and gyro- frequencies, respectively. Although their results were applied to laboratory plasmas, this condition may prevail in the vicinity of SCATHA during beam operations.

Here the problem will be approached in a manner suggested by the work of Tataronis and Crawford (1970). They used the quasi-static approximation in deriving a dispersion relation for a warm magnetoplasma and proceeded to examine under what conditions unstable electrostatic cyclotron harmonic waves (Bernstein modes) exist. They looked at several types of distribution functions and examined ranges of plasma parameters for finding unstable modes. They show that if the analytic solution to the dispersion relation undulates about zero for a given distribution function, non-convective mode coupling instabilities occur. These occur between specific ranges of the two ratios, the plasma frequency/electron

219

gyrofrequency and the gyroradius/wavelength, for each harmonic pair. For two component distributions, the density and velocity ratios of the two components must also be considered. Similar solutions are sought here for electromagnetic, cyclotron harmonic waves (extraordinary and ordinary modes).

In the next section the electromagnetic dispersion relation for a warm, uniformly magnetized, homogeneous plasma is examined. Analytical solutions will be presented for the three perpendicularly propagating modes, the Bernstein, extraordinary, and ordinary modes, using a two component distribution function. The ambient plasma is represented as a Maxwellian; the electron beam is represented as a delta-function in velocity space. Sample calculations show that instabilities may exist for both the Bernstein and the extraordinary modes. The frequencies and wave numbers of the excited modes vary with the beam-to-ambient-plasma density and velocity ratios.

THEORY

The dispersion relation is derived using the linearized Vlasov equation and Maxwell's equations (in cgs units):

$$[\partial/\partial t + \underline{v} \cdot \underline{\nabla} + ((\underline{v} \times \underline{B}_0)/c) \cdot \underline{\nabla}_v] f_{j1} =$$
$$- (q_j/m_j)[\underline{E}_1 + (\underline{v} \times \underline{B}_1)/c] \cdot \underline{\nabla}_v f_{jo} \tag{1}$$

$$\underline{\nabla} \times \underline{E}_1 = -c^{-1} \partial \underline{B}_1/\partial t$$
$$\underline{\nabla} \times \underline{B}_1 = c^{-1} \partial \underline{E}_1/\partial t + (4\pi q_j n_{j1}/c) \int \underline{v} d\underline{v} f_{j1}$$
$$\underline{\nabla} \cdot \underline{E}_1 = 4\pi q_j n_{j1} \int d\underline{v} f_{j1} \tag{2}$$
$$\underline{\nabla} \cdot \underline{B}_1 = 0$$

The equilibrium electron velocity distribution is $f_{j0}(v_\perp, v_{||})$ where $\perp$ and $||$ refer to components perpendicular and parallel to the external magnetic field, $B_0 = B_{0z}$. There is assumed to be no external electric field, $E_0 = 0$. The perturbation electric and magnetic fields are $\underline{E}_1$ and $\underline{B}_1$, respectively. The perturbed particle distribution and density are f_{j1} and n_{j1}, respectively, where particle species is indicated by the subscript j. The charge and mass for each particle species are q_j and m_j, respectively; c is the velocity of light in a vacuum.

The plasma is assumed to be infinite, spatially homogeneous and uniformly magnetized, since variations in time and space may be neglected. Equations (1) and (2) are solved by introducing a Fourier transform in space, a Laplace transform in time, and integrating along unperturbed particle orbits. This leads to the nine element dielectric tensor, from Krall and Trivelpiece (1973):

$$\begin{vmatrix} D_{xx} & D_{xy} & D_{xz} \\ D_{yx} & D_{xy} & D_{yz} \\ D_{zx} & D_{zy} & D_{zz} \end{vmatrix} \begin{vmatrix} E_x \\ E_y \\ E_z \end{vmatrix} = 0 \tag{3}$$

where the elements of the dielectric coefficient are $(\text{Im}(\omega)>0)$:

$$D_{xx} = 1 - (c^2 k_{||}^2/\omega^2) - (2\pi/\omega) \sum_j \sum_N \omega_{pj}^2 \ II \ x_j J_N^2 N^2 \Omega_j^2/k_\perp^2$$

$$D_{xy} = - (2\pi i/\omega) \sum_j \sum_N \omega_{pj}^2 \ II \ x_j J_N J_N' v_\perp N\Omega_j/k_\perp$$

$$D_{xz} = (c^2 k_{||} k_\perp/\omega^2) - (2\pi/\omega) \sum_j \sum_N \omega_{pj}^2 \ II \ \Lambda_j J_N^2 v_{||} N\Omega_j/k_\perp$$

$$D_{yx} = - D_{xy}$$

$$D_{yy} = 1 - [c^2(k_{||}^2 - k_\perp^2)/\omega^2] - (2\pi/\omega) \sum_j \sum_N \omega_{pj}^2 \ II \ x_j (J_N')^2 v_\perp^2$$

$$D_{yz} = (2\pi i/\omega) \sum_j \sum_N \omega_{pj}^2 \; II \; \Lambda_j J_N J_N' v_\perp v_\parallel$$

$$D_{zx} = (c^2 k_\parallel k_\perp/\omega^2) - (2\pi/\omega) \sum_j \sum_N \omega_{pj}^2 \; II \; \chi_j J_N^2 v_\parallel N\Omega_j/k_\perp$$

$$D_{zy} = - (2\pi i/\omega) \sum_j \sum_N \omega_{pj}^2 \; II \; \chi_j J_N J_N' v_\parallel v_\perp$$

$$D_{zz} = 1 - (c^2 k_\perp^2/\omega^2) - (2\pi/\omega) \sum_j \sum_N \omega_{pj}^2 \; II \; \Lambda_j J_N^2 v_\parallel^2$$

where:

$$II \equiv \int_{-\infty}^{\infty} dv_\parallel \int_0^{\infty} dv_\perp^2 v_\perp/(N\Omega_j + k_\parallel v_\parallel - \omega$$

$$\chi_j \equiv [1-(k_\parallel v_\parallel/\omega)](\partial f_{jo}/\partial v_\perp^2) + (k_\parallel v_\parallel/\omega)$$
$$(\partial f_{jo}/\partial v_\parallel^2)$$

$$\Lambda_j \equiv (N\Omega_j/\omega)[(\partial f_{jo}/\partial v_\perp^2) - (\partial f_{jo}/\partial v_\parallel^2)]$$
$$+ (\partial f_{jo}/\partial v_\parallel^2)$$

For simplicity in the above derivation, the wave vector $\underline{k}$ is defined as follows:

$$\underline{k} = \underline{k}_\perp + \underline{k}_\parallel = k_\perp \underline{x} + k_\parallel \underline{z}.$$

The definition of other terms are:

ω = wave frequency

ω_{pj} = plasma frequency = $(4\pi n_j q_j^2/m_j)^{1/2}$

Ω_j = particle gyrofrequency = $q_j B_0/m_j c$

J_N = Nth order Bessel function of the first kind

$k_\perp v_\perp/\Omega_j$ = argument of the Bessel function

J_N' = derivative of J_N with respect to the argument.

There is no separation of electrostatic and electromagnetic modes in the dispersion tensor (3). However, by considering parallel propagation ($k_\perp = 0$) and perpendicular propagation ($k_\parallel = 0$) separately, it is possible to simplify the dispersion tensor and examine some

characteristic wave modes. Setting $k_\perp = 0$ in (3) singles out the modes that propagate parallel to the equilibrium magnetic field. These modes are:

(1)   The longitudinal, electrostatic, Landau damped, Langmuir waves and ion acoustic waves.

(2)   The weakly damped transverse electromagnetic Alfven waves at frequencies below the ion cyclotron frequency; the Whistler waves at $\omega = (1/2)\Omega$ and the cyclotron waves which occur at $\omega = \Omega$. The cyclotron waves are strongly damped for $\omega = k_\parallel c$, which is also the band in which spontaneous emission of radiation occurs.

By taking $k_\parallel = 0$, the characteristic waves that propagate perpendicular to the equilibrium magnetic field are singled out. These modes are:

(1)   the almost purely longitudinal, nearly electrostatic Bernstein modes that correspond to the electrostatic waves discussed at the beginning of this section.

(2)   The transverse, electromagnetic, cyclotron-harmonic waves which include the extraordinary mode with $\underline{E} \perp \underline{B}_0$ and the ordinary mode with $\underline{E} \parallel \underline{B}_0$. These modes are normal modes of a high density, magnetized plasma ($\omega_p \gg \Omega_e^2$), (Ohnuma et al., 1981) and are excited near ion and electron cyclotron harmonics. The SCATHA observations are within the range of these emissions. It will be determined if these modes are unstable within the local beam-background plasma.

For $k_\parallel = 0$, the dispersion tensor (3) reduces to:

$$\begin{vmatrix} D_{xx} & D_{xy} & 0 \\ -D_{xy} & D_{yy} & 0 \\ 0 & 0 & D_{zz} \end{vmatrix} = 0 \qquad (4)$$

223

At the frequencies of oscillation considered here, ions may be regarded as providing a charge neutral background. The approximation $\omega_p^2 \ll k^2c^2$ is also valid since:

$$\omega_p^2/k^2c^2 < \omega_p^2 v_h^2/\omega^2c^2 < \omega_p^2 v_b^2/\Omega^2c^2 < 0.1$$

where: v_b = beam velocity.

Since the D_{xy} terms are second order in ω_p^2/k^2c^2, they may be neglected. Then (4) may be approximately solved for the three eigenmodes:

(1) $D_{xx} = 0$: Bernstein mode

(2) $D_{yy} = 0$: extraordinary mode

(3) $D_{zz} = 0$: ordinary mode

where the elements of the dispersion matrix reduce to:

$$D_{xx} = 1 - (4\pi\omega_p^2/k^2) \sum N^2\Omega^2/\omega(N\Omega - \omega) \int dv_\parallel$$
$$\int dv_\perp v_\perp J_N^2 \, \partial f_0/\partial v_\perp^2 \tag{5}$$

$$D_{yy} = 1 - (k^2c^2/\omega^2) - 4\pi\omega_p^2 \sum (\omega(N\Omega - \omega))^{-1} \int dv_\parallel$$
$$\int dv_\perp v_\perp^3 (J_N')^2 \, \partial f_0/\partial v_\perp^2 \tag{6}$$

$$D_{zz} = 1 - (k^2c^2/\omega^2) - 4\pi\omega_p^2 \sum (\omega(N\Omega - \omega))^{-1} \int dv_\parallel$$
$$\int dv_\perp v_\perp v_\parallel^2 J_N^2 [N\Omega/\omega \, (\partial f_0/\partial v_\perp^2$$
$$- \partial f_0/\partial v_\parallel^2) - \partial f_0/\partial v_\parallel^2)] \tag{7}$$

Unstable solutions are now sought for each of the eigenmodes using the SCATHA data to evaluate the necessary parameters.

ANALYTICAL SOLUTIONS

The SCATHA observations presented in Donatelli et al. (1983) for 24 April 1979, indicate that beam-injected electrons may create a dense

plasma where electromagnetic cyclotron harmonic instabilities are gener-
ated. At the time of interest the magnetospheric plasma was made up of
two populations: a low-energy component with a temperature about 300 eV,
and a high-energy component about 25 keV (Mullen et al., 1981). The
ejection energy of the beam from the electron gun was either 50 eV or
150 eV. After passing through the satellite sheath the beam electrons had
energies of 1-3 keV due to acceleration through the vehicle potential.
Emission bands were detected consistently at or near the first and
second harmonic of the electron gyrofrequency, Ω, which was about 2 kHz.
From the data, beam-to-background velocity ratios are estimate. A ratio
of 2-3 is reasonable for the "artificial" beam (electrons from the beam
systems on SCATHA), and a ratio of 9-10 for the natural beam (injec-
tions of high energy magnetosperic electrons). The density ratios are
assumed to be greater than one, both for the natural beam (Mullen et
al., 1981) and the "artifical" beam. Although the current and radius
of the artificial beam are known, the effective beam density is not,
since the electrostatic forces between beam electrons contribute to
rapid spreading as does the external magnetic field (Gendrin, 1973).
Furthermore, at these low emission energies the electron beam cannot be
highly focussed.

The dimensionless variables to be used in these solutions are de-
fined as follows:

$$s^2 \equiv 2KTk^2/m\Omega^2 = v_T k^2/\Omega^2$$

$$x_b \equiv v_{\perp b}/v_T$$

where:

$$v_{\perp b} = v_b \sin \phi_b;$$

ϕ_b = pitch angle of the electron beam, $15^0 < \phi < 165^0$.

Then:

$$sx_b = kv_{\perp b}/\Omega = (kv_h/\Omega)\sin\phi_b$$

and:

$$0.26 (kv_b/\Omega) < sx_b < kv_h/\Omega$$

where sx_b is the argument of the Bessel function in equations (5), (6), and (7).

The ambient density is between 0.5 and 1.0 cm^{-3}. If the density is set at 1.0 cm^{-3}, the value of the following non-dimensionalized parameters are:

$$(\omega_b/\Omega)^2 = 20$$
$$(\omega_b/kc)^2 = 0.1$$

The distribution function is approximated as follows:

$$f_0 = n_p(m/2\pi KT)^{3/2}\exp[-(m/2KT)(v_{\parallel}^2 + v_{\perp}^2)] +$$
$$(n_b/2\pi v_{\perp b})\,\delta(v_{\parallel} - v_{\parallel b})\,\delta(v_{\perp} - v_{\perp b}) \qquad (8)$$

where:

    T = temperature (°K)

    K = Boltzmann constant

    n_p = low energy ambient electron density

    n_b = density of electron beam

This distribution function is a Maxwellian combined with a ring distribution in velocity space and including motion parallel to the magnetic field. The Maxwellian represents the ambient plasma, and the delta-function represents the beam, with the ring distribution describing the portion of the monoenergetic beam electrons moving in the plane perpendicular to the magnetic field, uniformly distributed in gyrophase angle. Tataronis and Crawford (1970) conducted a numerical

study of the propagation characteristics of perpendicularly propagating electrostatic waves in a combined ring-Maxwellian distribution. They state that instability occurs if the analytic function for the dispersion relation is undulatory about zero. Their results show that mode coupling is a feature of the ring distribution leading to strong non-convective instability. Combining the ring and Maxwellian distributions leads to non-convective instability with higher growth rate and lower instability threshhold than for the ring distribution alone. The electromagnetic dispersion relation may be solved for each of the three eigenmodes of perpendicularly propagating waves. Solutions to the dispersion relation may be found as functions of x_b and n_b/n_p, using preceding definitions.

A. The Bernstein Mode

The dispersion relation for the Bernstein mode, obtained by substituting equation (8) into equation (5) and integrating, is the following:

$$D_{xx} = 1 - (4\omega_p^2/\Omega^2) \sum N^2\Omega^2 A_{Nx}/(\omega^2 - N^2\Omega^2) = 0 \qquad (9)$$

where:

$$A_{Nx} = s^{-2}\exp(-s^2/2)I_N(s^2/2) + (n_b/n_p sx_h)J_N J_N'$$

I_N is the modified Bessel function of the first kind with argument $s^2/2$. The prime denotes the derivative of the Bessel function with respect to the argument. $\sum$ is now the summation from N=1 to ∞. Since A_{Nx} is undulatory about zero, unstable solutions are anticipated (Tataronis and Crawford, 1970). In Appendix A it is shown that in using a three-term approximation to equation (9), unstable solutions are found for:

$n_b/n_p = 2$ and $x_b = 2$

such that:

227

$$\omega/\Omega = 1.7 + 0.9i \qquad (10)$$

and:

$$n_b/n_p = 4.5 \text{ and } x_b = 10$$

such that:

$$\omega/\Omega = 1.8 + 1.1i \qquad (11)$$

The Bernstein Mode is nearly a pure electrostatic mode. The solutions are equivalent to those obtained by Tataronis and Crawford (1970) using the electrostatic approximation to the dispersion relation. They found unstable solutions in this frequency range with the growth rate, γ, a finite fraction of the real part of the frequency, ω_r. In equation (10), with $\omega_r = 1.7\ \Omega$, $\gamma = 0.5\omega_r$; for equation (11), $\gamma = 0.6\omega_r$. In both equations (9) and (10) ω_r is in the range of emissions detected by the SCATHA broadband receiver (Donatelli et al., 1983). However, this mode is not expected to have the observed magnetic field component. the presence of a magnetic component requires the existence of electromagnetic extraordinary and/or ordinary modes.

B. The Extraordinary Mode

The dispersion relation for the extraordinary mode is obtained by substituting equation (8) into equation (6) and integrating to obtain:

$$n_{yy} = 1 - (k^2 c^2/\omega^2) - (2\omega_p^2 A_0/\omega^2) - 4\omega_p^2 \sum A_{Ny}/(\omega^2 - N^2\Omega^2) \qquad (12)$$

where:

$$A_{Ny} = (N^2/s^2)\exp(-s^2/2)I_N(s^2/2) + (n_b/n_p)[(J_N')^2 + (sx_b/2)J_N'J_N'']$$

The function A_{Ny} is undulatory about zero, therefore, meeting the instability condition of Tataronis and Crawford (1970). Using a four-term approximation to the dispersion relation, instabilities are found

228

for (see Appendix B):

$$n_b/n_p = 10 \text{ and } x_b = 9$$

such that:

$$\omega/\Omega = 1.5 + 0.2i$$

and:

$$n_b/n_p = 10 \text{ and } x_b = 3$$

such that:

$$\omega/\Omega = 1.8 + 0.6i$$

Here it is shown that unstable solutions exist within the desired frequency range. The larger beam-to-background density ratios required to support the extraordinary mode are consistent with the work of Ohnuma et al. (1981).

C. The Ordinary Mode

The dispersion relation for the ordinary mode is obtained by substituting equation (8) into equation (7) and integrating to obtain:

$$D_{zz} = 1 - (k^2 c^2/\omega^2) - (A_{oz} \omega_p^2/\omega^2) - 2\omega_p^2 \sum A_{Nz}/(\omega^2 - N^2\Omega^2) \qquad (13)$$

where:

$$A_{Nz} = \exp(-s^2/2) I_N(s^2/2) + (n_b/n_p) J_N^2$$

Since A_{Nz} is always positive, no unstable solutions are anticipated.

CONCLUSIONS

The analytical solutions presented here show that electromagnetic non-resonant instabilities may be excited in a plasma represented as a Maxwellian background with a monoenergetic beam of electrons. The electromagnetic dispersion relation was solved for $k_\parallel = 0$, using the

229

approximation $\omega_p^2 \ll k^2 c^2$. These simplifications permit the elements of the dispersion relation to be separated and solved as three distinct eigenmodes of perpendicularly propagating waves:

1. Bernstein Mode; $\underline{E} \perp \underline{Bo}$, $\underline{k} \parallel \underline{E}$

2. Extraordinary Mode; $\underline{E} \perp \underline{Bo}$, $\underline{k} \perp \underline{E}$

3. Ordinary Mode; $\underline{E} \parallel \underline{Bo}$, $\underline{k} \perp \underline{E}$

In the first two cases it is shown that cyclotron harmonic modes may couple between the first two harmonics of the electron gyrofrequency, exciting non-convective instabilities with growth rates, γ, that are a finite fraction of ω_r. In the third case no unstable solutions exist. Sample solutions presented for the Bernstein and extraordinary modes are shown to depend on the ratios n_b/n_p and $x_b = v_{\perp b}/v_T$. These ratios must be greater than one.

The ratio, n_b/n_p, for the nearly electrostatic Bernstein mode can be compared quantitatively to the α of Tataronis and Crawford (1970) and the ratio N_c/N_H of Ashour-Abdalla et al. (1975) by considering the Maxwellian portion of the electron distribution as the "cold" component and the delta-function as the "hot" or "ring" component. The results for $n_b/n_p = 4.5$ and $x_b = 10$ agrees with the results for $\alpha = 0.2$ and $N_c/N_H = 0.2$. These are values associated with non-convective electrostatic instabilities at frequencies between the first two harmonics of the electron gyrofrequency.

For the extraordinary mode a larger density ratio, $n_b/n_p \approx 10$, is required to excite instabilities, consistent with the results of Ohnuma et al. (1981). These instabilities may be excited for velocity ratios of 3 and 9, representing ratios of the "artificial" and "natural" electron beam densities, respectively, to the ambient density. These

electromagnetic instabilities are non-convective, non-resonant, with large growth rates. They may be excited by electron beams, given sufficient beam-to-ambient density and velocity ratios. The full range of parameters over which they may occur will be explored through numerical calculations. For further understanding of the relationship of these waves to effects observed in the SCATHA data and in the magneto-sphere, the full electromagnetic dispersion relation, including the $k\parallel$ terms, must be solved for conditions pertaining to space vehicles in space plasmas.

ACKNOWLEDGEMENTS

REFERENCES

Abramowitz, M., and I. A. Stegun (Editors), Handbook of mathematical functions, NBS, AMS-55, 1964.

Ashour-Abdalla, M., G. Chanteur, and R. Pellat, A contribution to the theory of the electrostatic half-harmonic electron gyrofrequency waves in the magnetosphere, J. Geophys. Res., 80, 2775, 1975.

Ashour-Abdalla, M., and C. F. Kennel, Non-convective and convective electron cyclotron harmonic instabilities, J. Geosphys. Res., 83, 1531, 1978.

Donatelli, D. E., H. A. Cohen, and H. C. Koons, Waves observed during the SCATHA beam operations on day 114 1979, to be published.

Fredericks, R. W., Plasma instability at $(n+1/2)f_c$ and its relationship to some satellite observations, J. Geophys. Res., 76, 5344, 1971.

Gendrin, R., Initial expansion phase of an artificially injected elec-tron beam, Planet. Space Sci., 22, 633, 1974.

Krall, N. A., and A. W. Trivelpiece, Principles of plasma physics, McGraw-Hill Inc., 1973.

Kurth, W. S., M. Ashour-Abdalla, L. A. Frank, C. F. Kennel, D. A. Gurnett, D. D. Sentman, and B. G. Burek, A comparison of intense electrostatic waves near f_{UHR} with instability theory, Geophys. Res., Lett. 6, 487, 1979.

Mullen, E. G., M. S. Gussenhoven, H. B. Garrett, A "worst case" spacecraft environment as observed by SCATHA on 24 April 1979, AF geophs. Lab., AFGL-TR-81-0231, 1981, ADA108680.

Ohnuma, T., T. Watanabe, and K. Hamamatsu, Electromagnetic cyclotron waves, Jpn. J. Appl. Phys., 20, L705, 1981.

Sentmann, D. D., L. A. Frank, D. A. Gurnett, W. S. Kurth, and C. F. Kennel, Electron distribution functions associated with electrostatic emissions in the dayside magnetosphere, Geophs. Res. Lett., 6, 781, 1979.

Tataronis, J. A., and F. W. Crawford, Cyclotron harmonic wave propagation instabilities, part I, J. Plasma Phys., 4, 231, 1970.

Young, T. S. T., J. D. Callen, and J. E. McCune, High-frequency electrostatic waves in the magnetosphere, J. Geophys. Res., 78, 1082, 1973.

APPENDIX A

Solution for Bernstein Modes:

The dispersion equation for the Bernstein modes is:

$$D_{xx} = 1 - (4\omega_p^2/\Omega^2) \sum N^2\Omega^2 A_{Nx}/(\omega^2 - N^2\Omega^2) \tag{A-1}$$

where:

$$A_{Nx} = s^{-2}\exp(-s^2/2)I_N(s^2/2) + (n_b/n_p sx_b)J_N(sx_b)J_N'(sx_b)$$

This may be approximated:

$$D_{xx} = 1 - (4\omega_p^2/\Omega^2)[(A_1\Omega^2/(\omega^2 - \Omega^2)) + (4A_2\Omega^2/(\omega^2 - 4\Omega^2))] \tag{A-2}$$

Setting $D_{xx} = 0$ leads to the fourth order equation:

$$\omega^4/\Omega^4 - [5 + (4\omega_p^2/\Omega^2)(A_1+4A_2)] \omega^2/\Omega^2 +$$
$$4[1 + (4\omega_p^2/\Omega^2)(A_1 + A_2)] = 0 \tag{A-3}$$

This may be solved as a quadratic, then transformed to polar coordinates, to obtain:

$$\omega/\Omega = (Kr)^{1/2}[\cos(0/2 + m\pi) \mp i\sin(0/2 + m\pi)], \quad m = 0,1 \qquad (A-4)$$

where:

$$K = [5 + (4\omega_p^2/\Omega^2)(A_1 + 4A_2)]/2$$

$$r^2 = x^2 + y^2$$

$$0 = \tan^{-1}(y/x)$$

$$x = 1$$

$$y = [[16(1 + (4\omega_p^2/\Omega^2)(A_1 + A_2))/(5 + (4\omega_p^2/\Omega^2)(A_1 + 4A_2))^2] - 1]^{1/2}$$

For instability, the following condition must be satisfied:

$$0 < [5 + (4\omega_p^2/\Omega^2)(A_1 + 4A_2)]^2 < 16[1 + (4\omega_p^2/\Omega^2)(A_1 + A_2)] \qquad (A-5)$$

A_1 and A_2 are evaluated as functions of n_b/n_p using tabulated values of Bessel functions from Abramowitz and Stegun (1970) for the approximate range of the argument, as defined by the constraints on sx_b. Substituting these and the value of ω_p/Ω into the inequality (A-5), determines the constraints on n_b/n_p.

For $sx_b = 3.6$; $x_b = 20$; $n_b/n_p = 2$:

$$A_1 = 0.0464; \quad A_2 = -0.0132.$$

Substituting in equation (A-4) and solving for 0 and Kr:

$$\omega/\Omega = 1.95(0.89 + 0.45i) = 1.73 + 0.886i \qquad (A-6)$$

A second solution is found for $sx_b = 3.2$, $x_b = 10$. Then with $n_b/n_p = 4.5$; $A_1 = 0.078$, $A_2 = -0.0223$; and

$$\omega/\Omega = 1.83 + 1.14i$$

233

Solution for Extraordinary Modes:

The dispersion equation for the extraordinary mode is:

$$n_{yy} = 1 - (k^2c^2/\omega^2) - (2\omega_p^2 A_0/\omega^2) - 4\omega_p^2 \sum A_{Ny}/(\omega^2 - N^2\Omega^2) \qquad (B-1)$$

where:

$$A_{Ny} = (N^2/s^2)\exp(-s^2/2)I_N(s^2/2) + (2n_b/n_p)[(J_N'(sx_b))^2 + sx_b J_N'(sx_b)J_N''(sx_b)]$$

This may be approximated:

$$n_{yy} = 1 - (k^2c^2/\omega^2) - (2\omega_p^2 A_0/\omega^2) - 4\omega_p^2[(A_1/(\omega^2 - \Omega^2)) + (A_2/(\omega^2 - 4\Omega^2))] \qquad (B-2)$$

Setting $n_{yy} = 0$ leads to the sixth order equation:

$$(\omega^4 - 5(\omega\Omega)^2 + 4\Omega^4)[(\omega^2/k^2c^2) - 1 - (2\omega_p^2 A_0/k^2c^2)]$$
$$- (4\omega_p^2/k^2c^2)[\omega^4(A_1+A_2) - (\omega\Omega)^2(4A_1+A_2)] = 0 \qquad (B-3)$$

This may be reduced to a fourth order equation by using the approximation $\omega^2/k^2c^2 \ll 1$:

$$[1 + (2\omega_p^2 A_0/k^2c^2) + (4\omega_p^2/k^2c^2)(A_1+A_2)] (\omega/\Omega)^4 -$$
$$[5(1 + (2\omega_p^2 A_0/k^2c^2)) + (4\omega_p^2/k^2c^2)(4A_1+A_2)] (\omega/\Omega)^2 +$$
$$4[1 + (2\omega_p^2 A_0/k^2c^2)] = 0 \qquad (B-4)$$

This may be solved as a quadratic, then transformed to polar coordinates, analogous to the solution for the Bernstein mode of Appendix A, to obtain:

$$\omega/\Omega = (Kr)^{1/2}[\cos(\theta/2 + m\pi) \pm i\sin(\theta/2 + m\pi)], \quad m = 0,1 \qquad (B-5)$$

where:

$$r = [5(1 + 2\omega_p^2 A_0/k^2c^2) + (4\omega_p^2/k^2c^2)(4A_1+A_2)]/$$
$$2[1 + (2\omega_p^2 A_0/k^2c^2) + (4\omega_p^2/k^2c^2)(A_1+A_2)]$$

$$r^2 = x^2 + y^2$$

$$\theta = \tan^{-1}(y/x)$$

$$x = 1$$

$$y = [[16(1 + 2\omega_p^2 A_0/k^2c^2)[1 + (2\omega_p^2 A_0/k^2c^2) + (4\omega_p^2/k^2c^2)(A_1+A_2)]/$$
$$[5(1 + 2\omega_p^2 A_0/k^2c^2) + (4\omega_p^2/k^2c^2)(4A_1+A_2)]^2] - 1]^{1/2}$$

For instability, the following condition that must be satisfied:

$$0 < [5(1 + 2\omega_p^2 A_0/k^2c^2) + (4\omega_p^2/k^2c^2)(4A_1+A_2)]^2$$
$$< 16(1 + 2\omega_p^2 A_0/k^2c^2)[1 + 2\omega_p^2 A_0/k^2c^2 + (4\omega_p^2/k^2c^2)(A_1+A_2)] \quad (B-6)$$

A_N and A_{N+1} are evaluated as functions of n_b/n_p using the tabulated values of Bessel functions from Abramowitz and Stegun (1970) for the appropriate range of the argument as defined by the constraints on sx_b. Substitute these and the value of ω_p^2/k^2c^2 into the inequality (B-6) to obtain the constraints on n_b/n_p.

For $sx_b = 4.0$; $x_b = 9.0$; $n_b/n_p = 10$:

$A_0 = 1.05$, $A_1 = -0.714$, $A_2 = 2.72$. Substituting and solving for 0 and Kr:

$$\omega/\Omega = 1.55(0.99 + 0.14i) = 1.53 + 0.22i \quad (B-7)$$

A second solution is found for $sx_b = 4.4$; $x_b = 3$. Then with $n_b/n_p = 10$: $A_0 = 3.06$, $A_1 = -2.4$, $A_2 = 2.79$, and

$$\omega/\Omega = 1.8 + 0.6i$$

V. PAPERS, REPORTS, AND PRESENTATIONS

A. PAPERS

1. DMSP/F2 electron observations of equatorward auroral boundaries and their relationship to the solar wind velocity and north-south component of the interplanetary magnetic field, D.A. Hardy, W.J. Burke, M.S. Gussenhoven, N. Heinemann, and E. Holeman, J. Geophys. Res., 86, 9961-9974, 1981.

2. Extremely high latitude auroras, M.S. Gussenhoven, J. Geophys. Res., 87, 2401-2412, 1982.

3. DMSP optical and electron measurements in the vicinity of polar cap arcs, D.A. Hardy, W.J. Burke, and M.S. Gussenhoven, J. Geophys. Res., 87, 2413-2430, 1982.

4. Systematics of the equatorward diffuse auroral boundary, M.S. Gussenhoven, D.A. Hardy, and N. Heinemann, J. Geophys. Res., 88, 5692-5708, 1983.

5. Average electron precipitation in the polar cusps, cleft and cap, M.S. Gussenhoven, D.A. Hardy, and R.L. Carovillano, to be published in Proceedings of the Conference on the Morphology and Dynamics in the Polar Cusp, Lillehammer, Norway, 7-11 May 1984, D. Reidel, 1985.

6. A statistical model of auroral electron precipitation, D.A. Hardy, M.S. Gussenhoven, and E. Holeman, accepted for publication, J. Geophys. Res., 1984.

7. Equatorward auroral boundary variations with AE and D_{st}, R.E. Sheehan, M.S. Gussenhoven, and D.A. Hardy, to be submitted for publication.

8. The equatorward boundary of auroral ion precipitation, D.A. Hardy, M.S. Gussenhoven, and N. Heinemann, to be submitted for publication.

B. REPORTS

1. 1978 Diffuse Auroral Boundaries and a Derived Auroral Boundary Index, M.S. Gussenhoven, D.A. Hardy, N. Heinemann, and E. Holeman, Rep. AFGL-TR-82-0398, Air Force Geophysics Laboratory, Hanscom AFB, MA, 1982, ADA130175.

2. Electron Beam-Induced Electromagnetic Waves in a Magnetospheric Plasma, D.E. Donatelli and T.S. Chang, Rep. AFGL-TR-83-0085, Air Force Geophysics Laboratory, Hanscom AFB, MA, 1983, ADA130116.

3. "Requirements for validating system models," M.S. Gussenhoven, in Proceedings of the Air Force Geophysics Laboratory Workshop in Natural Charging of Large Space Structures in Near Earth Polar Orbit; 14-15 September 1982, R.C. Sagalyn, D.E. Donatelli, and I. Michael, eds. Rep. AFGL-TR-83-0046, Air Force Geophysics Laboratory, Hanscom AFB, MA, 1983, ADA134894.

4. Precipitating Electron and Ion Detectors (SSJ/4) for the Block 5D/Flights 6-10 DMSP Satellites: Calibration and Data Presentation, D.A. Hardy, L.K. Schmitt, M.S. Gussenhoven, F.J. Marshall, H.C. Yeh, T.L. Schumaker, A. Huber, and J. Pantazis, Rep. AFGL-TR-84-0317, Air Force Geophysics Laboratory, Hanscom AFB, 1985 (in press).

C. PRESENTATIONS AT MEETINGS

1. Presented at the Fourth Scientific Assembly of the International Association of Geomagnetism and Aeronomy (IAGA), Edinburgh, Scotland, August 2-15, 1981:

> THE SYSTEMATICS IN THE LOCATION OF THE EQUATORWARD BOUNDARY OF AURORAL ELECTRON PRECIPITATION AND THEIR RELATIONSHIP TO THE LARGE SCALE MAGNETOSPHERIC ELECTRIC FIELD, D.A. Hardy, M.S. Gussenhoven, W.J. Burke, N. Heinemann, and E. Holeman
>
> AURORAL ARCS IN THE POLAR CAPS, M.S. Gussenhoven, W.J. Burke, and D.A. Hardy
>
> PARTICLE PRECIPITATION IN THE POLAR CAPS, M.S. Gussenhoven (invited)

2. Presented at Yosemite '82 Conference on Origins of Plasmas and Electric Fields in the Magnetosphere, January 25-29, 1982, Yosemite, CA:

> THE BASELINE MAGNETOSPHERE; EMPIRICAL CONTRIBUTIONS, M.S. Gussenhoven (invited)

3. Presented at XXIV COSPAR, May 16-June 2, 1982, Ottawa, Canada:

> DYNAMICS OF THE DISTURBED IONOSPHERE, D.A. Hardy, M.S. Gussenhoven, E. Holeman, W.J. Burke, N. Saflekos, and R.C. Sagalyn
>
> ELECTRIC FIELD AND CURRENT MEASUREMENTS FROM S3-2: A SYNOPSIS, W.J. Burke, M. Smiddy, F.J. Rich, D.A. Hardy, R.C. Sagalyn, M.S. Gussenhoven, and M.A. Doyle.

4. Presented at Workshop in Natural Charging of Large Space Structures in Near Earth Polar Orbits, September 14-15, 1982, Air Force Geophysics Laboratory, Hanscom AFB, MA:

> REQUIREMENTS FOR VALIDATING SYSTEM MODELS, M.S. Gussenhoven

5. Presented at the Spring Meeting, American Geophysical Society, May 30-June 3, 1983, Baltimore, MD:

HIGH LATITUDE MAPS OF PRECIPITATING AURORAL ELECTRONS, D.A. Hardy, M.S. Gussenhoven, and E. Holeman

COMPARISON OF NEAR-SIMULTANEOUS ELECTRON POPULATIONS AT GEOSYNCHRONOUS AND LOW ALTITUDE REGIONS, T.L. Schumaker, M.S. Gussenhoven, and D.A. Hardy

6. Presented at the International Union of Geodesy and Geophysics, XVIII General Assembly, August 18-30, 1983, Hamburg, Germany:

COMPARISON OF GEOSYNCHRONOUS PARTICLE POPULATIONS WITH LOW ALTITUDE PRECIPITATING ELECTRONS, M.S. Gussenhoven, D.A. Hardy, and E.G. Mullen

SYSTEMATICS OF THE LOCATION OF THE EQUATORWARD BOUNDARY OF AURORAL PRECIPITATION, D.A. Hardy, M.S. Gussenhoven, E. Holeman, and R. Sheehan

7. Presented at the Fall Meeting, American Geophysical Society, December 5-9, 1983, San Francisco, CA:

THE EQUATORWARD BOUNDARY OF AURORAL ION PRECIPITATION, D.A. Hardy, M.S. Gussenhoven, and N. Heinemann

THE PRECIPITATING AURORAL IONS ASSOCIATED WITH THE ELECTRON INVERTED-V, H.C. Yeh, M.S. Gussenhoven, and D.A. Hardy

MORPHOLOGY OF THE POLAR RAIN, M.S. Gussenhoven and D.A. Hardy

END

FILMED

5-85

DTIC